7-2020

Piezoresistive Hybrid Nanocomposites for Strain and Damage Sensing: Experimental and Numerical Analysis

Audrey Jean-Miche Gbaguidi

PIEZORESISTIVE HYBRID NANOCOMPOSITES FOR STRAIN AND DAMAGE SENSING: EXPERIMENTAL AND NUMERICAL ANALYSIS

By

Audrey Jean-Miche Gbaguidi

A Dissertation Submitted to the Faculty of Embry-Riddle Aeronautical University
In Partial Fulfillment of the Requirements for the Degree of
Doctor of Philosophy in Aerospace Engineering

July 2020
Embry-Riddle Aeronautical University
Daytona Beach, Florida

PIEZORESISTIVE HYBRID NANOCOMPOSITES FOR STRAIN AND DAMAGE SENSING: EXPERIMENTAL AND NUMERICAL ANALYSIS

By

Audrey Jean-Miche Gbaguidi

This Dissertation was prepared under the direction of the candidate's Dissertation Committee Co-Chairs, Dr. Sirish Namilae and Dr. Daewon Kim, Department of Aerospace Engineering, and has been approved by the members of the Dissertation Committee. It was submitted to the Office of the Senior Vice President for Academic Affairs and Provost, and was accepted in the partial fulfillment of the requirements for the Degree of Philosophy in Aerospace Engineering.

DISSERTATION COMMITTEE

Co-Chairman, Dr. Sirish Namilae

Sirish Namilae
Digitally signed by Sirish Namilae
Date: 2020.07.08 12:20:04 -04'00'

Co-Chairman, Dr. Daewon Kim

Daewon Kim
Digitally signed by Daewon Kim
Date: 2020.07.16 10:37:13 -04'00'

Member, Dr. Marwan Al-Haik

Marwan Al-Haik
Digitally signed by Marwan Al-Haik
DN: cn=Marwan Al-Haik, o=Embry-Riddle Aeronautical University, ou=Aerospace Engineering, email=alhaikm@erau.edu, c=US
Date: 2020.07.13 13:39:44 -04'00'

Member, Dr. Jeff Brown

Jeff R. Brown
Digitally signed by Jeff R. Brown
Date: 2020.07.09 13:04:02 -04'00'

Member, Dr. Foram Madiyar

Foram Madiyar
Digitally signed by Foram Madiyar
Date: 2020.07.09 12:33:43 -04'00'

Graduate Program Coordinator,
Dr. Marwan Al-Haik

Marwan Al-Haik
Digitally signed by Marwan Al-Haik
DN: cn=Marwan Al-Haik, o=Embry-Riddle Aeronautical University, ou=Aerospace Engineering, email=alhaikm@erau.edu, c=US
Date: 2020.07.13 13:39:12 -04'00'

Date

Dean of the College of Engineering,
Dr. Maj Mirmirani

Date

Senior Vice President for Academic
Affairs and Provost,
Dr. Lon Moeller

Date

7-15-20

ACKNOWLEDGEMENTS

I would like to express my sincere appreciation and thanks to my advisors Dr. Sirish Namilae and Dr. Daewon Kim who provided me with the opportunity to perform this research work. Without their continuous support, guidance, suggestions and time, it would have not be possible to come this far. I would also like to thank Dr. Marwan Al-Haik, Dr. Jeff Brown and Dr. Foram Madiyar for being very patient and helpful while serving as committee members. I wish to thank Dr. Virginie Rollin, Dr. David Sypeck and Mike Potash for their help through the experimental work in this dissertation. Special thanks to my colleagues Boutros, Madhur, Nirmit, Pierrot, Rossana, Sandeep and Suma. Above all, I am grateful to my parents Septime and Juliette, my siblings and my girlfriend Laure, for believing in me and supporting me throughout these past years. This work was funded by NASA SBIR grant "Integrated Structural Health Sensors for Inflatable Space Habitats", ERAU internal grant and IGNITE grant.

ABSTRACT

Carbon nanomaterials such as carbon nanotubes (CNTs) and graphite nanoplatelets (GNPs) demonstrate remarkable electrical and mechanical properties, which suggest promising structural and functional applications as fillers for polymer nanocomposites. The piezoresistive behavior of these nanocomposites makes them ideal for sensing applications. Besides, hybrid nanocomposites with multiple fillers like carbon nanotubes (CNTs) and graphite nanoplatelets (GNPs) are known to exhibit improved electrical and mechanical performance when compared to mono-filler composites.

To comprehensively understand the mechanisms of electrical percolation, conductivity, and piezoresistivity in hybrid nanocomposites, the author develops a two-dimensional (2D) and a three-dimensional (3D) computational Monte Carlo percolation network models for hybrid nanocomposites with CNT and GNP fillers.

In the experimental studies correlated to the computational models, the author fabricates the hybrid nanocomposites made of both fillers using resin infiltration techniques and show an improvement of their electromechanical performance when compared to CNT nanocomposites. Due to the limitations of the resin infiltration techniques, the author develops an inkjet printing procedure with a new water-based CNT ink to fabricated printed nanocomposites on both polyimide film (Kapton) and paper with high device-to-device reproducibility. The ink formulation, as well as the substrate surface treatment, have been optimized to obtain conductive and piezoresistive devices. the author shows the effectiveness of the printed devices as strain sensors and impact damage sensors respectively under mechanical strains and hypervelocity impact damages. Devices printed with the minimum number of ink deposited layers lead to the best sensing performance.

TABLE OF CONTENTS

LIST OF FIGURES

Figure Page

4.10 Impact of addition of GNP fillers on the conductivity of CNT nanocomposites with different (a) CNT densities in equiaxed agglomerates and (b) cluster angles in high density agglomerates. CNT microstructures at their respective percolation threshold (P = 100%)…………………………………………... 99

Figure Page

Figure Page

Figure Page

LIST OF TABLES

NOMENCLATURE

d_{cutoff}	Tunneling cut-off distance
D	Filler's diameter
d_{mn}	Minimum distance between adjacent fillers
R_{int}^{CNT}	Carbon nanotube intrinsic resistance
σ_{cnt}	Carbon nanotube intrinsic conductivity
m_e	Mass of electron
ΔE, λ	Height of the barrier
M	Total number of conduction bands for CNT walls
R_c, R_t	Tunneling resistance
R_S	Sheet resistance
R_{int}^{GNP}	Graphene nanoplatelets intrinsic resistance
ν	Polymer Poisson's ratio
e	Electron charge
a_0	Ellipse semi-minor axis length
b_0	Ellipse semi-major axis length
d_{vdw}	Van der Waals separation distance
ε	Uniaxial strain
(a, b)	Weibull distribution parameters
SiO_2	Silicon dioxide
R_0	Unstrained or undamaged or initial resistance
R	Resistance after strain or after damage

K	Resistance change ratio
L_x, L_y, L_z	RVE length in x, y and z direction
rand	Random number
h	Planck constant
V_f^{agg}	Volume fraction of agglomerated fillers
$V_f^{non-agg}$	Volume fraction of non-agglomerated fillers
r_{agg}	Agglomeration cluster radius
r_{agg}	Agglomerate cluster angle
V_{50}	Percolation threshold or onset
V_{100}	Volume content at percolation probability of 100%
CNT	Carbon Nanotube
GNP	Graphene/Graphite Nanoplatelet
GP	Graphene/Graphite Platelet
RVE	Representative Volume Element
1D	One-dimensional
2D	Two-dimensional
3D	Three-dimensional
GF	Gauge factor
SWCNT	Single-wall carbon nanotube
MWCNT	Multi-wall carbon nanotube
PNC	Polymer Nanocomposites
GNS	Graphene Nanosheet

AC	Alternating Current
DC	Direct Current
MC	Monte Carlo
RSA	Random Sequential Addition
MMOD	Micrometeoroid and orbital debris
PBC	Periodic Boundary Condition
PET	Polyethylene Terephthalate
PE	Polyethylene
PDMS	Polydimethylsiloxane
NDE	Non-Destructive Evaluation
NASA	National Aeronautics and Space Administration
ISS	International Space Station
SEM	Scanning electron microscope

1. Introduction

In this first chapter the author talks about the importance of carbon nanotube and graphene nanoplatelets as well as their general applications while he discusses how that motivates the work in this dissertation. He also discusses the main objectives of this work and the different steps taken to achieve them.

1.1. Motivation

Electrically conductive nanofillers such as carbon nanotubes (CNTs) and graphene nanoplatelets (GNPs) exhibit outstanding mechanical (Changgu Lee, Wei, Kysar, & Hone, 2008; Q. Wang & Liew, 2009), electrical (J. C. Charlier, Eklund, Zhu, & Ferrari, 2008; Schönenberger, Bachtold, Strunk, Salvetat, & Forró, 1999), and electromechanical (Smith et al., 2013; Tombler et al., 2000) properties with unique morphologies. This combination of properties makes the nanostructures, ideal fillers to transform insulating polymers into conductive nanocomposites, enhancing both the mechanical and electrical properties. The global carbon nanotubes market was estimated at USD 3.5 Billion in 2016 and is expected to reach 15.02 Billion by 2026 (Watson, 2019). This huge market growth comes from the fact that CNTs are suitable for applications demanding durability, high strength, electrical conductivity, thermal conductivity, and lightweight. Also, their applications in end-use industries such as electrical and electronics are predicted to drive market growth. Graphene, the world’s thinnest and strongest material, has seen a market size of USD 42.8 million in 2017 and is projected to reach USD 552.3 million by 2025 (Grand View Research, 2019b, 2019a).

Applications such as automotive and aerospace, for their need in high strength and low weight composites; and semiconductors, energy storage, and sensors, for their need in highly conductive polymer composites will witness the fastest growth. These specifics applications of CNTs and graphene are primarily based on their nanocomposites which exhibit high electrical and thermal conductivities as well as excellent piezoresistivity. Conductive nanocomposites have found applications in advanced aerospace and medical technologies (X. Huang et al., 2011; I. Kang, Heung, et al., 2006), flexible electronics, anti-static coatings, sensors, batteries and solar-cells (Singh et al., 2011). Besides, the electromechanical behavior of these conductive nanocomposites enables their use in structural health monitoring as strain and damage sensors (Bae et al., 2013; Namilae & Choudhary, 2018). Multi-Walled Carbon Nanotubes (MWCNT) and Graphene Nanoplatelets (GNP) dominate the market due to the ease of their mass production. With the aforementioned reasons, it is critical to understand the mechanisms that control the electrical conductivity and the piezoresistivity of the nanocomposites made of one or both of the two fillers. This will help optimize and predict the properties of the nanocomposites and guide the production of the fillers as well as the fabrication processes and the design of the devices made from the nanocomposites. Moreover, rapid, scalable and affordable fabrication methods leading to high device-to-device reproducibility and more control over the device’s electrical properties are needed to make nanocomposites more competitive.

To understand the behavior of the nanocomposites, several numerical modeling and simulation techniques have been utilized. Due to the hierarchical nature of nanocomposites, ranging from molecular scale, mesoscale to macroscale, several phenomena occurring simultaneously at different time and length scales have to be studied (Masoud Safdari & Al-Haik, 2013; Zeng, Yu, & Lu, 2008). The molecular scale techniques, also called atomistic techniques are mainly based on molecular dynamics (MD) and study the time-evolution of atoms, molecules or their clusters. The formulation is based on a set of initial conditions (positions, velocities …), a potential field that defines the interactions between the particles, and the time evolution of the clusters that is governed by Newton equations of motion. The main advantage of atomistic models is that they enable the study of fundamental properties of the nanocomposites such as the formation kinetics of nanocomposites (Baljon, Lee, & Loring, 1999), the binding energy between polymer matrix and fillers (Tanaka & Goettler, 2002) and the molecular structure at the surface of nanoparticlea embedded in polymer matrix (Starr, Schrøder, & Glotzer, 2002). Limitations of these techniques are mainly computational due to very short time and length scales; thus they are very limited in scope (G. T. Pham, 2008). For numerical stability, the simulations usually require short time steps (about $2 \times 10^{-15} s$) with up to millions to trillions of sequential time steps needed. In addition, the analysis of systems with bigger size implies that each time step takes even a longer time.

At the upper end of the length spectrum, macroscale methods also called continuum methods such as finite element methods (FEM) homogenize the behavior of the material at the atomic and microscopic scales. FEM usually ignores the discrete and molecular structure of the nanocomposites and assumes that the material is continuous through its volume in order to predict its macroscopic behavior. It uses mesh generation to fully capture the spatial discontinuities in the materials. These methods are generally computationally efficient and very good at analyzing the thermo-mechanical behavior of the nanocomposites due to their bigger time and length scales. Several works have used FEM to study the electrical and piezoresistivity behaviors of nanocomposites (Oliva-

Avilés, Sosa, & Avilés, 2013; Prakash & Seidel, 2016). Their main disadvantage is the fact that the microstructural of the nanocomposites cannot be controlled. Besides, the fundamental properties of nanocomposites at atomistic scales cannot be examined.

The mesoscale techniques bridge the gaps between the atomistic methods and the continuum methods to solve some of their shortcomings. In mesoscale techniques, the material is modeled as a repetitive, representative volume element (RVE) with periodic boundary conditions (PBC) to represent the full-scale materials. Different microstructure phenomena at the microstructure levels such as agglomeration, tunneling effects, filler orientations have been modeled in the RVE using these techniques (Shen Gong & Zhu, 2014; B. Hu et al., 2012). In this dissertation, the author modeled nanocomposites with CNT and/or GNP fillers using and RVE with PBC enforced on all sides. Quantum tunneling effects at the nanoscale coupled with conductive networks due to adjacent fillers, at the microscale are both modeled in the RVE. Monte Carlo simulations are used to generate random configurations of the nanofillers in the RVE, based on the topological disorder in the microstructures of full-scale nanocomposites. Percolation theory (Crawford, 1991; Kirkpatrick, 1973; Seager & Pike, 1974; Stauffer, 2009) is then used to predict the electrical behavior of the RVE based on the tunneling effects and the conductive networks. The effective properties of the nanocomposites, such as electrical percolation onset, conductivity, and piezoresistivity are then derived from the RVE.

As explained earlier, applications in end-use industries such as electrical and electronics are driving the market growth of both CNT and GNP (Watson, 2019). Many deposition methods such as spray coating (S. Kim et al., 2010; V. H. Pham et al., 2010) and dip coating (Andrew Ng, Hartadi, Tan, & Patrick Poa, 2008; J. Liu, Hua, Li, & Yu,

2015) have been studied as ways to deposit CNTs and graphene on different substrates. However, these methods present limitations such as homogeneity and thickness control of the deposited films as well as their industrial productivity (Kholghi Eshkalak et al., 2017). Thus, alternative methods such as screen printing (Hyun, Secor, Hersam, Frisbie, & Francis, 2015; Karuwan, Wisitsoraat, Chaisuwan, Nacapricha, & Tuantranont, 2017; G. Zhang, Chen, Deng, She, & Xu, 2009), transfer printing (Abdelhalim, Abdellah, Scarpa, & Lugli, 2013; D. Song et al., 2017), and aerosol printing (Jabari & Toyserkani, 2015; D. Zhao, Liu, Zhang, Chen, & Wang, 2012) for printed nanocomposites based on CNTs or graphene have also been developed. However, recent developments in digital printing have made inkjet printing the most favorable method for printed electronics applications (Karim et al., 2017; Mattana & Briand, 2016; Torrisi et al., 2012; R. Tortorich & Choi, 2013) because of several advantages it has over traditional methods. Precise control of the electrical properties, thickness, and shape of the printed film is possible while maintaining high edge sharpness (Kholghi Eshkalak et al., 2017; Kwon et al., 2013). The possibility of using commercial or professional existing printers with no modification for the printing of nanocomposites makes this technique more versatile.

Also, since no prefabrication of templates or masks and no post-printing steps are required, due to the precision of the printing using a simple template in word processing or CAD software, it facilitates rapid and low-cost printing (Abulikemu et al., 2014; R. Tortorich & Choi, 2013). A wide variety of printing patterns and substrates can be accommodated. Multiple nanomaterials can also be simultaneously deposited on the substrates using the multiple cartridge setup that inkjet printers allow. All these aforementioned parameters are more challenging to control using traditional fabrication methods for nanocomposite. In this work, the author develops an inkjet printing procedure to fabricate CNT nanocomposites devices deposited on Kapton (polyimide films) and paper. The ink formulation, as well as the substrate surface treatment, have been optimized to obtain conductive and piezoresistive devices used as strain sensors and impact damage sensors.

1.2. Objectives of This Dissertation

In Chapter 2, the author reviews the current literature on conductive CNT or GNP polymer nanocomposites with a focus on hybrid nanocomposites made of CNT and GNP. While this area has attracted a lot of research, many questions on the fundamental aspects of the structure-property correlation of hybrid CNT-GNP nanocomposites remain unanswered. Particularly, the correlation between the microstructure (filler morphology, alignment, agglomeration, etc.) and electro-mechanical properties (conductivity, percolation, piezoresistivity), needs to be explored for the optimal design of materials. The primary objectives of this dissertation are to:

Investigate the behavior of thin-film nanocomposites. The author develops a 2D percolation based model in Chapter 3 to predict the performance of “thin films” CNT nanocomposites. The improvement of both electrical conductivity and gauge factor of the thin films, with the addition of GNP fillers to a CNT percolated network is examined. The effect of the content, the size, the aspect ratio and the alignment of the elliptical GNP filler on the percolation onset, the electrical conductivity, and the piezoresistivity is also studied. A validation of the numerical model with experimental works is also performed.

Study the effect of CNT agglomeration on the electrical properties of

nanocomposites. The author develops in Chapter 4 a novel agglomeration formulation to study realistic microstructures with CNT agglomeratea with non-uniform filler density, inhomogeneous distribution, and different agglomerate morphologies. This allows better control of the microstructure of hybrid CNT-GNP nanocomposites. Using a Monte Carlo model, the author studies the percolation threshold, electrical conductivity and piezoresistivity of the nanocomposites in the presence of agglomeration. The author finds the agglomeration parameters that can improve the aforementioned electrical properties of both monofiller and hybrid nanocomposites. The present results match the previous experimental and numerical works on CNT agglomeration.

Understand the mechanisms of electrical conductivity and piezoresistivity in hybrid nanocomposites with a focus on synergistic effects. In Chapter 5, a 3D percolation-based numerical model is developed to study hybrid CNT-GNP nanocomposites with different CNT-to-GNP volume content. The conditions that lead to synergistic enhancement of the electrical percolation threshold and conductivity are found while the microstructure parameters that control the behavior of hybrid nanocomposites are revealed for the first time. Additionally, the effect of both planar and transversal aspect ratio of elliptical GNP filler on the electrical performance of the nanocomposites are discussed for the first time. A comparison to experimental works is performed to validate the present results.

Evaluate current fabrication procedures of CNT/GNP polymer nanocomposites and develop an effective procedure to fabricate more performant and tailored conductive nanocomposites using inkjet printing technology. A wet layup or resin infiltration fabrication procedure is initially used in Chapter 6 to fabricate hybrid nanocomposite made of CNT buckypaper and GNP platelets. The electromechanical behavior under different loading conditions as well as the thermomechanical behavior under various temperature and frequency environments are studied. The limitations in terms of nanocomposite's performance and challenges due to the fabrication technique are addressed. In Chapter 7, the author develops a procedure to fabricate nanocomposites films printed on paper and Kapton substrates. A new ink formulation for very conductive materials is developed while a surface treatment of hydrophobic Kapton films is performed for improved quality and electrical properties of the printed nanocomposites. The sheet resistance of the printed nanocomposites is studied with respect to the number of deposited ink layers and compared to previous works in literature.

Demonstrate the effectiveness of the nanocomposites for strain sensing and damage sensing applications. The strain sensing performance, as well as the sensitivity to static and low-velocity impact damage of the hybrid nanocomposites fabricated through resin infiltration technique, are examined in Chapter 6. The strain sensing and damage sensing performances of the hybrid nanocomposites and the CNT monofiller nanocomposites are compared. In Chapter 7, the author uses inkjet printing technology to fabricate conductive devices for strain sensing and damage sensing. The performance of the strain sensors printed on Kapton films is evaluated in function of the number of printed layers of ink. The performance of the damage sensors printed on both paper and Kapton films is also evaluated in function of the number of layers. The author demonstrates the effectiveness of the damage sensors under static impact damage and hypervelocity impact damage to show their use as MMOD damage sensors.

2. Scientific Background and Literature Review

In this chapter, the author will discuss the fundamental properties of carbon nanotubes and graphene nanoplatelets and their use in nanocomposites. He will review the different fabrication processes, applications and numerical models for the behavior of nanocomposites. Special attention is given to the electrical and piezoresistive performance of the hybrid nanocomposites with CNT and GNP fillers.

2.1. Carbon Nanotubes

Carbon nanotubes (CNTs), specifically multi-wall carbon nanotubes (MWCNTs) were discovered in 1991 by Ijima (1991) as needle-like tubular carbon structures made of 2 to up to 50 concentric graphitic sheets, each separated by a distance of 0.34 nm. They were deposited on the hot tip of carbon cathode by the arc-discharge evaporation of carbon. Two years later, single-wall carbon nanotubes (SWCNTs), grown in the gas phase of carbon were discovered independently by two research groups (Bethune et al., 1993; Iijima & Ichihashi, 1993). A SWCNT is a sheet of graphene rolled up into a seamless cylindrical tube. The diameter of SWCNT is usually in the range of 1-2nm. MWCNT consists of several nested graphene cylindrical tubes, with an outer diameter ranging from 5 nm to hundreds of nanometers (Njuguna, 2012). CNTs can be a million times longer than their diameter.

The longest carbon nanotube reported so far is 550 mm long, grown on Si substrates using an improved chemical vapor deposition method (R. Zhang et al., 2013). CNTs price vary in function of several parameters such as purity, production methods, and type of CNT. MWCNTs usually cost between $0.5-100/g while SWCNTs, much more expensive, cost between $20-2000/g. The global carbon nanotubes market was estimated at USD 3.5 Billion in 2016 and is expected to reach 15.02 Billion by 2026 due to their unmatched mechanical and transport properties (Watson, 2019). MWCNTs are currently the more used type of CNTs due to their advantages over SWCNTs such as the ease of mass production, relatively low production cost per unit, enhanced thermal and chemical stability and improved technical know-how among the end-users.

2.1.1. Mechanical Properties

Carbon nanotube's unique molecular structure gives rise to, among others, impressive electrical and mechanical properties. Carbon nanotubes are the materials with one of the highest tensile strength and the highest elastic modulus, yet discovered. With their low density of 1.3 g/cm^3 for SWCNTs (Meyyappan, 2005) and 2.1 g/cm^3 for MWCNTs (Lehman, Terrones, Mansfield, Hurst, & Meunier, 2011) they have the best specific strength of known materials. Their strong covalent carbon-carbon (C-C) sp^2 bonds give them stiffness and axial strengths up to 100 times higher than steel (R. Zhang et al., 2013). Several experimental and theoretical studies have examined the elastic, inelastic, buckling, yield and fracture behaviors of both MWCNTs and SWCNTs (Chandra, Namilae, & Shet, 2004; Krishnan, Dujardin, & Ebbesen, 1998; Namilae, Chandra, & Shet, 2004; Nardelli, Yakobson, & Bernholc, 1998; Peng et al., 2008; Robertson, Brenner, & Mintmire, 1992; Treacy, Ebbesen, & Gibson, 1996; Wong, Sheehan, & Lieber, 1997; Yakobson, Brabec, & Bernholc, 1996; M. F. Yu, Lourie, et al., 2000; Q. Zhao, Nardelli, & Bernholc, 2002).

Due to the difficulty to fabricate isolated SWNTs, most of the reported mechanical properties are obtained through experimental studies of ropes or bundles of SWCNTs or using theoretical and numerical techniques. CNTs are characterized by tensile strengths in the range of 60 GPa, Young’s modulus in the range of 1TPa, with good bending behavior and easy recovery of their original shape after deformation. Also, they were found to fail at tensile strain up to 12% (Walters et al., 1999; M. F. Yu, Files, Arepalli, & Ruoff, 2000). The mechanical properties of CNTs can be affected mainly by their diameter (Salvetat et al., 1999; Q. Wang & Liew, 2009) and the presence of defects (Chandra et al., 2004; Namilae et al., 2004).

2.1.2. Electrical Properties

Due to their unique electronic graphitic structure and nanoscale tubular character (one-dimensional), CNTs have superior electrical properties. Generally, the electrical resistance (resistance to electron flow) in materials is enabled by electron collision with defects in the materials, which scatter electrons from their path and hence lowers the electrical conductance. With their 1-D structure, electrons can only travel forward or backward in CNTs. Defect-free metallic CNTs allow ballistic electronic transport i.e. without scattering and with essentially no heating (R. Zhang et al., 2013). Consequently, CNTs can carry high currents without heating with a current density in the range of 10^9 – 10^{10} A/cm^2, which is more than 1000 times greater than metals such as copper (Berger, Poncharal, Yi, & De Heer, 2003; Hong & Myung, 2007; W. Liang et al., 2001).

The electronic properties of CNT are determined by their chirality. The direction in which the graphene sheet is rolled up to obtain the CNT tube is determined by their chiral vector and is described by a pair of integer indices (n, m). n and m denote the number of unit vectors along the two directions in the crystal lattice of graphene. The chiral angle ϕ is the angle of the chiral vector. The CNT is a armchair CNT, if $n = m$ and $\phi = 0$. It is a zigzag CNT if $m = 0$ and $0^o<\phi<30^o$. Otherwise, the CNT is called chiral. CNTs are metallic if 2n+m = 3k, and non-metallic/semiconducting otherwise, where k is a nonzero integer (Bandaru, 2007). The lowest electrical resistivity of individual MWCNTs reported is $5 \times 10^{-6} \Omega cm$ (Schönenberger et al., 1999). The maximum electrical conductance of SWCNT is the double of the conductance of a single ballistic quantum channel (Jean Christophe Charlier, Blase, & Roche, 2007). This leads to a resistivity value as low as $10^{-6} \Omega cm$ (Meyyappan, 2005). Note that with the weak coupling between MWCNTs walls, the electronic properties of perfect MWCNTs are similar to those of SWCNTs.

With those exceptional electrical and mechanical properties, and due to the limitations of copper interconnects current densities by electromigration, many researchers are attempting to fabricate and commercialize highly conductive electrical wire assembled from individual CNTs (Kurzepa, Lekawa-Raus, Patmore, & Koziol, 2014). The electrical properties of individual CNTs are mainly influenced (lowered by orders of magnitude) by the presence of structural defects or impurities (W. Huang, Wang, Luo, & Wei, 2003), gazes (Jung, Han, & Lee, 2014; J. Kong et al., 2000; Zettl, 2000), strain and distortions (Rochefort, Salahub, & Avouris, 1998). Distortions of CNTs can happen when nanotubes tend to bend to conform to the morphology of the substrate, or during dispersion in polymer composites.

2.1.3. Electromechanical Properties

Regarding their excellent mechanical and electrical properties, as well as the well-known effect of strain and distortion on the electrical properties of CNTs, several authors have focused their work on the electromechanical behavior of CNTs. Piezoresistivity, piezoresistive or electromechanical behavior are terms used interchangeably to describe the change in electrical resistance of CNT due to mechanical deformation or strain. Tombler et al. (2000) used the tip of an atomic force microscope to deflect individual SWCNTs suspended over trenches fabricated on SiO_2 surface while measuring its electrical conductance. Both the deformation and electrical conductance of the CNTs were highly reversible, as the tip retracts. A decrease by more than two orders of magnitude of the electrical conductance was observed with a strain of 3%. Additionally, non-orthogonal tight-binding molecular dynamic simulations were performed and showed that strong local bonding deformation in the SWCNT is the cause of the piezoresistive behavior. For small bending angles (strain less than 0.7%), the nanotube retains its sp^2 bonding, however large bond distortion for the atoms under the tip creates the initial decrease of conductance. With an increase of the strain (up to 3.4%), with larger structural changes, the local bonding configuration changes from sp^2 to sp^3.

Furthermore, at the tip vicinity of the bent CNT, an increase in the $\sigma - electrons$ was seen to contribute to the decrease of the density in $\pi - electrons$. Since delocalized $\pi - electrons$ are responsible for electrical conduction in CNT, the decrease of their density leads to the reduction of the conductance (Rochefort et al., 1998). A second mechanism behind the electromechanical behavior of CNT is the change or alteration of their band gap due to mechanical strain (Crespi, Cohen, & Rubio, 1997; Minot et al., 2003). Using an atomic force microscope tip, Minot et al. (2003) were able to dramatically alter the band gap structure of CNTs (up to 60% reduction), through mechanical strain. Under strain, the conductance of the CNT was seen to increase or decrease, due to the increase or decrease in the band gap of the CNT under strain.

Different authors examined the performance of individual CNTs as nano electromechanical devices. R. C. Stampfer et al. (2006) fabricated a SWCNT pressure sensors using individual CNTs as the active transducer elements, deposited on top of an alumina membrane. A gauge factor of 210 was achieved. In another related work, a gauge factor of up to 2900 was obtained in their nano-electromechanical displacement sensor, based on an individual doubly cantilevered SWCNT subject to bending forces (Hierold, Jungen, Stampfer, & Helbling, 2007; C. Stampfer et al., 2006). Earlier works have proven the potential of individual CNTs as piezoresistors. Grow, Wang, Cao, Wang, and Dai (2005) investigated the electromechanical response of semiconducting and small-gap semiconducting SWCNTs used on silicon nitride membranes. Gauge factors up to 400 and 856 respectively for semiconducting and small-gap semiconducting were achieved. The electromechanical response and gauge factors of CNT composites are discussed later in Section 2.3.

With regard to their exceptional properties, there is a great interest in the use of individual CNTs in application such as data store (Rueckes et al., 2000), relays (Kinaret, Nord, & Viefers, 2003; Sang et al., 2004), oscillators (Nishio, Sawaya, Akita, & Nakayama, 2005; Papadakis et al., 2004), thermometer (Popov, Bichoutskaia, Lozovik, & Kulish, 2007), switches (Acquaviva et al., 2010; Cha et al., 2005), sensors (Fung, Zhang, Chan, & Li, 2005; Fung, Zhang, Dong, & Li, 2005; Grow et al., 2005; R. C. Stampfer et al., 2006), transducers (Miyashita, Ono, & Esashi, 2003; Walter et al., 2003; Williams et al., 2003), actuators (Akita et al., 2001; Baughman, Zakhidov, & De Heer, 2002; Fraysse et al., 2001; P. Kim & Lieber, 1999; J. Lee & Kim, 2005; Roth & Baughman, 2002; Spinks et al., 2002) and electrical wiring (Kurzepa et al., 2014; Lekawa-Raus, Patmore, Kurzepa, Bulmer, & Koziol, 2014).

2.2. Graphene

Graphene, which is a single layer of graphite, is a two-dimensional single-atom-thick structure of sp^2 bonded carbon atoms. It was discovered using a micromechanical cleavage also called scotch tape technique (Novoselov et al., 2004). That discovery resulted in the winning of the Nobel Prize in Physics, for “groundbreaking experiments regarding the two-dimensional material graphene” (A. Geim & Novoselov, 2010). Single-wall carbon nanotubes are one-dimensional objects obtained by rolling graphene into a cylindrical tube. Graphite is a three-dimensional allotrope of carbon made of stacks of graphene layers, weakly coupled by van der Waals forces. It became widely known after the invention of pencils in 1564 (Gordon & Petroski, 1992). Before its discovery and even though, it is the mother of all graphitic material (A. K. Geim & Novoselov, 2007), graphene was once thought impossible to exist in a free-standing or isolated form. It was finally spotted using an optical microscope, decades after the discovery of graphite, fullerenes, and CNTs, due to the subtle optical effect it creates on top of a chosen SiO_2 substrate.

Graphene or graphite nanoplatelet (GNP) are made from graphene sheets stacked on top of each other and separated by 3.8 Angstrom, to form a platelet morphology. In general, GNPs are 0.35-100 nm thick and have almost identical properties as graphene inside the graphitic planes and different properties along their stacking direction (Jang & Zhamu, 2008). Also, GNPs are structurally more stable than graphene, less expensive to produce and more versatile in size and aspect ratio (Masoud Safdari & Al-Haik, 2013).

2.2.1. Mechanical Properties

The theoretical specific surface area of graphene, of 2630 m^2/g is much larger than that of CNTs (100 to 1315 m^2/g) (Peigney, Laurent, Flahaut, Bacsa, & Rousset, 2001) and similar to that of activated carbon (3100 m^2/g) (Zhu et al., 2011). This allows graphene to be used as supercapacitors (Zhu et al., 2011). Several experimental and theoretical studies have examined the elastic properties of graphene (A. Geim & Novoselov, 2010; H. Kim, Abdala, & MacOsko, 2010; Changgu Lee et al., 2008). With an intrinsic strength of 130 GPa and Young’s modulus of 1 TPa, graphene is the strongest material ever measured (Changgu Lee et al., 2008). It was illustrated by the Nobel announcement by saying that a cat of 4 Kg could be held by a 1 m^2 of hammock made of graphene, weighting only 1 mg which corresponds to the weight of one of the cat’s whiskers (A. Geim & Novoselov, 2010).

Graphene is stretchable up to approximately 20% (Tomori et al., 2011). Graphene has a density of 2.2 g/cm^3 (J. H. Lee, Loya, Lou, & Thomas, 2014), an area density of 0.77mg/ m^2, and a breaking strength of 42 N/m (A. Geim & Novoselov, 2010). Despite its strength, graphene is also relatively brittle, with a fracture toughness of 4 MPa$\sqrt{m}$ measured as the critical stress intensity factor (P. Zhang et al., 2014), which is lower than many metallic materials (15-50 MPa$\sqrt{m}$). In work led by Edwin, the ability of graphene to absorb sudden impacts was studied. The specific penetration energy of multilayer graphene was found to be 10 times greater than that of macroscopic steel sheets at 0.6 km/s (J. H. Lee et al., 2014). Graphene could then make an excellent choice for lightweight ballistic body armor. Moreover large-angle-bent graphene was fabricated through uniaxial bending. Negligible strains were observed in the bent graphene which shows the mechanical robustness of graphene (Briggs et al., 2010).

2.2.2. Electrical Properties

Unlike CNTs, graphene is a zero band gap semiconductor, which charge carriers can be tuned continuously between hole and electron. With a remarkable electron mobility at room temperature around 15000 $cm^2V^{-1}s^{-1}$, hole and electron mobilities are nearly identical (J. C. Charlier et al., 2008). That mobility is independent of temperature in the range of 10 – 100 K. By minimizing impurity scattering, exceptional mobilities over 200 000 $cm^2V^{-1}s^{-1}$ were achieved in suspended graphene (Bolotin et al., 2008) at a carrier density of 10^{12} cm^{-2}, 10^7 times greater than that of copper. The corresponding conductivity of graphene is then $0.96 \times 10^6 \Omega^{-1} cm^{-1}$ which is higher than that of copper ($0.60 \times 10^6 \Omega^{-1} cm^{-1}$) (A. Geim & Novoselov, 2010). However, the charge transport of graphene is affected by the adsorption of contaminants such as water and oxygen molecules. Overall, transport is dominated by two modes: temperature-independent ballistic and thermally activated.

2.2.3. Electromechanical Properties

As shown in the case of CNTs, alteration of band gap structure is the source of CNT piezoresistivity. Despite its exceptional properties, graphene is inherently a zero-gap semiconductor. This means that it has no band gap and hence its change in resistivity due to strain is small (Castro Neto, Guinea, Peres, Novoselov, & Geim, 2009; Min, Sahu, Banerjee, & MacDonald, 2007). Several studies focused on ways to open a band gap in graphene in order to make it piezoresistive, such as fabrication of graphene nanoribons (Han, Ozyilmaz, Zhang, & Kim, 2007; Son, Cohen, & Louie, 2006) and use of electric field on bilayer graphene (Min et al., 2007). However, it was found that those techniques lead to significant deterioration of the graphene electronic performance (Cheng et al., 2010; Han, Brant, & Kim, 2010).

Recently, several groups were able to induce a band gap in graphene through the application of strain (Hosseinzadegan et al., 2012; Z. H. Ni et al., 2008; Smith et al., 2013; Tomori et al., 2011). Graphene was deposited on a flexible substrate, and tensile strain up to 0.8% was induced to the graphene through the strain loading of the substrate (Z. H. Ni et al., 2008). A small bang gap opening of 300meV was achieved. Later on, a method for inducing higher and non-uniform strain in graphene films using pillars made of dielectric material was developed (Tomori et al., 2011). A maximum stretch of up to 20% in the graphene film was achieved; showing the possibility of opening graphene band gap using this method. Using a similar technique, graphene membrane on a SiO_2 film was fabricated and strain was induced through pressure in a vacuum chamber (Smith et al., 2013). A gauge factor about 2.92 was obtained. Despite all the efforts, the gauge factor obtained through those studies was very low compared to individual CNTs. The highest gauge factor obtained with graphene was done using graphene films, two to three layers thick (Hosseinzadegan et al., 2012). Graphene films were placed over Si_xN_y membranes using a film transfer method. The resultant graphene membrane was deformed using a PZT actuator at resonance to obtain high strains. Using the resistance change of the membrane, a gauge factor of 17980 was obtained at a very small strain.

Due to their excellent mechanical and electrical properties and lower cost when compared to CNTs, individual graphene, more specifically GNPs offer an alternative to CNTs. They have similar applications as CNTs such as electronics (Eda, Fanchini, & Chhowalla, 2008; K. S. Kim et al., 2009), batteries, sensors, hydrogen storage and supercapacitors (A. K. Geim & Novoselov, 2007; Z. S. Wu et al., 2009) and nanosensor

(Hosseinzadegan et al., 2012; Smith et al., 2013).

2.3. Polymer Nanocomposites

Composites are materials made of at least two different components in order to utilize the best properties of each component. Nanocomposites are composites where at least one of the components has one dimension less than 100 nm (Ajayan, Schadler, & Braun, 2003). Polymer nanocomposites (PNCs) are a special type of nanocomposites where the host matrix is a polymeric material. The filler phase of PNCs is usually nanomaterials in the form of nanoparticles, nanofibers or nanoplatelets due to their ability to enhance the overall properties of the polymer. In addition, the enhanced properties obtained with low volume addition of the nanoparticles (1-5 vol%) into the matrix is comparable with the properties obtained with higher loadings of traditional macroscale material (15-40 vol%) (Erukhimovich & de la Cruz, 2004). This facilitates composites processing with very low weight. Here, the author is only interested in PNCs comprising CNTs or/and GNPs as the filler phase. With their exceptional mechanical and electrical properties, CNTs and GNPs enhance the overall mechanical, electrical, and thermal properties of the obtained PNCs and are also able to transform them into electromechanical polymers. Single filler phase PNCs, as well as hybrid ternary (two different filler phases) PNCs made of CNTs and/or GNPs, are reviewed in the following sections.

2.3.1. Carbon Nanotube Polymer Nanocomposites

The unique nanoscale tubular structure of CNTs (Bandaru, 2007; Baughman et al., 2002; De Volder, Tawfick, Baughman, & Hart, 2013), provides them with impressive intrinsic properties that make them very useful for many potential engineering applications as a filler in composite materials (Coleman, Khan, & Gun’ko, 2006; Javey, Guo, Wang, Lundstrom, & Dai, 2003). They have exceptional mechanical properties due to their high aspect ratios, and the fact that their surface, like each layer of graphene, consists of strong carbon-carbon covalent bonds (Bandaru, 2007). Despite those interesting properties, CNTs tend to agglomerate in their pristine form, which makes it challenging to harness their full potential (Vaisman, Wagner, & Marom, 2006). It is understood from previous research that huge improvement of the electrical and mechanical properties of carbon nanotubes (CNTs) can be obtained by dispersing them into insulating polymer matrices (Bauhofer & Kovacs, 2009; Breuer & Sundararaj, 2004; Gojny, Wichmann, Köpke, Fiedler, & Schulte, 2004; Kovacs, Velagala, Schulte, & Bauhofer, 2007). Depending on the polymer matrix and the type of CNTs, a conductivity order of magnitude between 10^{-5} and $10\ S\ m^{-1}$ for the composites were observed (Sandler, Kirk, Kinloch, Shaffer, & Windle, 2003). The application of these functional nanocomposites varies from lightning strike protection for aircraft, damage sensing, flexible and stretchable electronics, conductive coatings, electromagnetic shielding to solar cells (Berson, De Bettignies, Bailly, Guillerez, & Jousselme, 2007; Chou, Gao, Thostenson, Zhang, & Byun, 2010; Shang, Zeng, & Tao, 2011; C. Yu, Masarapu, Rong, Wei, & Jiang, 2009).

2.3.1.1. Electrical Conductivity of CNT-PNCs

Generally, the electrical behavior of nanocomposites is characterized using either their direct current (DC) properties or alternate current (AC) properties. For strain sensors applications, for example, the DC resistance of the PNCs is used. However, in the case of electromagnetic interference materials, AC impedance measurements are necessary. In the past decades, several experimental and theoretical/numerical studies have been carried out to study the electrical properties of CNT-PNCs. The investigator will focus this review on the DC electrical properties of PNCs.

The addition of very small loadings of CNT (0.1 wt% or less) to an insulating polymer enhances its electrical conductivity by several orders of magnitude, through the percolation process (Kirkpatrick, 1973). The percolation process is divided into three stages. In the first stage, the electrical conductivity of the PNC is very low since they are only a few fillers, and they are not able to form a conductive network (a path of filler which spans both electrodes of the PNC) through electron tunneling. In the second stage, as the amount of filler increases, the first conductive path is created and the conductivity of the PNC increases drastically, following the percolation power law. The volume fraction of filler at the sharp increase in conductivity is called the percolation threshold. In the final stage, numerous conductive paths are formed with the addition of more fillers. This leads to a further increase of the conductivity until its value converges at filler saturation. Several experimental and numerical works have shown that the electrical behavior of CNT-PNCs follows the percolation process (Behnam & Ural, 2007; C. Li, Thostenson, & Chou, 2008; Rahman & Servati, 2012; Yin et al., 2011; W. Zhang, Suhr, & Koratkar, 2006). With the huge amount of work done on the electrical conductivity of CNT-PNCs, the investigator will focus this discussion on a brief review of the different parameters that affect the electrical conductivity of CNT-PNC.

The fabrication process. Several fabrication processes such as bulk mixing (Y. Y. Huang & Terentjev, 2012), melt mixing (McNally et al., 2005; Meincke et al., 2004; Pötschke, Abdel-Goad, Alig, Dudkin, & Lellinger, 2004; Seo & Park, 2004), curing/in situ polymerization (Kymakis, Alexandou, & Amaratunga, 2002; Nogales et al., 2004;

Ounaies, Park, Wise, Siochi, & Harrison, 2003; C. Park et al., 2006) and coagulation (F. Du, Fischer, & Winey, 2003; G. Hu, Zhao, Zhang, Yang, & Wang, 2006; Ismail, Aziz, & Jaafar, 2012) have been used in literature to fabricate CNT-PNCs. Different polymer matrices can be used depending on the targeted application. Some common polymers are epoxy resins (N. Hu, Masuda, Yamamoto, et al., 2008; Martone, Formicola, Giordano, & Zarrelli, 2010; Montazeri, Javadpour, Khavandi, Tcharkhtchi, & Mohajeri, 2010), polycarbonate (PC) (F. Du et al., 2003; I. Kang, Schulz, Kim, Shanov, & Shi, 2006; E. J. Park, Kim, Park, & Shim, 2011; Pötschke, Bhattacharyya, & Janke, 2004), poly(methyl methacrylate) (PMMA) (I. Kang, Schulz, et al., 2006; G. T. Pham, Park, Liang, Zhang, & Wang, 2008) and polypropylene (Barber, Zhao, Wagner, & Baillie, 2004; Seo & Park, 2004). The choice of fabrication process depends also on the type of polymer. For example, in situ polymerization is usually preferred in case of epoxy resins. Due to all parameters involved in every fabrication process, which affect the formation of conductive paths in each polymer, it is very difficult to make a comparison of electrical properties across different polymers and fabrication processes (Bauhofer & Kovacs, 2009; N. Hu, Masuda, Yamamoto, et al., 2008). Nonetheless, using in situ polymerization process, it was shown that the curing temperature, as well as the mixing conditions, are the key factors in the fabrication process for highly conductive nanocomposites (N. Hu, Masuda, Yamamoto, et al., 2008).

Besides these conventional fabrication methods, inkjet printing has recently been used to fabricate conductive printed CNT nanocomposites (Beecher et al., 2007; Benchirouf et al., 2012; Homenick et al., 2016; Michelis, Bodelot, Bonnassieux, & Lebental, 2015). One of the main advantages is the ease of control of the electrical conductivity of the printed materials. The maximum filler content of the ink can be controlled and depend on the solvent used, as well as the sonication and centrifugation steps (R. Tortorich & Choi, 2013). In addition, the amount of ink ejected in each drop from the printer nozzle can be controlled with some professional inkjet printers (Castrejón-Pita et al., 2013). However, the main control of the electrical conductivity comes from the fact that the sheet resistance of the material can be controlled by the overwriting process where multiple layers of inks can be successively deposited on the same area of the substrate for higher conductivity (da Costa, Song, Tortorich, & Choi, 2015; Kwon et al., 2013; Lesch et al., 2014).

The percolation threshold of CNT composites. The possibility to transform an insulating polymer into a conductive one, with the lowest possible filler content is often desired in conductive PNCs (Njuguna, 2012). Experimental percolation thresholds ranging from 0.0021% to over 10 wt% for CNT in polymer matrix have been compiled from the literature (Bauhofer & Kovacs, 2009; Sandler et al., 2003). The lowest percolation thresholds have been obtained using epoxy matrix (Njuguna, 2012; Sandler et al., 2003). The wide variation of the percolation threshold is due to its dependence on the type of CNT and the fabrication process. A few papers focus on the influence of the fabrication process on the percolation threshold (Faiella, Piscitelli, Lavorgna, Antonucci, & Giordano, 2009; N. Hu, Masuda, Yamamoto, et al., 2008; Martin et al., 2004). Low stirring rates, shear forces, and high temperatures helped to obtain uniformly dispersed CNTs with lower percolation threshold and higher conductivity (Martin et al., 2004). This is explained by the fact that high temperature increases the mobility of CNTs, which leads to a dense conductive network with uniformly dispersed CNTs. Low stirring rates and shear forces limit the break-up of the conductive network.

The CNT aspect ratio. CNTs inherently have a high aspect ratio due to their one-dimensional structure. Several experimental works (Bai & Allaoui, 2003; M. J. Jiang, Dang, Xu, Yao, & Bai, 2007; Jing Li, Ma, et al., 2007; Martin et al., 2004; Rosca & Hoa, 2009) and numerical simulations (S. Gong, Zhu, & Meguid, 2015; Shen Gong & Zhu, 2014; B. M. Lee & Loh, 2015; Takeda, Shindo, Kuronuma, & Narita, 2011) have focused on the effect of aspect ratio on the percolation threshold and the electrical conductivity of CNT-PNCs. Lower percolation thresholds are usually obtained with CNTs of higher aspect ratio, for the same filler loading (Jing Li, Ma, et al., 2007). In addition, an increase of the conductivity by almost 10 times was observed with an increase in the aspect ratio of the CNT fillers (Rosca & Hoa, 2009). Those two experimental observations are confirmed in the numerical studies cited above.

The alignment of CNTs. Several techniques, including force, magnetic and electric field, induced alignment are used to align CNT individually in polymer composites (Akima et al., 2006; F. Du, Fischer, & Winey, 2005; Joselevich & Lieber, 2002; S. J. Kang et al., 2007; Lu et al., 2011; Lynch & Patrick, 2002; Oliva-Avilés, Avilés, & Sosa, 2011; Ural, Li, & Dai, 2002). Theoretical and experimental reports (Behnam, Guo, & Ural, 2007; F. Du et al., 2005; Qing Wang, Dai, Li, Wei, & Jiang, 2008; White, DiDonna, Mu, Lubensky, & Winey, 2009) show that the electrical conductivity and percolation threshold of CNT-PNCs are highly influenced by the alignment of CNT in the matrix. It is understood that the electrical conductivity has a non-monotonic dependence with the CNT alignment and reaches a maximum at a specific orientation, that varies with the CNT loading (F. Du et al., 2005). Compared to randomly aligned CNT-PNCs, higher conductivity (up to three orders of magnitude higher) and lower percolation thresholds were obtained in PNCs with CNTs aligned in specific directions (Qing Wang et al., 2008). Those results are validated by several numerical simulations in the literature (W. S. Bao, Meguid, Zhu, Pan, & Weng, 2012; Behnam et al., 2007; F. Du et al., 2005; S. Gong et al., 2015; C. Li & Chou, 2009).

2.3.1.2. Piezoresistivity of Conductive CNT-PNCs

With the excellent electromechanical behavior of individual CNTs shown earlier, several works have fabricated piezoresistive CNT-PNCs for strain sensing application using SWNTs (Dharap, Li, Nagarajaiah, & Barrera, 2004; I. Kang, Schulz, et al., 2006; Loh, Lynch, Shim, & Kotov, 2008; Nagarajaiah, Li, Dharap, & Barrera, 2008) or MWCNTs (Chang et al., 2010; M. Park, Kim, & Youngblood, 2008; G. T. Pham et al., 2008; Wichmann, Buschhorn, Böger, Adelung, & Schulte, 2008; Wichmann, Buschhorn, Gehrmann, & Schulte, 2009). The piezoresistivity is usually described by the resistance change ratio *K* (B. M. Lee, Loh, Burton, & Loyola, 2014):

$$K = \frac{R - R_0}{R} \tag{2.1}$$

where R_0 is the unstrained electrical resistance and R the resistance at a given strain. It is also described by the sensitivity or gauge factor *GF*:

$$GF = \frac{K}{\varepsilon} \tag{2.2}$$

where ε is the strain, GF is measured at. A brief review of the parameters that affect CNT-PNCs piezoresistivity will be done in this section. Note that the parameters are generally the same as the ones affecting the electrical conductivity even though their effect is usually different.

The sensor's unstrained resistance. Several experimental works have shown that nanocomposites with higher resistivity lead to higher sensitivity to strain (N. Hu et al., 2010; N. Hu, Karube, Yan, Masuda, & Fukunaga, 2008; I. Kang, Schulz, et al., 2006). This is explained by the fact that higher resistivity is usually the sign of a more sparse conductive network with very low CNT loading. Hence, the breaking of a conductive network, with very few conductive paths, due to strain will result in a huge variation of the resistivity (Alamusi et al., 2011). Inversely, for a conductive network with high CNT loading, and hence several conductive paths, the loss of one path due to strain shows a minor variation of resistivity.

The fabrication process. As in the case of electrical conductivity, the piezoresistivity of the nanocomposites is highly dependent on the fabrication factors such as stirring rate and curing temperature. N. Hu et al. (2010) showed that low curing temperature and high mixing speed result in higher nanocomposites sensitivities. This is in agreement with earlier results wherein high curing temperature and low stirring rate lead to nanocomposites with higher electrical conductivity. With the multitude of factors involved in a specific fabrication technique, with many different polymers studied in the literature for CNT-PNCs, it is difficult to correlate the fabrication techniques to the nanocomposite's sensitivity. It is possible however, to find some specific examples of the effect of processing. Using PMMA as the matrix, G. T. Pham et al. (2008) investigated the effect of dry blending and solution casting on the CNT- PNC sensitivity. The results show that a lower percolation threshold was observed for solution-based (1 wt%) nanocomposites compared to the dry blended ones (6 wt%). This is explained by the well-dispersed CNTs with the solution casting technique. However, the dry blended nanocomposites have much higher gauge factors than the solution based ones. It confirms once again that sensors with lower percolation, hence higher conductivity, lead to lower piezoresistivity.

The choice of the polymer matrix. The most significant effect of the polymer type on the piezoresistivity of the nanocomposites comes from its viscosity. This is because it has a huge effect on the mixing process and dispersion state of the CNT-PNCs depending on the fabrication process used (Alamusi et al., 2011). In addition, the maximum strain that the nanocomposites can reliably record depends on its polymer matrix. Polyurethane infiltrated CNT forests have recorded maximum strains in the range of 1000% (Njuguna, 2012). However, most of the nanocomposites made using epoxy, PMMA, PC or PS could only record small strain up to 1% (Anand & Roy Mahapatra, 2009; Bautista-Quijanoa, Avilésa, Aguilara, & Tapia, 2010; Chang et al., 2010; N. Hu et al., 2010; N. Hu, Karube, et al., 2008; Oliva-Avilés et al., 2011; M. Park et al., 2008; G. T. Pham et al., 2008; Rein, Breuer, & Wagner, 2011).

The CNT content. In most of the experimental works, the sensitivity to strain of the nanocomposites increases as the CNT loading decreases. The highest gauge factors are commonly observed close to the percolation threshold (N. Hu et al., 2010; I. Kang, Schulz, et al., 2006; M. Park et al., 2008; G. T. Pham et al., 2008; Wichmann et al., 2009; Yin et al., 2011). This can be explained by the fact that lower CNT loading leads to a sparse conductive network with few conductive paths as discussed previously. However, there have been some works which observed an increase of the piezoresistivity with the increase of CNT loading (Loh et al., 2008). The numerical simulations so far, to the author’s knowledge show that the decrease of CNT loading leads to an increase of the strain sensitivity of the CNT-PNCs (Shen Gong & Zhu, 2014; N. Hu et al., 2010; B. M. Lee & Loh, 2015; Z. Wang & Ye, 2013).

The morphological characteristics such as alignment and aspect ratio of CNT. There is little experimental work, characterizing the role of alignment (Oliva-Avilés et al., 2011) and aspect ratio on the piezoresistivity of the nanocomposites. However, few simulation studies have been performed to predict the effect of those parameters. The piezoresistivity of CNT-PNCs increased monotonically with the decrease of the CNT aspect ratio in highly dispersed nanocomposites (Shen Gong & Zhu, 2014). This prediction is intuitively acceptable since composites with lower conductivity seem to have higher piezoresistivity and CNTs with higher aspect ratio lead to lower percolation threshold and higher conductivity of the nanocomposites. Using numerical simulations, the piezoresistivity of the nanocomposites was very sensible to the orientation of the CNTs (N. Hu et al., 2010). However, due to instability in the numerical algorithm, maximum alignment of less than 50^o could not be investigated in that study.

The piezoresistivity increases with the increase of the maximum alignment of CNTs. The nanocomposites with randomly aligned CNTs (maximum alignment of 90^o) had the highest gauge factor. In another numerical investigation, the gauge factor of the composites with perfectly aligned CNTs (maximum alignment of 0^o) had a higher gauge factor than the composites with CNTs with a maximum alignment of 30^o (Theodosiou & Saravanos, 2010). The piezoresistivity of CNT-polysulfone (PS) composites as a function of alignment was experimentally studied (Oliva-Avilés et al., 2011). The gauge factor of the nanocomposites with CNTs aligned in the direction of the load (maximum alignment of 0^o) was two times higher than the one with randomly aligned CNT.

The strain-loading mode of the nanocomposites. Several works have experimentally studied the electromechanical behavior of CNT-PNCs under tensile strains (N. Hu, Karube, et al., 2008; Paleo et al., 2010; M. Park et al., 2008; Wichmann et al., 2009; Yasuoka, Shimamura, & Todoroki, 2007) and compressive strains (Dharap et al., 2004; N. Hu et al., 2010; Loh et al., 2008; Yin et al., 2011). It was observed experimentally that generally, for very small strain, about $\pm 1000\ \mu\varepsilon$ the piezoresistive behavior was linear and anti-symmetric about zero strain in both tensile and compressive loadings (Dharap et al., 2004; N. Hu et al., 2010; I. Kang, Schulz, et al., 2006; Nagarajaiah et al., 2008). However, for higher strain, the sensor gauge factor is higher in tension than in compression (Alamusi et al., 2011; N. Hu et al., 2010). This is explained by the fact that under tensile strain, the intertube distance between CNTs can increase indefinitely. The tunneling resistances between fillers will then most likely keep increasing which leads to a good sensitivity for all strain range. However, in compression, there is a minimum intertube distance constraint due to the non-overlapping restriction between CNTs.

As a result, for very small compressive strain, the sensor gauge factor is similar to the one in tension. However, with increasing strain, the intertube gap will more likely decrease until the CNTs come into contact and saturate (for strain greater than $1000\ \mu\varepsilon$). This will lead to almost no variation of the tunneling resistances due to saturation, and hence lower sensitivity to strain (Alamusi et al., 2011; Njuguna, 2012). Those observations were validated through several numerical simulations (S. Gong, Zhu, & Meguid, 2014; Shen Gong & Zhu, 2014; N. Hu et al., 2010).

2.3.2. Graphene Polymer Nanocomposites

CNTs have proven very effective as nanofillers for conductive and piezoresistive polymer nanocomposites. One of the drawbacks of CNTs as filler is their higher production cost, compared to GNPs (N. Liu et al., 2008; Y. Liu, Zhang, Wang, Liu, & Shang, 2016). Hence, the mass fabrication of CNT-PNCs can be relatively expensive. This difficulty is well explained by this thought: “When carbon fibers just won’t do, but nanotubes are too expensive, where can a cost-conscious materials scientist go to find a practical conductive composite? The answer could lie with graphene sheets” (Kotov, 2006, p. 254). Graphene with exceptionally good mechanical, thermal and electrical properties as well as cheap manufacturing cost is quite suitable as nanofiller in polymer matrixes for the development of high-performance nanocomposites (Kuilla et al., 2010).

2.3.2.1. Electrical Conductivity of GNP-PNCs

Similar to the review on CNT-PNCs, only the DC properties of the nanocomposites are discussed here. The addition of a minute quantity of GNP (as small as 0.1 wt%) to an insulating polymer enhances its electrical conductivity by several orders of magnitude like in the case of CNT. However, the electrical performance of CNT-PNCs and GNP-CNTs is not similar. Even though the conductivity of GNP-PNCs also follows the percolation theory (Halperin, Feng, & Sen, 1985; Kuilla et al., 2010; Y. C. Li, Tjong, & Li, 2010; Y. Li et al., 2011; Potts, Dreyer, Bielawski, & Ruoff, 2011), they usually result in higher percolation thresholds compared to CNT-PNCs. It has been demonstrated through theoretical and numerical studies that, for identical aspect ratio, disk-shaped particles percolate in volume contents two folds more than rod-shaped particles (Garboczi, Snyder, Douglas, & Thorpe, 1995; Jing Li & Kim, 2007). This is due mainly to the 2D shape of GNPs compare to 1D for CNTs.

Percolation threshold ranging from 0.1 to 15 wt% for graphene nanocomposites have been reported (Kuilla et al., 2010; V. Mittal, 2014; Potts et al., 2011) with induced composite electrical conductivity between 10^{-10} to 3300 S/m. A comparison of the lowest percolation threshold reported in the literature for CNT-PNCs (Bauhofer & Kovacs, 2009) and GNP-PNCs (Potts et al., 2011) shows an advantage for CNT-PNCs. In particular, epoxy-CNT composites have the lowest percolation threshold (0.0025 wt%) so far reported (Martin et al., 2004; Sandler et al., 2003). To prove that fact, J. Du et al. (2011) using the same polymer and same fabrication process for MWCNT-PNCs and GNP-PNCs, observed a percolation threshold of MWCNT-PNCs 7 times lower (volume fraction) with much higher conductivities compared to GNP-PNCs. Nonetheless, the cost and ease of manufacturing of GNP-PNCs make them ideal candidates to replace CNT-PNCs. Numerous experimental and numerical studies have focused on understanding and controlling the parameters that affect the percolation and electrical conductivity of GNP-PNCs (Biswas, Fukushima, & Drzal, 2011; Bora, Bharali, Baglari, Dolui, & Konwar, 2013; Filippone, Salzano De Luna, Acierno, & Russo, 2012; Gómez et al., 2011; Y. Li et al., 2011; J. Liang, Xu, et al., 2009; Pang, Chen, Zhang, Zeng, & Li, 2010; P. Song et al., 2011; Jialiang Wang et al., 2012; Jingchao Wang, Wang, Xu, Zhang, & Shang, 2011; J. Wu et al., 2013; H. Bin Zhang et al., 2010). Note that the parameters are very similar to the ones discussed in the case of CNT-PNCs.

They are generally four main fabrication techniques for incorporating graphene into a polymer: template synthesis, in situ intercalative polymerization, solution intercalation and melt intercalation (Kuilla et al., 2010; V. Mittal, 2009, 2014; Pavlidou &

Papaspyrides, 2008). A variety of polymer matrix have been used in literature for GNP-PNCs such as polystyrene (PS) (J. Liang, Wang, et al., 2009; Stankovich et al., 2006; W. P. Wang & Pan, 2004; Ye, Meng, Ji, Li, & Tang, 2009; Zheng, Lu, & Wong, 2004), poly (methyl methacrylate) (PMMA) (G. Chen, Wu, Weng, & Wu, 2003; Mutlay & Tudoran, 2014; Jialiang Wang et al., 2012), polystyrene sulfonate (PSS) (Kornmann, 2001), polyimide (PI) (Moujahid, Besse, & Leroux, 2003), poly(ethylene terepthalae) (PET) (Hsueh & Chen, 2003), polyethylene grafted maleic anhydride (PE-g-MA) (Hussain, Hojjati, Okamoto, & Gorga, 2006) and epoxy (Hsueh & Chen, 2003; Monti et al., 2013; Shen, Huang, Zuo, & Hou, 2005; J. Yu et al., 2007).

The conductivity of the GNP-PNCs is sensitive to the fabrication process as well as the type of polymer, even though the specific parameters affecting the sensitivity are sometimes unclear (He & Tjong, 2013; Kalaitzidou, Fukushima, & Drzal, 2007; H. Kim et al., 2011; Kuilla et al., 2010; Monti et al., 2013). Effect of different polymers and fabrication techniques on the conductivity of the nanocomposites has been observed (Gao, Picot, Bilotti, & Peijs, 2017; X. Jiang & Drzal, 2012; Jing Li, Vaisman, Marom, & Kim, 2007; Mahmoud, 2011; V. Mittal, 2014; Sullivan et al., 2015). Specific parameters such as coating (pre-mixing), or coating combined with compression molding lead to lower percolation onset and higher conductivities (Kalaitzidou, Fukushima, & Drzal, 2010; H. Wu & Drzal, 2013). Percolation thresholds of composites prepared by the solvent method using poly(ethylene oxide) were lower than that of melt blended method (Mahmoud, 2011), while the use of three roll mill technique produced higher conductivities and lower percolation thresholds than sonication (Chandrasekaran, Seidel, & Schulte, 2013).

Microstructural parameters like GNP aspect ratio and alignment affect its electrical behavior. Analytical and numerical models (Hicks, Behnam, & Ural, 2009; Jing Li & Kim, 2007; Mutlay & Tudoran, 2014; Sagalianov, Vovchenko, Matzui, & Lazarenko, 2017) and experiments (Eda & Chhowalla, 2009; Gao et al., 2017; He & Tjong, 2013; Kalaitzidou et al., 2010; H. Wu & Drzal, 2013) suggest that filler aspect ratio affects the percolation threshold and conductivity of the nanocomposites. Higher aspect ratio leads to higher conductivity and lower percolation (Eda & Chhowalla, 2009; Jing Li & Kim, 2007; Potts et al., 2011), similar to CNT-PNCs. The aspect ratio is usually controlled by varying the diameter or thickness of GNPs (Gao et al., 2017)

Similar to CNTs, GNPs alignment plays a major role in the percolation threshold. Aligned fillers in the nanocomposites result in higher percolation threshold values compared to randomly aligned fillers (Kalaitzidou et al., 2007, 2010; H. Kim & Macosko, 2008, 2009; Potts et al., 2011). Filler’s alignment was experimentally controlled by injection molding, compression molding, and long term annealing. In addition, it was observed that slight aggregation of the filler may also improve the electrical conductivity (Potts et al., 2011).

2.3.2.2. Piezoresistivity of Conductive GNP-PNCs

The mechanism of the piezoresistivity of CNT-PNCs, which is governed by modification of tunneling distance between filler and modification of percolating network due to breaking of conductive paths or construction of new conductive paths due to strain is the same for GNP-PNCs. Several experimental and numerical works have focused on the piezoresistivity of graphene-based nanocomposites (Bae et al., 2013; Bonavolontà et al., 2016; Das & Prusty, 2013; Eswaraiah, Balasubramaniam, & Ramaprabhu, 2011;

Filippidou, Tegou, Tsouti, & Chatzandroulis, 2015; Moriche, Jiménez-Suárez, Sánchez, Prolongo, & Ureña, 2017; Paek et al., 2017; Tian et al., 2014; Yan Wang et al., 2014; Zha, Zhang, Li, & Dang, 2016; J. Zhao et al., 2015). To validate the experimental findings, numerical simulations, that model the interaction between adjacent fillers were used by different authors. The parameters that affect the strain sensitivity of GNP-PNCs are somewhat similar to the one affecting CNT-PNCs.

The first parameter is the sensor unstrained resistance. Similar, to the case of CNT, it was observed through experimental studies that higher piezoresistivity is usually achieved in PNCs with higher unstrained resistance (Eswaraiah, Balasubramaniam, & Ramaprabhu, 2012; Hempel, Nezich, Kong, & Hofmann, 2012; Y. Liu et al., 2016; J. Zhao et al., 2012). The gauge factor increases monotonically with the unstrained resistance. The same conclusion was obtained through numerical simulations (Hempel et al., 2012). In addition, CNT-PNCs and GNP-PNCs with the same filler content were compared. Both the unstrained resistances and gauge factors of GNP-PNCs were much higher than the ones for CNT-PNCs (Y. J. Kim et al., 2011).

The second parameter is the GNP content. In the majority of experimental works, the increase of the GNP loading or number in the nanocomposites, above percolation, leads to the decrease of its unstrained resistance and sensitivity to strain (Eswaraiah et al., 2012; Jeong et al., 2015; Y. Liu et al., 2016; Moriche, Sánchez, Jiménez-Suárez, Prolongo, & Ureña, 2016; Ugarte et al., 2017; B. Wang, Lee, Kwak, & Lee, 2013; J. Zhao, Zhang, & Shi, 2013). Those findings were validated using several numerical analysis (Chiacchiarelli et al., 2013; D’Aloia, Tamburrano, De Bellis, & Sarto, 2011).

The third parameter is the aspect ratio of GNP. Very few experimental works examined the effect of GNP aspect ratio on the piezoresistivity. Lower GNP aspect ratio generally leads to higher unstrained resistance and sensitivity (Serra, Maeder, & Ryser, 2012). In the experimental investigation done by Sanchez, the aspect ratio was varied by using thicker GNPs. GNPs with lower aspect ratio leads to higher sensitivities to strain in both flexural, tensile and compressive load (Sanchez, Moriche, Prolongo, Rams, & Ureña, 2014). Their observation was confirmed by numerical modeling (Maxian, Pedrazzoli, & Manas-Zloczower, 2015).

The sensor sensitivity in tension was much higher than the one in compression, shearing and torsion loadings, for very large strain (6 to 10%) (Chun, Choi, & Park, 2017; X. Li et al., 2012; Moriche et al., 2016). However, for smaller strain (less than 0.4%), the piezoresistive behavior was found to be linear and the antisymmetric (Eswaraiah et al., 2012; Y. J. Kim et al., 2011; Moriche et al., 2016; B. Wang et al., 2013; J. Zhao et al., 2012). In several works done for GNP-PNCs, strains higher than 6% were achieved with gauge factors varying from 3 to more than 1000. On average, this indicates a higher performance than that observed in CNT-PNCs.

2.3.3. Electrical Conductivity of Carbon Nanotube-Graphene Hybrid Polymer Nanocomposites

The goal of hybrid composites is to be able to decrease the total filler loading, while maintaining comparable performance, or increase the performance by maintaining comparable total filler loadings, using a combination of two fillers. For example, polyetherimide (PEI) filled with 0.25 wt% CNT and 0.25 wt% GNP was found to have electrical conductivity significantly higher than that of 0.5 wt% CNT-PEI or 0.5 wt% GNP-PEI nanocomposites (Kumar et al., 2010). That is called a synergy effect. Synergy happens when the mixing of two fillers gives hybrid PNCs with performance greater than the performance obtained with mono-filler PNCs made of each filler separately; the total filler content of the PNCs (hybrid or mono-filler) are the same (Sagalianov et al., 2017). The cause of that synergy is related to the formation of a hybrid conductive network in which the CNT particles create bridges between the isolated GNPs. In addition, the presence of GNP may improve the dispersion of CNT and leads to better electrical properties (Al-Saleh, 2015). However, that synergy does not seem to happen for every conductive nanoparticle. In the fabrication of hybrid mixed copper nanoparticle (CuNP)-CNT-polypropylene (PP) nanocomposites, the presence of CNT was found to improve the dispersion of the CuNP particles but with no effect on the electrical conductivity (Palza, Garzón, & Arias, 2012). Similar conclusions were observed for mixed silver nanoparticle (AgNP)-CNT-PP nanocomposites (G. D. Liang, Bao, & Tjong, 2007).

Al-Saleh (2015) fabricated mixed CNT-GNP-PP nanocomposites to study their synergistic properties. The electrical percolation thresholds of CNT-PP was found to be twice lower than the one of GNP-PP. The addition of CNT fillers drastically lowers the electrical resistivity and percolation threshold of the hybrid composite. For example the GNP:CNT weight fraction combination 2:1 in GNP-CNT-PP has the same resistance as the 20 wt% GNP-PP nanocomposites. Note that the percolation threshold of GNP-PP composites was 7 wt%. In addition, the effect of the GNP-to-CNT wt% ratio (GNP:CNT) on the electrical conductivity of the hybrid nanocomposites with constant nanofiller total volume fraction was studied. The electrical resistance decreases from its maximum (resistance of GNP-PP) to its minimum (resistance of CNT-PP) as the GNP:CNT decreases from 5:0 to 0:5. Even though the addition of CNT, improves greatly the electrical behavior of the CNT-GNP-PP hybrid composites compared to GNP-PP composites, no synergistic effect was observed since the performance was still lower than the one of CNT-PP composites. Similar observations were made for CNT-GNP-epoxy with a ratio of 1:1 (Jing Li, Wong, & Kim, 2008) and for different ratios of CNT:GNP for CNT-GNP-polycarbonate (PC) (Wegrzyn, Ortega, Benedito, & Gimenez, 2015).

Ren et al. (2012), fabricated mixed CNT-GNP-polyethylene (PE) nanocomposites with segregated network of CNT and graphene nanosheet (GNS) instead of well-dispersed fillers. This is because, as explained above, segregated filler leads to lower percolation threshold and higher conductivity compared to well-dispersed ones. The percolation threshold and resistivity of segregated CNT-PE were lower than the ones with randomly dispersed CNT and lower than the segregated GNS-PE ones. The percolation thresholds of CNT-GNS-PE with GNS:CNT ratio of 1:1 and 1:3 are lower than the one for CNT-PE and GNS-PE at the same content of all fillers. To understand the effect of GNS:CNT ratios, the classification of the hybrid with lower percolation threshold and electrical resistivity in decreasing order is the GNS:CNT ratio 1:3, 1:1 and 3:1. Similar synergistic observations are reported for CNT-GNP-polycarbonate (PC) with a GNP-CNT weight ratio of 3:2, where much lower percolation threshold and resistivity was observed at lower fillers content compared to CNT-PC or GNP-PC (Maiti & Khatua, 2016).

2.3.3.1. Piezoresistive Behavior

The goal of adding a second filler to a mono-filler composite for the piezoresistive performance is two folds. First, since for monofiller composites the highest gauge factor happens close to the percolation threshold, it would be interesting to achieve much higher gauge factors by adding a second filler to the existing monofiller percolated network. Secondly, if the gauge factor of the hybrid CNT-GNP-PNCs at a CNT+GNP filler content lower or equal to the percolation threshold of CNT-PNC and or GNP-PNC, is higher than the gauge factor of CNT-PNC and GNP-PNC close to percolation, a synergistic effect on the piezoresistivity exists. Very few works have been found in literature, examining the piezoresistive behavior of hybrid CNT-GNP nanocomposites (S. H. Hwang, Park, & Park, 2013; S. H. Hwang, Park, Park, et al., 2013; Curtis Lee, Jug, & Meng, 2013; Luo & Liu, 2013)

The piezoresistivity of hybrid CNT-GNP-polyethylene terephthalate (PET) was investigated and compared with the behavior of CNT-PET and GNP-PET composites (Luo & Liu, 2013). The piezoresistivity and resistivity of GNP-PET close to its percolation threshold is higher than the ones of CNT-PET close to its percolation threshold (lower than GNP-PET percolation). The addition of more GNP to the CNT-PET (CNT loading kept constant) increases the conductivities and gauge factors of the hybrid composites, compared to CNT-PET conductivity and gauge factor. However, for the same content of GNP, in GNP-PET and CNT-GNP-PET composites, the conductivity and piezoresistivity of GNP-PET are always higher but decreases with the increase of the GNP content. The improvement of piezoresistivity can be observed here by the addition of GNPs to CNT-PET.

The investigator has shown in above discussions that increasing the CNT loading in CNT-PNCs, after percolation leads to a decrease of the composite resistance and hence the decrease of its sensitivity. However, after the percolation of CNT-PNCs the addition of GNPs (instead of CNTs) leads to the opposite behavior. Even though the resistance decreases, the sensitivity increases. If for CNT-PET the highest gauge factor is obtained close to the percolation onset, adding a GNP filler unlock that limitation and allows for an even higher gauge factor. In the case of GNP-PET, no improvement of piezoresistivity happens. The addition of a fixed amount of CNT to the GNP-PET leads to the decrease of resistance and sensitivity of the CNT-GNP-PET when compared to GNP-PET performance. Note that the addition of a second filler is done here on an already percolated network of the mono-filler composites.

The effect of the addition of a second filler to a non-percolated mono-filler network has been examined (Curtis Lee et al., 2013). Polydimethylsiloxane (PDMS)-CNT and PDMS-GNP were fabricated with respective percolation threshold of 5 wt% and 12.5 wt%. The two mono-filler composites are then compared to CNT-GNP-PDMS composites with 2.5% wt% for each filler. The resistance and gauge factor of the hybrid composites were at least four times higher than the ones for GNP-PDMS but still slightly lower than the ones for CNT-GNP-PDMS. In this case, the addition of CNT to GNP-PDMS enhanced the sensitivity of hybrid composites, with lower fillers concentration, compared to GNP-PDMS. Similar experimental work was done where the fillers’ total weight fraction was kept constant for CNT-PNCs and CNT-GNP-PNCs. The GNP content was varied to see the effect on the piezoresistivity (S. H. Hwang, Park, & Park, 2013; S. H. Hwang, Park, Park, et al., 2013). The resistivity and piezoresistivity of the hybrid increases with the increase of the GNP content from 0 to 70 wt%. The addition of GNP to CNT-PNCs enhanced the piezoresistivity of the hybrid composites.

2.3.3.2. Numerical Simulations for Hybrid Nanocomposites

Hybrid nanocomposites consisting simultaneously of CNTs and GNPs fillers have been fabricated to improve the performance and reduce the cost of fabrication for their use as multifunctional materials (Sagalianov et al., 2017; A. Yu et al., 2008; Yue, Pircheraghi, Monemian, & Manas-Zloczower, 2014). However, the existing experimental data report disparate and sometimes contradictory information about the influence of parameters such as CNT and GNP content on the different performance of the hybrid nanocomposites (Maxian et al., 2015; Sagalianov et al., 2017). In addition, very little attention is paid to parameters such as fillers aspect ratio and relative aspect ratio on the results of the different experimental works. A combination of CNT and GNP with different ratios have given different results in the literature. This calls for the development of numerical models that can explain to some extent those observations and guide researchers toward a good choice of hybrid microstructures. Few numerical and theoretical works have been implemented for that purpose. They all model only the percolation behavior of the hybrid nanocomposites, with no information on its piezoresistive behavior (Yuli Chen, Pan, Wang, Liu, & Zhang, 2015; Maxian et al., 2015; Masoud Safdari, 2012; Sagalianov et al., 2017).

A 3D Monte Carlo percolation model without tunneling interaction, with fillers modeled with the softcore approach, was used very recently to study hybrid CNT-GNP-PNCs (Sagalianov et al., 2017). For CNT and GNP of equal aspect ratio, the CNT length-to-GNP diameter ratio was seen to have little effect on the percolation of the hybrid composites. For CNT length-to-GNP diameter ratio of 1, the increase of the GNP aspect ratio with a fixed CNT aspect ratio (and vice versa) reduces the percolation threshold. For CNT length-to-GNP diameter ratio of 1, with CNT and GNP of equal aspect ratio, percolation thresholds up to 35% lower than the one for CNT-PNCs and 60% lower than the one for GNP-PNCs were obtained (presence of synergy). When the difference between the aspect ratios of CNT and GNP increases, the synergy effect degrades. For hybrid PNCs with CNT and GNP aspect ratio respectively of 200 and 50, the synergistic effect on percolation disappears. Even in that case small addition of CNT to GNP-PNCs leads to hybrid PNCs with percolation threshold 5 times lowers than GNP-PNCs and almost equal to CNT-PNCs. The electrical conductivity was not modeled in the study.

Maxian et al. (2015) performed a similar study, where the tunneling effect was taking into account with fillers modeled with a hardcore approach. The effect of different contents of CNT and GNP in the hybrid PNCs was examined. Hybrid PNCs with percolation threshold values lower than the one of GNP-PNCs was obtained. The percolation threshold decreases with the increase of CNT content in the hybrid PNC but is still 16 times higher than the one of CNT-PNCs (no synergy effect). Also increasing the aspect ratio of GNP in the hybrid PNCs decreases the percolation threshold. The opposite happens with CNT. The electrical conductivity was not included in the model.

M. Safdari and Al-Haik (2012) developed a numerical model, based on the tunneling effect to predict both percolation threshold and electrical conductivity of hybrid CNT-GNP nanocomposites. GNP is modeled as the main filler and CNT as the auxiliary filler using a hardcore approach. The CNT-to-GNP volume fraction ratio was kept constant at 0.01. Increasing the aspect ratio of CNT leads to a huge decrease in the hybrid percolation threshold, with values always lower than the one for GNP-PNCs. This effect is dominant for small values of GNP aspect ratio. The conductivity follows the same trend as the aspect ratio, with higher conductivity for the hybrid PNCs.

With regard to those numerical models, there is a need of numerical modeling that studies both the electrical conductivity and percolation threshold of hybrid CNT-GNP PNCs and that can predict the effect of the fillers aspect ratio, volume fraction as well as CNT aspect ratio, relative to GNP aspect ratio. In addition, the specific hybrid microstructures that can lead to a synergistic effect should be predicted by the model. With the lack of piezoresistive models for CNT-GNP hybrid PNCs in literature, it is urgent to develop a numerical framework capable to simulate the electromechanical behavior of the hybrid PNCs.

Overall, this section demonstrates experimentally and numerically that it is possible to effectively substitute a small amount of GNP by CNT and vice versa to obtain a hybrid PNC with percolation better than any of CNT-PNCs or GNP-PNCs separately. However, only specific CNT-GNP microstructures enable that synergy effect. Since CNT is usually more expensive, and have better percolation threshold compared to GNP, it is possible to gain in both cost and performance using the hybrid PNCs.

2.4. Fabrication Techniques of Nanocomposites

As explained in Section 2.3, several processing methods have been used in the literature for the fabrication of nanocomposites made of CNT and/or graphene. The main goal of the fabrication techniques is to incorporate uniformly, dispersed CNTs or GNPs into the polymer matrix such that a good interfacial interaction or wetting between the polymer and the fillers is obtained (Khan, Kausar, & Siddiq, 2015). The most common nanocomposites processing methods are solution processing, melt processing and in situ polymerization. Depending on the desired properties (mechanical, electrical, thermal) of the nanocomposites, the thermal and chemical properties of the polymer as well as the ease of its synthesis from the chosen monomer and the fabrication cost, a suitable processing method can be used.

2.4.1. Solution Processing

In this method, either the polymer or the nanoparticles or both are separately dissolved into a solvent and then mixed using dispersion methods such as shear mixing, magnetic stirring or sonication. The solvent is then evaporated or removed by filtration to obtain the nanocomposites. The main advantage of this method is the possibility to achieve a good dispersion of the nanofillers in the solvent before incorporation into the polymer. In addition, the viscosity of the polymer can be reduced with the addition of the solvent, which also facilitates the dispersion in the nanocomposites (Breuer & Sundararaj, 2004). However, this technique cannot be used for insoluble polymers (Byrne & Guin'Ko, 2010; Dey, Bajpai, Sikder, Chattopadhyay, & Shafeeuulla Khan, 2016). Several CNT and GNP-based nanocomposites have been fabricated with this method (Q. Bao, Tang, Zhang, & Loh, 2012; Breuer & Sundararaj, 2004; Coleman et al., 2003).

2.4.2. Melt Processing

Common alternative for insoluble polymers, melt mixing techniques are specially developed for thermoplastics. A molten polymer is obtained by melting polymer pellets and is mixed with nanoparticles. Compared to solution processing, melt processing lead to less contamination because of their solvent-free nature (Masoud Safdari & Al-Haik, 2013). The advantages of this technique are its speed, simplicity, affordability, while it is compatible with standard industrial techniques such as extrusion, injection molding and compression molding (Andrews, Jacques, Minot, & Rantell, 2002). However, the high temperatures needed for this method can lead to unexpected degradation and oxidation of the polymer and damage to the nanofillers (Jordan, Jacob, Tannenbaum, Sharaf, & Jasiuk, 2005). Examples of nanocomposites filled with CNTs or GNPs using this method are (Kalaitzidou et al., 2010; Sennett et al., 2003).

2.4.3. In Situ Polymerization

Nanoparticles are first dispersed in a monomer or multiple monomers and the mixture is polymerized under certain conditions (Coleman, Khan, Blau, & Gun'ko, 2006). One main advantage of this technique is that unlike solution processing and melt mixing, insoluble and thermally unstable polymers can be processed with in situ polymerization (Saini, 2013, 2015). Also, this method allows the fabrication of composites with high nanoparticle loadings (Byrne & Guin'Ko, 2010) because it improves dispersion state and integration between the polymer and the fillers (Breuer & Sundararaj, 2004). This method is also widely used for conductive polymers (G. Z. Chen et al., 2000; Maser et al., 2003). However, because low viscosity polymer is usually needed for materials like elastomer (Papageorgiou, Kinloch, & Young, 2015), this technique is not as popular as the others. In addition, the macromolecular chains of the polymer may become attached to the nanofillers, hence preventing the formation of conductive networks between fillers and leading to lower electrical conductivity values (Ghaleb, Jaafar, & Rashid, 2019). Several works have been done using this technique (Ma, Siddiqui, Marom, & Kim, 2010;

Moniruzzaman & Winey, 2006; O'Neill, Bakirtzis, & Dixon, 2014; L. Zhang, Tu, Wang, & Du, 2018).

2.4.4. Inkjet Printing

Applications in end-use industries such as electrical and electronics are driving the market growth of both CNT and GNP composites (Watson, 2019). Printed flexible electronics made of those fillers have demonstrated great potential in applications in transistors (Beecher et al., 2007; C. Cao, Andrews, & Franklin, 2017; Homenick et al., 2016), radio frequency identification tags (Chauraya et al., 2013; L. Yang, Staiculescu, R. Zhang, Wong, & Tentzeris, 2009; Li Yang, Zhang, Staiculescu, Wong, & Tentzeris, 2009), health industry (Abera & Choi, 2010; D. H. Kim et al., 2011; Yeo et al., 2013), sensors (Kulkarni, Apte, Naik, Ambekar, & Kale, 2013; Trichur, 2014; Varghese, Lonkar, Singh, Swaminathan, & Abdala, 2015; T. Zhang, Mubeen, Myung, & Deshusses, 2008), energy storage (P. Chen, Chen, Qiu, & Zhou, 2010; Grande et al., 2012; Siliang Wang et al., 2015; Y. Xu et al., 2014) and photonics (Azoubel, Shemesh, & Magdassi, 2012; Dodoo-Arhin et al., 2016; Marquardt et al., 2010). Many deposition methods such as spray coating (S. Kim et al., 2010; V. H. Pham et al., 2010) and dip coating (Andrew Ng et al., 2008; J. Liu et al., 2015) have been studied as ways to deposit CNTs and graphene on different substrates.

However, these methods present limitations such as homogeneity and thickness control of the deposited films as well as their industrial productivity (Kholghi Eshkalak et al., 2017). Thus, alternative methods such as screen printing (Hyun et al., 2015; Karuwan et al., 2017; G. Zhang et al., 2009), transfer printing (Abdelhalim et al., 2013; D. Song et al., 2017) ,and aerosol printing (Jabari & Toyserkani, 2015; D. Zhao et al., 2012) for printed nanocomposites based on CNTs or graphene have also been developed. Nonetheless, recent developments in digital printing have made inkjet printing the most favorable method for printed electronics applications (Karim et al., 2017; Mattana & Briand, 2016; Torrisi et al., 2012; R. Tortorich & Choi, 2013).

With inkjet printing, the thickness of the printed layer, its electrical conductivity as well as its size is precisely controlled while maintaining high edge sharpness. This is enabled by the fact that the amount of ink deposited in a single printed layer is determined by the distance between two droplets of ink and the volume of the droplets (Seifert et al., 2015), while the thickness and the conductivity of the layer can be increased by printing in the same position on the substrate as many time as needed using the overwriting method (da Costa et al., 2015; Kwon et al., 2013; Lesch et al., 2014). These parameters are more challenging to control using the previous method of nanocomposite fabrication discussed earlier. The possibility of using commercial or professional existing printers with no modification for the printing of nanocomposites made this technique more popular. In addition, since no prefabrication of templates or masks and no post-printing steps are required, due to the precision of the printing using a simple template in word processing or CAD software, it facilitates rapid and low-cost printing (Abulikemu et al., 2014; R. Tortorich & Choi, 2013).

A wide variety of printing patterns and substrates can be accommodated. Figure 2.1 shows the printed logo of Embry-Riddle Aeronautical University (ERAU) on Kapton film using several inkjet-printed layers of CNT ink. Multiple nanomaterials can also be simultaneously deposited on the substrates using the multiple cartridge setup that inkjet printers allow. Inkjet printing is to some degree insensitive to irregularities of the substrate surface, while the possibility of dispensing precise (from pico to nano liter) volume droplet inks at high rates (kHz) makes it capable of fabricating tailored nanocomposite devices with high device-to-device reproducibility (Dinh et al., 2016; Michelis et al., 2015). The technology is considered environmentally friendly since it generates very little or no waste (Secor, Prabhumirashi, Puntambekar, Geier, & Hersam, 2013) and is compatible with mass production on an industrial scale.

Figure 2.1 Inkjet printing of Embry-Riddle Aeronautical University logo with CNT ink.

Despite the outstanding advantages and advances of inkjet printing, several challenges related to the ink formulation and the printing have been dealt with, mainly due to restrictions imposed by the print head (Castrejón-Pita et al., 2013). The formulated ink must maintain a low surface tension and a low viscosity (in the accepted range of the specific printer). This might limit the polymer or solvents used for inkjet printing as high viscosity materials increase the risk of clogging and affect the printing quality.

For example, ink made of organic solvents which are usually volatile leading to nozzle clogging if the cartridge is not sealed properly. The viscosity limitations also limit the content of filler in the ink. The nanofillers in the ink should be well dispersed for optimal mechanical and electrical performance of the printed device and should be free of flocculation or big agglomerates to avoid clogging of the inkjet nozzle (R. Tortorich & Choi, 2013). The corrosive nature of the solvent or polymer used might prevent the use of inkjet printing depending on the materials of the cartridge. For optimal ejection of the ink, a low surface tension is necessary, due to the extremely small volume of the ink droplets. A high surface tension will make the ejection of the droplet very difficult.

Problems related to the inkjet printing of nanocomposites are mainly due to the coffee ring effects and the contact angle of the ink on the chosen substrate for printing. The coffee ring effect happens when after ejection of the droplet on the substrate, the nanofillers are pushed towards the perimeter of the droplet due to an internal flux, during drying (Deegan et al., 1997). To overcome that phenomenon, heating the substrates during the printing of surface treatment of the substrates can accelerate the drying process (J. W. Song et al., 2008). A good choice of the polymers and solvents used for the ink can also minimize the coffee stain effect (Denneulin, Bras, Carcone, Neuman, & Blayo, 2011). For good print quality, the surface tension or contact angle of the ink should be low for good adhesion on the substrates. Wetting agents or surfactants can be used in the ink formulation to lower the surface tension. In addition, in the case of hydrophobic substrates, surface treatment is often necessary for the printing of water-based inks (Fang et al., 2016; Fang & Tentzeris, 2018).

2.5. Applications of Conductive Polymer Nanocomposites Examined in This Dissertation

The first part of this chapter reviewed the current state of art about the properties of CNT, GNP and the nanocomposites made with each of them. In addition, a detailed review of the work done so far for hybrid nanocomposites comprising both CNT and GNP was performed. With regard to the review, the different nanocomposites were fabricated for two general applications: conductive nanocomposites for use as resistor or electrodes and piezoresistive nanocomposites for use as strain or gas sensor. In this dissertation, the investigator will manufacture nanocomposites for the following applications: strain sensing and MMOD impact detection. Since their use as strain sensor has been covered in the review above, the state of research on MMOD impact detection and how polymer nanocomposites will be used as MMOD impact detection sensors will be briefly discussed.

2.5.1. Space Debris Impact Detection in Inflatable Structures

Inflatable structures for space habitat are highly prone to damage caused by micrometeoroid and orbital debris (MMOD) impacts. The size of orbital debris varies from few microns to meters but the probability of an impact increases significantly for particle diameter size of 0.001 cm to 1 cm due to their high flux. The velocity of these MMOD is very high, i.e. of the order of 1 km/s to 15 km/s with an average velocity of about 9 km/s in lower earth’s orbit (E. Christiansen et al., 2009). Due to the high momentum, the material of the colliding particles has less significance, since even soft materials such as foams can cause damage and rupture of the structure. The disaster of the space shuttle Columbia is an example of such a case where a piece of insulating foam struck the left wing of the orbiter. Depending on the size of the colliding particle, the induced damage may vary from micrometer size hole to rupture of the whole structure.

Long term exposed space structures, such as ISS, face many such collisions throughout their service life and therefore are shielded heavily against MMOD impacts. Even with safety precautions of shielding and orientation change, several incidents have been reported of damage to the ISS by MMOD, leading to the occurrence of a hole or a crack (E. L. Christiansen & Rollins, 2012). If damage occurs to any of the pressurized structure such as habitat modules, it may result in depressurization and leakage and can be a serious threat to the life of the astronauts. Therefore, it is very important to know of any event of impact occurrences as well as the severity of the damage as early as possible. Previous space structures have been using different sensors for impact detection. After the loss of Columbia, the Space Shuttle Orbiter was equipped with WLEIDS impact detection system to qualitatively estimate the impact and location of damage for a limited period of time (E. Christiansen et al., 2009; Studor & George, 2007). Currently, the techniques used by NASA and other space agencies to detect the damage occurrences vary from pressure sensors for leak detection, monitoring cameras to inspect the damage through images, ultrasonic testing to other NDE techniques (Koshti, 2015). There is a great need for a structural health monitoring system that can detect impact damage, such as its location and severity, and keep the crew updated with the health of the structure.

The current development of the space program is moving towards inflatable habitat structures (de la Fuente, Raboin, Spexarth, & Valle, 2000). An active health monitoring system for inflatable structures against MMOD impact damage would be needed. One approach is to develop a blanket/layer that detects the impact damage. A second approach can be the installation of sensors on the existing structure that can remotely detect the event of an impact. Similar attempts have been made in the past. Brandon et al. (2011) developed a blanket type layer with wireless communication, which works on the principle of a capacitor. When a capacitor is damaged due to the hole created by the impact, capacitance of the sensor changes due to change in the area, and this can be used to get information about the event of an impact. The layer consists of a number of such sensors installed in an array to cover the whole structure.

Similarly, Woodard et al. (2011) used an open-circuit electrically conductive spiral trace sensor for damage detection. Due to damage, the magnetic field response of the sensor changes that can be used for detection. Moreover, a piezoelectric film sensor layer (E. Christiansen et al., 2009) and conductive traces (Patent No. 9,233,765, 2016) were used as a coating material or embedded between the laminates for sensing purposes. Fiber optics (Cadogan et al., 2006) were also woven inside a fabric, for strain sensing as an indication of damage. Imaging by scanning the habitat walls with different electromagnetic radiation wavelengths has also been studied for MMOD damage detection and yielded positive results (Madaras et al., 2008). More complex techniques involved the use of acoustic and impedance tomography to provide information about the location of damage in the layer (Cadogan et al., 2006). It was shown in Chapter 2, that conductive CNT-PNCs, or GNP-PNCs exhibit a change in their electrical resistance with strain, mainly due to the breaking of conductive paths in the filler percolated network (Alamusi et al., 2011; Gbaguidi, Konduru, & Kim, 2016; Njuguna, 2012). Thus, those nanocomposites can be used to detect MMOD impact, since the addition of a hole of any size onto the nanocomposites would create the same change in electrical resistance because part of their conductive network would be removed.

In this section, the different properties of CNT and GNP as nanofillers and their use in monofiller and hybrid nanocomposites have been discussed. The investigator reviewed the different works both experimental and numerical done in the literature about the nanocomposites and examined the main parameters that affect their use as conductive and piezoresistive materials. The conventional fabrication processes used so far for the nanocomposites were discussed and it was shown that inkjet printing can overcome their shortcomings with the goal of producing more performant nanocomposites with controllable properties. Various applications of the nanocomposites were also discussed and it was explained that their electrical behavior could be used for damage sensing as shown in the coming chapters.

3. 2D Numerical Simulation on Electrical Conductivity and Piezoresistivity of CNT/GNP Hybrid Nanocomposites

Hybrid nanocomposites with multiple fillers like carbon nanotubes (CNT) and graphene nanoplatelets (GNP) are in the forefront of nanomaterials studies due to their synergistic effect. Several reports have established a decrease of the percolation threshold, and an enhancement of the electrical and mechanical properties of the hybrid composites when compared to mono-filler composites. In this chapter, the investigator showed using numerical simulations that the addition of graphene fillers to CNT-nanocomposites improves the electrical conductivity and the piezoresistivity of the obtained hybrid nanocomposites. In literature, CNT nanocomposites are usually classified into CNT thin films and CNT polymer nanocomposites. Thin films composites are thin enough that there is essentially a single layer of CNTs lying relatively flat in the plane of the film (Maxwell, 2013). Those films exhibit two-dimensional (2D) network percolation behavior, because similar to percolation results from 2D numerical simulations (L. Hu, Hecht, & Gruner, 2004; Ishida & Nihey, 2008; Kumar, Pimparkar, Murthy, & Alam, 2006; Maxwell, 2013; Topinka et al., 2009).

The thickness of polymer nanocomposites, on the other hand are usually much greater than the length of the incorporated CNTs; hence, they exhibit three-dimensional (3D) percolated network behavior (Maxwell, 2013). CNT thin films (usually made of SWCNTs) are mostly used as transistors (Simien et al., 2008; Snow, Novak, Campbell, & Park, 2003), electroluminescent devices (Yu Wang et al., 2008) and strain sensors (Loh et al., 2008; Nagarajaiah et al., 2008). 2D numerical models are computationally more efficient (less intensive) than their 3D counterparts (Maxwell, 2013; Theodosiou &

Saravanos, 2010). More importantly, (Theodosiou & Saravanos, 2010) showed that the percolation results predicted by a fast and simpler 2D model can be scaled and calibrated to match a more complicated and time consuming 3D model percolation.

Taking advantage of the computation efficiency of the 2D model, in this chapter, the author has developed a 2D Monte Carlo model to estimate the electrical conductivity and the piezoresistivity of hybrid nanocomposites. To model the fillers in an RVE, two main approaches are available in literature. In the softcore model, geometric and electrical contacts occur simultaneously, because the fillers are allowed to overlap or to occupy the same space. That leads to cases where no tunneling resistance exists between fillers even though they are electrically connected. In hardcore model, an impenetrable core, surrounded by a soft penetrable shell, represents the filler. Electrical contact can occur only inside the soft shell through tunneling resistance. Using the hardcore model for CNTs, which are the primary fillers in this chapter, in a two-dimensional RVE, will result in a very small number of particles generated due to space restriction. Hence, in this chapter, the author used a modified softcore approach to model CNTs. He specifically consider that there is a tunneling resistance between the CNTs even if they overlap. This reduces the underestimation of tunneling resistance occasioned by softcore modeling.

In this chapter, using the modified softcore model for CNT and the hardcore model for GNP, the author has developed a two-dimensional Monte Carlo model to estimate the electrical conductivity and the piezoresistivity of nanocomposites, with microstructures consisting of elliptically shaped GNPs, mixed in with a two-dimensional CNT network. Stochasticity is naturally inherent in these microstructures; consequently, there is uncertainty in the constituent model parameters. The author studies the uncertainty in the model outputs by simulating a large number of samples (Monte Carlo simulations) and address the uncertainty due to model assumptions as well as parametric uncertainty due to the input parameters in simulating the microstructures. Some of the parameters considered include filler geometry, aspect ratio, orientation, CNTs to GNPs volume fraction ratio and mechanical loading. The effect of these parameters on the percolation threshold, electrical conductivity and piezoresistivity is examined with the objective of designing responsive microstructures of hybrid nanocomposites. Part of this chapter previously appeared in (Gbaguidi, Namilae, & Kim, 2018b).

3.1. Model Formulation

3.1.1. Modeling of the Hybrid Filler Network

A percolation based model was simulated by first generating a random distribution of CNT network in a two-dimensional (2D) representative volume element (RVE) of size $L_x \times L_y$. Every CNT added in the model can be described by a line segment with a starting point (x_1^i, y_1^i) and an ending point (x_2^i, y_2^i) such that:

$$\begin{bmatrix} x_2^i \\ y_2^i \end{bmatrix} = \begin{bmatrix} x_1^i \\ y_1^i \end{bmatrix} + l^i \begin{bmatrix} \cos\theta^i \\ \sin\theta^i \end{bmatrix} \tag{3.1}$$

where l^i and θ^i are the length and polar angle of the i^th^ CNT, respectively, as shown in Figure 3.1(a) x_1^i , y_1^i and θ^i follow a uniform distribution while l^i follows a Weibull distribution such that:

$$\begin{bmatrix} x_1^i \\ y_1^i \\ \theta^i \\ l^i \end{bmatrix} = \begin{bmatrix} L_x \times rand \\ L_y \times rand \\ 2\pi \times rand \\ a \times (-\,ln(1 - rand))^{\frac{1}{b}} \end{bmatrix} \tag{3.2}$$

where ‘rand’ indicates uniformly distributed random numbers in the interval $]0,1[$ and

(a, b) are the parameters of Weibull distribution. The Weibull parameters are determined by the nominal and standard deviation of experimental CNT lengths (Shiren Wang, Liang, Wang, & Zhang, 2006). Some of the earlier modeling studies consider CNTs of uniform length (B. M. Lee & Loh, 2015; Rahman & Servati, 2012; Z. Wang & Ye, 2013); however, including the length distribution according to experimental parameters results in a more realistic representation of the microstructure.

This CNT generation procedure was performed continuously until the desired CNT volume fraction was reached. Even though CNTs are represented as one-dimensional structures, a fixed diameter D is assigned to the CNTs to facilitate computing the intersections and volume fraction. Here the volume fraction is simply defined as the ratio of the total area of all the CNTs $(l_i \times D)$ and the area of RVE $(L_x \times L_y)$. Periodic boundary conditions (PBC) (B. M. Lee & Loh, 2015) were used to reposition the CNTs when the end points of CNTs generated by Equation 3.1 were located outside of the RVE.

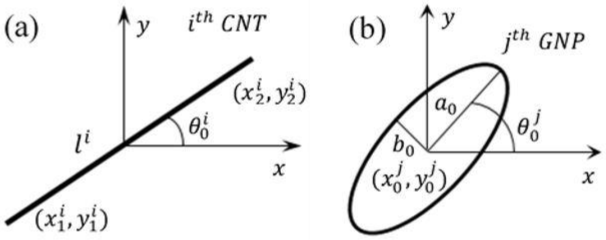

Figure 3.1 Parameters to generate (a) i^{th} CNT and (b) j^{th} GNP particle in Representative Volume Element.

Next, the author considers the incorporation of elliptical graphene platelets to form a hybrid filler network. Most studies on percolation of graphene based nanocomposites modeled graphene as circular particles because of the simplicity in geometry definition, and ease in computation of the distance between particles (Oskouyi, Sundararaj, & Mertiny, 2014b, 2014a; Masoud Safdari, 2012). Note that the two fillers generated in this work are in plane with the 2D RVE.

Elliptical particles are a more realistic assumption because they are not equiaxed and allow for rotation in the particle plane. Moreover, elliptical shape enables parametric studies of the aspect ratio and texture distribution. Nonetheless, there is no closed-form solution available for distance computation between elliptical particles (Yi & Tawerghi, 2009), which makes the implementation more difficult and computationally intensive. The ith graphene particle, generated in the RVE is described by an ellipse with a center (x_0^i, y_0^i), and direction angle θ_0^i, a semi-major axis a_0 and a semi-minor axis b_0 (see Figure 3.1(b)) such that:

$$\begin{bmatrix} x_0^i \\ y_0^i \\ \theta_0^i \end{bmatrix} = \begin{bmatrix} L_x \times rand \\ L_y \times rand \\ \pi \times rand \end{bmatrix} \tag{3.3}$$

The elliptical particles were added to the RVE until the desired graphene volume fraction was reached. Equation 3.3 suggests that the center of the ellipse is always located inside the RVE. However, the ellipse may intersect with one or two of the RVE boundaries. Periodic boundary conditions were used in such cases. Note that the implementation of PBCs for elliptical particles has additional steps compared to circular particles (W. Xu, Chen, & Lv, 2010). If an ellipse intersects with a single boundary segment, one additional ellipse $(x_0^{i+1}, y_0^{i+1}, \theta_0^i)$ was compensated (Figure 3.2(a)). If the ellipse intersects with two boundary lines, on or outside the segments, two additional ellipses $(x_0^{i+1}, y_0^{i+1}, \theta_0^i)$ and $(x_0^{i+2}, y_0^{i+2}, \theta_0^i)$ were compensated (Figure 3.2(b) and (c)). If one of the RVE corner is located inside the ellipse, three additional ellipses$(x_0^{i+1}, y_0^{i+1}, \theta_0^i)$, $(x_0^{i+2}, y_0^{i+2}, \theta_0^i)$ and $(x_0^{i+3}, y_0^{i+3}, \theta_0^i)$ were compensated (Figure 3.2(d)). Figure 3.2(c) can happen only with radially asymmetric shapes like ellipses. As a modeling constraint, the ellipses are impenetrable, i.e. not allowed to overlap. This constraint is needed to make the 2D model closer to a three-dimensional microstructure.

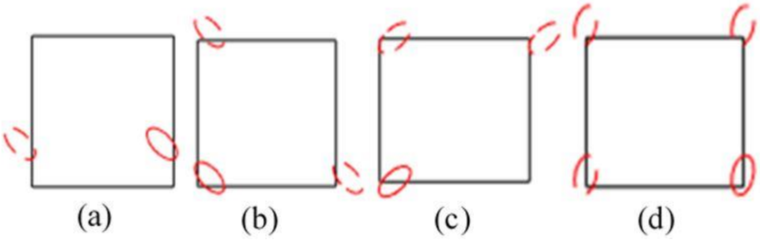

Figure 3.2 Periodic compensation procedure.

$$\left(\frac{\cos^2\theta_0}{{a_0}^2}+\frac{\sin^2\theta_0}{{b_0}^2}\right)(x-x_0)^2 + 2\sin\theta_0\cos\theta_0\left(\frac{1}{{a_0}^2}-\frac{1}{{b_0}^2}\right)(x-x_0)(y-y_0) + \left(\frac{\sin^2\theta_0}{{a_0}^2}+\frac{\cos^2\theta_0}{{b_0}^2}\right)(y-y_0)^2 = 1 \tag{3.4}$$

$$[x \quad y \quad 1]\begin{bmatrix} A & C & D \\ C & B & E \\ D & E & F \end{bmatrix}\begin{bmatrix} x \\ y \\ 1 \end{bmatrix} = 0 \tag{3.5}$$

Equation 3.4 represents the standard equation for an ellipse with the five parameters $(a_0, b_0, x_0, y_0, \theta_0)$, that describe its size, position, and rotation. Equations 3.5 and 3.6 are compact form of Equation 3.4 for computation purpose. They are obtained by expansion and rearrangement of Equation 3.4 following the procedure in (W. Xu et al., 2010).

$$\begin{bmatrix} A & C & D \\ C & B & E \\ D & E & F \end{bmatrix}$$
$$= \begin{bmatrix} \frac{\cos^2\theta_0}{{a_0}^2} + \frac{\sin^2\theta_0}{{b_0}^2} & \sin\theta_0\cos\theta_0\left(\frac{1}{{a_0}^2} - \frac{1}{{b_0}^2}\right) & -Ax_0 - Cy_0 \\ \sin\theta_0\cos\theta_0\left(\frac{1}{{a_0}^2} - \frac{1}{{b_0}^2}\right) & \left(\frac{\sin^2\theta_0}{{a_0}^2} + \frac{\cos^2\theta_0}{{b_0}^2}\right) & -Cx_0 - By_0 \\ -Ax_0 - Cy_0 & -Cx_0 - By_0 & A{x_0}^2 + B{y_0}^2 + 2Cx_0y_0 - 1 \end{bmatrix} \quad (3.6)$$

Suppose that during the simulation, the jth elliptical particle $(a_0, b_0, x_0^j, y_0^j, \theta_0^j)$ is generated after the ith particle $(a_0, b_0, x_0^i, y_0^i, \theta_0^i)$. The impenetrability of ith and jth ellipses can be ascertained if:

$$\begin{bmatrix} x^j & y^j & 1 \end{bmatrix} \begin{bmatrix} A^i & C^i & D^i \\ C^i & B^i & E^i \\ D^i & E^i & F^i \end{bmatrix} \begin{bmatrix} x^j \\ y^j \\ 1 \end{bmatrix} > 0 \quad (3.7)$$

In order to reduce computational effort, the author used an algorithm wherein a small number np of equidistant points (x_k^j, y_k^j) on ellipse j satisfy Equation 3.7, with $k = 1,2,\dots,n_p$.

3.1.2. Tunneling Junctions Between Fillers

Percolation network conductivity models use either softcore or hardcore approaches to determine the junctions between filler particles. Softcore approach assumes fully permeable fillers wherein geometric and electrical contact occur simultaneously (B. M. Lee & Loh, 2015). In hardcore approaches, a soft shell encompasses impenetrable hardcore and tunneling intersections occur in the soft shell. Most of the 2D numerical studies (Behnam & Ural, 2007; Rahman & Servati, 2012) as well as many 3D modeling studies (W. S. Bao, Meguid, Zhu, Pan, et al., 2012; W. S. Bao, Meguid, Zhu, & Weng, 2012; S. Gong et al., 2015; Shen Gong & Zhu, 2014), use a softcore model for determining junctions between fillers. Berhan and Sastry (2007) show that softcore model reduces the contribution of tunneling, due to the overestimation of the number of chemically bonded junctions and thereby introduces non-negligible error in percolation modeling. Hardcore approach is more accurate and realistic but computationally more intensive, especially for fillers with complex geometries.

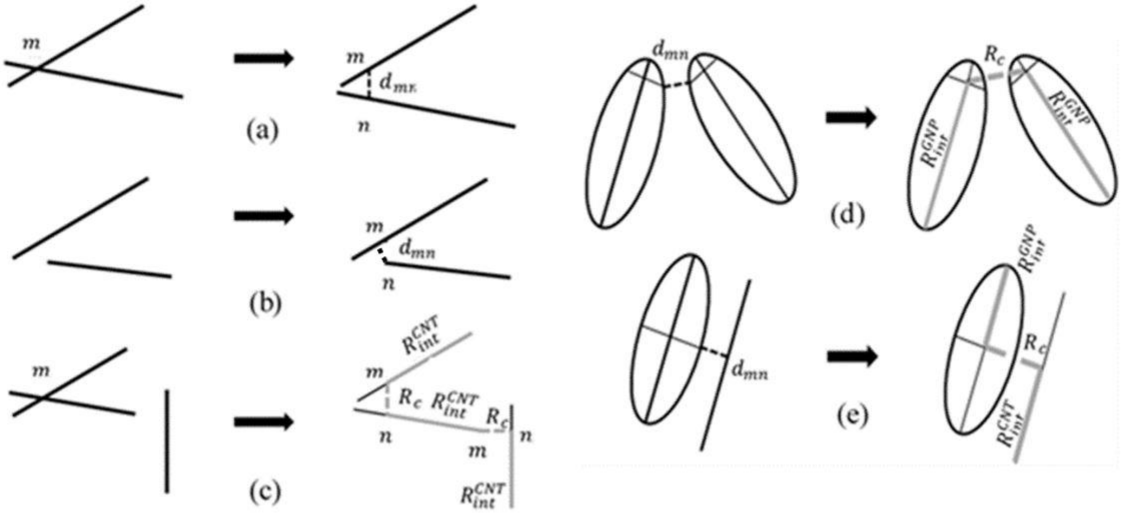

Figure 3.3 Schematic of (a) a transformation of direct nanotube-to-nanotube contact, from junction point m to tunneling segment of length d_{mn}, randomly generated, (b) tunneling effect when $d_{mn} \leq D + d_{cutoff}$, (c) CNT resistor network conductive path, (d) graphene-to-graphene tunneling contact and (e) graphene-to-nanotube tunneling contact, with tunneling segment of length d_{mn} into resistor network conductive path (solid gray, dotted gray, and thin solid black lines represent intrinsic resistance, tunneling resistance, and fillers parts not involved in the conductive path, respectively).

In his model, the author used a modified softcore approach for CNT-CNT and CNT-GNP interactions. Tunneling effect happens between two filler particles when the shortest distance between them is less than the maximum effective distance (d_{cutoff}) for tunneling effect (see Figure 3.3(b)). The geometrical contact between CNTs in the model was transformed into a tunneling junction for resistance calculation. For any CNT-CNT intersection, a random tunneling distance, d_{mn} $(D \leq d_{mn} \leq D + d_{cutoff})$, was generated, to create two distinct contact nodes m and n (one on each of the two CNTs in contact) such that the distance between those points (m and n) was equal to the generated tunneling distance d_{mn} (see Figure 3.3(a)). This tunneling distance is used for percolation and resistance calculations, thereby reducing the error in softcore method due to underestimation of tunneling junctions, without adding significant computation. A similar approach was used for the intersection between GNPs and CNTs as shown in Figure 3.3(e). The junctions between two GNPs were treated using a hardcore approach. Note that geometrical overlap of graphene particles is not allowed as a modeling constraint.

For resistance calculation, the major axis segment of each ellipse was used as a resistor segment of resistance equal to the graphene intrinsic resistance for resistance computation. The tunneling junctions between i^th^ and j^th^ GNPs was determined as follows. The semi-minor axis and semi-major axis of the i^th^ ellipse were transformed to incorporate a tunneling softcore such that:

$$ae^{i} = a_0 + d_{cutoff} \tag{3.8}$$

$$be^{i} = b_0 + d_{cutoff} \tag{3.9}$$

The parameters of i^th^ ellipse were obtained by replacing a_0 and b_0 in Equation 3.6 by ae^{i} and be^{i}. Then, overlapping between the i^th^ ellipse's tunneling softcore and the j^th^ ellipse was checked using n_p points (x_k^j, y_k^j) and applying Equation 3.7, with $k =$

$1,2,\ldots,n_p$. In the case of overlapping, the shortest distance between (x_k^j, y_k^j) points on the jth ellipse and (x_k^i, y_k^i) points on the ith ellipse (not its softcore) were used to generate a tunneling resistor segment with a tunneling distance d_{mn}, as shown in Figure 3.3(d). The tunneling segments between the filler particles along with the filler particles were used to create clusters that lead to percolation networks. Note that all the nodes created due to tunneling on GNPs are projected on the GNP resistor segment (see Figure 3.3(d) and (e), from left to right).

3.1.3. Network Percolating Resistance

The network resistance and percolation effects were computed using both, intrinsic resistance of fillers and tunneling junction resistance between fillers. The intrinsic resistance of CNTs, along a CNT between two nearest contact points j and k, created by two adjacent fillers through tunneling, was evaluated as (W. S. Bao, Meguid, Zhu, Pan, et al., 2012).

$$R_{int}^{CNT} = R_{jk} = \frac{4l_{jk}}{\sigma_{cnt}\pi D^2} \tag{3.10}$$

where l_{jk} is the CNT length between the contact points j and k, D is the diameter of the CNT and σ_{cnt} is the CNT intrinsic electrical conductivity. In this study, the author used an experimentally determined effective mean conductivity as σ_{cnt} (Shen Gong & Zhu, 2014). Note that the electrical conductivity of the polymer matrix is neglected.

In literature and in vendor datasheets, graphene particles are usually described by their sheet resistance, R_s since they are 2D particles. For a conductive rectangular particle of dimension $L \times W$, with current, assumed to be flowing in the direction parallel to L, the electrical resistance is:

$$R = R_s \frac{L}{W} \tag{3.11}$$

For an ellipse's resistor segment of length L=$2a_0$, Equation 3.11 was modified as:

$$R_{GNP} = R_s \frac{4a_0}{\pi b_0} \tag{3.12}$$

For GNPs, several nodes might be created on the resistor segment of each ellipse due to tunneling junctions (i.e. one node created for each tunneling junction the filler is part of). The region between two consecutives nodes i and k on the filler can be defined as a resistor segment and the corresponding intrinsic resistance of the resistor segment in the case of GNP could be computed as:

$$R_{int}^{GNP} = \frac{R_{GNP}}{L} L_{ik} \tag{3.13}$$

where L_{ik} is the distance between the nodes i and k and L is the sum of all the L_{ik} on that specific ellipse resistor segment. The Landauer-Buttiker equation was followed to compute the current at a tunneling junction (W. S. Bao, Meguid, Zhu, Pan, et al., 2012; W. S. Bao, Meguid, Zhu, & Weng, 2012). The equation to compute the contact resistance of an undeformed particle junction is described as in (W. S. Bao, Meguid, Zhu, Pan, et al., 2012).

$$R_c = \frac{h}{2e^2MT} \tag{3.14}$$

where e is the electron charge, h is the Planck constant, T is the elctron transmission probability and M is the total number of conduction bands for CNT walls. The transmission probability T could be estimated by solving the Schrodinger equation with a rectangular potential barrier or from the Wentzel-Kramers-Brilloing (WKB) approximation (Simmons, 1963a, 1963b). T is expressed by Equations 3.15, 3.16 and 3.17, respectively, for contact between CNTs, between graphene particles and between CNT and graphene particles:

$$T = \begin{cases} \exp\left(-\frac{d_{vdw}}{d_{tunnel}}\right) & 0 \le d_{mn} \le D + d_{vdw} \\ \exp\left(-\frac{d_{mn} - D}{d_{tunnel}}\right) & D + d_{vdw} < d_{mn} \le D + d_{cutoff} \end{cases} \tag{3.15}$$

$$T = \begin{cases} \exp\left(-\frac{d_{vdw}}{d_{tunnel}}\right) & 0 \le d_{mn} \le d_{vdw} \\ \exp\left(-\frac{d_{mn}}{d_{tunnel}}\right) & d_{vdw} < d_{mn} \le d_{cutoff} \end{cases} \tag{3.16}$$

$$T = \begin{cases} \exp\left(-\frac{d_{vdw}}{d_{tunnel}}\right) & 0 \le d_{mn} \le \frac{D}{2} + d_{vdw} \\ \exp\left(-\frac{d_{mn} - \frac{D}{2}}{d_{tunnel}}\right) & \frac{D}{2} + d_{vdw} < d_{mn} \le \frac{D}{2} + d_{cutoff} \end{cases} \tag{3.17}$$

$$d_{tunnel} = h/\left(2\pi\sqrt{8m_e\Delta E}\right) \tag{3.18}$$

where m_e is the mass of electron, ΔE (1 eV) is the height of the barrier (the difference of the work functions between the CNT and the polymer), d_{vdw} is the van der Waals separation distance. Examples of resistance network between fillers are shown in Figure 3.3(c), (d) and (e), with the different type of electrical resistances.

Following (W. S. Bao, Meguid, Zhu, Pan, et al., 2012; B. M. Lee & Loh, 2015), the percolation threshold and the electrical conductivity were evaluated by recognizing the connective percolating network linking two opposite faces (or electrodes) of the RVE ($y = 0$ and $y = L_y$). The percolation of the composite was evaluated using the percolation probability, which is the probability that there is at least one conductive path spanning the two electrodes of the RVE, transforming the insulating polymer to a conductive material. The percolation probability is defined as:

$$P = \frac{n_p}{N} \tag{3.19}$$

where n_p is the number of simulations with the existence of at least one conductive path, in a total of N simulations. The electrical percolation threshold corresponds to a percolation probability of 0.5.

Once a conductive network, which spans both electrodes was found, the segments that did not participate in conducting current were removed for computational efficiency using the Dulmage-Mendelsohn decomposition method (Pothen & Fan, 1990). Then the remaining conductive network was transformed into a resistor network by calculating the resistance between the different nodes ($R_{int}^{CNT} = \frac{4l_{jk}}{\sigma_{cnt}\pi D^2}$, $R_{int}^{GNP} = \frac{R}{L}L_{ik}$ and $R_c = \frac{h}{2e^2MT}$). The final step was to calculate the resistance of that percolating network from the positive semi-definite matrix equations representing Kirchhoff's current and Ohm's laws (W. S. Bao, Meguid, Zhu, Pan, et al., 2012; Rommes & Schilders, 2010). Cholesky decomposition algorithm for sparse matrices (Rommes & Schilders, 2010) was used to solve these matrix equations and find the conductance of the RVE. Monte Carlo simulations on several representative rectangles were performed to obtain the averaged conductance of the networks.

3.1.4. Piezoresistivity of Hybrid Nanocomposites

Several experimental studies confirm that nanocomposites with CNTs or graphene particles exhibit a change in resistance when subject to mechanical deformation (C.

Li et al., 2008; Yin et al., 2011; W. Zhang et al., 2006). The author studies this phenomenon by subjecting the RVE to uniaxial tensile deformation. Consider a CNT-graphene nanocomposite under an incremental uniaxial strain $\Delta\varepsilon$ along the y-axis of the RVE. Any applied strain resulted in a change in position and orientation of the particles. The re-orientation model for the piezoresistivity for CNTs in (B. Hu et al., 2012) was applied for both CNTs and graphene particles in this study. In the reorientation model described in Equations 3.20 and 3.21, a uniform strain field and a constant Poisson's ratio is assumed in the polymer. In addition, a perfect interface between the polymer matrix and the fillers is assumed. Hence, all points in the RVE including fillers are assumed to deform under mechanical strain with elastic properties of the matrix. Since the intrinsic piezoresistivity of the fillers are not considered in this work, the effects of this assumption on the accuracy especially for small strains is expected to be very small.

The coordinates of the two end points of the ith CNT segment or the GNP resistor segment in the RVE, $\left(x_1^i, y_1^i\right)$ and $\left(x_2^i, y_2^i\right)$ became:

$$\left(\bar{x}_1^i, \bar{y}_1^i\right) = \left(x_1^i(1 - \nu\Delta\varepsilon), y_1^i(1 + \Delta\varepsilon)\right) \tag{3.20}$$

$$\left(\bar{x}_2^i, \bar{y}_2^i\right) = \left(x_2^i(1 - \nu\Delta\varepsilon), y_2^i(1 + \Delta\varepsilon)\right) \tag{3.21}$$

where $\left(\bar{x}_1^i, \bar{y}_1^i\right)$ and $\left(\bar{x}_2^i, \bar{y}_2^i\right)$ are the updated coordinates of the two end points of the i^{th} CNT segment or graphene resistor segment after strain is applied, and ν is the Poisson's ratio. This resulted in a new state of microstructure in the RVE with increase or decrease in number of conducting paths in the percolated network. Further, there were changes in the tunneling junction locations on the resistor segments, as well as changes in the tunneling distance between particles. All those phenomena changed the resistance of the new percolating network. The new electrical resistance for the network was then computed as a function of applied strain to characterize the piezoresistivity of the hybrid nanocomposite. Piezoresistivity is characterized using the resistance change ratio (K) and the gauge factor (GF), described in Equations 2.1 and 2.2.

3.2. Results and Discussion

The author uses Monte Carlo simulations based on the model described above to compute the percolation probability and the electrical conductivity, first with only CNTs as fillers and then with CNTs and GNPs as fillers. The different parameters (size, content and aspect ratio) of GNP as well as CNT content are kept constant to specific set of values, while the position and alignment of GNP and CNT as well as the length of CNT are randomly generated using Monte Carlo simulations, as shown in Equations 3.2 and 3.3.

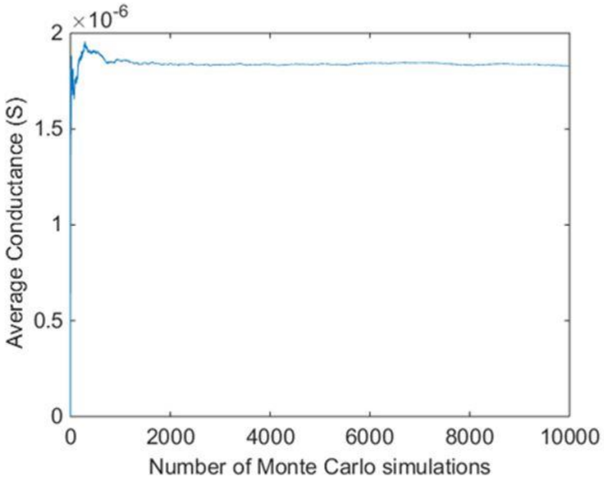

Figure 3.4 Convergence of average conductance value with Monte Carlo simulations.

To have a conductive nanocomposite, after the application of strain, the percolation network should remain after deformation. The present simulations show that when the CNT volume fraction is less than 0.10, the percolation network becomes discontinuous (i.e. the percolation path does not hold all the time) at a strain of 0.6% or less. Therefore, to study the piezoresistivity of hybrid composites, the CNT volume fraction was fixed at 0.10 in all the piezoresistivity simulations and only the GNP parameters were varied for determining optimal microstructures. This ensures that a percolated network of CNTs per se exists before and after the application of strain.

Table 3.1

Physical parameters used in numerical analysis.

Parameters		**Values**
Polymer	Poisson's ratio, ν	0.3
	Van der Waals distance, d_{vdw}	0.34 nm
	Cut-off distance, d_{cutoff}	1.4 nm
MWCNT	Diameter, D	50 nm
	Nominal length, L	19.5 µm
	Conduction channel, M	460
	Weibull parameters, (a, b)	(5.6403 µm, 2.4)
	Intrinsic conductivity, σ_{cnt}	1×10^4 S/m
Graphene Nanoplatelets (GNP)	Sheet resistance, Re	2.8×10^2 Ω /sq

Note. The parameters of CNT are obtained from (Shen Gong & Zhu, 2014). The electrical property of GNP is obtained from Graphene Supermarket vendor's data sheet (Graphene supermarket, n.d.).

The simulation parameters for the fillers are tabulated in Table 3.1. Statistical variation in microstructures is reduced by averaging over a large number of randomized microstructures. RVE cell of size 25 µm × 25 µm is used. Figure 3.4 shows the convergence study over 10000 Monte Carlo simulations. Convergence of the electrical conductivity is reached after 2000 simulations. A minimum of two thousand Monte Carlo simulations were performed for each variation of geometric features or fillers loading for both conductivity and piezoresistivity calculation.

3.2.1. Effect of GNP Content on Electrical Conductivity and Piezoresistivity

In order to investigate the effect of GNP content on the behavior of hybrid nanocomposites, the GNP size was kept constant while the content of GNP (controlled by the GNP-to-CNT volume fraction ratio) was varied. GNP-to-CNT volume fraction ratios (GNP/CNT) of 0.5, 1 and 2 were considered. Three different elliptical graphene dimensions were studied: the ellipses with semi-major and minor axes, a=4 µm and b=2 µm, a=2 µm and b=1 µm, and a=1 µm and b=0.5 µm named respectively as GNP (4,2), GNP (2,1) and GNP (1,0.5). Figure 3.5(a) reveals that the addition of GNP (4, 2) to the CNT nanocomposites, for any GNP-to-CNT volume fraction ratio, increased the percolation threshold of the hybrid nanocomposites, compared to nanocomposites with only CNT fillers. Moreover, an increase of the GNP-to-CNT volume fraction ratio led to a steady increase of the percolation threshold.

Figure 3.5(b) shows that the addition of GNP (4, 2) for any GNP content increased the conductivity of the nanocomposites. It also shows that a higher GNP-to-CNT volume fraction ratio led to a higher conductivity of the nanocomposites. Since the size of the GNP was constant while the GNP-to-CNT ratio was increased, more GNP particles were being added to the nanocomposites. Increase of the number of GNP particles might have increased the possibility of forming more junctions between the fillers. Figure 3.5(c) shows that the addition of GNPs to the nanocomposites increased the piezoresistive performance of the nanocomposites for all three graphene contents, compared to the CNT mono-filler nanocomposites.

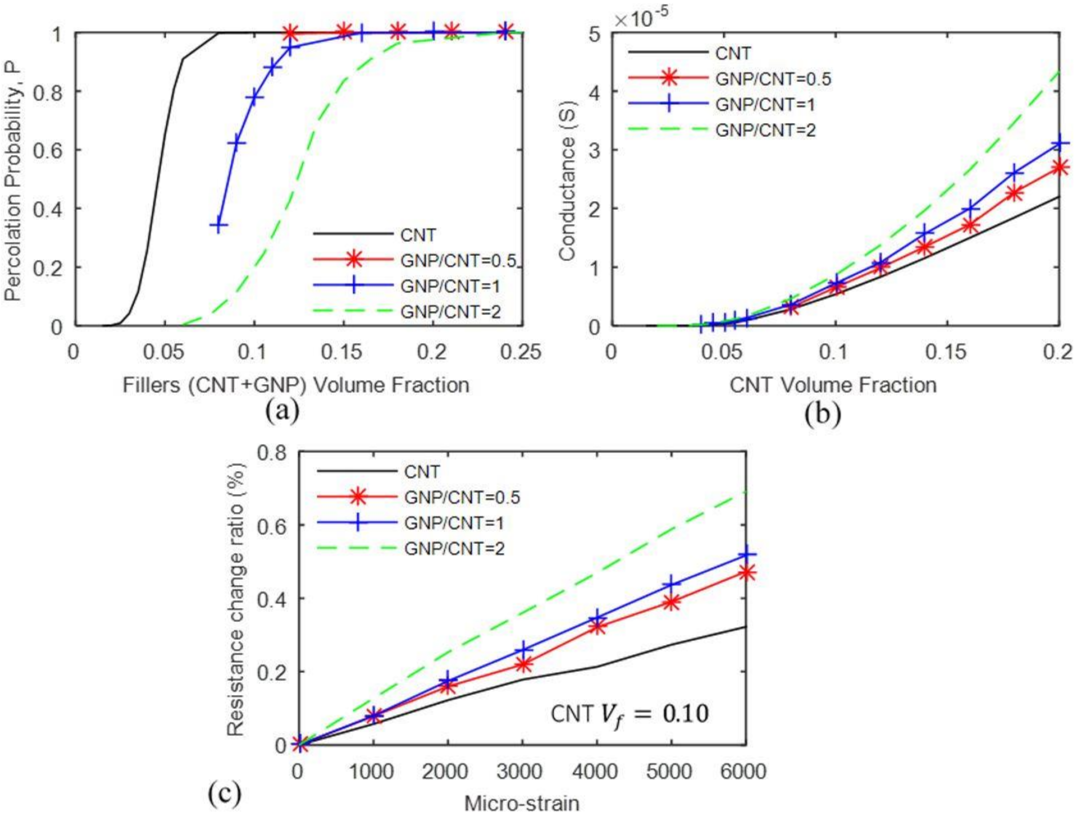

Figure 3.5 Effect of addition of GNP (4, 2) with different GNP-to-CNT volume fraction ratios (GNP/CNT) on (a) percolation probability (b) electrical conductance and (c) the piezoresistivity (CNT volume fraction of 0.10) of the hybrid nanocomposite.

The simulations for the piezoresistivity were all performed for a CNT volume fraction of 0.10. Figure 3.5(c) also shows that when the content of GNP was increased the piezoresistivity also increased for all the values of applied mechanical strains. It means that the hybrid nanocomposite with increased GNP content is more sensitive to the applied strain. A similar trend for percolation, conductivity and piezoresistivity was observed for the other two graphene sizes (GNP (2, 1) and GNP (1, 0.5)). It is known that the piezoresistivity of CNT-based nanocomposites with lower CNT content is more sensitive to the applied strain (Shen Gong & Zhu, 2014). This limits the gauge factor because of the limit imposed by the percolation threshold. The present result indicates that the gauge factor of hybrid CNT-GNP nanocomposites does not have that limitation (the GNP content can be increased for better piezoresistivity). In addition, the addition of GNP (4, 2) at a GNP/CNT ratio of 2 doubled the piezoresistivity of the hybrid nanocomposite compared to a pure CNT nanocomposite.

3.2.2. Effect of GNP Size on Electrical Conductivity and Piezoresistivity

This section investigates the impact of the size of GNP particles on the hybrid nanocomposite. The GNP aspect ratio and content were kept constant. Only the size (surface area) of the GNP particles was changed. The three sizes of graphene particles mentioned above (range of semi-major axis from 1 μm to 4 μm), were used in the simulations. The electrical conductivity of the nanocomposites was determined for varying CNT volume fractions. The results in Figure 3.6(a) shows that an increase of the size of GNP led to a steady decrease of the percolation threshold of the hybrid nanocomposites. Also, Figure 3.6(b) reveals that nanocomposites with bigger graphene particles have higher conductivity. Bigger GNP fillers in smaller number worked better than smaller particles in larger number. Hence, the effect of GNP size on the conductivity of hybrid nanocomposites is similar to the effect of CNT length on the conductivity of CNT-based nanocomposites (Shen Gong & Zhu, 2014). The probability of forming more junctions between the fillers seems to increase with larger particles.

The piezoresistivity behavior of the hybrid nanocomposites was modeled for a fixed CNT volume fraction of 0.10, in all the simulations. Figure 3.6(c) shows that the increase of the GNP particles size increased the piezoresistivity of the hybrid nanocomposites. A similar trend for percolation, conductivity and piezoresistivity was seen for the two other GNP-to-CNT volume fraction ratio values (0.5 and 1).

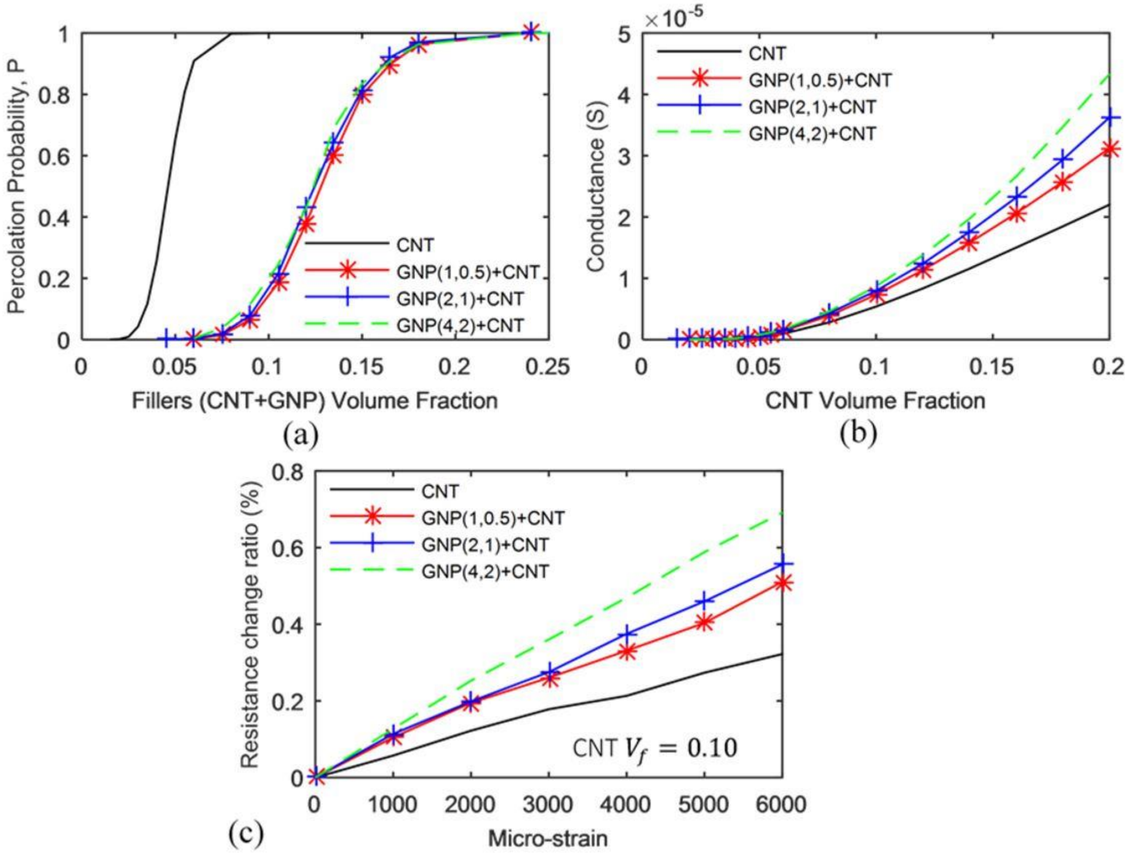

Figure 3.6 Effect of addition of three type of graphene of different sizes with a GNP-to-CNT volume fraction ratio (GNP/CNT) of 2 on (a) percolation probability (b) electrical conductance and (c) the piezoresistivity (CNT volume fraction of 0.10) of the hybrid nanocomposites.

3.2.3. Effect of GNP Aspect Ratio on Electrical Conductivity and Piezoresistivity

To investigate the impact of the aspect ratio of the GNP particles on the hybrid nanocomposites, the GNP particles size (surface area) and content were kept constant while the aspect ratio of the GNP was varied. The simulations were performed for two aspect ratios (2 and 8) with GNP (2, 1) and GNP (4, 0.5). The percolation threshold decreased (Figure 3.7(a)) with an increase of the electrical conductivity (Figure 3.7(b)) when the GNP aspect ratio of the hybrid nanocomposites is increased from 2 to 8. The simulations on the piezoresistivity of the hybrid nanocomposites, in Figure 3.7(c), with a CNT volume fraction of 0.10, show that the piezoresistivity increased when the aspect ratio of GNP was increased. Since the size of the GNPs was the same, the same number of GNPs is present in the RVE for the two aspect ratios.

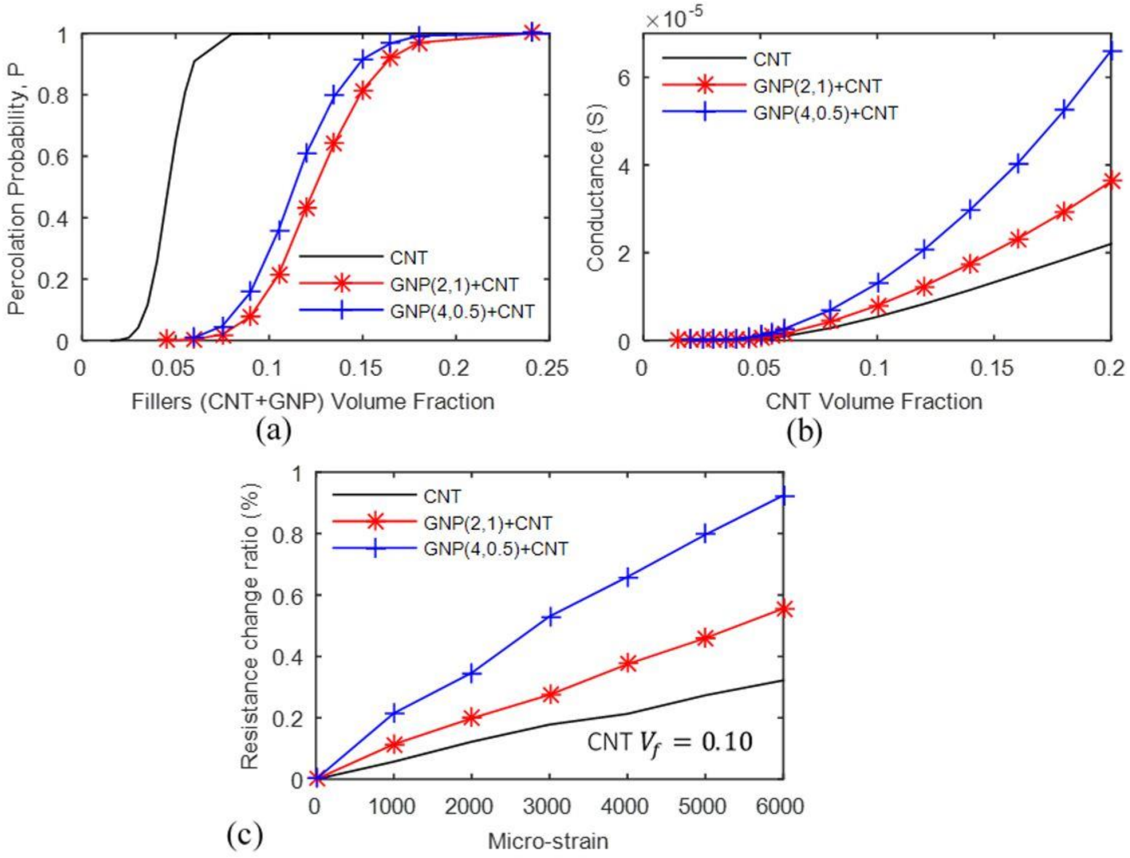

Figure 3.7 Effect of addition of two types of graphene of different aspect ratio, with equal size on (a) percolation probability (b) electrical conductance and (c) the piezoresistivity (CNT volume fraction of 0.10) of the hybrid nanocomposites. The GNP-to-CNT volume fraction ratio (GNP/CNT) is 2.

The author now analyzes the effect of aspect ratio for varying GNP size. The major axis length and the content of the GNP particles were kept constant for two aspect ratios, 2 and 8 corresponding to GNP (4, 2) and GNP (4, 0.5) fillers. Figure 3.8 confirms that a higher aspect ratio leads to a better percolation, electrical conductivity and piezoresistive performances.

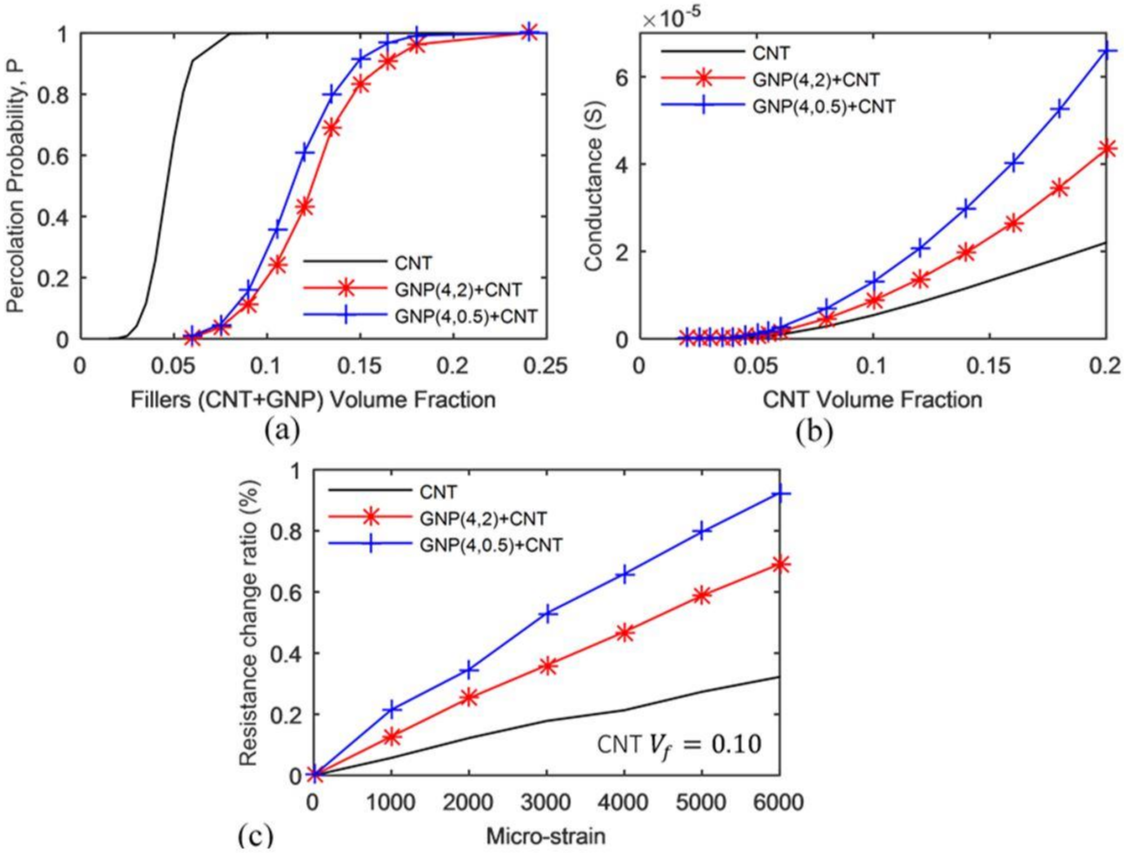

Figure 3.8 Effect of addition of two types of graphene of different aspect ratio, with different sizes on (a) percolation probability (b) electrical conductance and (c) the piezoresistivity (CNT volume fraction of 0.10) of the hybrid nanocomposites. The GNP-to-CNT volume fraction ratio (GNP/CNT) is 2.

However, since the major axis length of the two types of GNP were all equal, it is seen that the GNP particle with a bigger size (GNP (4,2)) did not lead in this case to the higher conductivity or piezoresistivity (unlike in Section 3.2, where the aspect ratio was constant). The electromechanical properties appear to exhibit a higher sensitivity to aspect ratio compared to GNP size. This can be a useful pointer in designing microstructures for optimal behavior. The trend in Figure 3.7 and Figure 3.8 was observed for the two other GNP-to-CNT volume fraction ratio values (0.5 and 1).

3.2.4. Effect of GNP Alignment on Piezoresistivity

It has been shown in previous studies that CNT alignment could have a huge effect on the piezoresistivity of CNT-based nanocomposites (S. Gong & Zhu, 2015). In this section, the author investigates the influence of the alignment of GNP particles on the piezoresistivity of the hybrid nanocomposites. Firstly, the GNP (4, 0.5) fillers were randomly generated with different orientations with the angle bounded by θ_{max} i.e. graphene particles were oriented at an angle between 0 and θ_{max}. Figure 3.9(a) shows the effect of the alignment of GNP (4, 0.5) on the piezoresistivity of the hybrid nanocomposites for values of θ_{max} (30°, 60°, 90°, 120°, 180°). It also shows the direction of measurement of the conductivity and of the fillers orientation. For small values of θ_{max}, lower piezoresistivity was observed. The resistance ratio reached its minimum for values of θ_{max} of 30° and 60°. There is an increase in piezoresistivity at higher angles of θ_{max} but there is no linear or monotonic correlation between piezoresistivity and θ_{max}. Note that smaller angle results in more transversely oriented particles while larger angles denote a more random orientation. The author however observes a significant increase (five times compared to θ_{max} of 30°) in piezoresistivity when all GNPs were oriented longitudinally i.e. at a 90° angle.

A second set of simulations for GNP alignment was performed where GNP (4, 0.5) were randomly generated with orientations chosen from equal adjacent ranges of angle, of amplitude 30° as shown in Figure 3.9(b). It was observed that angle values adjacent to 90° gives the highest piezoresistivity values (60°-90° and 90°-120°) while the angle ranges adjacent to 0° or 180° gives the lowest piezoresistivity values (0°-30° and 150°-180°). Moreover, the piezoresistive performance of the hybrid nanocomposite in function of GNP orientation seems to be symmetric to 90° orientation and decreases monotonically when away from 90°. A similar trend was found when the simulations were repeated with GNP (4, 2) fillers.

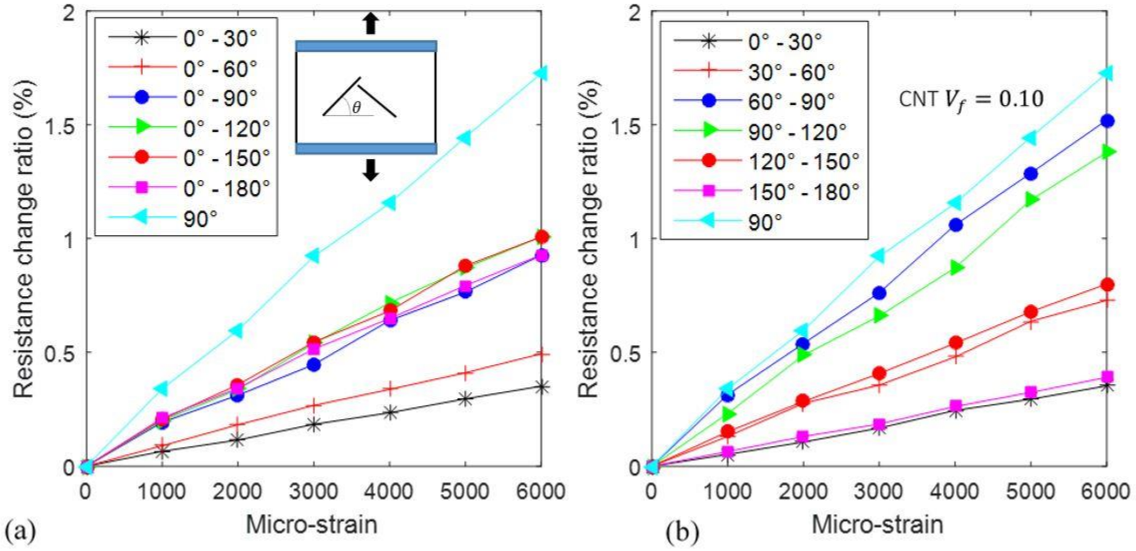

Figure 3.9 Effect of alignment of GNP (4, 0.5) with GNP-to-CNT volume fraction ratio (GNP/CNT) of 2 on the piezoresistivity of the hybrid nanocomposites with CNT volume fraction of 0.10.

3.2.5. Discussion and Validation

Figure 3.10 shows the different parameters of GNP examined as well as their effect on the piezoresistivity of the hybrid nanocomposites with CNT and GNP content kept the same for all microstructures. The resistance change ratio of a nanocomposite purely based on CNT at 0.6% of strain is shown to be about 0.32%, with a corresponding gauge factor of 0.53. To validate the present 2D model for CNT-PNCs, the author compared the present results with previous experimental results of CNT thin films in literature.

Table 3.2 shows that the gauge factor obtained for different CNT thin films nanocomposites varies from 0.299 to 1.13, which is comparable to the present numerical simulations. Moreover, B. M. Lee and Loh (2015) performed a 2D percolation-based numerical simulation to characterize the gauge factor of CNT thin films. A maximum gauge factor of 0.48 was obtained for randomly dispersed CNT near percolation. This is very close to the gauge factor of 0.53 obtained in this work. Unfortunately, no information about the percolation threshold, as fraction of the CNT was available in the study. However, Theodosiou and Saravanos (2010) through their 2D percolation models obtained a percolation threshold around 1.5 – 2 vol.% for randomly dispersed CNT, with no information about the CNT geometry. Their percolation threshold is however close to the computed value of 4.5 vol.% in the present work.

Table 3.2

Gauge factor of different CNT thin films nanocomposites.

Type of polymer and reference	**Parameters studied**	**Strain range**	**Gauge Factor**
MWCNT/Polysulfone (Bautista-Quijanoa et al., 2010)	Weight fraction (0.2% /1%)	0.1 - 1%	0.48/0.73
MWCNT/Polysulfone (Oliva-Avilés et al., 2011)	Random orientation/aligned (wt% = 0.75)	Less than 1.5%	0.70 /1.49
SWCNT/polyelectrolyte (Loh et al., 2008)	Number of Deposition layers (50 /100/200)	0 – 0.50%	1.13/0.421/0.299

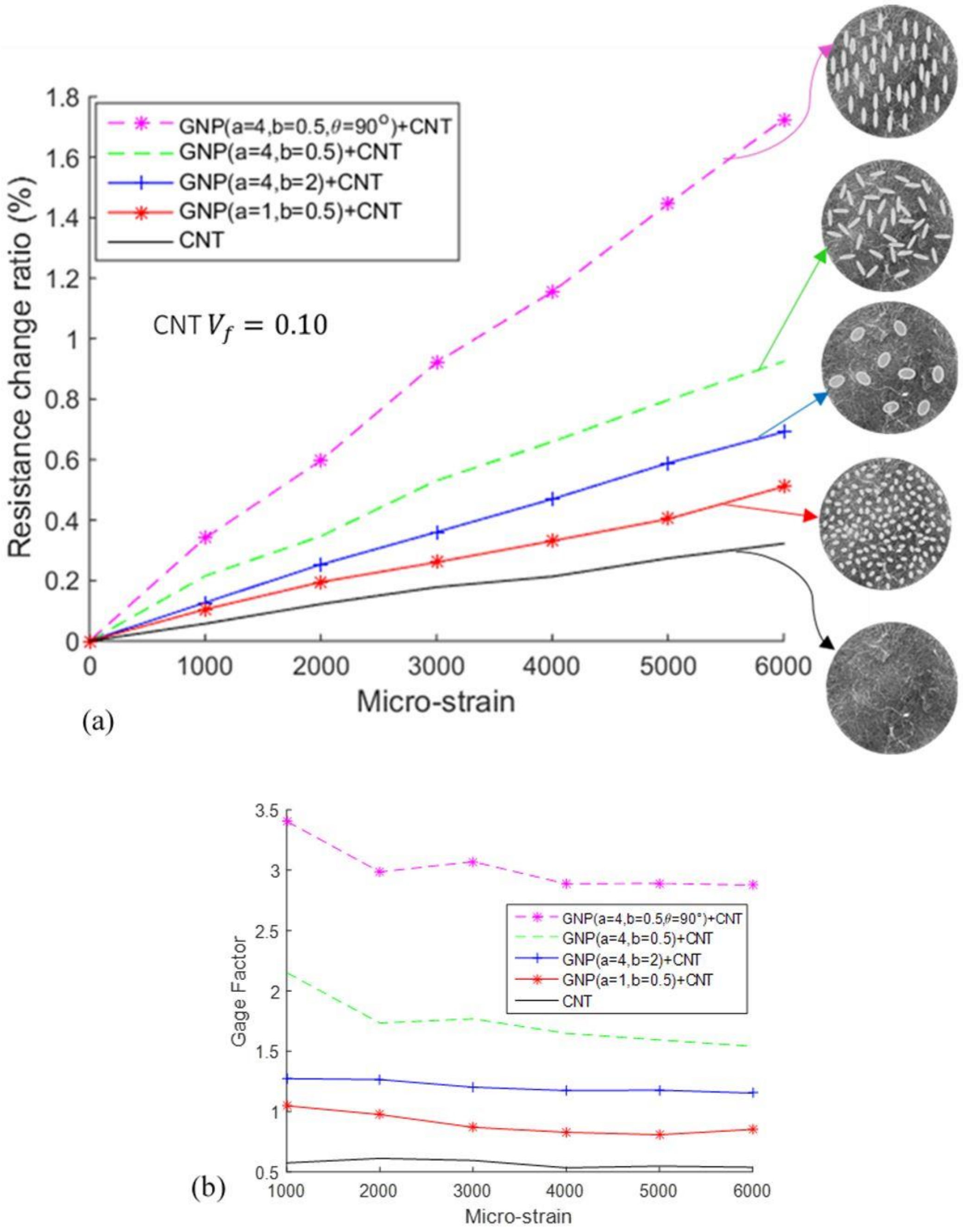

Figure 3.10 Effect of different GNP microstructures with GNP-to-CNT volume fraction ratio (GNP/CNT) of 2 on the piezoresistivity of the hybrid nanocomposites with a CNT volume fraction of 0.10.

With the addition of the smallest size of graphene particle examined in this study, GNP (1, 0.5) to the CNT nanocomposites, the gauge factor of the hybrid nanocomposites increased 1.6 times. Shen Gong and Zhu (2014) showed that the addition of more CNT (instead of graphene particles) to the initial CNT nanocomposites decreased the gauge factor of the nanocomposite, because an increase in CNT volume fraction leads to the decrease of the rate of change of junction numbers between fillers after strain was applied. Thus, the improvement of the piezoresistivity of the hybrid nanocomposite means that the rate of change of the junction number between fillers after strain, might have increased, with addition of GNP particles. This might be due to the fact that GNP as two-dimensional particles are able to make more junctions with neighboring fillers in the RVE, compared to one-dimensional CNTs.

The next microstructure simulated was with bigger graphene particles (GNP (4, 2)), with the same graphene content as before. A gauge factor 1.5 times greater than with the smaller GNP was observed. This improvement with a bigger particle size might be explained by the fact that, with a network of CNTs already existing, smaller particles, even though in bigger number are more likely to fall in between the CNTs or to overlap CNTs that do not participate in the percolated network. However bigger GNP particles, even in smaller number, are more likely to overlap more neighboring fillers, some of which will be part of the percolated network. This allows the bigger GNP particles to increase, more effectively the number of fillers in the percolated network, compared to smaller GNP particles.

A microstructure with the same content of GNP, but with higher aspect ratio (GNP (4, 0.5) fillers, is compared to the previous microstructure. An increase of the gauge factor up to 1.7 times was observed for the same strain of 0.6%. This indicates that piezoresistivity is more sensitive to aspect ratio than to size of the particles.

Finally, GNP (4, 0.5) fillers, at the same GNP content as in the previous microstructure are used but all oriented parallel to the loading direction. The gauge factor is shown to double when compared to the randomly oriented microstructure of GNP (4, 0.5). This might be due to the fact that with an existing percolated network of CNTs, GNP fillers oriented in the direction of the conductivity measurements are able to form junctions and span the existing CNT fillers to a greater extent.

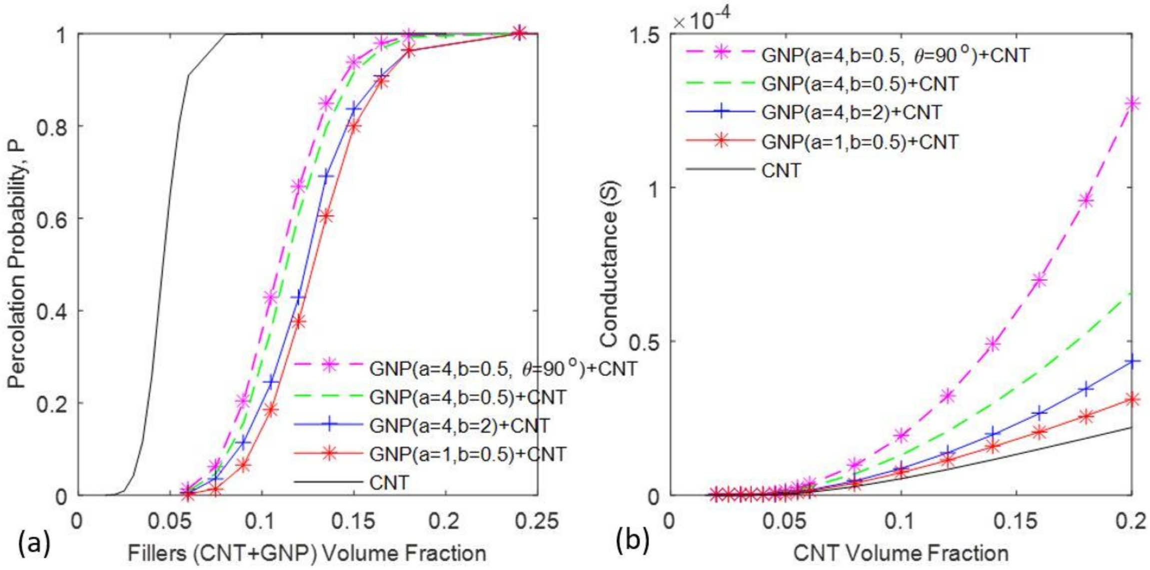

Figure 3.11 Effect of different GNP microstructures with GNP-to-CNT volume fraction ratio (GNP/CNT) of 2 on (a) percolation probability and (b) electrical conductance of the hybrid nanocomposites.

Effect on the electrical conductivity of the same microstructures is shown in Figure 3.11. In these simulations CNT volume fraction is also varied along with GNP parameters. Figure 3.11 shows that the improvement of the percolation threshold, and of the electrical conductivity, when the GNP parameters are varied, follows the same trend as the one of the piezoresistivity. The reason behind those improvements are the same as the one mentioned for the piezoresistivity i.e. rate of change of the number of CNT-GNP tunneling junctions.

Ranking the parameters, it is found that GNP alignment (all 90° orientation) had the highest influence resulting in 5.94 times increase in gauge factor compared to CNT mono-filler composite. Other factors in the decreasing order are aspect ratio, GNP size, and simply the effect of adding the second phase (GNP) enhanced the gauge factor up to 3.75, 2.21 and 1.83 times that of CNT mono-filler composite respectively.

3.3. Summary

The author developed a new CNT-GNP percolation network model, and used it to investigate the mechanisms of electrical percolation, conductivity and piezoresistivity of hybrid CNT-GNP nanocomposites, where tunneling is the electron transport mechanism. This model considers for the first time, the effect of addition of GNP on the piezoresistivity behavior of hybrid nanocomposites. The GNP fillers are modeled as ellipses in the Monte Carlo simulations. The author finds that the addition of GNP particles to CNT nanocomposites enhances significantly the electrical conductivity and piezoresistive behavior of the nanocomposites. Furthermore, parametric analysis has been conducted to investigate the impact of different GNP parameters on the piezoresistivity of the hybrid nanocomposites.

The author shows that: (i) a conductive network with higher GNP loadings, has a higher percolation threshold, and a higher electrical conductivity and piezoresistivity, (ii) an increase of the GNP size or aspect ratio decreases the percolation threshold and increases the conductivity and piezoresistivity of the hybrid nanocomposites, (iv) alignment of the GNP particles has a big effect on both the piezoresistivity and electrical conductivity, and (v) GNPs uniformly aligned in the direction of electrical conductivity measurements (or in a direction close to that) lead to a significantly higher piezoresistive behavior, up to 6 times greater than that of nanocomposites based on only CNT. The author also attempts to elaborate on the reasons behind the improvement of piezoresistivity behavior observed in the different microstructures in this study.

4. Effect of Nanotube Agglomeration on Electrical Conductivity and Piezoresistivity of CNT/GNP Hybrid Nanocomposites

The reported percolation thresholds for CNT nanocomposites range from 0.001 wt.% to more than 10% for different polymeric matrix materials, fabrication techniques and type of nanotubes used (Kymakis et al., 2002; Sandler et al., 2003). In addition, the electrical conductivities usually vary from 10-5 to 10-2 S/m beyond percolation, with the value reaching as high as 481 S/m for high content of nanotubes (Kilbride et al., 2002; Ramasubramaniam, Chen, & Liu, 2003). Large variations in the reported properties are mainly attributed to the dispersion state, and aspect ratio of CNT used (N. Hu, Masuda, Yamamoto, et al., 2008; Jing Li, Ma, et al., 2007; Martin et al., 2004; Ounaies et al., 2003). CNTs tend to agglomerate into bundles due to van der Waals attractions and Coulomb forces (Ma et al., 2010). The low bending stiffness of CNTs, their high aspect ratio, and the incompatibility of their surfaces with most solvents makes it difficult to obtain homogenous dispersion during composite processing (Ramasubramaniam et al., 2003). Besides, commercially available CNTs are usually supplied in the form of heavily entangled bundles, which need further processing to create a dispersed network of nanotubes in composites (Ma et al., 2010).

Conventionally, it is accepted that CNT agglomerates have a negative effect on the effective mechanical properties of CNT-polymers, because they act as defects, rather than reinforcements by creating matrix rich areas (Haslam & Raeymaekers, 2013; Y. S. Song & Youn, 2005). Similarly, it was observed that agglomeration is detrimental to the electrical conductivity of CNT nanocomposites, since it leads to high percolation threshold values, compared to well dispersed CNT nanocomposites(Blanchet, Fincher, &

Gao, 2003; Jing Li, Ma, et al., 2007; Ramasubramaniam et al., 2003; Y. S. Song & Youn, 2005). However, some experimental studies showed that limited CNT agglomeration could reduce the nanocomposites percolation threshold and enhance its conductivity through an easier formation of a percolating network in the polymer (Aguilar, Bautista-Quijano, & Avilés, 2010; N. Hu, Masuda, Yamamoto, et al., 2008; Jing Li, Ma, et al., 2007; Martin et al., 2004; Seidel, Boehringer, & Lagoudas, 2008). In this context, it is necessary to understand and quantify the effect of CNT agglomeration on the percolation network formation to design the nanocomposites for optimal electrical and electromechanical performance.

A few modeling studies take CNT agglomeration into account in investigating the electrical (W. S. Bao, Meguid, Zhu, Pan, et al., 2012; S. Gong et al., 2014; Grujicic, Cao, & Roy, 2004; N. Hu, Masuda, Yan, et al., 2008; Jing Li, Ma, et al., 2007; Ounaies et al., 2003) and piezoresistive (S. Gong et al., 2014; Prakash & Seidel, 2016) behavior of CNT nanocomposites. Primarily, two agglomerate morphologies are considered in these studies: agglomerates formed by aligned CNTs (denoted rope-like agglomerates in the rest of the paper) and agglomerates formed by randomly oriented CNT (denoted equiaxed agglomerates in the rest of the paper). Only one of the two agglomerate morphologies is modeled in all of the above studies; further, in most of the studies, the agglomerate size, location, filler density (CNT content within an agglomerate) and number are predetermined and are not varied. However, experimental observations and micrographs indicate presence of both rope-like (Jarali, Basavaraddi, Kiefer, Pilli, & Lu, 2014; Prakash & Seidel, 2016) and randomly oriented (Ma et al., 2010; Yue et al., 2014; X.

Zhang et al., 2007) agglomerate morphologies with large variations in agglomerate size, number and density (Kasaliwal, Pegel, Göldel, Pötschke, & Heinrich, 2010).

In this chapter, the author utilizes a two-dimensional Monte Carlo model to comprehensively investigate the effect of agglomeration on the electrical percolation, conductivity and piezoresistive behavior of CNT monofiller and CNT-GNP hybrid nanocomposites. Agglomeration levels ranging from a perfectly dispersed microstructure with no agglomerates to a very high level of agglomeration are studied. The model formulation presented in Section 4.1 is novel in the following aspects. The first is its ability to model all agglomerate morphologies ranging from equiaxed to rope-like agglomerate. The second is that the number and location of agglomerates are not predefined, and are random for a given agglomeration level. This leads to realistic agglomerates with non-uniform filler density and inhomogeneous distribution. The third is the ability to model agglomerates in both CNT monofiller composites and/or CNT-GNP hybrid composites. Utilizing this Monte Carlo model, the author analyzes the electrical and piezoresistivity properties of nanocomposites with various microstructures and identify the conditions in which low levels of CNT agglomeration improve these material behaviors. The results, discussion, and conclusions are presented in Sections 4.2, 4.3 and 4.4 respectively. Part of this chapter previously appeared as (Gbaguidi, Namilae, & Kim, 2019b).

4.1. Model Formulation

4.1.1. Modeling of CNT and GNP in Polymer Nanocomposites

Conductive nanocomposites can be obtained by adding electrically conductive nanofillers into a polymer. The fillers are able to form a conductive path that imparts conductivity to the insulating polymer. This is due to the formation of quantum tunneling junctions at electrical contacts between adjacent fillers. A two-dimensional continuum percolation model and Monte Carlo simulations as described in Section 3.1 are used to predict the conductive behavior of nanocomposites filled with CNT and GNP particles. The fillers generation and modeling is the same as in Section 3.1.

4.1.2. Modeling of CNT Agglomeration in Polymer Nanocomposites

In realistic microstructures of nanocomposites, the fillers are not uniformly dispersed in the nanocomposites; instead, they form entangled clusters or agglomerates loosely bonded by van der Waals interactions. Microstructures with varying quantity and morphology (rope vs equiaxed) of agglomerates are generated for the Monte Carlo simulations. First a seed layer of completely randomized and uniformly distributed fillers is generated according to Equations 3.1 to 3.7. Additional fillers are then generated such that they form agglomerates around a fraction of the initial seed layer. The total volume fraction of CNTs, V_f in the RVE is the sum of the agglomerated and non-agglomerated volume fractions (respectively V_f^{agg} and $V_f^{non-agg}$).

$$V_f = V_f^{agg} + V_f^{non-agg} \tag{4.1}$$

The following procedure is followed to generate the microstructures:

First generate a seed layer of non-agglomerated uniformly distributed CNTs of volume fraction, $V_f^{non-agg}$.

Let N^a be the number of agglomerated CNTs. Choose randomly, N^a CNTs, of mid-point C^k and orientation ϕ^k, from the non-agglomerated seed layer (a CNT can be chosen more than once). The mid-point C^k of those CNTs will represent the agglomerate centers of the N^c clusters ($1 \leq k \leq N^c$and $N^c \leq N^a$), see Figure 4.1.

The new CNTs generated to be part of the agglomerates (say kth CNT) are placed such that their mid-point is randomly positioned inside the circle of center C^k and radius r_{agg}. In addition, the agglomerated CNT orientation θ^k is random, such as $\theta^k \in [\phi^k - \alpha_{agg}, \phi^k + \alpha_{agg}]$. α_{agg} defines the orientation of CNTs within the agglomerate and also the morphology of the agglomerate ranging from a rope like agglomerate (α_{agg}~0) to a completely equiaxed entanglement (α_{agg}~180^o).

The kth agglomerated CNT is described as a line segment of length, l_k, orientation, θ^k, with mid-point (x_c^k, y_c^k), starting point (x_1^k, y_1^k) and ending points (x_2^k, y_2^k) such that:

$$\begin{bmatrix} x_1^k \\ y_1^k \end{bmatrix} = \begin{bmatrix} x_c^k \\ y_c^k \end{bmatrix} - \frac{l_k}{2} \begin{bmatrix} cos\,\theta^k \\ sin\,\theta^k \end{bmatrix} \tag{4.2}$$

$$\begin{bmatrix} x_2^k \\ y_2^k \end{bmatrix} = \begin{bmatrix} x_c^k \\ y_c^k \end{bmatrix} + \frac{l_k}{2} \begin{bmatrix} cos\,\theta^k \\ sin\,\theta^k \end{bmatrix} \tag{4.3}$$

$$\begin{bmatrix} x_c^k \\ y_c^k \end{bmatrix} = \begin{bmatrix} C_x^k \\ C_y^k \end{bmatrix} + r_{agg}\sqrt{rand_1^k} \begin{bmatrix} cos(2\pi \times rand_2^k) \\ sin(2\pi \times rand_2^k) \end{bmatrix} \tag{4.4}$$

where (C_x^k, C_y^k) are the coordinates of C^k, $rand_1^k$ and $rand_2^k$ are two random numbers and r_{agg} is the cluster radius (W. S. Bao, Meguid, Zhu, Pan, et al., 2012). Equations 4.2 to 4.4 are derived from (W. S. Bao, Meguid, Zhu, Pan, et al., 2012) to fit the present formulation. The second and third steps of the above procedure enable creation of microstructures with agglomerates in non-predetermined positions and numbers with non-uniform filler density. In addition, agglomerate morphologies varying from rope-like to equiaxed can be modeled utilizing this procedure. This is the first modeling study to consider these variations to the best of the author's knowledge. The non-agglomerated CNT seeds chosen to generate the agglomerates are accounted inside V_f^{agg}, and new uniformly distributed CNTs (non-agglomerated) are generated to compensate for $V_f^{non-agg}$.

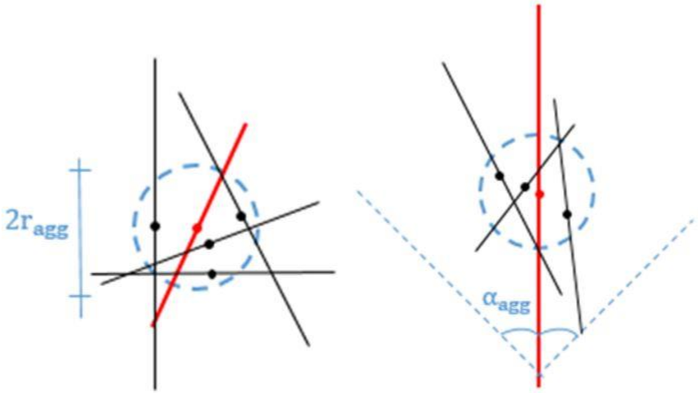

Figure 4.1 Schematic of a CNT agglomerate with the cluster radius, r_{agg} (Left) for random agglomeration alignment $\alpha_{agg} = 180^0$ and (Right) for cluster angle $\alpha_{agg} = 45^0$. Black lines represent the agglomerated CNTs, red lines represent the non-agglomerated CNT that define the agglomerate.

Three parameters are introduced to describe the state of CNT aggregation: the agglomeration level or volume fraction of agglomeration $\left(\xi_{agg} = V_f^{agg}/V_f\right)$ (S. Gong et al., 2014), the cluster radius $\left(r_{agg}\right)$ and the cluster angle $\left(\alpha_{agg}\right)$ as shown in Figure 4.2. When $\xi_{agg} = 0$, the CNTs are uniformly dispersed in the RVE with no aggregation and with the increase in ξ_{agg}, the aggregation level is more severe. r_{agg} is inversely proportional to the filler density of the aggregates or clusters. When r_{agg} is on the order of the size of the RVE, the CNTs in the agglomerates are randomly positioned anywhere in the RVE, hence no aggregation. With the decrease of r_{agg}, the aggregates have higher filler density and form inclusions in the RVE. The CNTs are randomly oriented in the agglomerate when $\alpha_{agg} = 180^0$ but form a bundle of ropes with $\alpha_{agg} = 0^0$.

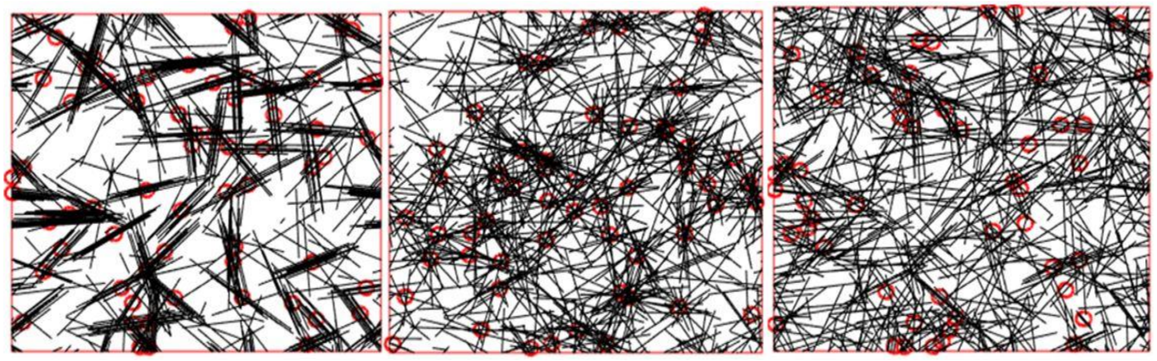

Figure 4.2 Microstructures with parameters (Left) $\xi_{agg} = 0.9$, $\alpha_{agg} = 0^0$, (Middle) $\xi_{agg} = 0.9$, $\alpha_{agg} = 180^0$and (Right) $\xi_{agg} = 0.5$, $\alpha_{agg} = 0^0$ with $r_{agg} = L_x/50$ at their respective percolation onset.

4.1.3. Modeling of Percolation, Electrical Resistance and Piezoresistivity in CNT-GNP Hybrid Network

The percolation of the composite is evaluated using the percolation probability, which is the probability that there is at least one conductive path in the RVE spanning the two electrodes. It is defined in Equation 3.19. The percolation threshold or onset corresponds to the volume fraction (V_T) where the RVE transitioned from insulator to a conductor at P = 50% (B. M. Lee et al., 2014). Additionally, the volume fraction (V_{100}), where the material is a conductor, at P = 100% will also be computed. To compute the conductivity of the RVE, the tunneling distances (distance between adjacent fillers less than the tunneling cutoff) are first transformed in resistors of resistance (tunneling resistance) proportional to the distances. Assuming a square tunneling barrier height λ, the tunneling resistance is approximated in (Simmons, 1963b) by:

$$R_t = \frac{h^2 d}{Ae^2\sqrt{2m\lambda}} exp\left(\frac{4\pi d}{h}\sqrt{2m\lambda}\right) \tag{4.5}$$

where h is Planck's constant, d is the tunneling distance, e is the quantum of electricity, m is the mass of electron, and A is the cross section area of the tunnel (approximated as cross section area of CNT here). In addition, the fillers inside the percolated network are transformed in resistors of resistance (intrinsic resistance) proportional to their size and inversely proportional to their conductivity as described in Equations 3.12 and 3.13. With the percolated network, transformed into resistors, Kirchhoff's current and Ohm's laws are used with the incomplete Cholesky conjugate gradient method (Rommes & Schilders, 2010) to calculate the resistance of the RVE.

To simulate the piezoresistivity of the nanocomposites, the RVE is subject to uniaxial deformation. Due to the high Young's modulus of the fillers compared to the polymer matrix, and with the weak interface between fillers and matrix, the change of the fillers position follows affine transformation (Taya, Kim, & Ono, 1998). The size of the RVE $(\bar{L}_x, \bar{L}_y)$, the center $(\bar{x}_c^i, \bar{y}_c^i)$ and orientation angle $\bar{\theta}^i$ of the ith filler, after an incremental strain $\Delta\varepsilon$ along the y – axis are derived from (Taya et al., 1998):

$$(\bar{L}_x, \bar{L}_y) = \left(L_x(1-\nu\Delta\varepsilon), L_y(1+\Delta\varepsilon)\right) \tag{4.6}$$

$$(\bar{x}_c^i, \bar{y}_c^i) = \left(x_c^i(1-\nu\Delta\varepsilon), y_c^i(1+\Delta\varepsilon)\right) \tag{4.7}$$

$$\bar{tan}\,\theta^i = \frac{1+\Delta\varepsilon}{1-\nu\Delta\varepsilon} tan\,\theta^i \tag{4.8}$$

ν is the polymer Poisson's ratio, (L_x, L_y), (x_c^i, y_c^i) and θ^i are respectively the size of the RVE, the center and orientation angle of the ith filler, before strain. The change of position and orientation of the fillers due to strain will lead to a modification in the tunneling distances. The resistance of the RVE (R) at a fixed strain is then re-evaluated in an iterative way and compared to the resistance (R_0) of the unstrained RVE. The piezoresistivity is characterized using the resistance change ratio (K) and the gauge factor (GF), described in Equations 2.1 and 2.2.

Square RVE cell of length L=25 μm is used in this numerical study, with polymer and fillers parameters summarized in Table 4.1. This approach can be used as a tool to model more realistic agglomerates of different morphologies in nanocomposites, which have applications as conductors or strain and damage sensors. In addition, the state of CNT agglomeration experimentally observed using scanning electron microscope (SEM) images could be reproduced using this formulation.

Table 4.1

Physical parameters used in numerical analysis.

Parameters		Values
Polymer	Poisson's ratio, ν	0.3
	tunneling barrier height, λ	1 eV
MWCNT	Diameter, D	50 nm
	Nominal length, L	5 μm
	Weibull parameters, (a, b)	(5.6403 μm, 2.4)
	Cutoff distance, d_{cutoff}	1.4 nm
	Intrinsic conductivity, σ_{cnt}	1×10^4 S/m
	Van der Waals distance, d_{vdw}	0.34 nm
Graphene Nanoplatelets (GNP)	Sheet resistance, Re	2.8×10^2 Ω /sq
	Semi-major axis, a_0	4 μm
	Semi-minor axis, b_0	0.5 μm

Note. The parameters of CNT are obtained from (Shen Gong & Zhu, 2014). The electrical property of GNP is obtained from Graphene Supermarket vendor's data sheet (Graphene supermarket, n.d.).

4.2. Results

The author uses Monte Carlo simulations based on the model described above to compute the effective percolation probability, electrical conductivity and piezoresistivity of the nanocomposites, first with only CNTs as fillers and then with CNTs and GNPs as fillers. The statistical variation of the measured properties of the nanocomposites was reduced by averaging over a large number of randomized microstructures. The effective value of the measured properties (each data point) in all the plots below is the average value over 5000 microstructures. Most of the properties converged after 2000 Monte Carlo simulations. In the following subsections, it will be shown in details the effect of agglomeration level on first the percolation, then the conductivity and finally the piezoresistivity of the nanocomposites. For each of those properties, the results will be presented in two categories. First, the effect of agglomeration level, when the agglomerate radius, r_{agg} (inverse of agglomerate filler density) is varied, while the agglomerate morphology is kept to entangled clusters $\left(\alpha_{agg} = 180^0\right)$. Second, the effect of agglomeration level, when the agglomerate morphology, $\alpha_{agg}$is varied, while the agglomerate radius is kept constant ($r_{agg} = 2L/100$).

4.2.1. Effect of Agglomeration on the Percolation Threshold of CNT Monofiller Nanocomposites

4.2.1.1. Effect of Agglomerate Filler Density on Percolation for a Fixed Cluster Angle

The author starts by simulating the effect of agglomeration level, ξ_{agg} and cluster radius, r_{agg} on the percolation probability for entangled clusters $\left(\alpha_{agg} = 180^0\right)$. Figure 4.3(a) and 3(b) show the plots of agglomeration level (ξ_{agg}) vs volume fraction of fillers needed to reach percolation threshold with 50% and 100% percolation probability respectively. For a data point on Figure 4.3(a), 50% of the stochastically varying microstructures with a corresponding ξ_{agg} and r_{agg} have a percolated network.

Figure 4.3(a) shows that for low filler density agglomerates (high r_{agg}), the percolation threshold is the same for low agglomeration level $\left(\xi_{agg} \leq 40\%\right)$, as that for the microstructures without any agglomeration. The effect of agglomeration is more pronounced for high filler density agglomerates (low r_{agg}). In these cases, the percolation threshold starts increasing for $\xi_{agg} \geq 20\%$. Nonetheless for high agglomerate level $\left(\xi_{agg} \geq 60\%\right)$ the percolation threshold values increases drastically, for all values of r_{agg} , compared to microstructures without agglomeration. Figure 4.3(b) shows that the trend of both percolation probability of 50% and 100% are similar. However, at low agglomeration level $\left(\xi_{agg} < 30\%\right)$, the percolation threshold of microstructures with low filler density agglomerate is lower than the ones without agglomeration.

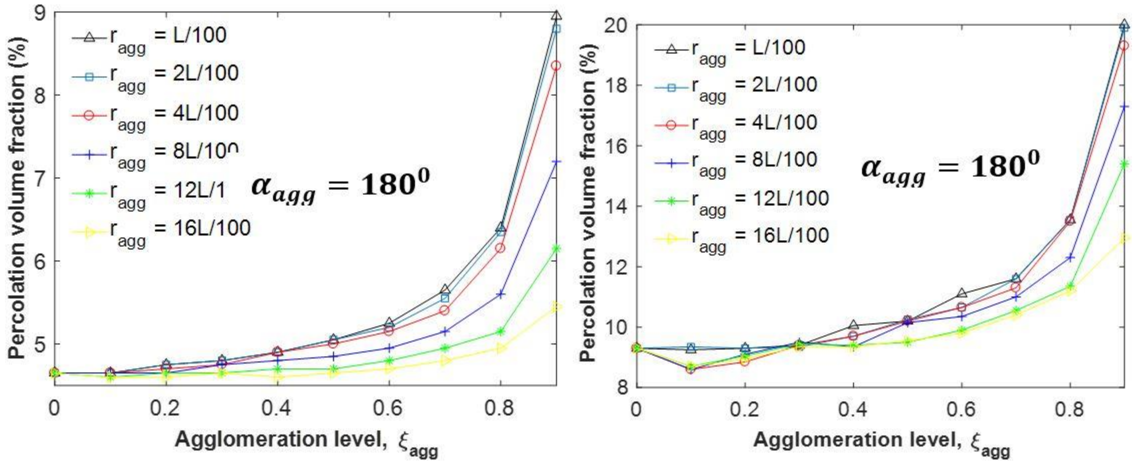

(a) **(b)**

Figure 4.3 Impact of agglomeration level (ξ_{agg}) and cluster radius (r_{agg}) on percolation thresholds, at percolation probability of (a) 50% and (b) 100%.

This suggests that low level of agglomeration (small ξ_{agg}) has no negative effect on percolation, on the contrary, it lowers the percolation threshold especially at low filler density (high r_{agg}). Note that several experimental studies have reported lower percolation threshold in presence of limited agglomeration (Aguilar et al., 2010; N. Hu, Masuda, Yamamoto, et al., 2008). In general, for high agglomeration level, the increase of the agglomerate filler density (decrease of r_{agg}) leads to the increase of the percolation threshold.

4.2.1.2. Effect of Agglomerate Cluster Angle on Percolation for a Fixed Cluster Radius

Here the author simulates the effect of agglomeration level, $\xi_{agg}$and cluster angle, α_{agg} on the percolation probability for a fixed cluster radius ($r_{agg} = 2L/100$). In Figure 4.4, the effect of agglomerate morphology, from bundle like agglomerates to entangled agglomerates is investigated by varying the cluster angle $\left(\alpha_{agg}\right)$. The Y-axis is again the volume fraction of fillers needed for percolation at percolation probabilities of 50% and 100% in Figure 4.4(a) and Figure 4.4(b) respectively. Both plots suggest that α_{agg} has little or no effect in increasing the percolation, for low agglomeration levels $\left(\xi_{agg} \leq 30\%\right)$. Here again the percolation threshold is lowered in some instances due to agglomeration. However, for higher values of ξ_{agg}, the effect of cluster angle is very pronounced. The agglomerates modeled as ropes or bundles of aligned nanotubes $\left(\alpha_{agg} \leq 10^0\right)$ lead to very high percolation thresholds, compared to agglomerates modeled as equiaxed entanglements $\left(\alpha_{agg} = 180^0\right)$.

In general, the percolation threshold increases with the decrease of the cluster angle. In modeling literature, agglomerates have been modeled either as randomly oriented

CNTs in a cluster or as rope of perfectly aligned CNTs. The present simulations show that these two modeling abstractions lead to very different percolation predictions and the necessity to choose appropriate agglomerate morphology.

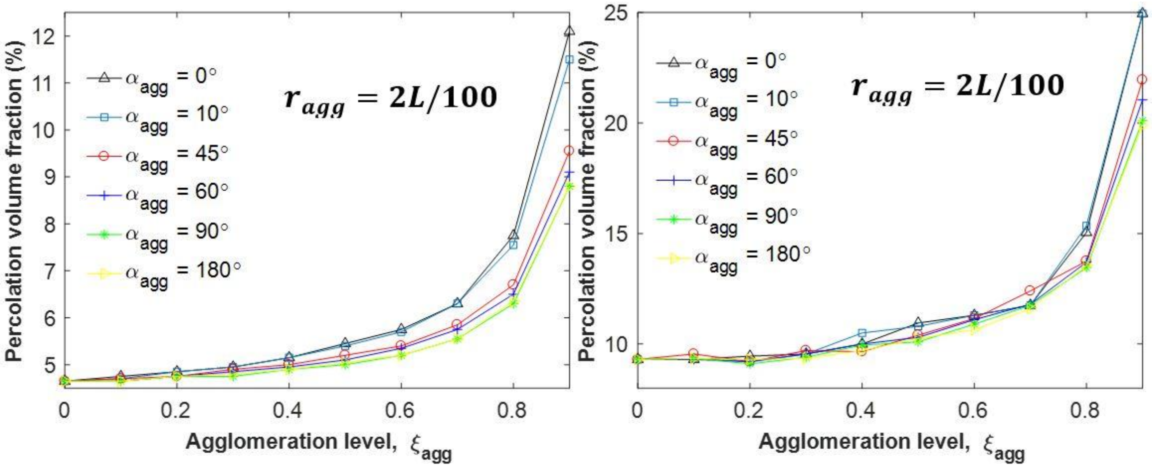

(a) **(b)**

Figure 4.4 Impact of agglomeration level (ξ_{agg}) and cluster angle (α_{agg}) on percolation thresholds, at percolation probability of (a) 50% and (b) 100%.

4.2.2. Effect of Agglomeration on the Conductance of CNT Monofiller Nanocomposites

To fully understand the percolation behavior of nanocomposites with agglomeration, the author shows the percolation probability and conductance of the nanocomposites, from low to very high filler content. Figure 4.5(a) and (b) show the results for the lowest density (highest r_{agg}) of equiaxed agglomerates analyzed in this work. First, it is seen that the agglomeration level does not have a big effect on the conductance curves for low density of equiaxed agglomerates, even though it affects the percolation probability. In addition, for low content of CNT (less than 5%), the conductance of most agglomerated microstructures is better than the uniformly

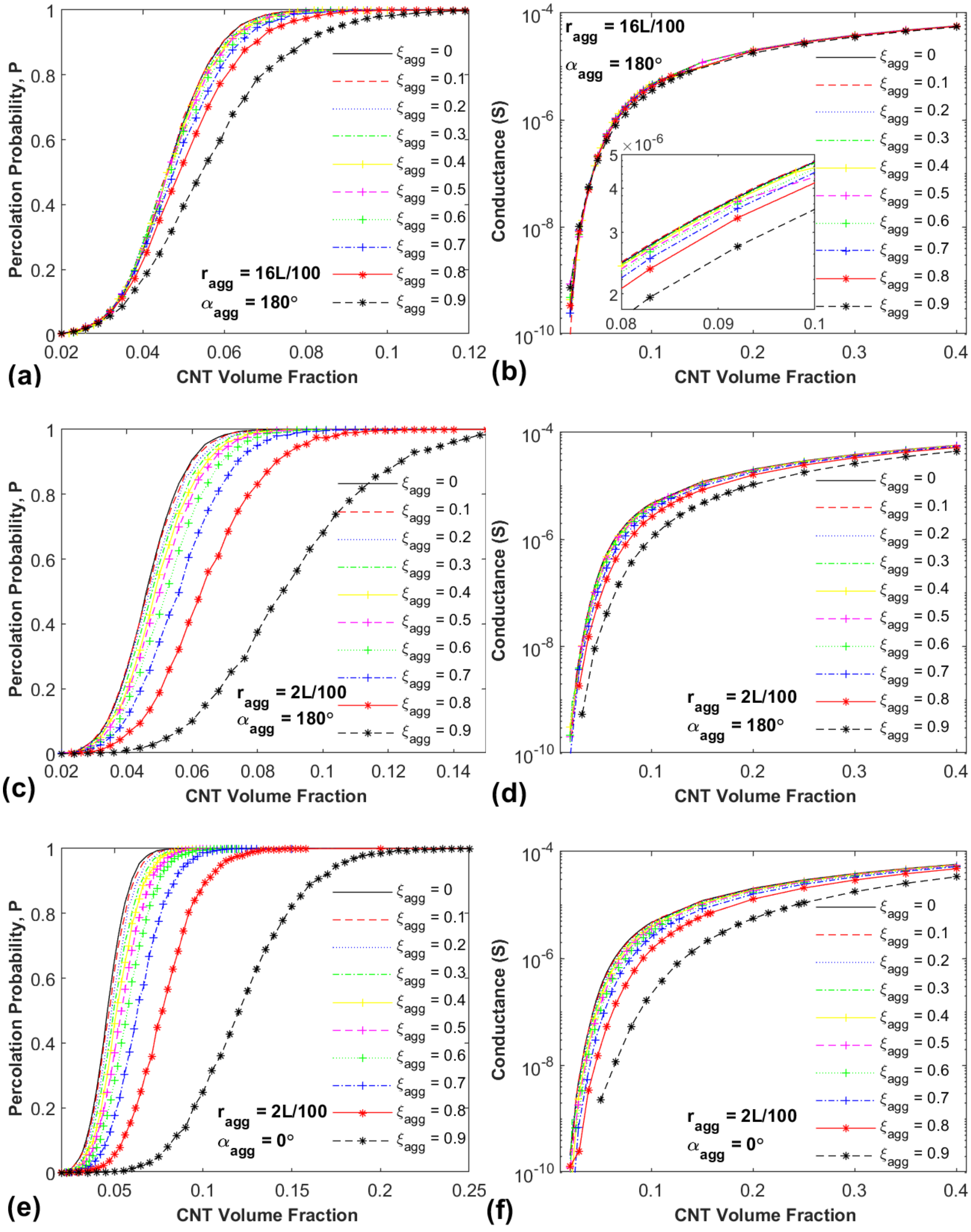

Figure 4.5 Effect of agglomeration on percolation probability and conductance of CNT nanocomposites with (a) & (b) low density and equiaxed agglomerates (c) & (d) high density and equiaxed agglomerates and (e) & (f) high density and rope-like agglomerates.

dispersed ones. With the increase of the filler content, the conductance of most agglomerated structures becomes lower than the dispersed microstructures. However, the conductance of the microstructures with 10% agglomeration level remains better than the fully dispersed state (see inset Figure 4.5(b)).

For the same microstructures, but with the highest density (lowest r_{agg}) of equiaxed agglomerates, Figure 4.5(c) and (d) show that agglomeration level (ξ_{agg}) has an important effect on both the conductance and percolation probability of the nanocomposites. In this case, agglomeration was seen to hinder the conductance of the nanocomposites, for all agglomeration level. Low agglomeration levels (10% and 20%) lead to conductance very close to the uniform microstructures. In Figure 4.5(e) and (f) the author analyzes high density (lowest r_{agg}) of rope-like agglomerates. It is seen that the effect of agglomeration levels on conductance and percolation probability is even more pronounced in these microstructures. Here, agglomeration levels less than 10% lead to slightly higher conductance values, but all agglomeration levels higher than 10%, reduce the conductance of the nanocomposites.

4.2.3. Effect of Agglomeration on the Piezoresistivity of CNT Monofiller Nanocomposites

Many functional applications of CNT nanocomposites are based on their piezoresistive behavior, which is the change in resistance as a function of the deformation state. It is commonly accepted that piezoresistivity in CNT composites is due to the modification of the percolated network with application of strain (Namilae & Choudhary, 2018). In order to compare the piezoresistive behavior of all microstructures examined, tensile and compressive strains of 0.6% are induced to all microstructures at their percolation thresholds for both percolation probabilities of 50% and 100%.

4.2.3.1. Effect of Agglomerate Filler Density on Piezoresistivity, for a Fixed Cluster Angle

Figure 4.6 shows that low agglomeration levels $(\xi_{agg} \leq 40\%)$ have very little effect on the piezoresistivity for all filler densities. Increasing the agglomeration levels leads to a noticeable reduction of the piezoresistivity for high filler density (low r_{agg}) while, the piezoresistivity of low filler density (high r_{agg}) agglomerated microstructures is not sensitive to agglomeration levels up to 70%. Figure 4.7 shows that the piezoresistivity at percolation threshold P = 100% follow the same trend as for P = 50%. However, it can be seen that for low filler density agglomerates, low levels of agglomeration improves the piezoresistivity.

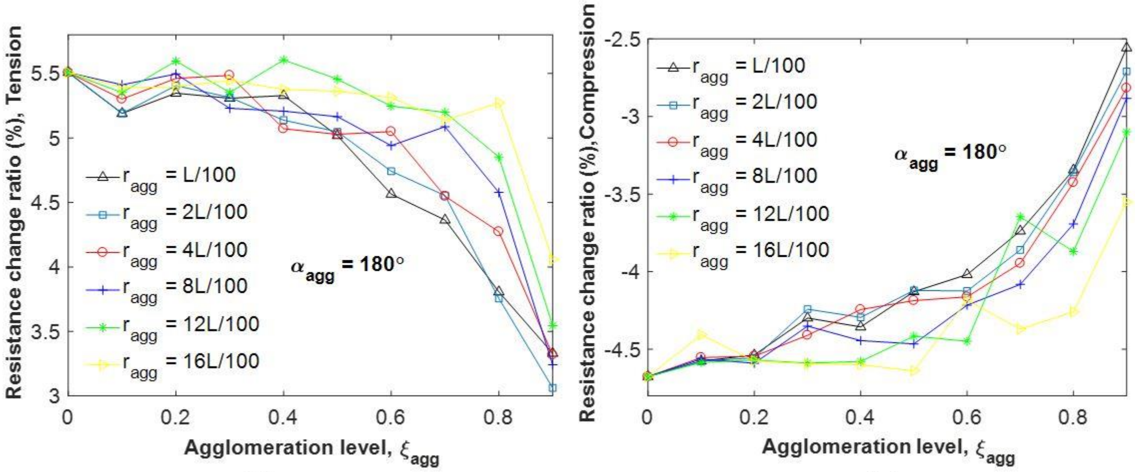

(a) (b)

Figure 4.6 Impact of agglomeration level (ξ_{agg}) and cluster radius (r_{agg}) on RVE piezoresistivity under (a) tensile and (b) compressive strains. Microstructures at their respective percolation threshold (P = 50%).

This is similar to the observations in Figure 4.3 for percolation thresholds. In addition Figure 4.6 and Figure 4.7 shows that the piezoresistivity at P = 100% is three times lower than the one at P = 50%. This is due to the fact that an increase of filler content in CNT monofiller composites usually decreases the piezoresistivity (I. Kang, Schulz, et al., 2006; M. Park et al., 2008; Yin et al., 2011).

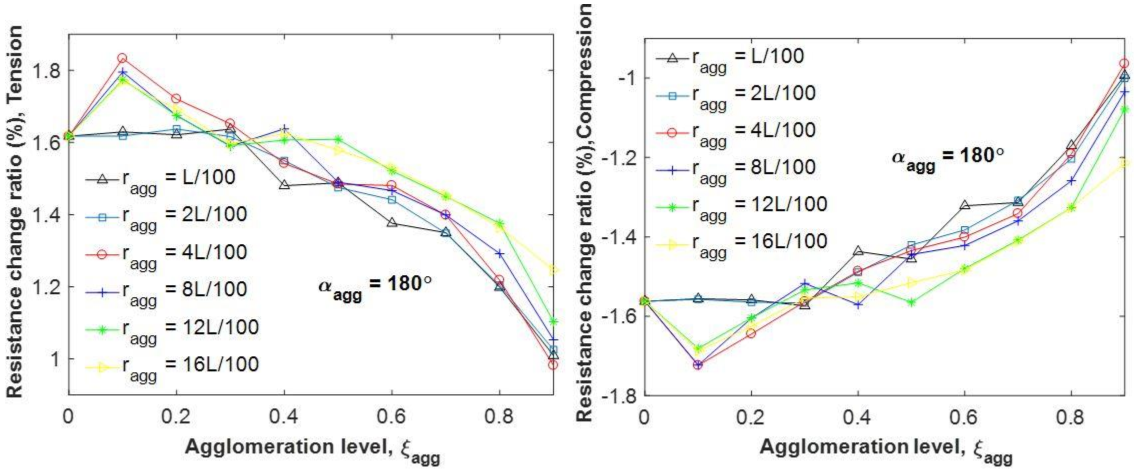

(a) **(b)**

Figure 4.7 Impact of agglomeration level (ξ_{agg}) and cluster radius (r_{agg}) on RVE piezoresistivity under (a) tensile and (b) compressive strains. Microstructures at their respective percolation threshold (P = 100%).

4.2.3.2. Effect of Agglomerate Cluster Angle on Piezoresistivity for a Fixed Cluster Radius

The author now examines the effect of agglomerate morphology and cluster angle on piezoresistivity, for the highest filler density of agglomerate. Figure 4.8 and Figure 4.9 show that the agglomerate cluster angle have very limited effect on the piezoresistivity, even though it affects the percolation threshold. However, increasing the agglomeration level, leads to a noticeable decrease of the piezoresistivity. In general, the piezoresistivity of rope-like agglomerates is lower than that of equiaxed agglomerates.

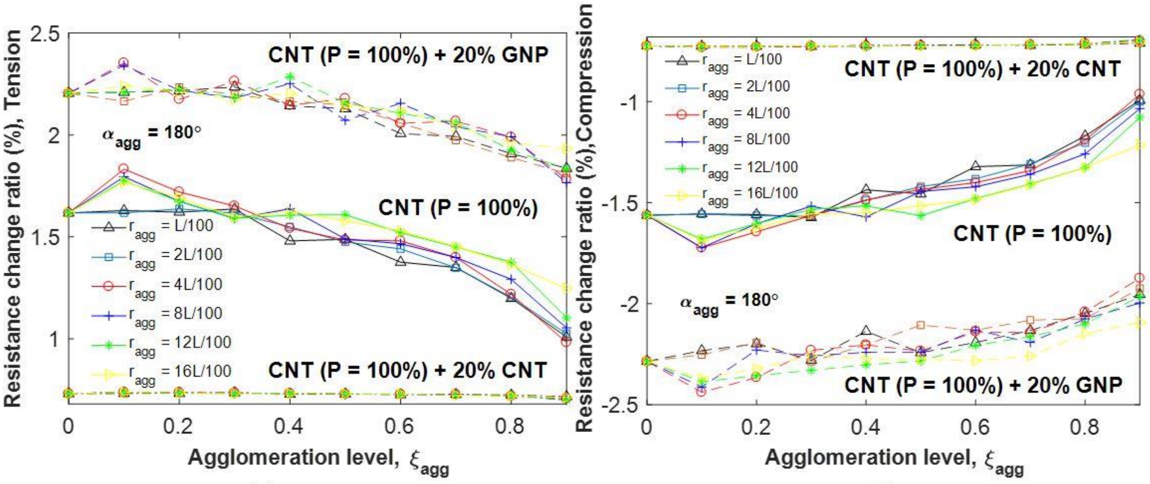

(a) **(b)**

Figure 4.8 Impact of agglomeration level (ξ_{agg}) and cluster angle (α_{agg}) on RVE piezoresistivity under (a) tensile and (b) compressive strains. Microstructures at their respective percolation threshold (P = 50%).

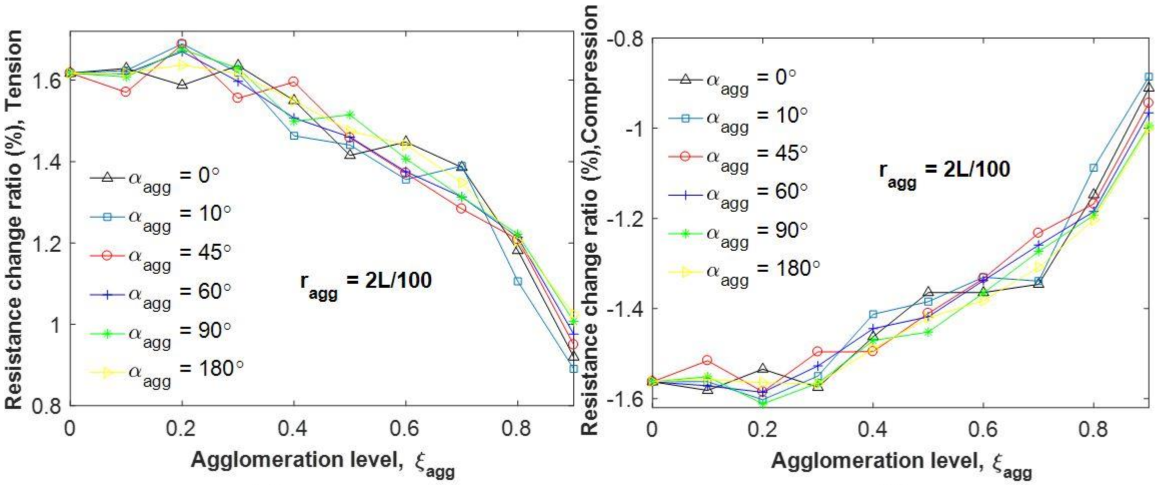

(a) **(b)**

Figure 4.9 Impact of agglomeration level (ξ_{agg}) and cluster angle (α_{agg}) on RVE piezoresistivity under (a) tensile and (b) compressive strains. Microstructures at their respective percolation threshold (P = 100%).

4.2.4. Impact of Addition of Graphene Nanoplatelets to CNT Nanocomposites

In this section, the author studies the effect of CNT agglomeration in CNT-GNP hybrid nanocomposites. Twenty percent (20%) of GNPs is added to each CNT microstructures at their percolation threshold (P = 100%). All GNPs are modeled as elliptical platelets with dimensions (semi major and minor axes) 4μm x 0.5μm and are randomly oriented. In Figure 4.10 the conductance of the CNT nanocomposites is compared to the one of the hybrid composites after the addition of GNPs.

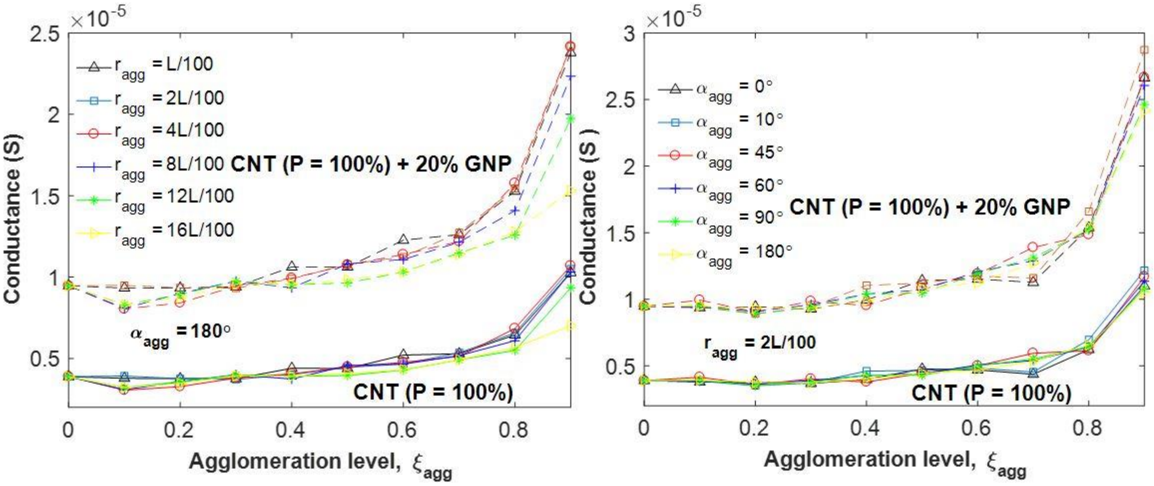

(a) (b)

Figure 4.10 Impact of addition of GNP fillers on the conductivity of CNT nanocomposites with different (a) CNT densities in equiaxed agglomerates and (b) cluster angles in high density agglomerates. CNT microstructures at their respective percolation threshold (P = 100%).

Figure 4.10(a) shows an increase of the conductivity in all cases of agglomerate density, for equiaxed agglomerates with the addition of GNPs. The addition of GNPs to CNT microstructures with the highest agglomerate density leads to a similar increase in conductance, for all the different agglomerate cluster angles, as shown in Figure 4.10(b). It is interesting to note that the conductance of the CNT nanocomposites with and without GNPs follows the same trend, which is identical to the trend of percolation threshold in Figure 4.3(b) and Figure 4.4(b). Hence, the addition of GNPs only increases the conductivity of the nanocomposites without modifying the effect of the different agglomeration parameters on the nanocomposites.

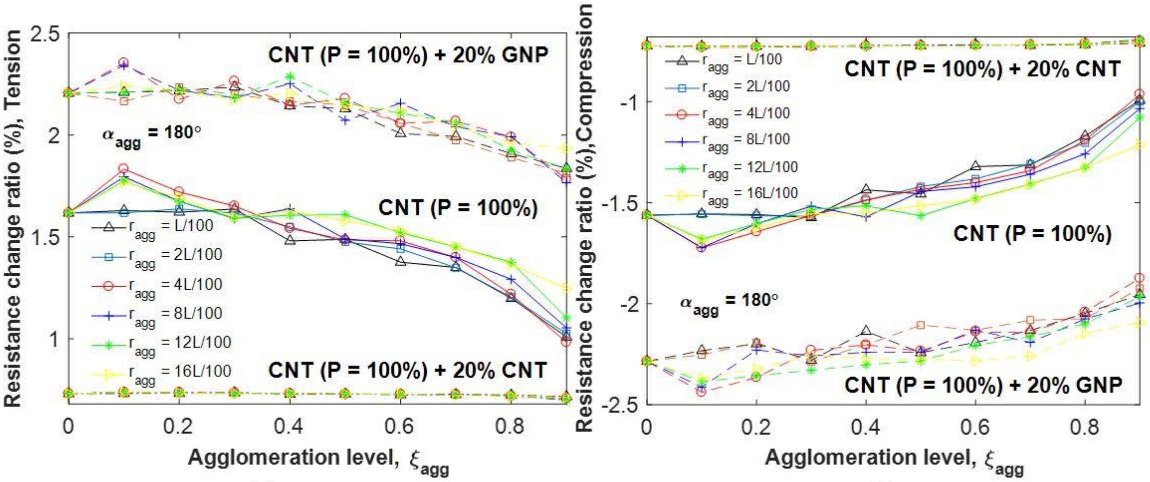

(a) **(b)**

Figure 4.11 Impact of addition of GNP fillers on hybrid nanocomposites piezoresistivity with varying CNT density in equiaxed agglomerates under (a) tensile and (b) compressive strain. CNT microstructures at their respective percolation threshold (P = 100%).

In his previous work (Gbaguidi et al., 2018b; Gbaguidi, Namilae, & Kim, 2018a), the author showed using both 2D and 3D simulations that piezoresistivity of CNT nanocomposites after percolation decreases with the increase in CNT content. However, if GNPs are added instead, an improvement of the piezoresistivity is observed. In this section, the author studies three types of microstructures. The first are CNT microstructures at the volume fraction corresponding to the percolation probability of 100%, denoted CNT (P =100%). To obtain the second type of microstructures, the author adds 20% CNT to the CNT microstructures at their percolation. This is denoted CNT

(P=100%)+20% CNT. In the last microstructures, denoted CNT (P=100%)+20% GNP, 20% GNP are added to the CNT microstructures at their percolation. The piezoresistivity before and after addition of GNPs is then compared. The author first starts evaluating the piezoresistivity on microstructures with equiaxed agglomerates and varying agglomerate filler density.

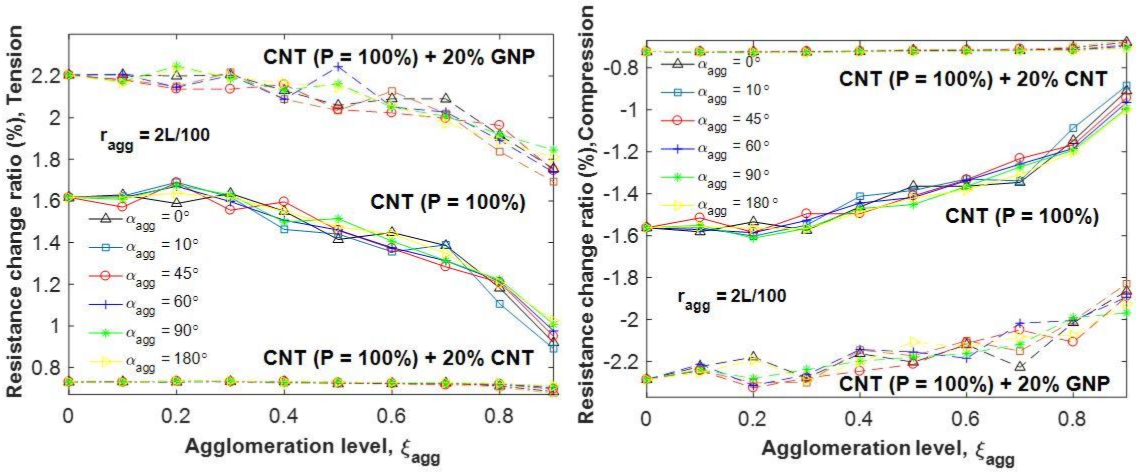

(a) (b)

Figure 4.12 Impact of addition of GNP fillers on hybrid nanocomposites piezoresistivity with varying cluster angles in high-density agglomerates under (a) tensile and (b) compressive strain. CNT microstructures at their respective percolation threshold (P = 100%).

Figure 4.11 shows that the addition of more CNTs decreases the piezoresistivity of the composites for both tensile and compressive deformation. It is also seen that at that high content of CNT filler, the piezoresistivity is almost the same for all agglomeration levels and agglomerate filler densities. This suggests, as in the case of conductivity, that at high content of CNT fillers, the effect of agglomeration on piezoresistivity is very limited. However, if GNPs are added instead of CNTs, there is an improvement of the piezoresistivity, for all levels of agglomeration and all filler densities. Modification of CNT network by two-dimensional GNPs is responsible for this behavior. Figure 4.12 shows the same improvement with the addition of GNP to CNT microstructures, where the cluster angle is varied from equiaxed to rope-like agglomerates. In addition, for the highest level of agglomerate, it can be seen that the addition of GNP actually leads to piezoresistivity higher than the piezoresistivity of uniformly dispersed CNT nanocomposites at percolation. This shows that it might be possible to reduce the negative effect of agglomeration on piezoresistivity by adding a second filler.

4.3. Discussion

Many experimental studies indicate that agglomeration is detrimental to electrical properties of nanofiller composites (Blanchet et al., 2003; Jing Li, Ma, et al., 2007; Ramasubramaniam et al., 2003; Y. S. Song & Youn, 2005). For example, Y. S. Song and Youn (2005) found the electrical conductivity of the well dispersed composites to be an order of magnitude higher than the agglomerated composites at percolation. Blanchet et al. (2003) shows that the poor dispersion of CNT in ethylcellulose leads to a high percolation threshold while the good dispersion in polyaniline leads to a percolation threshold ten times lower. In contrast, some experimental studies show that limited CNT agglomeration reduces the nanocomposites percolation threshold and enhance its conductivity (Aguilar et al., 2010; N. Hu, Masuda, Yamamoto, et al., 2008; Jing Li, Ma, et al., 2007; Martin et al., 2004; Seidel et al., 2008). Experimental observations by Aguilar et al. (2010) indicate that percolation threshold for the uniformly dispersed CNT composites is higher than the composites with small level of agglomeration. This has been explained by the increased density of CNT-to-CNT junctions in the agglomerated composites, after percolation, which favors the formation of conductive networks.

The present model qualitatively matches most of the above observations and identifies the parameter space in which limited agglomeration leads to improved electrical properties. Firstly, the author finds that when agglomeration levels are moderately high, i.e. when 50% or more of the fillers are in agglomerates, in general the author observes an increase in percolation threshold and decrease in conductivity and piezoresistivity. There is however improvement in some electrical properties at low agglomeration levels. The most significant factor affecting this improvement is the density of nanofillers within the agglomerate. Figure 4.3 shows that, the decrease of percolation threshold at low agglomeration levels $\left(\xi_{agg} < 30\%\right)$ is observed primarily in lower density agglomerates (high r_{agg}). Similarly, the conductance of the composite due to agglomeration increased only for low density agglomerates (Figure 4.5 (d)) and not for high density agglomerates (Figure 4.5(b)). Also, the piezoresistivity of low filler density (high r_{agg}) agglomerated microstructures is same as dispersed microstructures and higher than those with high density agglomerates (Figure 4.6 (a) and (b)).

These results indicate that small amount of low-density agglomerates are better than uniformly dispersed microstructures in generating conducting networks. Some experimental studies indicate the possibility of tailoring the microstructures to vary the filler density within agglomerates. Socher, Krause, Müller, Boldt, and Pötschke (2012) have observed agglomerates with different internal filler densities in polyamide 12 (PA12) matrix nanocomposites and associate lower density agglomerates with lower viscosity matrix. Jing Li, Ma, et al. (2007) list different treatments that lead to varying packing density within agglomerates and identify specific treatments that reduce density. Such methods used in conjunction with the present numerical model could lead to optimally agglomerated microstructures.

Specifically, a close look at the critical points in the different plots in Figures 4(b), 5(b), 8 and 10 can help designing target microstructures to test experimentally for optimum performance. Per example in applications where equiaxed agglomerates are desired, microstructures with agglomeration level less or equal to 20% (preferably at 10%) and with low filler density in the agglomerates will lead to lower percolation threshold and optimum conductivity and piezoresistivity. However, in case of nanocomposites, where only high filler density in agglomerates are possible, due to the viscosity of the matrix used, it is more desirable to have microstructures with agglomeration level of 20% to have lowest percolation threshold with optimum conductivity and piezoresistivity.

Another experimental observation is that both agglomerated and dispersed composites have similar conductivity values at very low and very high CNT content, whereas the conductivity of the agglomerated composites is higher around percolation (Aguilar et al., 2010). Similar behavior as in the experimental study can be observed in Figure 4.5(d) and (f). The conductive networks are densely packed with fillers at high CNT content, and completely disconnected at low CNT content, which limit the effect of any agglomeration. However, close to percolation the effect of agglomeration on enhancing connectivity between fillers is most pronounced.

Table 4.2

Review of different analytical and numerical works on CNT agglomeration for electrical properties

Modeling Approach	Agglomerate Morphology	Extent of Agglomeration
Excluded volume approach (Ounaies et al., 2003) (Analytical)	Rope of 1, 7 or 19 aligned CNTs in hexagonal arrangement	Either 0 or 100% (uniform agglomerate size and distribution)
Improved interparticle distance (Jing Li, Ma, et al., 2007) (Analytical)	Entangled bundle in spherical inclusion	Varies (uniform agglomerate size and distribution)
Statistical percolation Monte Carlo (N. Hu, Masuda, Yan, et al., 2008) (Numerical)	Randomly oriented CNTs in sphere-like agglomerate	100% (4 equidistant aggregates with uniform agglomerate size, density and distribution)
Excluded volume (Analytical) and Statistical percolation Monte Carlo (Grujicic et al., 2004) (Numerical)	Rope of 3, 7 and 19 aligned CNTs in hexagonal arrangement	Either 0 or 100% (uniform agglomerate size, density and distribution)
Statistical percolation Monte Carlo (W. S. Bao, Meguid, Zhu, Pan, et al., 2012) (Numerical)	Randomly oriented CNTs in sphere-like agglomerate	Either 0 or 100% (uniform agglomerate size, density and distribution)
Statistical percolation Monte Carlo (S. Gong et al., 2014) (Numerical)	Randomly oriented CNTs in sphere-like agglomerate in multiscale modeling	Varies (uniform agglomerate size and density)
Peridynamics (Prakash & Seidel, 2016) (Numerical)	Rope of 7 aligned CNTs in hexagonal arrangement	100% (uniform agglomerate size, density and distribution)

Another important factor that affects the electrical and electromechanical properties of the nanocomposites is agglomerate morphology (see Figure 4.4, Figure 4.5, Figure 4.8, Figure 4.9, Figure 4.10 and Figure 4.12). In terms of experimental studies, most micrographs in agglomeration studies suggest a more equiaxed sphere-like entangled structure for agglomerates (Ma et al., 2010; Yue et al., 2014; X. Zhang et al., 2007), while studies on nanoropes or aligned CNT exhibit rope-like configurations (Jarali et al., 2014; Prakash & Seidel, 2016). From a modeling perspective, there have been no study that compares the electrical or electromechanical behaviors in these two kinds of agglomerates. The modeling studies tend to focus on one or the other type of agglomerate morphology (see Table 4.2), dictated primarily by model capabilities assumptions. For example, excluded volume approach was used to model CNT agglomerates as ropes of 3, 7 or 19 aligned nanotubes in hexagonal arrangement (Ounaies et al., 2003).

Similar hexagonal construct for agglomerate is used in peridynamics model (Prakash & Seidel, 2016) and in statistical (stochastic) percolation model (Grujicic et al., 2004). Models based on stochastic percolation networks (W. S. Bao, Meguid, Zhu, Pan, et al., 2012; S. Gong et al., 2014; N. Hu, Masuda, Yan, et al., 2008) tend to model the agglomerates as equiaxed sphere-like entanglements. When the agglomerates morphology is varied from rope like (low α_{agg}) to equiaxed entanglements $\left(\alpha_{agg} = 180^0\right)$ in this study, the author observes some interesting trends. The author finds that in general percolation threshold (Figure 4.4) is higher for rope-like agglomerates compared to equiaxed agglomerates. Similarly, piezoresistivity (see Figure 4.8 and Figure 4.9) is lower for rope-like agglomerates. Aligned nanofillers are expected to have higher mechanical properties, and efforts to align nanotubes often result in rope like agglomerates (Jarali et al., 2014). The decrease in electrical properties for these composites presents an additional consideration in the design and fabrication of multifunctional nanocomposites. Further, the results indicate the need to select appropriate agglomerate morphology to represent realistic microstructures.

Both experimental studies (I. Kang, Schulz, et al., 2006; M. Park et al., 2008; Yin et al., 2011) and numerical simulations (Gbaguidi et al., 2018a, 2018b) indicate that piezoresistivity and gauge factor of monofiller CNT composites is highest around percolation and reduces if additional CNTs are added. Likely reason for this is that the increased number of contacts at high CNT content results in lesser rate of change of tunneling junctions under deformation. The results for monofiller composites confirm this observation for agglomerated CNT composites. For example, adding 20% CNT to percolated composites with different agglomeration parameters still results in decreased resistance change ratio in Figure 4.11 and Figure 4.12. However, addition of 20% GNP as second filler increases not only the conductivity but also the piezoresistivity in hybrid composites with agglomerated CNTs. Notice that the difference between CNT monofiller and CNT-GNP hybrid resistance change is more at higher agglomeration levels (see Figure 4.11 and Figure 4.12) indicating a more prominent effect of GNP addition when large portions of CNT are in agglomerates.

The improvement of the piezoresistivity of the hybrid nanocomposite implies that the rate of change of the junction numbers between fillers after strain increased with addition of GNP particles. This is because GNPs as two-dimensional particles are able to bridge CNTs that are further apart in the RVE, compared to one-dimensional CNTs. At high agglomeration content, this bridging happens between agglomerates leading to a more prominent effect of GNP addition.

4.4. Summary

A stochastic percolation network model was developed to quantify the effect of CNT agglomeration on the percolation threshold, electrical conductivity and piezoresistivity of both CNT monofiller and CNT-GNP hybrid nanocomposites. The main contributions of the new model formulation are to consider the following: (i) the effect of different agglomerate morphologies varying from rope-like to equiaxed, (ii) more realistic agglomerate features such as non-uniform filler density and non-homogeneous distribution, and (iii) the effect of adding GNP as a second filler, on the electrical and piezoresistive behaviors. One of the new findings in the present results is that the agglomerate morphology (equiaxed vs rope-like) has an important effect on the electrical and piezoresistive properties of both CNT monofiller and CNT-GNP hybrid nanocomposites.

The author finds that in general, percolation threshold and piezoresistivity are respectively higher and lower for rope-like agglomerates compared to equiaxed agglomerates. The present results correspond with experimental observations, which show that high agglomeration level is detrimental to the electrical percolation threshold and conductivity as well as the piezoresistivity of the nanocomposites, for all the different agglomerate morphologies. However, it is found that small levels of agglomeration enhance the aforementioned properties, especially when the CNT density within the agglomerates is low. It is also shown that while the addition of more CNTs, after percolation reduces the piezoresistivity of CNT nanocomposites with or without agglomeration, the addition of GNPs leads to higher piezoresistivity. This implies that the negative effect of high agglomeration level on the conductivity and piezoresistivity of CNT nanocomposites could be counterbalanced by the addition of GNP. Finally, the author identifies the microstructures that achieve the optimal agglomeration level for improved electrical and piezoresistive behaviors.

5. Synergy Effect in Hybrid Nanocomposites Based on Carbon Nanotubes and Graphene Nanoplatelets

Carbon nanomaterials such as graphene nanoplatelets (GNPs) and carbon nanotubes (CNTs) exhibit excellent electrical, mechanical (G. Mittal, Dhand, Rhee, Park, & Lee, 2015) as well as electromechanical (L. Kong & Chen, 2014) properties, and are ideal fillers for functional nanocomposites. The low percolation threshold in CNT composites coupled with their high conductivity (Bauhofer & Kovacs, 2009; Sandler et al., 2003) has led to extensive work directed towards the fabrication and testing of these materials (De Volder et al., 2013). However, because of the relatively higher production cost of CNTs, compared to GNP, GNP nanocomposites have attracted considerable interest as a replacement to CNT composites in recent years (N. Liu et al., 2008; Y. Liu et al., 2016). This is explained by this thought, “When carbon fibers just won’t do, but nanotubes are too expensive, where can a cost-conscious materials scientist go to find a practical conductive composite? The answer could lie with graphene sheets” (Kotov, 2006, p. 254). Despite a percolation threshold lower than that of traditional macroscale fillers and carbon black, GNP nanocomposites usually exhibit higher percolation and resistivity compared to CNT nanocomposites (J. Du et al., 2011). Conductive nanocomposites filled with CNTs or/and GNPs have been used in medical and advanced aerospace technologies, and for sensors, solar cells and flexible electronics (De Volder et al., 2013; L. Kong & Chen, 2014; Curtis Lee et al., 2013; Luo & Liu, 2013; Maiti & Khatua, 2016).

To overcome the limitations of both CNT and GNP monofiller nanocomposites, hybrid composites filled simultaneously with both CNTs and GNPs have been increasingly investigated as performant multifunctional materials (Al-Saleh, 2015; Anees, Gbaguidi, Kim, & Namilae, 2017, 2018; Gbaguidi, Anees, Namilae, & Kim, 2017; Gbaguidi, Namilae, & Kim, 2019a, 2017; S. H. Hwang, Park, & Park, 2013; S. H. Hwang, Park, Park, et al., 2013; Kumar et al., 2010; Curtis Lee et al., 2013; Jing Li et al., 2008; W. Li, Dichiara, & Bai, 2013; Luo & Liu, 2013; Maiti & Khatua, 2016; Ren et al., 2012; Masoud Safdari, 2012; Wegrzyn et al., 2015; Yue et al., 2014). Even though the cost reduction of the polymer nanocomposites is the main objective, achieving synergistic improvement in the electrical properties of the hybrid CNT-GNP nanocomposites will lead to increased performance. Thus far, the experimental works exhibit unclear trends as of the effect of different parameters of the two fillers on the electrical properties of their hybrid composites, compared to their monofiller composites.

Two main trends are observed for the electrical properties of hybrid composites: additive effects (Anees et al., 2017; W. Li et al., 2013) and synergistic effects (Gbaguidi, Namilae, et al., 2017; Maiti & Khatua, 2016; Masoud Safdari & Al-Haik, 2013). The additive effect happens when the hybrid composite leads to a performance (e.g., conductivity, percolation threshold) that is better than one of the monofiller, but worse than the second monofiller, similar to the rule of mixtures. By synergy, the author implies that the hybrid composite performs better than both monofiller composites, therefore the synergistic effect is more desirable than the additive effect. For example, the 8:2 weight ratio mix of CNT and GNP of specific aspect factors in an epoxy matrix causes synergistic enhancement of electrical percolation and conductivity, i.e. better properties than the weight ratios of 10:0 and 0:10 (Yue et al., 2014). This is attributed to GNPs improving the CNT dispersion. In another experimental work, the mix of CNT and GNP in propylene leads only to additive effects in the electrical properties (Al-Saleh, 2015).

Increasing the CNT: GNP ratio leads to a monotonous increase in the conductivity between its lowest value at a weight ratio of 0:10 to its highest value at a ratio of 10:0. These reports suggest that the morphology, as well as the relative volume content of the two fillers, affect the likelihood of a synergistic enhancement.

Much work has been done in the literature to extensively study the electrical and piezoresistive performance of CNT and GNP monofiller composites using mostly percolation-based Monte Carlo models (Abad, Ganjeh, Zolriasatein, Shabani-Nia, & Siadati, 2017; S. Gong et al., 2014; Shen Gong & Zhu, 2014; Hicks et al., 2009; N. Hu et al., 2010; Javidjam, Hekmatshoar, Hedayatifar, & Abad, 2019; B. M. Lee et al., 2014; Oskouyi & Mertiny, 2011; Rahman & Servati, 2012). In the case of hybrid composites made of CNT and GNP fillers, only a few numerical works studied the electrical performance of hybrid composites (Gbaguidi et al., 2018a; Maxian et al., 2015; X. Ni, Hui, Su, Cutler, & Liu, 2019; X. Ni, Hui, Su, Jiang, & Liu, 2018; M. Safdari & Al-Haik, 2012; Sagalianov et al., 2017). Despite the novelty of those works, several modeling-related limitations exist in their formulation. The main limitation comes from the fact that their formulation can only predict the additive effects, or that the synergy improvement in the hybrid composites is observed by comparison only to GNP monofiller composites (Maxian et al., 2015; X. Ni et al., 2019; M. Safdari & Al-Haik, 2012).

However, CNT composites usually have better electrical properties than the GNP ones due to their 1D geometry; hence, synergy should be analyzed with respect to both monofiller composites. Another limitation is the use of softcore (sometimes hardcore) particles without tunneling interactions (X. Ni et al., 2018; Sagalianov et al., 2017). While this enables computational efficiency, the models are limited to computing only the percolation threshold and cannot compute the electrical conductivity of the composites. Note that tunneling is considered the primary mechanism for conductivity in nanocomposites (Kirkpatrick, 1973). Also, only GNP with circular planar geometry (instead of ellipses) is usually modeled, not considering the unsymmetrical lateral dimensions of GNP after exfoliation. While the aforementioned limitations are modeling-related, the most important feature lacking in the existing numerical works is the fundamental understanding of the mechanisms of electrical conductivity and synergy improvement in hybrid nanocomposites. So far, to the author’s knowledge, the present work is the first modeling study to examine the synergistic effects in both electrical percolation and conductivity, and the underlying mechanisms that lead to synergy in hybrid CNT-GNP nanocomposites. It is also the first study to evaluate the effect of the type of CNT, its chirality and its intrinsic conductivity on the electrical properties of hybrid nanocomposites.

In this section, the author develops a three-dimensional (3D) Monte Carlo model to examine the microstructures and the mechanisms that lead to synergy in the electrical behavior of CNT-GNP hybrid nanocomposites, beyond the simple additive improvements. The content of both fillers, as well as the planar and transversal aspect ratios of GNP, were parametrically varied to examine the hybrid microstructures that exhibit synergistic enhancement in percolation threshold and conductivity. The effect of aspect ratio, intrinsic conductivity, and chirality of CNT is also studied. The author utilizes this model to study the parameters related to tunneling junctions that control the hybrid electrical properties, and the mechanisms responsible for the synergistic behavior. The author analyzes the experimental work from the literature in the context of the findings of the present model. Part of this chapter previously appeared as (Gbaguidi, Namilae, & Kim, 2020).

5.1. Model Formulation

5.1.1. Three-Dimensional Modeling of the Hybrid Composites

The author simulated a percolation-based model with the generation of a random distribution of CNTs and GNPs, as shown in Figure 5.1, in a Representative Volume Element (RVE) of size $L_x \times L_y \times L_z$. Every CNT is modeled as a cylinder of diameter D_{CNT} represented by its centerline segment, with midpoint (x_c^i, y_c^i, z_c^i), starting point (x_1^i, y_1^i, z_1^i) and ending point (x_2^i, y_2^i, z_2^i) such that:

$$\begin{bmatrix} x_2^i \\ y_2^i \\ z_2^i \end{bmatrix} = \begin{bmatrix} x_c^i \\ y_c^i \\ z_c^i \end{bmatrix} + l^i \begin{bmatrix} \sin\theta^i \cos\emptyset^i \\ \sin\theta^i \sin\emptyset^i \\ \cos\theta^i \end{bmatrix} \text{ and } \begin{bmatrix} x_1^i \\ y_1^i \\ z_1^i \end{bmatrix} = \begin{bmatrix} x_c^i \\ y_c^i \\ z_c^i \end{bmatrix} - l^i \begin{bmatrix} \sin\theta^i \cos\emptyset^i \\ \sin\theta^i \sin\emptyset^i \\ \cos\theta^i \end{bmatrix} \tag{5.1}$$

$$\begin{bmatrix} x_c^i \\ y_c^i \\ z_c^i \\ \emptyset^i \\ \theta^i \end{bmatrix} = \begin{bmatrix} L_x \times rand_1^i \\ L_y \times rand_2^i \\ L_z \times rand_3^i \\ 2\pi \times rand_4^i \\ \cos^{-1}\left(1 - 2 \times rand_5^i\right) \end{bmatrix} \tag{5.2}$$

l^i, $\emptyset^i$ and θ^i are the length, polar angle and azimuthal angle of the ith CNT, respectively. In his previous works (Gbaguidi et al., 2018b, 2019b), the author modeled CNTs with a variable length that follows a Weibull distribution, similar to experimental observations of CNT micrographs. In this work, to study the effect of the CNT aspect ratio on the properties of the hybrid nanocomposites, CNTs with fixed length l^i were used. Every GNP is modeled as an elliptical platelet of thickness t, represented by its mid-plane elliptical disk, with center $\boldsymbol{C_j}$ (x_c^j, y_c^j, z_c^j), major axis length and vector a and $\boldsymbol{U_j}$, minor axis length and vector b and $\boldsymbol{V_j}$, and orthonormal vector $\boldsymbol{W_j} = \boldsymbol{U_j} \times \boldsymbol{V_j}$, where $\left[\boldsymbol{U_j}, \boldsymbol{V_j}, \boldsymbol{W_j}\right] = \boldsymbol{R}.\boldsymbol{T}$, such as:

$$\begin{bmatrix} x_c^j \\ y_c^j \\ z_c^j \\ \emptyset^j \\ \theta^j \end{bmatrix} = \begin{bmatrix} L_x \times rand_1^j \\ L_y \times rand_2^j \\ L_z \times rand_3^j \\ 2\pi \times rand_4^j \\ \cos^{-1}\left(1 - 2 \times rand_5^j\right) \end{bmatrix} \tag{5.3}$$

$$\boldsymbol{R} = \begin{bmatrix} \cos\theta^j \cos\emptyset^j & -\sin\emptyset^j & \sin\theta^j \cos\emptyset^j \\ \cos\theta^j \sin\emptyset^j & \cos\emptyset^j & \sin\theta^j \sin\emptyset^j \\ -\sin\theta^j & 0 & \cos\theta^j \end{bmatrix} \tag{5.4}$$

$\boldsymbol{R}$ is the rotation matrix for random orientation, $\boldsymbol{T}$ is the Cartesian unit vector, and $\emptyset^j$ and θ^j are the polar angle and azimuthal angle of the jth GNP. rand is a uniformly distributed random number in]0,1[.

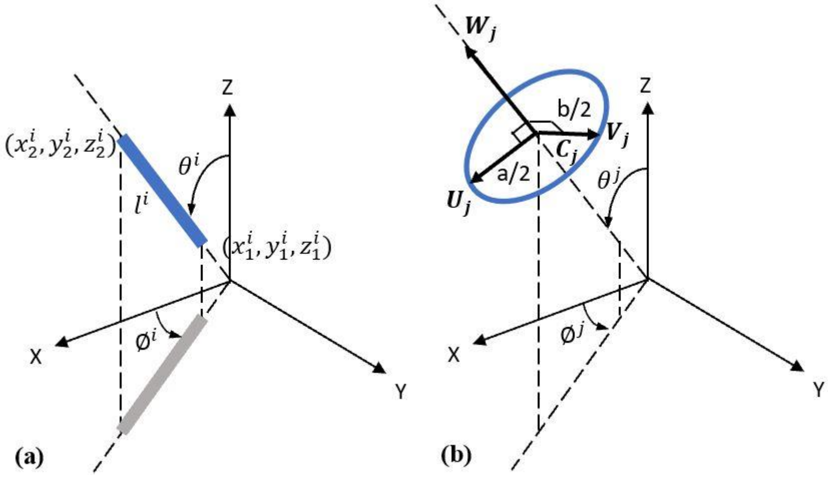

Figure 5.1 Schematics of (a) line segment of the ith CNT and (b) the mid-plane elliptical disk of the jth GNP.

To obtain realistic microstructures, fillers' interpenetration is prevented by computing the minimum distance d_{min} between either adjacent elliptical disk and line segment, adjacent line segments or adjacent elliptical disks, depending on the fillers in consideration. The algorithm to compute the minimum distance between line segments (CNTs) is relatively simple and easy to implement. However, computing the minimum distance between two elliptical curves is more involved, and can be reduced to the numerical computation of the real-valued roots of a degree 16 polynomial. The author has previously derived the minimum distance between two adjacent elliptical disks (GNPs) and the distance between adjacent elliptical disk and line segment (GNP and CNT) in (Gbaguidi et al., 2018a). These require additional calculations, compared to the case of two elliptical cures as shown below:

Let the plane of each of the two adjacent elliptical disks (GNPs) have coordinate systems $\{\boldsymbol{C}_j; \boldsymbol{U}_j, \boldsymbol{V}_j, \boldsymbol{W}_j\}$, where $\mathbf{C}_j$ is the plane's origin and $j = 0, 1$. The coordinate's axis directions are the three specified vectors that form a right-handed orthonormal set. Let a_j and b_j be respectively the semi-major and semi-minor axis lengths of the ellipse. The elliptical disks are described by:

$$\mathbf{X}_j = \mathbf{C}_j + s_j\mathbf{U}_j + t_j\mathbf{V}_j \tag{5.5}$$

where the parameters (s_j, t_j) are constrained by:

$$\left(\frac{s_j}{a_j}\right)^2 + \left(\frac{t_j}{b_j}\right)^2 \leq 1 \tag{5.6}$$

To compute the interaction between two ellipses the author defines:

$\mathbf{p} = [s_0 \quad t_0 \quad s_1 \quad t_1]^{\mathrm{T}}$, $\mathbf{k}_j = [0 \quad 0 \quad 0 \quad 0]^{\mathrm{T}}$, $d_j = -1/2$, for $j = 1, 2$ and

$$\boldsymbol{H_0} = \begin{bmatrix} 1/a_0^2 & 0 & 0 & 0 \\ 0 & 1/b_0^2 & 0 & 0 \\ 0 & 0 & 0 & 0 \\ 0 & 0 & 0 & 0 \end{bmatrix}, \qquad \boldsymbol{H_1} = \begin{bmatrix} 0 & 0 & 0 & 0 \\ 0 & 0 & 0 & 0 \\ 0 & 0 & 1/a_1^2 & 0 \\ 0 & 0 & 0 & 1/b_1^2 \end{bmatrix}$$

Now, the constraints in Equation 5.6 are written in the form of Equation 5.7, while the function to be minimized is written in the form of Equation 5.8.

$$\frac{1}{2}\mathbf{p}^{\mathrm{T}}\boldsymbol{H}_j\mathbf{p} + \mathbf{k}_j{}^{\mathrm{T}}\mathbf{p} + d_j \leq 0 \tag{5.7}$$

$$\emptyset = \frac{1}{2}\mathbf{p}^{\mathrm{T}}\boldsymbol{Q}\mathbf{p} + \mathrm{f}^{\mathrm{T}}\mathbf{p} + c \tag{5.8}$$

Half of the squared distance between elliptical disks $\boldsymbol{X}_0(s_0, t_0)$ and $\boldsymbol{X}_1(s_1, t_1)$ is defined as $\emptyset$:

$$\begin{aligned} \emptyset(s_0, t_0, s_1, t_1) &= \frac{1}{2}\|\mathbf{X_0}(s_0, t_0) - \mathbf{X_1}(s_1, t_1)\|^2 \qquad (5.9) \\ &= \frac{1}{2}(s_0^2 + t_0^2 + s_1^2 + t_1^2) - s_0 s_1(\mathbf{U_0}^T \cdot \mathbf{U_1}) - s_0 t_1(\mathbf{U_0}^T \cdot \mathbf{V_1}) \\ &\qquad - t_0 s_1(\mathbf{V_0}^T \cdot \mathbf{U_1}) \\ &- t_0 t_1(\mathbf{V_0}^T \cdot \mathbf{V_1}) + s_0(\mathbf{U_0}^T \cdot \Delta) + t_0(\mathbf{V_0}^T \cdot \Delta) - s_1(\mathbf{U_1}^T \cdot \Delta) \\ &\qquad - t_1(\mathbf{V_1}^T \cdot \Delta) + \frac{1}{2}\|\Delta\|^2 \\ &= \frac{1}{2}\mathbf{p}^{\mathrm{T}} \begin{bmatrix} 1 & 0 & -\mathbf{U_0}^T \cdot \mathbf{U_1} & -\mathbf{U_0}^T \cdot \mathbf{V_1} \\ 0 & 1 & -\mathbf{V_0}^T \cdot \mathbf{U_1} & -\mathbf{V_0}^T \cdot \mathbf{V_1} \\ -\mathbf{U_0}^T \cdot \mathbf{U_1} & -\mathbf{V_0}^T \cdot \mathbf{U_1} & 1 & 0 \\ -\mathbf{U_0}^T \cdot \mathbf{V_1} & -\mathbf{V_0}^T \cdot \mathbf{V_1} & 0 & 1 \end{bmatrix} \mathbf{p} \\ &\quad + [\mathbf{U_0}^T \cdot \Delta \quad \mathbf{V_0}^T \cdot \Delta \quad -\mathbf{U_1}^T \cdot \Delta \quad -\mathbf{V_1}^T \cdot \Delta]\,\mathbf{p} + \frac{1}{2}\|\Delta\|^2 \\ &= \frac{1}{2}\mathbf{p}^{\mathrm{T}}\boldsymbol{Q}\mathbf{p} + \mathbf{f}^{\mathrm{T}}\mathbf{p} + c \end{aligned}$$

where $\mathbf{f} = [\mathbf{U}_0{}^T \cdot \Delta \quad \mathbf{V}_0{}^T \cdot \Delta \quad -\mathbf{U}_1{}^T \cdot \Delta \quad -\mathbf{V}_1{}^T \cdot \Delta]^T$, $\Delta = \mathbf{C}_0 - \mathbf{C}_1$, $\boldsymbol{Q}$ is the 4 × 4 matrix on the third line of Equation 5.9 and $c = \frac{1}{2}\|\Delta\|^2$.

To compute the minimum distance between elliptical disks, the author utilizes an inbuilt MATLAB function ‘fmincon’ which finds the minima of $\emptyset$ (Equation 5.9), subject to the quadratic constraints in Equation 5.7, using predefined initial conditions (s_0, t_0, s_1, t_1). The distance between an elliptical disk (GNP) and a line segment (CNT) follows a similar procedure.

Interpenetration between fillers happens if: (a) $d_{min} < d_{vdw} + t$ in case of adjacent GNPs, (b) $d_{min} < d_{vdw} + D_{CNT}$ for adjacent CNTs and (c) $d_{min} < d_{vdw} + \frac{t}{2} + \frac{D_{CNT}}{2}$ in case of adjacent GNP and CNT. In the case of interpenetration, the new particle is discarded and another one is generated until there is no interpenetration. d_{min} is stored as the tunneling distance between the two fillers, if $d_{min} \leq d_{cutoff}$. d_{cutoff} is the tunneling cutoff distance and is assumed to be $2.6\ nm$. For faster computation, in the case of adjacent CNTs, the RVE is partitioned into uniform grids. Every CNT is assigned to all the bins it intersects. Only the CNTs inside the assigned bins of the newly generated CNT or the bins directly adjacent to those are checked for distance calculation. Bins of size five times smaller than the CNT length are used, following (Vink & Schilling, 2005).

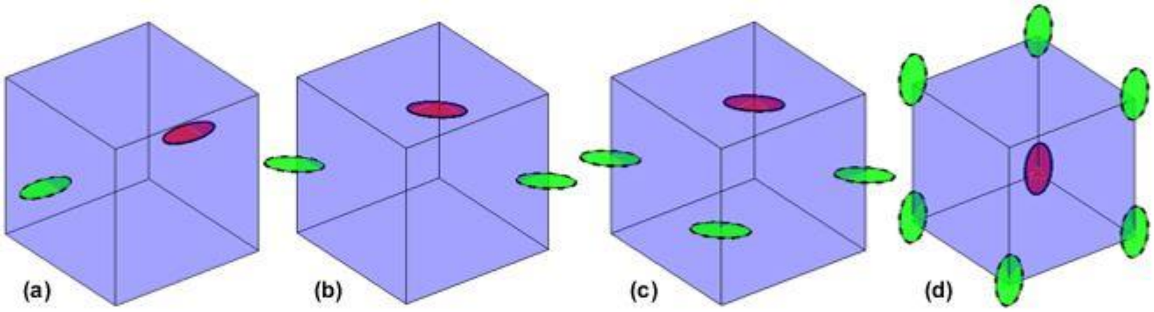

Figure 5.2 Periodic Boundary Conditions (PBC) procedure. Particles in red color with a full curve are initial particles and those with green color and a dashed curve are compensated particles.

Periodic Boundary Condition (PBC) was implemented on all sides of the RVE when part of a filler is outside of the RVE. PBC for CNT in 3D is relatively simple and similar to the procedure in 2D (B. M. Lee et al., 2014). PBC in 3D for elliptical GNP filler requires additional steps compared to linear or circular particles. If an elliptical particle intersects one (or two) boundaries, one (or two) additional elliptical particles are compensated back on the opposite boundaries, as shown in Figure 5.2(a) and (b). If the particle intersects two boundaries with their common edge, three particles are compensated, as shown in Figure 5.2(c). If the particle intersects boundaries, with one of their common edges, four particles are compensated. If it intersects three boundaries, with two of their common edges, five particles are compensated. In the case of three boundaries with their common three edges, six particles are compensated as shown in Figure 5.2(d). Figure 5.3 shows nanocomposites at their percolation onset, filled with different amounts of CNT and GNP, generated using the current modeling approach.

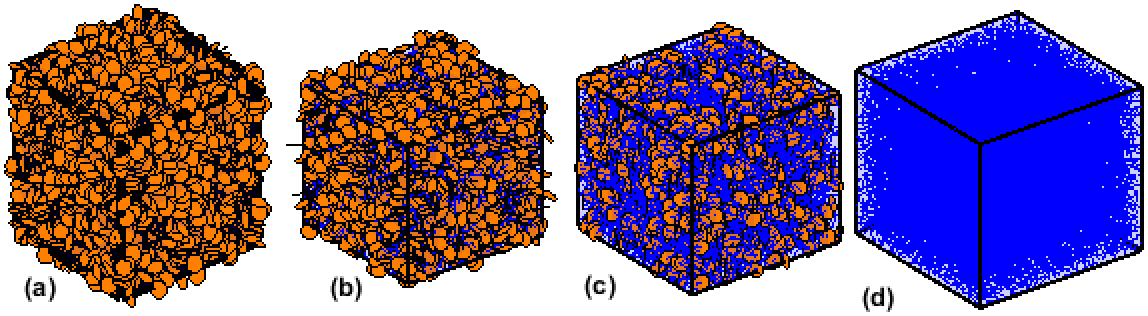

Figure 5.3 Hybrid RVE simulation cells filled with (a) only GNPs, (b) 20% of CNTs, (c) 80% of CNTs and (d) only CNTs at their respective percolation onset (10.80, 10.26, 9.91 and 10.35 vol.% respectively).

5.1.2. Electrical Percolation and Conductivity Modeling for Hybrid Microstructures

From section 5.1.1, hardcore hybrid microstructures were obtained with all the tunneling distances between adjacent fillers computed. Fillers with an inter-particle distance less or equal to the tunneling cutoff distance, d_{cutoff} are assumed electrically connected and form a cluster. When a cluster of connected fillers bridges the two electrodes of the RVE (planes $z = 0$ and $z = L_z$), there is percolation in the RVE, and the conductance of the nanocomposites is equal to that of the cluster. The percolation of the composite is evaluated using the percolation probability, which is the probability that there is at least one conductive path in the RVE spanning the two electrodes. It is defined as $\mathrm{P} = \frac{\mathrm{n_p}}{\mathrm{N}}$ where n_p is the number of microstructures with the existence of at least one conductive path in a total of N microstructures (B. M. Lee et al., 2014). The percolation threshold or onset (V_{50}) corresponds to the total volume fraction of fillers ($V_T = V_{CNT} + V_{GNP}$) when P = 50% (B. M. Lee et al., 2014). V_{CNT} and V_{GNP} are respectively the volume fraction of CNT and GNP inside the nanocomposites.

Additionally, The author also computes the volume fraction (V_{100}), which is the minimum volume fraction of fillers needed to have percolation in all N microstructures, when P = 100%. To compute the conductivity of the RVE, the tunneling distances, d_{min} between fillers are first transformed into resistors of resistance (tunneling resistance) proportional d_{min}. Assuming a square tunneling barrier height, $\lambda = 0.5\ eV$, the tunneling resistance is approximated in (Simmons, 1963b) by:

$$R_t = \frac{h^2 d}{Ae^2\sqrt{2m\lambda}} \exp\left(\frac{4\pi d}{h}\sqrt{2m\lambda}\right) \tag{5.10}$$

where h is Planck's constant, d is the tunneling distance, e is the quantum of electricity, m is the mass of an electron and A is the cross-section area of the tunnel. In addition, the fillers inside the percolated network are transformed into resistors of resistance (intrinsic resistance) proportional to their size and inversely proportional to their intrinsic conductivity. The calculations for intrinsic resistance R_{int} for CNT and GNP are provided elsewhere (Gbaguidi et al., 2018b). Kirchhoff's current and Ohm's laws are used with the incomplete Cholesky conjugate gradient method (Rommes & Schilders, 2010) to calculate the resistance of the RVE.

5.2. Results for CNT-GNP Hybrid Composites

Carbon nanotubes of constant length $L_{CNT} = 100\ nm$ and diameter $D_{CNT} = 10\ nm$ are modeled as multi-walled CNTs (MWCNT) unless stated otherwise in a cubic RVE of length $L_{RVE} = 1000\ nm$ for all the nanocomposites studied. GNP modeled as an elliptical cylinder with major axis length kept constant a = 100 nm is used as second filler. GNPs of different morphology are simulated, controlling the planar aspect ratio (AR_p) and the transversal aspect ratio (AR_t) such that: $AR_p = a/b$ and $AR_t = a/t$, where b and t are respectively the minor axis and the thickness of the GNP. $AR_p=1$ results in circular GNPs with the diameter equal to a = b. The following procedure is adopted for this section. First, a morphology of GNP is chosen by either fixing AR_p or AR_t. The chosen GNP is then mixed each time with CNT of different CNT volume ratios ($X = V_{CNT}/V_T$) to obtain eleven different nanocomposites, each corresponding to a value of X =0, 0.1, 0.2, …, 1.

The first nanocomposite is filled with only GNP, the second nanocomposite is filled with 10% vol. of CNT and 90% vol. of GNP and so forth. X=1 corresponds to CNT monofiller composite. For each of the 11 nanocomposites, their percolation threshold V_{50} and the minimum filler content for 100% percolation probability V_{100} were calculated. The percolation of the hybrid nanocomposites made with the GNP morphology is the curve connecting the 11 data points of V_{50}. Next, the electrical conductivity of each of the 11 nanocomposites is computed at the same filler content, to allow for comparison. Hence, V_{100Max}, which is the maximum of the 11 values of V_{100} was found and $V_C = 1.03 \times V_{100Max}$ was computed. The conductivity of each of the 11 nanocomposites is computed at the same filler content V_C. Finally, the total number of tunneling junctions between adjacent fillers in each of the 11 nanocomposites is computed at the same filler content V_C and plotted. The same procedure is followed for each morphology of GNP studied to obtain three 11-data-points curves (for percolation threshold, conductivity and number of tunneling junctions) for their hybrid composites.

The author uses Monte Carlo simulations based on the model described in section 2 to generate fillers with a random position and orientation and compute the effective value of the properties of the nanocomposites (percolation threshold and electrical conductivity) following the procedure described above. The statistical variation of the measured properties was reduced by averaging over 70 randomized microstructures. Seventy Monte Carlo sample microstructures were used due to computational limitations since the generation of each hardcore hybrid microstructure takes usually at least between 4 to 7 days.

5.2.1. Effect of GNP Transversal Aspect Ratio on Electrical Properties of Hybrid Microstructures

The exfoliation of graphite during the nanocomposite’s fabrication usually leads to a reduction of both the thickness and the lateral size of graphite. In this section, $AR_p = 1$ was fixed to model circular GNPs with a fixed diameter a = b =100 nm. Only the transversal aspect ratio AR_t is varied from 15 to 34. For each value of AR_t, the percolation threshold, conductivity, and the number of tunneling junctions at all hybrid compositions (all values of X) are computed as described above. The percolation threshold curves for each value of AR_t are plotted and compared in Figure 5.4(a) while the conductivity curves are compared in Figure 5.4(b).

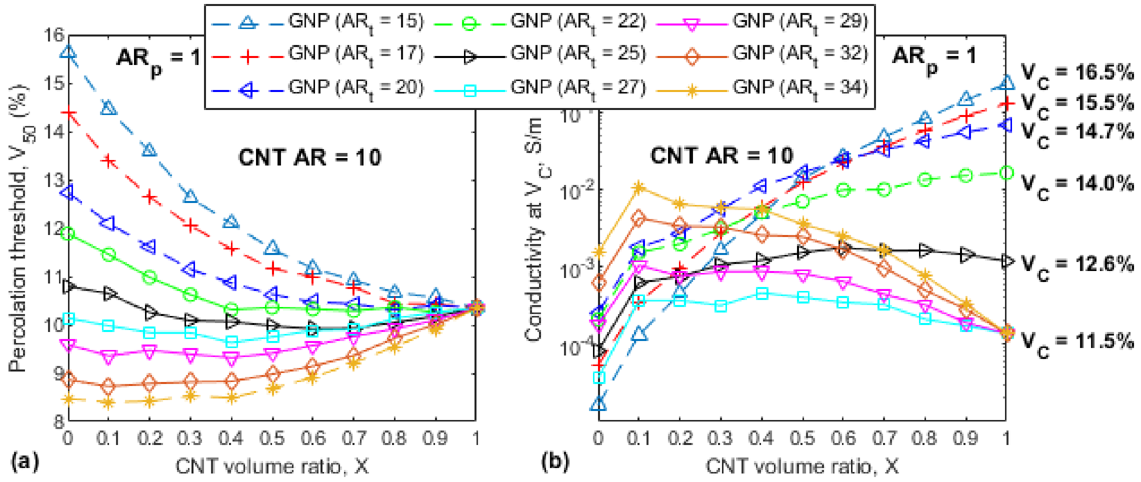

Figure 5.4 Synergistic and additive effects in (a) percolation threshold and (b) electrical conductivity in function of CNT volume ratio, X for different transversal aspect ratio of GNP mixed with CNT of aspect ratio AR =10 in hybrid composites. Full lines for the presence of synergy and dotted lines for additive effects.

Some of these curves in Figure 5.4 vary monotonically with respect to X, reflecting the additive effects while others exhibit a critical point, showing the synergy effects.

Figure 5.4(a) shows that the hybrid composites with GNP of AR_t values 15, 17, and 20 exhibit additive effect *(dashed lines)* in percolation onset. This implies that the monofiller composite with only CNT (X=1) has a lower percolation threshold compared to all the hybrid composites with GNPs of these aspect ratios. For all the other values of AR_t, the hybrid composites exhibit synergistic improvement *(represented by solid lines)* in percolation onset at some values of X. It is seen that increasing AR_t helps transition from hybrids with only additive effects in percolation to hybrids with synergistic effects. In addition, increasing AR_t too much seems to lead back to hybrids with additive effects, as shown in the plot for AR_t=34 in Figure 5.4(a).

Increasing AR_t similarly affects the presence of synergy in the conductivity of the hybrid composites, as shown in Figure 5.4(b). In general, increasing AR_t of the GNP systematically leads to lower values of percolation. Note that in Figure 5.4(b), for a chosen AR_t, conductivity is computed at the same filler content V_C. However, V_C is not the same for all the values of AR_t. Hence, a comparison between the conductivity curves of two different AR_t is not effective if their V_C is different. However, since the conductivity for the hybrids with GNP of AR_t = 27, 29, 32, 34 are computed at the same V_C, a comparison is possible. Comparing the four conductivity curves for AR_t = 27, 29, 32, 34,it is seen that increasing the AR_t of GNPs in the hybrid composites increases the conductivity and lowers the percolation threshold for all values of X. In addition, synergy in the percolation threshold usually leads to synergy in electrical conductivity.

Experimental studies on CNT-GNP hybrid composites have explained both synergistic and additive enhancements by the improved state of CNT dispersion in the presence of GNPs (Yue et al., 2014) and the ability of CNTs to easily bridge the distance between GNPs (Al-Saleh, 2015), leading to an easier formation of the percolated network in the composites. However, numerical studies have been unable to capture the microstructure’s parameters that control the performance of hybrid composites thus far. It is generally accepted, based on numerical simulations results, that the total number of tunneling junctions between fillers is a primary indicator of the electrical performance of CNT and GNP monofiller composites (Shen Gong & Zhu, 2014). A higher number of junctions leads to better electrical properties. Hence, for the first time, the author examined four different parameters related to the number of tunneling junctions in all the hybrid microstructures to understand which one of the parameters controls the electrical performance.

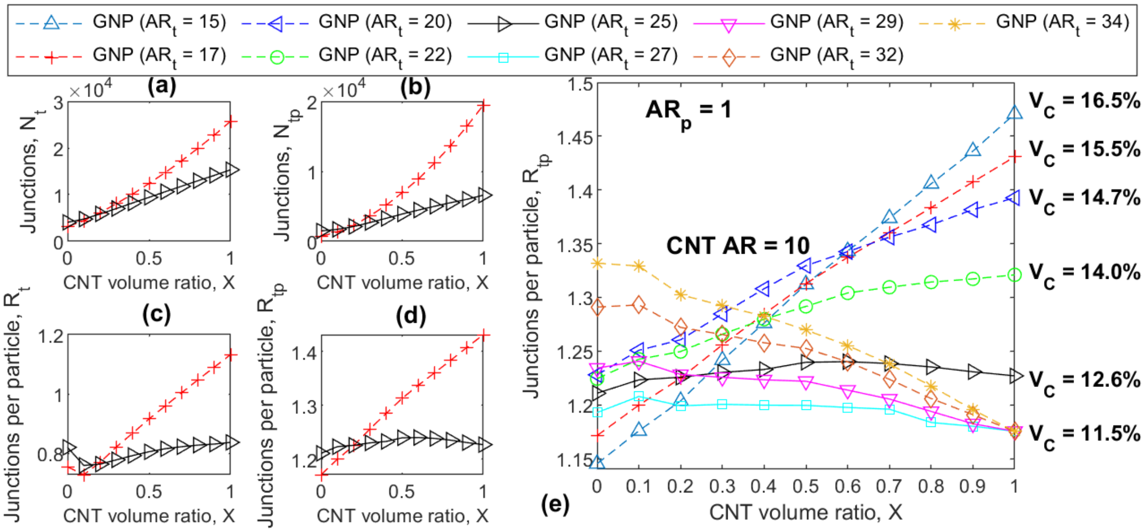

Figure 5.5 Variation of the number of tunneling junctions (a) in the entire microstructure (N_t) and (b) in only the percolated network, (N_{tp}). Variation of the number of tunneling junctions per filler (c) in the entire microstructure (R_t) and (d) in only the percolated network (R_{tp}). (a)-(d) are for AR_t = 17 and 25, which exhibit additive and synergistic properties respectively. (e) Variation of R_{tp} for all transversal aspect ratios of GNP mixed with CNT of aspect ratio AR =10 in hybrid composites. Full lines for the presence of synergy and dotted lines for additive effects.

Figure 5.5(a) to (d) show the plots respectively for (a) the number of tunneling junctions (between the fillers) in the entire RVE, N_t, (b) the number of tunneling junctions only in the percolated network in the RVE, N_{tp}, (c) the number of tunneling junctions per filler (ratio), in the entire RVE, R_t, and (d) the number of tunneling junctions per filler only in the percolated network in the RVE, R_{tp}. It is seen that R_{tp} in Figure 5.5(d) is the only microstructure's parameter that correlates with the electrical performance of the hybrid composites because it shows the same trend as the curves for conductivity in Figure 5.4(b), for GNP with $AR_t = 17$ and 25. Figure 5.5(e) shows the plots of R_{tp} for all the AR_t values, computed at their respective filler content V_C. Increasing AR_t leads to the improvement of R_{tp} and the transition between additive and synergistic effects in R_{tp}, like what was observed for percolation and conductivity.

5.2.2. Effect of GNP Planar Aspect Ratio on Electrical Properties of Hybrid Microstructures

In this section, to characterize the effect of the lateral dimensions of GNPs, the value of AR_t was fixed and the planar aspect ratio (AR_p) of GNP was varied from 1 to 2, 3, and 4. This changes the planar dimensions of the GNP from a circle to different ellipses, by varying the minor axis b, while the thickness t and major axis (a = 100 nm) are kept constant. This allows us to model GNPs with radially unsymmetric lateral dimensions. The same procedure in section 5.2.1 is followed here to examine the effect of AR_p on the electrical performance of the hybrid composites. The author starts with hybrids made of GNP $AR_t = 25$, which exhibit synergy in percolation and conductivity in Figure 5.4. Figure 5.6 shows that increasing AR_p systematically decreases the percolation threshold and increases the conductivity, as well as R_{tp}. The percolation threshold of the GNP nanocomposites (X=0) decreases from 10.80 to 8.73 vol.% when AR_p is varied from 1 to 4. A two order of magnitude increase (from 8.20×10^{-5} S/m to 1.5×10^{-2} S/m) is observed in the conductivity of GNP nanocomposites (X=0) when AR_p is varied from 1 to 4. While most of the hybrid composites with GNP $AR_p = 1$ exhibit synergy in percolation, all of them show synergy with GNP $AR_p = 2$. Increasing AR_p more to 3 and then 4 leads to fewer hybrids (fewer values of X) that exhibit synergy. Similar trends are observed in conductivity and R_{tp} values.

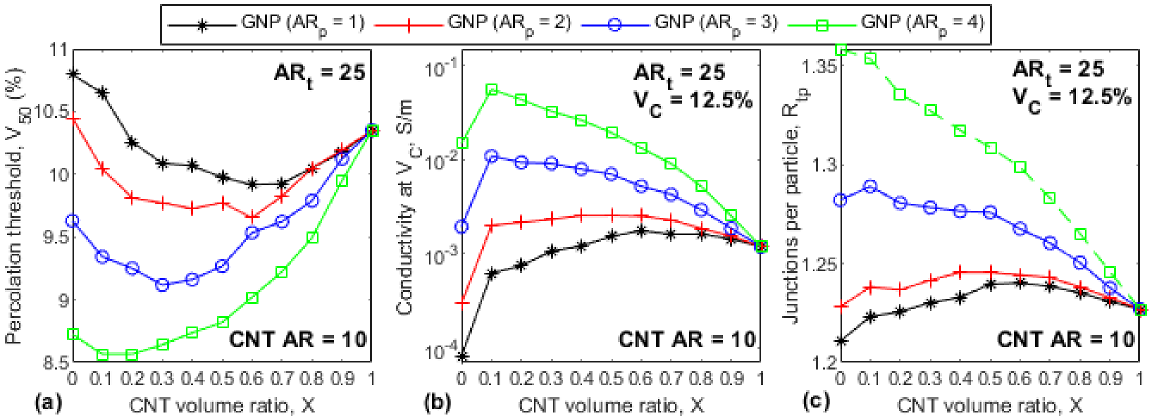

Figure 5.6 Variation of (a) percolation threshold (b) conductivity and (c) tunneling junctions per filler, R_{tp} in function of CNT volume ratio, X for GNP with different AR_p when $AR_t = 25$ and CNT aspect ratio is AR =10 in hybrid composites. Full lines for the presence of synergy and dotted lines for additive effects.

In Figure 5.7, the author studies hybrids made of GNP $AR_t = 17$, which exhibit additive effects in percolation and conductivity (in Figure 5.4), to examine the effect of varying AR_p from 1 to 4 with an increment of 1. As in the case of GNP $AR_t = 25$, increasing AR_p from 1 to 4 leads to the decrease in percolation threshold and the increase in conductivity.

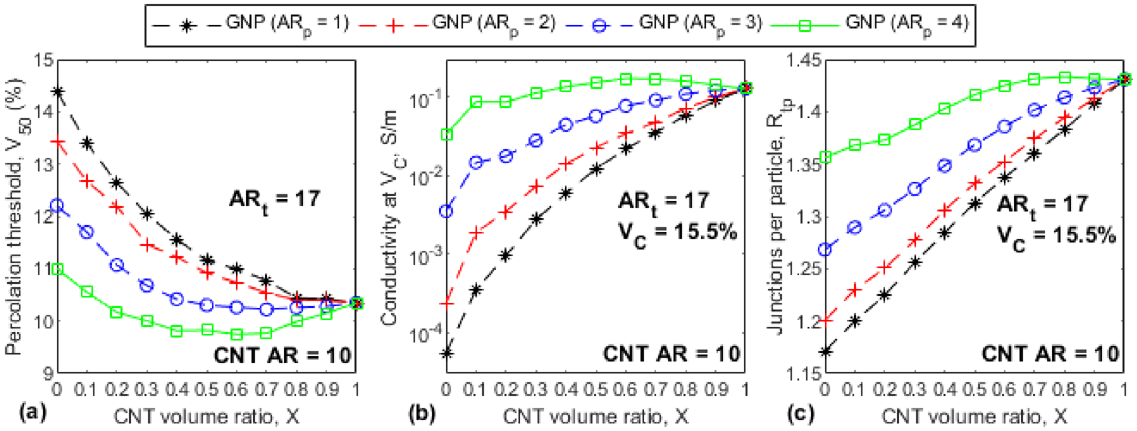

Figure 5.7 Variation of (a) percolation threshold (b) conductivity and (c) tunneling junctions per filler, R_{tp} in function of CNT volume ratio, X for GNP with different AR_p when $AR_t = 17$ and CNT aspect ratio is AR =10 in hybrid composites. Full lines for the presence of synergy and dotted lines for additive effects.

However, in the case of $AR_t = 17$, none of the hybrid composites with GNP $AR_p = 1$ shows synergy in either percolation, conductivity, or R_{tp}. Increasing AR_p to 2 and 3 still does not lead to synergy in any of the hybrids (all values of X). Only an increase of AR_p to 4, finally leads to synergy in percolation, conductivity, and R_{tp} in many of the hybrid microstructures. Compiling the results in Figure 5.4, Figure 5.6, and Figure 5.7, it can be concluded that decreasing the values of the GNP aspect ratios (AR_t and AR_p) does not directly lead to synergy. Only values of GNP aspect ratio in a specific range (e.g., AR_t = 22, 25, 27, 29 and 32 in Figure 5.4(a)), lead to hybrid with synergistic improvement. When looking at the percolation results for GNP aspect ratio in that range, it is seen that synergy happens only if the percolation threshold value of the chosen GNP in its monofiller composite (X=0) is very close to the one of the CNT composite (X=1). The closer the percolation threshold values of the two monofiller composites (X=0 and X=1) are, the more hybrid composites (more values of X) exhibit synergy (see AR_t=25 and AR_p=2 in Figure 5.6). Hence, it can be confirmed that the synergy effect in the electrical properties of hybrid composites is directly related to the closeness of the percolation threshold values of their GNP monofiller and CNT monofiller composites.

5.2.3. Effect of Chirality of CNT and CNT Intrinsic Conductivity on Electrical Properties of Hybrid Microstructures

The results presented so far are computed using CNTs with intrinsic conductivity $\sigma_{CNT} = 10^4\ S/m$ as MWCNTs since they are a cheaper alternative to single-walled CNTs (SWCNTs) and hence lead to cost-saving in addition to the synergistic enhancement when combined to GNP. In this section, the author studies how the intrinsic conductivity of CNT affects the conductivity as well as the presence of synergy and additive effects in the conductivity of hybrid nanocomposites. $\sigma_{CNT} = 2 \times 10^7 S/m$ is used for armchair SWCNTs and $\sigma_{CNT} = 10\ S/m$ for zig-zag SWCNTs, following the work done in (Doh, Park, Yang, & Raghavan, 2019). In this section, only the intrinsic conductivity value of the CNT is changed. Changing the diameter from MWCNT (10 nm) to SWCNTs (1 – 2 nm) would increase the aspect ratio of CNTs (decrease the percolation threshold) as studied in section 5.2.4. Thus, in this section, the percolation threshold values are not changed, only the conductivity of the nanocomposites is then studied. Figure 5.8(a) shows the conductivity of CNT monofiller nanocomposites when the intrinsic conductivity of CNT is varied. It is seen that for low content of CNT (< 12%) the conductivity of the composites is the same. With a higher content of CNT fillers, the conductivity of both MWCNT and armchair SWCNT composites becomes much higher than that of zig-zag SWCNT. The conductivity of MWCNT and armchair SWCNT composites remains very similar up to a CNT content of 16% even though the conductivity of armchair SWCNT composites is slightly higher than the one of MWCNT as shown in Table 5.1.

It can be predicted from Table 5.1 that increasing the content of CNT will lead to the conductivity of armchair SWCNT composites being much higher than the one for MWCNT composites. This is explained in (Doh et al., 2019; N. Hu, Karube, et al., 2008) by the fact that at low content of CNT, connectivity happens mainly due to tunneling effects because the fillers are apart and only a few of them are present in the percolated network; hence the conductivity of the composites is dominated by tunneling resistance. At high content of CNTs, the fillers are closer to each other and the percolated network is filled with CNTs, hence the conductivity of the composites is dominated by the CNT intrinsic resistance.

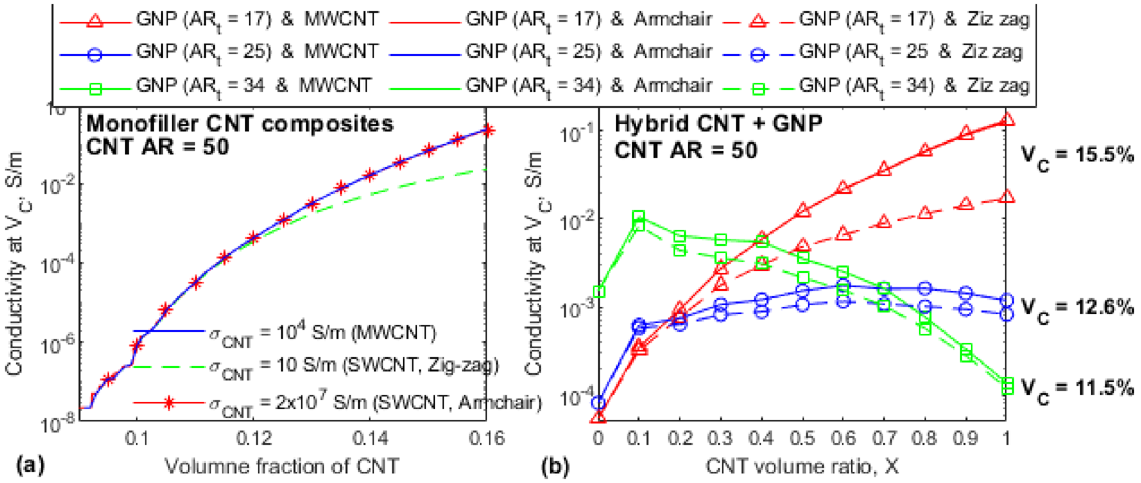

Figure 5.8 Effect of CNT chirality or CNT intrinsic conductivity on (a) the conductivity of CNT monofiller composites and (b) the conductivity and synergy/additive effects in hybrid CNT-GNP nanocomposites.

Table 5.1

Effect of CNT intrinsic conductivity and chirality on the electrical conductivity of CNT monofiller nanocomposites

CNT content (%)		10	11	12	13	14	15	16
Nanocomposites conductivity (S/m)	**Armchair SWCNT**	8e-7	3.22e-5	4.295e-4	3.167e-3	0.0164	0.0694	0.2407
	MWCNT	8e-7	3.22e-5	4.290e-4	3.160e-3	0.0163	0.0680	0.2299
	Zig-zag SWCNT	7.9e-7	3.04e-5	3.477e-4	1.745e-3	0.0053	0.0122	0.0232

In the case of hybrid CNT-GNP nanocomposites, Figure 5.8(b) shows that increasing the intrinsic conductivity of CNT leads to the increase of the conductivity of the entire set of hybrid (all values of X) for each morphology of GNP used. Note that the curves for hybrid composites made of armchair SWCNT and MWCNT overlap since the conductivity of their monofiller composites is very similar. In addition, it is seen that hybrid composites exhibiting synergy (hybrid with GNP of $AR_t = 25$) still exhibit synergy, while hybrid composites exhibiting additive effects (hybrid with GNP of $AR_t = 17$) still exhibit additive effects when the intrinsic conductivity of CNT is varied.

In summary, increasing the intrinsic conductivity of CNT leads to the increase of the conductivity of CNT monofiller composites and that of the hybrid CNT-GNP composites. Also, the effect of the intrinsic conductivity of CNT is more pronounced at higher filler content. However, the intrinsic conductivity of CNT does not affect the presence of synergy or additive effects in the hybrid composites. This proves as suggested in the previous section that synergy in hybrid composites is directly linked to the improved connectivity between the fillers in the hybrid microstructures.

5.2.4. Effect of CNT Morphology on Electrical Properties of Hybrid Microstructures

The results presented so far are computed using CNTs ($L_{CNT} = 100\ nm$) of aspect ratio AR = 10 as primary fillers, leading to the use of GNPs with transversal aspect ratio, AR_t between 15 to 50 in order to have hybrid composites exhibiting synergistic electrical properties. While CNT and GNP fillers with higher aspect ratios ~ 100 to 10000 are commonly used experimentally for nanocomposites, several works also exist with fillers of low aspect ratio ~10 to 50 (Yong Chen, Li, Tu, & An, 2012; Hassoun et al., 2014; Hernandez et al., 2008; I. H. Kim & Jeong, 2010; Kwon et al., 2013; Secor et al., 2013; Soum et al., 2019; H. Wu & Drzal, 2013; Zhou, Han, Xiao, Chang, & Zhai, 2015). In general, conductive nanocomposites fabricated using inkjet printing rely on CNT and GNP fillers of low aspect ratio to avoid clogging the printer nozzle (Kwon et al., 2013; Mejias-Morillo, Gbaguidi, Kim, Namilae, & Rojas-Nastrucci, 2019; Secor et al., 2013; Soum et al., 2019). In addition short CNTs (low aspect ratio) are increasingly used to reduce the extent of agglomeration in the nanocomposites (Zhou et al., 2015). The results presented so far correspond to such situations.

In this section, The author examines the effect of using CNTs with higher aspect ratios (by decreasing the diameter D_{CNT}) on the electrical properties of the hybrid nanocomposites, mainly in term of the morphology of GNP fillers needed for synergistic behavior. Figure 5.9 and Figure 5.10 respectively show hybrid nanocomposites made of CNTs of AR = 50 ($D_{CNT} = 2\ nm$) and AR = 100 ($D_{CNT} = 1\ nm$) as primary fillers. The CNTs fillers can also be assumed to be SWCNT which diameter is usually about 1-2 nm (Doh et al., 2019). It can be seen that for higher AR of CNTs, GNP fillers with higher

AR_t (compared to the case of CNTs with AR = 10) are needed to obtain hybrid composites exhibiting synergy in their electrical properties. While mixing GNPs of AR_t = 22 - 32 to CNT of AR = 10 leads to hybrids with synergy in Figure 5.4, GNPs of AR_t = 350 - 450 and GNPs of AR_t = 1000 – 1600 are needed respectively for CNT AR = 50 and CNT AR = 100.

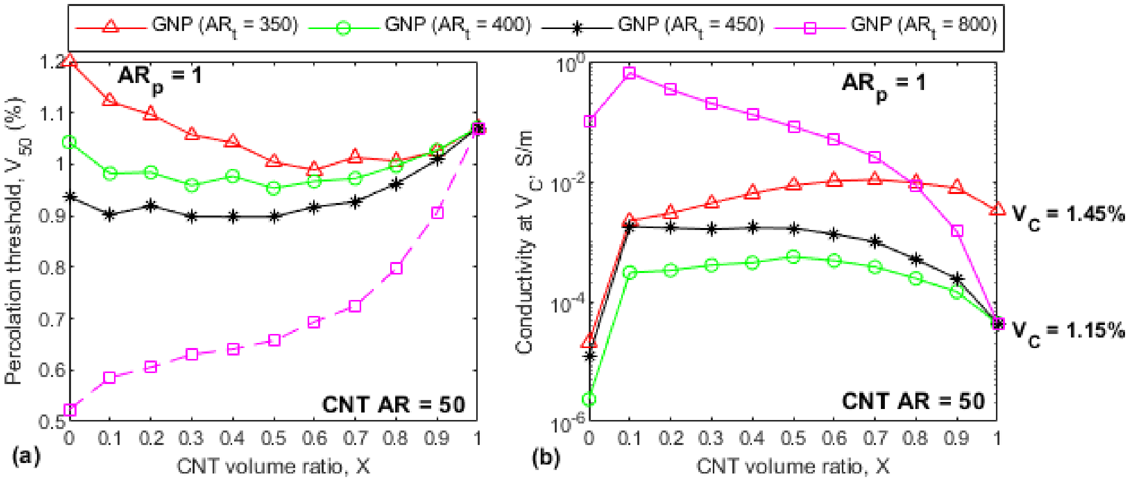

Figure 5.9 Synergistic and additive effects in (a) percolation threshold and (b) electrical conductivity in function of CNT volume ratio, X for different transversal aspect ratio of GNP mixed with CNT of aspect ratio AR =50 in hybrid composites. Full lines for the presence of synergy and dotted lines for additive effects.

In addition, the percolation curves for all hybrids that exhibit synergy decrease when the aspect ratio of CNT filler increases. Specifically, percolation threshold values of hybrids with synergy decrease from a range of 8.5 – 12%, for CNT AR = 10 (Figure 5.4(a)) to a range of 0.9 – 1.2%, for CNT AR = 50 (Figure 5.9(a)) and finally to a range of 0.27 – 0.53%, for CNT AR = 100 (Figure 5.10(a)). As explained in the previous sections, CNT and GNP fillers with close values of percolation threshold in their respective monofiller composites lead to synergy in their hybrid composites. Hence, a higher aspect ratio of CNTs (with lower percolation threshold in their monofiller composites) will require a much higher AR_t of GNPs with similarly low percolation threshold. This information in the context of the comparison between SWCNT and MWCNT means that using CNT fillers of same length, SWCNT will require higher AR_t of GNPs fillers to achieve synergy in the hybrid composites compared to MWCNTs. In addition, SWCNTs will lead to hybrids with lower percolation threshold and much higher conductivity. Hybrids with armchair SWCNTs will be more conductive than the ones with zig-zag SWCNTs.

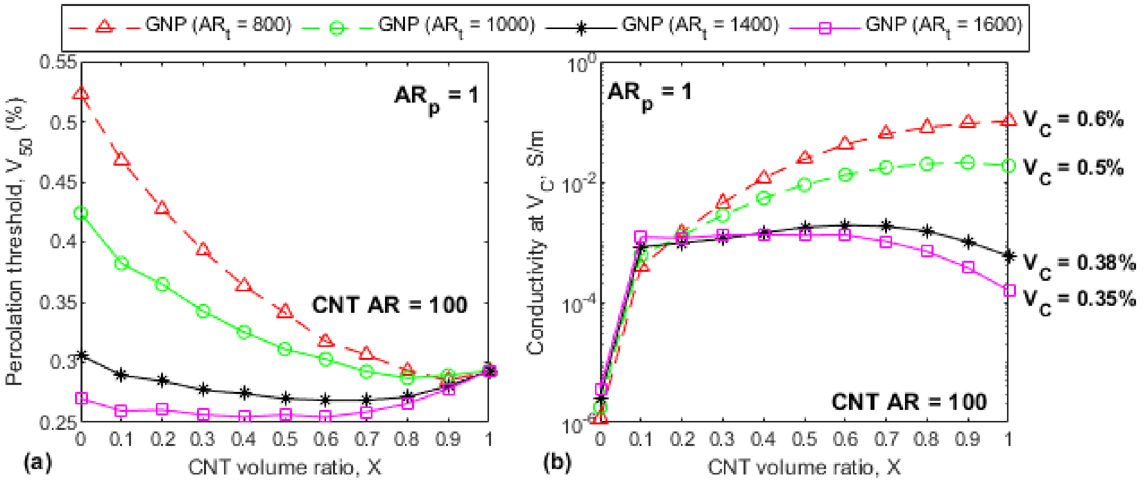

Figure 5.10 Synergistic and additive effects in (a) percolation threshold and (b) electrical conductivity in function of CNT volume ratio, X for different transversal aspect ratio of GNP mixed with CNT of aspect ratio AR =100 in hybrid composites. Full lines for the presence of synergy and dotted lines for additive effects.

There are some numerical issues related to the modeling of high aspect ratio fillers. In general, the relative size of the RVE to the length dimension of filler (major axis of elliptical cylinder for GNP and length of cylinder for CNT) is a key input for percolation onset. In multi-filler composites, this ratio (RVE size-to-filler length) should be similar for both GNP and CNT fillers in order to accurately compare the percolation properties of the two fillers. This has been shown in (Sagalianov et al., 2017) and has been observed in the present study as well. The author has also shown that percolation onset of the two fillers in their monofiller composites should be similar to achieve synergy in the hybrids. When combined with the limitation on the ratio of RVE size-to-filler length, this imposes certain limitations on the GNP dimensions. Since high aspect ratio of CNT requires a much higher aspect ratio (AR_t) of GNP to obtain synergy in hybrid composites, the thickness of GNP in the simulations could become unphysically low. Within the computational limitations, this could be addressed by non-dimensionalizing the system (e.g. (Sagalianov et al., 2017)), or by using low aspect ratio fillers with equal particles' length (X. Ni et al., 2019; Plyushch, Lamberti, Spinelli, Macutkevič, & Kuzhir, 2018; M. Safdari & Al-Haik, 2012; Sagalianov et al., 2017).

5.3. Results for GNP Monofiller Composites

Graphene nanoplatelets due to its ease of mass production is one of the cheapest carbon nanomaterials and hence has been extensively used in conductive nanocomposites (Cataldi, Athanassiou, & Bayer, 2018). However due to its 2D geometry, it usually leads to lower electrical properties in the composite, compared to CNTs of similar aspect ratio (J. Du et al., 2011). Nonetheless, conductive GNP nanocomposites have been used as sensors in advanced aerospace and medical technologies (X. Huang et al., 2011), flexible electronics, anti-static coatings, sensors, batteries and solar-cells (Singh et al., 2011), While several manufacturing methods have been used to produce GNPs, they usually result in a large variety of thickness and lateral size within the same batch (Svedberg & Pedersen, 1940). Several works have used additional centrifugation/ultracentrifugation steps to separate GNPs (sedimentation-based separation) by their lateral size and thickness in order to only retain the fillers leading to nanocomposites with optimum electrical properties (Hassoun et al., 2014; Svedberg & Pedersen, 1940).

Thus, there is a need for numerical simulations to guide researchers on GNP morphologies for nanocomposites with excellent electrical properties. On another note, despite the affordability of GNP, CNT composites are still very popular due to their good electrical properties. While it has been increasingly shown that combining both fillers in hybrid composites can lead to a more conductive and cost saving alternative (Al-Saleh, 2015; Jing Li et al., 2008; Yue et al., 2014), there is not much information about the fillers compositions that lead to best improvement and affordability when compared to GNP composites. In this section, the author shows using the present percolation based Monte Carlo numerical model that using GNP with less number of layers or with smaller width leads to better electrical properties. Reduction of number of graphene layer is more efficient compared to the reduction of the GNP width. The author also shows that substituting minimal amount of GNP by CNT in the GNP composite leads to substantial improvement of conductivity in the obtained hybrid composite.

5.3.1. Effect of GNP Transversal and Planar Aspect Ratios on the Electrical Properties of GNP Nanocomposites

Figure 5.11(a) and (b) present the percolation probability and the electrical conductivity of graphene nanocomposites with circular GNP of same planar dimensions but different thicknesses. Increasing AR_t of GNP leads to a systematic decrease of the percolation threshold and increase of the conductivity of the nanocomposite. This means that using graphite fillers with very few number of layers leads to lighter and more conductive nanocomposites. This trend has been observed in many experimental works (Gao et al., 2017; I. H. Kim & Jeong, 2010; Ravindran et al., 2018).

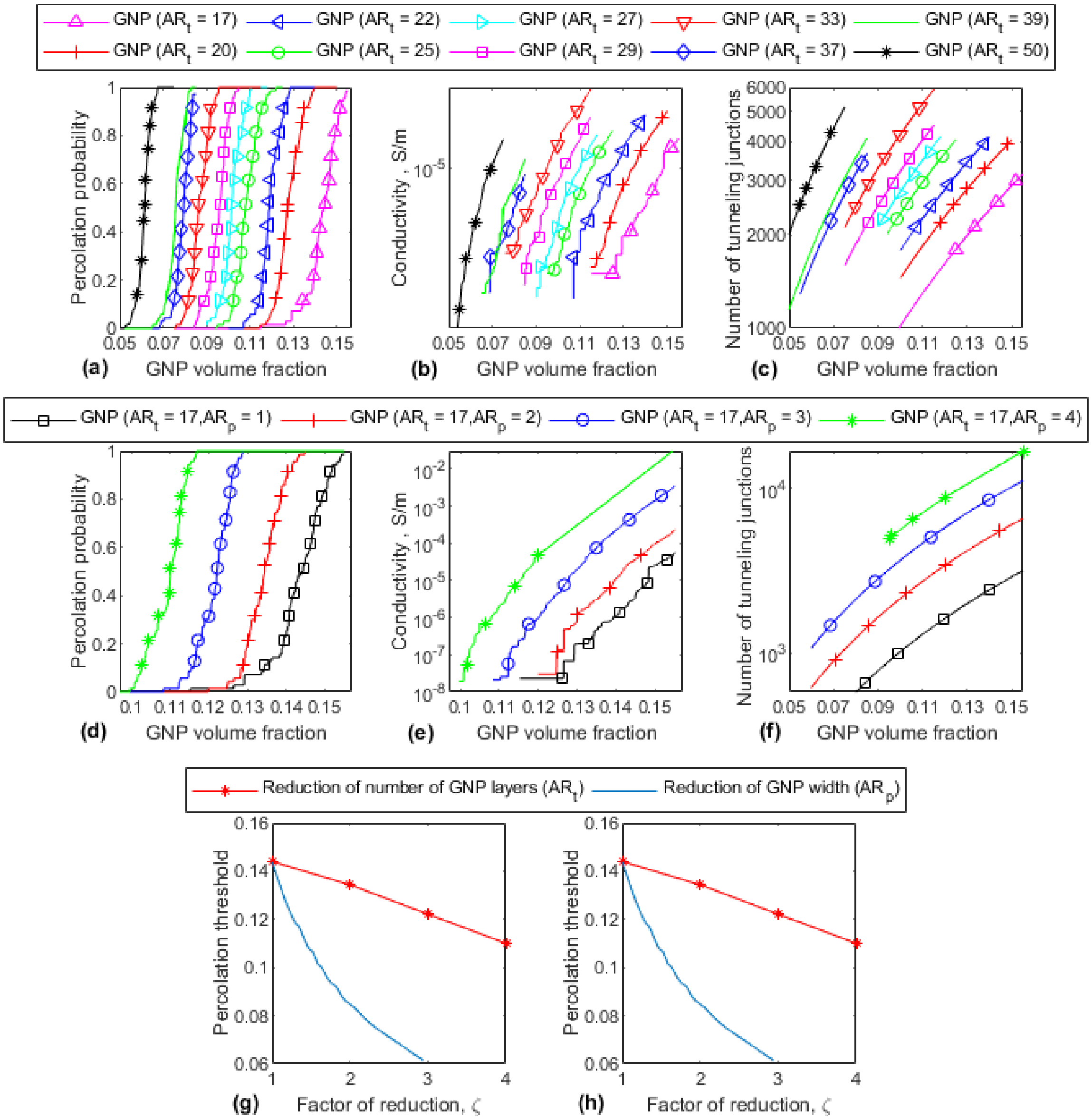

Figure 5.11 (a, d) Percolation probability (b, e) conductivity and (c, f) number of tunneling junctions between GNP fillers. Effect of (a-c) GNP transversal aspect ratio and (d-f) GNP planar aspect ratio on nanocomposites properties. Comparison of the improvement in (g) percolation and (f) conductivity due to AR$_t$ and AR$_p$ increase.

Next, the author starts with circular GNP fillers with $AR_t = 17$ and decreases their minor axis length, while keeping the thickness constant, to obtain slender elliptical GNP. Figure 5.11 (d) and (e) show an improvement in the electrical properties when AR_p of GNP is increased. To the author's knowledge only the experimental work in (Kalaitzidou et al., 2010) has studied the effect of AR_p. They observed trends similar to the present work.

Figure 5.11 (c) and (f) show that the improved electrical performance, obtained by the change of the GNP morphology is enabled by the improved connectivity between the fillers in the nanocomposites. Specifically, a 500% and 300% improvement in the number of tunneling junctions between fillers is obtained respectively with the increase of AR_t and AR_p. Finally the author compares in Figure 5.11 (g) and (h) the improvement respectively in percolation and conductivity obtained by reducing the number of layers and the width of GNP ($AR_t = 17$ and $AR_p = 1$). It is seen that thinner graphite leads to higher property improvement with exponential increase compared to the linear increase observed with slender graphite of same size. Specifically, reducing the number of graphite layers by a third ($AR_t = 50$ to 17) decreases the percolation threshold by 2.3, and the amount of fillers to reach a conductivity of 10-5 S/m by half.

5.3.2. Effect of the Substitution of GNP by CNT Fillers on the Electrical Properties of GNP Nanocomposites

Mixing CNT and GNP fillers to fabricate hybrid nanocomposites has proven to be an effective way to improve both the percolation and the electrical conductivity of nanocomposites (Al-Saleh, 2015; Jing Li et al., 2008; Yue et al., 2014). Figure 5.12(a) and (b) show that the substitution of the smallest amount of circular GNP with $AR_t = 17$

by CNT ($X_{CNT} = 0.10$) leads to the highest improvement in percolation and conductivity. Higher amount of CNT leads to smaller improvement.

Figure 5.12(c) shows the conductivity of hybrid nanocomposites made of different GNP morphologies and with different compositions of CNT and GNP fillers (X_{CNT}) analyzed numerically against previous experimental works. It can be confirmed that in all the composites, the highest improvement in conductivity (slope of conductivity curve) due to substitution with CNT always occurs with the smallest amount of substituted CNTs, X_{CNT}. Higher content of CNT in the hybrids leads to either smaller improvement or decay of the conductivity.

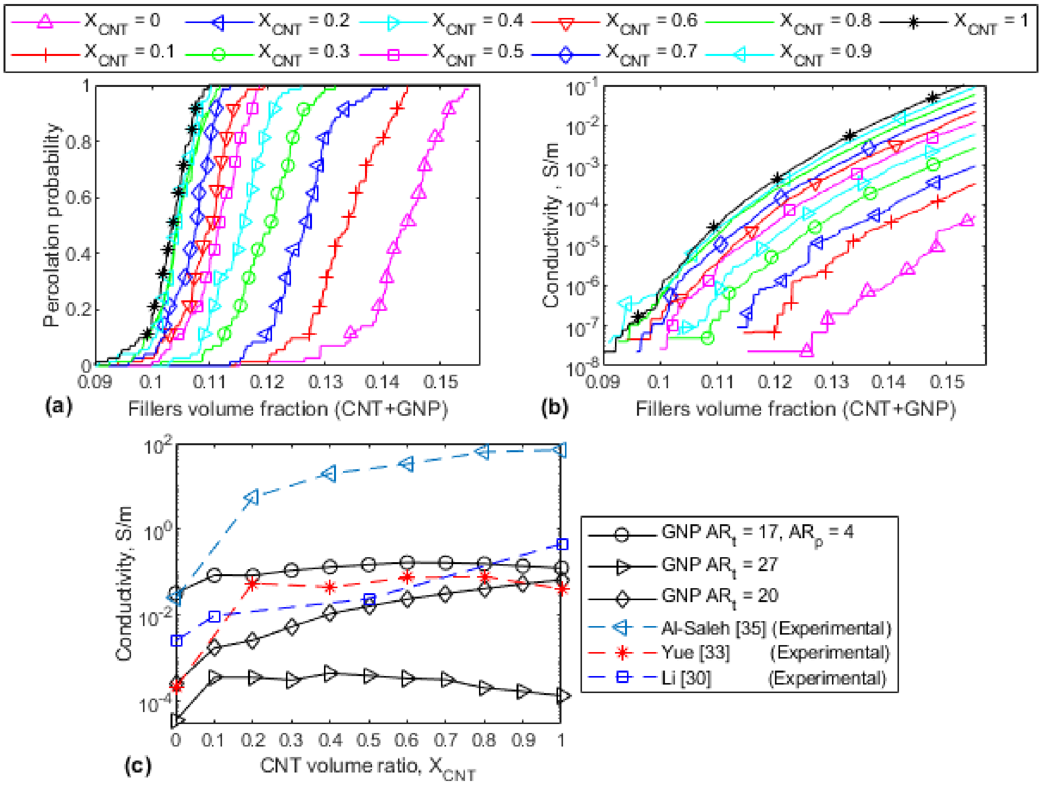

Figure 5.12 Percolation probability and (b) conductivity of hybrids nanocomposites filled with GNP ($AR_t = 17$ and $AR_p = 1$) in function of composition in CNT (X_{CNT}). (c) Comparison of numerical results with experimental works.

5.4. Discussion

All the experimental studies on the electrical properties of CNT-GNP hybrid nanocomposites indicate that the relative content of each of the fillers in the hybrid (X), controls the percolation and electrical conductivity of the hybrid nanocomposites. Some observed a synergistic improvement in percolation and /or in conductivity at some specific values of X (Kumar et al., 2010; Ren et al., 2012; Yue et al., 2014), while others only experienced an additive effect (Al-Saleh, 2015; Curtis Lee et al., 2013; Jing Li et al., 2008; Masoud Safdari, 2012). The present numerical model is able to predict those two effects in percolation and conductivity for CNT-GNP hybrid nanocomposites, by varying the CNT volume ratio (X) and also the morphology (planar and transversal aspect ratios) of the GNP filler.

The author shows that increasing either the planar or transversal aspect ratio of the GNP filler in the hybrids leads to a decrease in the percolation threshold and an increase in the conductivity of all the hybrid composite compositions (all values of X). Nonetheless, it is shown that no direct correlation exists between the variation of any of the GNP aspect ratios and the existence of synergy or addictive effects in the hybrid composites. It is also shown that the type of CNTs used, specified by the CNT aspect ratio, its chirality, and its intrinsic conductivity also affects the electrical properties of the hybrid nanocomposites. While the aspect ratio of CNTs (also the choice of MWCNT or SWCNT) affects the percolation threshold values as well as the morphology of GNPs required to achieve synergy, it is shown that the CNT intrinsic conductivity (also the chirality of SWCNT) only affect the electrical conductivity of the hybrids and does not affect the presence of synergy.

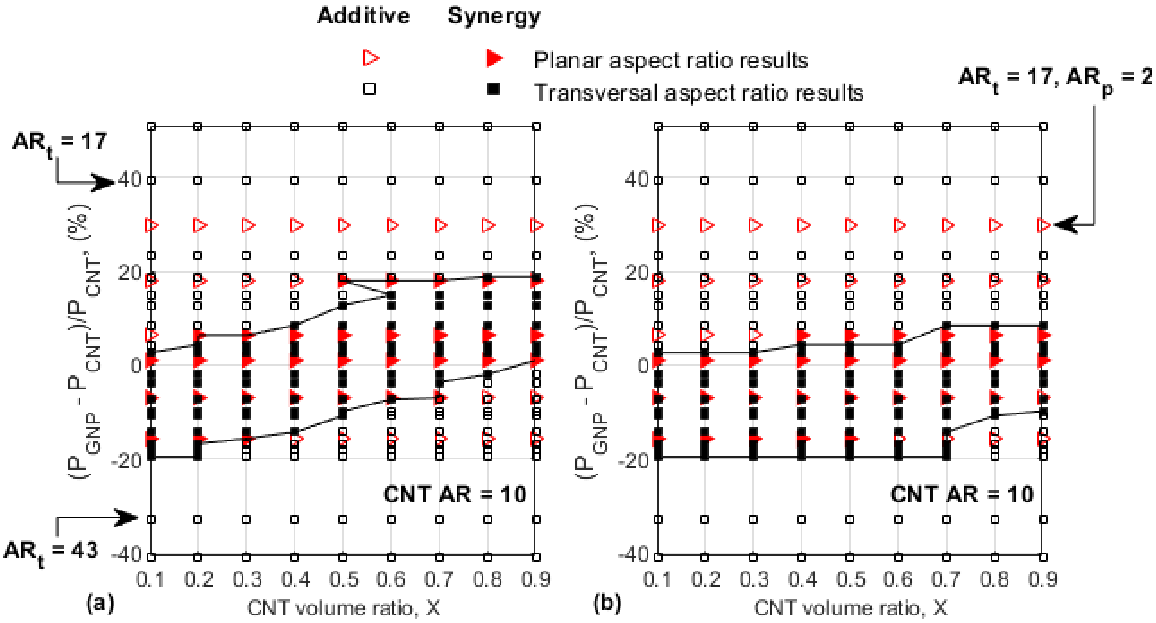

Figure 5.13 Synergy effect in (a) percolation threshold and (b) conductivity based on difference ratio between percolation threshold of GNP and CNT nanocomposites. Contour plot showing synergy zone.

To understand the property of the nanocomposites that creates synergy in the hybrids, the author analyzed all of the percolation and conductivity obtained in this study in Figure 5.13. To do so, the author first chooses a GNP morphology and compute the difference ratio between the percolation values of its GNP and CNT monofiller composites, $(P_{GNP} - P_{CNT})/P_{CNT}$. This represents the y-coordinate in Figure 5.13 for the hybrids with that GNP morphology. Next, for each of the 9 hybrid composites (X=0.1, 0.2, …, 0.9), either synergy (filled marker) or additive effects (empty marker) are present. Figure 5.13(a) and (b) analyze the synergy or additive effects in percolation threshold and conductivity using the data from varying both the GNP planar (triangle marker) and transversal (square marker) aspect ratios. For example, for hybrid composites with circular GNPs with AR$_t$ = 17, the percolation values, V_{50} of CNT and GNP nanocomposites are $P_{CNT} = 10.35$ vol.% and $P_{GNP} = 14.40$ vol.%, as shown in Figure 5.4(a). The y-coordinate for the 9 hybrids (X=0.1, 0.2, …, 0.9) made of that GNP is $(P_{GNP} - P_{CNT})/P_{CNT} = 38\%$. Figure 5.13 shows the presence of additive effects (empty square markers), respectively for percolation (Figure 5.13 (a)) and conductivity (Figure 5.13 (b)) for the hybrid composites with GNP of $AR_t = 17$.

Additionally, the author computes a synergy contour that encompasses all the instances of synergy in percolation and conductivity, respectively, in Figure 5.14(a) and (b). It shows that when the percolation threshold of the GNP monofiller composite (X=0) is close (±20%) to that of the CNT monofiller composite (X=1), the hybrids made of those two fillers will likely achieve synergistic improvement. In addition, the closer the values of the two percolation onsets are, the more hybrid compositions (more X) will exhibit synergy.

Figure 5.14(a) and (b) show the improvement in percolation and conductivity obtained from the hybrid composites examined in this work. To obtain the numerical value for the improvement in conductivity, the conductivity of each hybrid at a given CNT volume ratio (X) is compared to the highest of the conductivity values between monofiller CNT (X=1) and monofiller GNP (X=0) composites. For the improvement in percolation, the percolation value of each hybrid is compared to the lowest of the percolation threshold values between monofiller CNT and GNP composites. An improvement of 800% in conductivity was obtained through synergy, as shown in Figure 5.14(b).

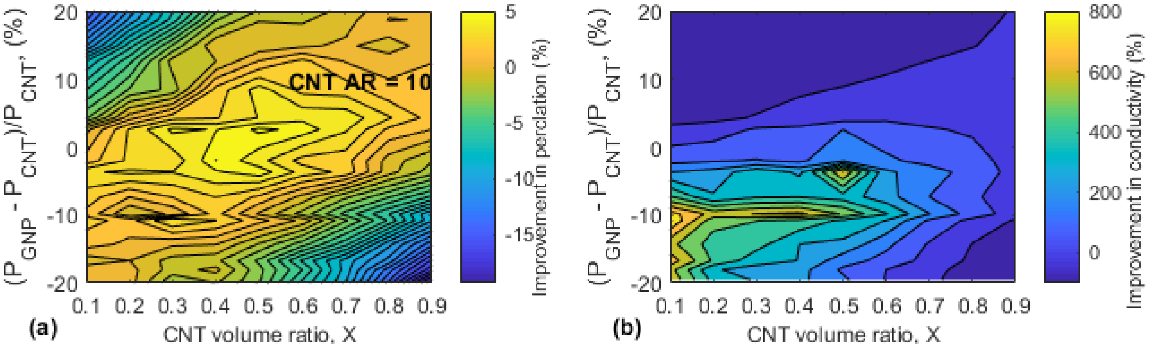

Figure 5.14 Improvement in (a) percolation threshold and (b) conductivity in hybrid nanocomposites due to synergy, using filled contour plot with isolines.

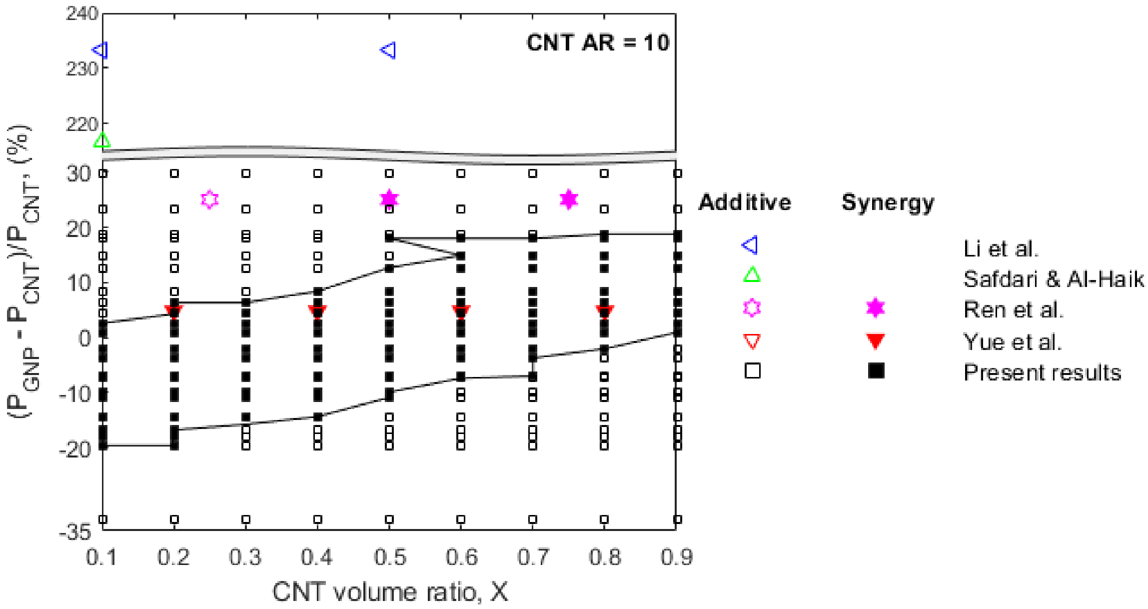

Figure 5.15 Synergy effect based on the difference ratio between the percolation threshold of GNP and CNT nanocomposites used in hybrid composites. Validation with experimental works (Markers in color). Contour plot showing synergy zone.

Figure 5.15 shows a comparison of the data from the present numerical simulations and several experimental works. It is seen that indeed synergy happens in hybrid nanocomposites filled with GNP and CNT fillers, if and only if, both fillers have percolation threshold values very close to each other in their monofiller composites.

When their percolation threshold values are far apart, only the additive effect is observed. To the author’s knowledge, this is the first time that the synergy effect in hybrid composites is linked to the percolation threshold of their monofiller composites. Note that some of the experimental works used molecular weight fraction instead of volume fraction. For comparison sake, their results are converted to volume fraction, assuming that the density of CNT and GNP is 2.1 g/cm^3.

In addition, some of the experimental studies have explained the improvement of electrical performance in CNT-GNP hybrid composites by the improved state of CNT dispersion in the presence of GNPs (Yue et al., 2014). The author has studied the effect of agglomeration on the electrical and piezoresistive performance of both monofiller and hybrid composites elsewhere (Gbaguidi et al., 2019b). The present numerical formulation considers the fillers to be uniformly dispersed in the composites. However, using this formulation, the author was able to isolate the microstructural mechanism which leads to synergy effects in hybrid nanocomposites. It is shown in Figure 5.5 that the number of tunneling junctions per filler, in the percolated network, R_{tp} controls the electrical performance of the hybrid composites. Further, the author also identifies that synergy occurs in hybrid composites only for compositions where the monofiller composites have similar percolation thresholds.

5.5. Summary

In this chapter, the author developed a three-dimensional (3D) Monte Carlo model to understand the mechanisms and microstructural features that control the electrical behavior of monofiller GNP composites; that of hybrid nanocomposites filled with CNT and GNP, and potentially lead to a synergistic effect. The primary conclusions of the study are as follows:

Very high conductivity and low percolation threshold are obtained using GNP fillers with high transversal or planar aspect ratios. However, higher exponential improvement in electrical properties is observed with thinner GNPs while only a linear improvement is obtained with slender GNPs with similar size.

Increasing either the planar or transversal aspect ratio of the GNP filler leads to the improvement of both percolation threshold and electrical conductivity of all the hybrid composites.

When the percolation threshold of the GNP fillers in its monofiller composite is within 20% of the percolation threshold of the CNT fillers in its monofiller composite, the hybrid composites made of those two specific fillers achieve synergistic improvement in electrical properties. The present model suggests an improvement in electrical conductivity as high as 800% in hybrid nanocomposites due to the synergy achieved using the above combination of fillers.

Increasing the aspect ratio of CNT leads to the increase of the planar aspect ratio of the GNP fillers required to achieve synergy and also leads to hybrids with lower percolation and higher conductivity.

Using CNT with a higher value of intrinsic conductivity increases the conductivity of the hybrids but does not affect the presence of synergy or additive effects.

Using SWCNT instead of MWCNT will require GNPs with a higher planar aspect ratio in order to achieve synergy in the hybrid composites. It will also lead to hybrids with better electrical properties. A change in the chirality of SWCNT will only affect the conductivity of the hybrid composites without altering the presence of synergy or additive effects.

A review of past experimental data matches the present numerical results and confirms the correlation between the closeness of the percolation threshold values of the two monofiller nanocomposites and the synergy effects in the corresponding hybrid.

The author also shows using both present numerical results and previous experimental works that substitution of GNP by CNT fillers to obtain hybrid nanocomposites improves the electrical properties, where the optimum improvement happens with the minimal amount of CNT.

The author finds that a key microstructural parameter that controls the electrical performance of the hybrid composites is the number of tunneling junctions per filler, in the percolated network. Improvement or synergy of that parameter leads to an improvement or synergy in percolation threshold and electrical conductivity in the hybrid nanocomposites.

6. Fabrication and Testing of Hybrid Nanocomposites made of CNT and GNP for MMOD detection and Piezoresistive Strain Sensors

Among many applications of polymer nanocomposites, the development of a strain sensor with good sensitivity and a relatively simple fabrication process has received much attention through several experimental works. The literature review regarding the successful use of CNT nanocomposites as piezoresistive sensors has been covered in Chapter 2. However, because the maximum gauge factor of CNT composites is obtained closed to percolation threshold, and decreases with addition of more CNTs, several works have been dedicated to the addition of GNP fillers to CNT nanocomposites in order to produce much higher sensitivity in the hybrid composites (S. H. Hwang, Park, & Park, 2013; S. H. Hwang, Park, Park, et al., 2013; Curtis Lee et al., 2013; Luo & Liu, 2013). Some of those works were able to successfully fabricate hybrid nanocomposites with better piezoresistive performance, compared to CNT mono-filler composites. In addition, the present numerical simulations described in the previous chapters show that the addition of GNP filler to CNT nanocomposites increases the piezoresistivity of the hybrid-PNC and that the increase of the GNP content leads to higher sensitivity in the hybrid-PNCs.

As a proof of concept for aerospace applications, the hybrid nanocomposites sensors are used in inflatable space structures. Inflatable structures for space habitat are highly prone to damage caused by micrometeoroid and orbital debris (MMOD) impacts. The size of orbital debris varies from few microns to meters but the probability of an impact increases significantly for particles that have a diameter less than 1 cm due to their high flux in low earth orbit. Although the inflatable structures are effectively shielded against these impacts through multiple layers of impact-resistant materials, there is a necessity for a health monitoring system to monitor the structural integrity and damage state within the structures. Assessment of damage is critical for the safety of personnel in the space habitat, as well as predicting the repair needs and the remaining useful life of the habitat. There have been several works on the development of sensors that can detect damage due to the presence of holes created by impact on the inflatable structure. However, most of those works are based on techniques such as fiber optics (Cadogan et al., 2006), electromagnetic radiation (Madaras et al., 2008), impedance tomography (Cadogan et al., 2006), magnetic field (Woodard et al., 2011) and piezoelectricity (E. Christiansen et al., 2009).

In the first part of this chapter, hybrid CNT-coarse graphene platelets (GP) nanocomposites were fabricated using a resin infiltration (wet layup) process and characterized. CNT in form of buckypaper alone as well as CNT-buckypaper with coarse GPs is mixed separately with epoxy using wet layup fabrication technique to obtain CNT nanocomposites and hybrid CNT-GP nanocomposites. In previous works (Jiukun Li, 2016; Jiukun Li & Namilae, 2016), the highest gauge factor was obtained with a 5 wt% of coarse GP. The piezoresistive response of the two types of sensors under uniaxial loadings was first characterized and then the hybrid CNT-GP nanocomposites with 5 wt% of coarse GP were shown to exhibit higher gauge factor (GF ~3.6), compared to the CNT nanocomposites (GF~0.5). The performance of the hybrid sensor under transverse dynamic loadings is later evaluated, with an even higher gauge factor (GF~24) at very small strains. In addition, the thermomechanical behavior of the nanocomposites is studied using Dynamic Mechanical Analyzer (DMA) to obtain the effect of temperature and frequency on the damping and storage modulus of the nanocomposites.

In the second part of this chapter, a unique impact detection and health monitoring system based on the hybrid nanocomposites fabricated was proposed. A thin flexible sensing layer is developed that can be incorporated into the layers of the inflatable structure in the form of a blanket. It consists of flexible 2.5 in × 2.5 in piezoresistive sensors composed of carbon nanotubes sheet and coarse graphene platelets, with an epoxy matrix material. The electrical conductivity of these flexible nanocomposite sensors is highly sensitive to strains as well as the presence of holes in the structure. An array of these sensors, when sandwiched between soft good layers in a space habitat, can provide MMOD detection capability. A schematic of such a layer in the inflatable structure and sensing array is shown in Figure 6.1. The sensors' sensitivity to the presence of 3mm holes due to an event of impact is evaluated through four-point probe electrical resistivity measurement.

In the event of an impact, a hole could be created in the sensor, which would change the resistance of that particular sensor. This change is measured and fed to the computer algorithm that determines the severity of damage by measuring the amount of change in electrical conductivity. The entire layer is scanned (electrical resistance measurement) after a preset amount of time, which provides the interval of impact occurrences. The damaged sensor's identification can provide information about the location of the damage. The sensing layer is sandwiched between Kapton layers for protection and insulation. These sensing layers can be stacked among the material layers at multiple locations, which can provide the depth perception of the damage. Part of this chapter previously appeared in (Anees et al., 2017; Gbaguidi, Anees, et al., 2017).

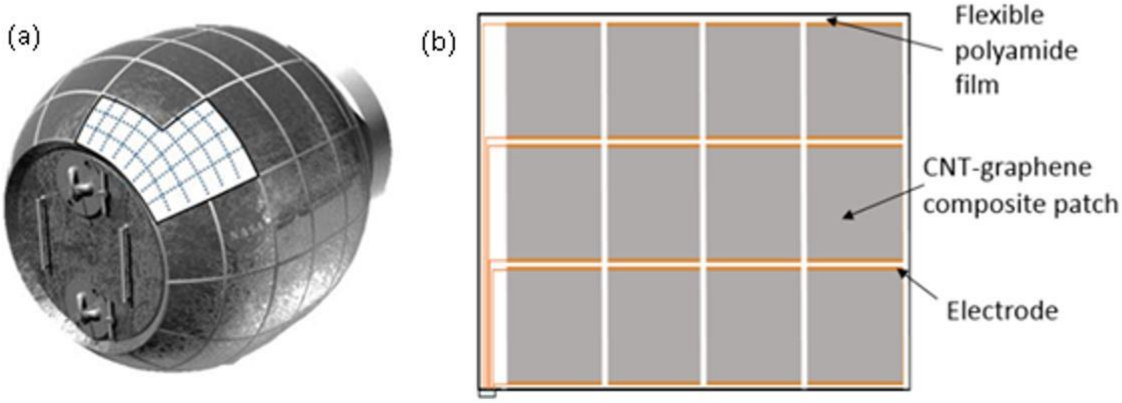

Figure 6.1 (a) Schematic of sensor array on inflatable structure and (b) tile and grid sensing patterns.

6.1. Fabrication and Characterization of Hybrid Nanocomposites to Study Their Electromechanical and Thermomechanical Behaviors

Through several studies, CNTs in form of buckypaper have shown great potential in the fabrication of high performance nanocomposites. Due to its brittleness, buckypaper is usually infiltrated with epoxy to achieve the desirable strength and stiffness for strain sensing application (Bahr et al., 2001).

In this chapter, neat epoxy resin and epoxy modified with coarse graphene platelets (GPs) were used with the CNT buckypaper to prepare the nanocomposites. The epoxy resin matrix is a combination of West System # 105 Epoxy resin with West System # 206 Slow Hardener at a ratio of 5:1 with a 20 minute working time. The multi-wall carbon nanotube sheet (buckypaper) consisting of 100% free standing nanotubes, with an area density of 21.7 g/m^2 and surface electrical resistivity of 1.5 Ω/m^2 was obtained from

Nano Tech Labs. The coarse (GPs) used as second filler were obtained by finely chopping graphene sheet obtained from Graphene Supermarket (see Figure 6.2(b)). The surface resistivity of the graphene sheet was $2.8 \times 10^{-2} \Omega/m^2$. Another silver epoxy resin with high conductivity and adhesive properties, obtained from MG Chemicals is used to attach electrodes (copper plates) to both ends of the nanocomposites.

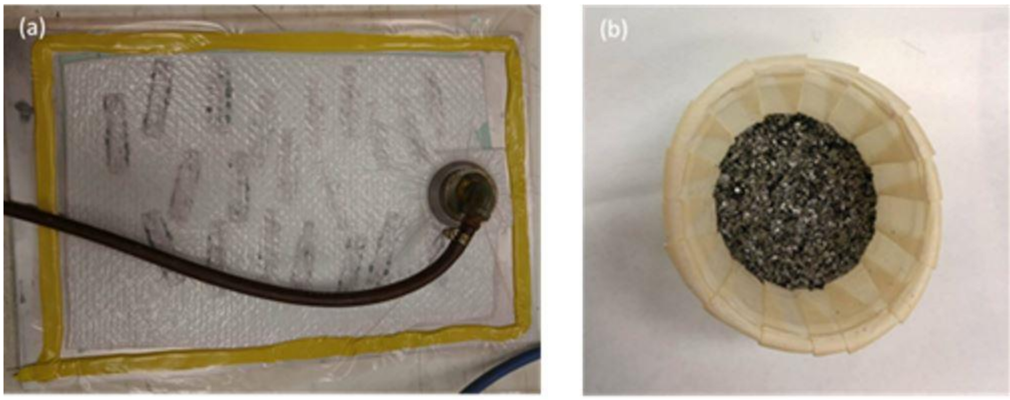

Figure 6.2 (a) Hybrid CNTs-GPs nanocomposites under vacuum, (b) chopped graphene sheet.

The hybrid CNTs-GPs nanocomposite specimen used for the experiments are strips, 6.35 cm long and 1.27 cm wide cut from the buckypaper sheet with laser blade. Copper plates gauging 32, 1.27 cm long and 1.27 cm wide are attached at both ends of the strips to serve as electrodes. The strips are then placed on a peel-ply on a flat aluminum mold. They are infiltrated, on both surfaces, with evenly mixed resin-coarse GPs, with coarse GPs of 5 wt%. The author’s previous experimental results indicate that the piezoresistivity in hybrid composites is higher for this combination of graphite platelets and CNTs (Gbaguidi & Kim, 2014; Jiukun Li, 2016). Another piece of peel-ply with a breather film on top of it is then used to cover the strips, in order to remove the excess of resin. The resin nanocomposite is then cured at room temperature for 12 hours, sealed in vacuum bag with a pressure of 88.05 kPa, as shown in Figure 6.2(a). After curing, two wires are soldered, one to each copper plate. Figure 6.3 shows the nanocomposite strips and a Scanning Electron Microscope (SEM) micrograph of the hybrid nanocomposite sample.

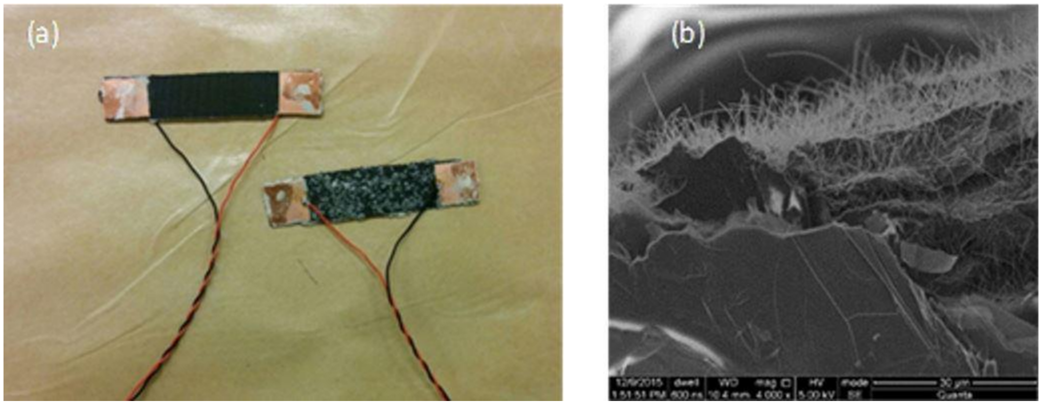

Figure 6.3 (a) Buckypaper infiltrated with pure epoxy resin (Left) hybrid CNTs-GPs nanocomposites (Right), (b) SEM micrograph showing graphene platelets and CNTs interactions.

Four point probe testing method was used to measure the resistance of the hybrid CNTs-GPs nanocomposites specimen before and during mechanical deformation, following IEEE (2009) and ASTM (2007, 2011) standard test methods. A constant intensity current of 0.5 Amperes is forced through the specimen and the resulting voltage drop is measured using the four point probe method. Ohm’s Law is then used to compute the specimen electrical resistance. In this study a LabVIEW code is used along with a DAQ system to monitor the drop of voltage and calculate the change in resistance before and during deformation.

6.2. Electromechanical Behavior of Hybrid Nanocomposites

The experimental results of the piezoresistivity performance of the hybrid CNTs-GPs nanocomposites, with 5 wt% of coarse graphene platelets are presented in this section. The experiments measure the electrical resistivity of the nanocomposites with application of strain. The electrical resistivity of nanocomposites strips of length L, width w and thickness t can be calculated as follow:

$$\rho = R(w \times t)/L \tag{6.1}$$

The thickness of the samples is obtained using SEM micrographs of the specimen cross sections. An average thickness value of 100 µm is used to compute Equation 6.1. The piezoresistive behavior of the nanocomposites is usually quantified by calculating either the gauge factor or strain sensitivity or the resistance change ratio. The resistance change ratio (K) and the gauge factor (GF) are computed as shown in Equations 2.1 and 2.2. Experimental studies show that gauge factors of individual SWCNTs ranges from 60 to 1000 (J. Cao, Wang, & Dai, 2003). In comparison, copper and aluminum have respectively a gauge factor of 2.2 and 2.5. However, gauge factor for CNT based nanocomposites sensors are usually lower compared to an individual CNT.

6.2.1. Electromechanical Behavior Under Uniaxial Tensile Loading

The experimental results of the piezoresistivity performance of the hybrid CNTs-GPs nanocomposites under static uniaxial tensile loading are presented in this section. The experiments also measure the stress induced in the nanocomposite with the application of mechanical strain. The test is conducted in the CS-225 Digital Force Tester at constant displacement speed of 1 cm/s, while simultaneous measurement of the specimen electrical resistance is performed.

Figure 6.4 shows an increase of the piezoresistivity response of the hybrid CNTs-GPs nanocomposites with 5 wt% of coarse graphene platelets, with increasing mechanical strain. A resistance change ratio of 20 % was achieved for a strain of 0.06. A young modulus of 163 MPa was measured for the nanocomposite specimen. The gauge factor increases from a relatively low value of 0.49 with 0 wt% of coarse GPs (pure CNT nanocomposites) to 3.6 with a coarse GPs content of 5 wt% (hybrid CNTs-GPs nanocomposite), at a strain of 6.5%.

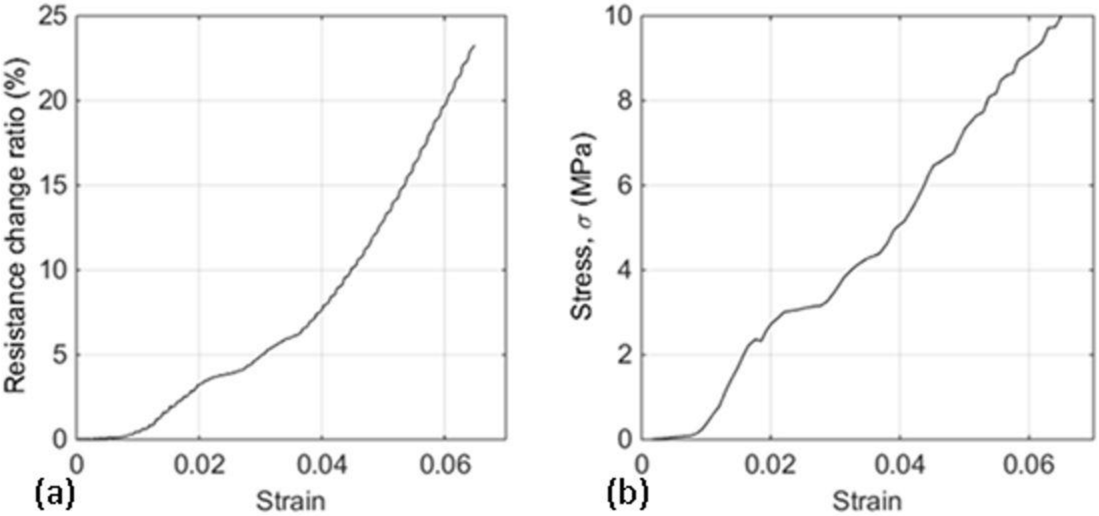

Figure 6.4 (a) Resistance change ratio Vs strain and (b) stress Vs strain curves for hybrid CNTs-GPs nanocomposites with 5 wt% of coarse graphene platelets, under uniaxial tensile loading.

6.2.2. Electromechanical Behavior Under Transverse Loading

The purpose of this experiment is to perform a transverse cyclic loading test on the nanocomposite and to examine the change in its sensing performance. Both ends of the nanocomposites strip are gripped horizontally, at the copper electrodes as shown in Figure 6.5. A function generator is used to send a square wave signal, which is amplified by a DC power supply amplifier, to control a woofer magnet. A vertical rod is placed vertically between the woofer magnet and the strip, to apply a transverse load at a frequency of 1 Hz, with a vertical displacement from 0.1 to 0.6 mm at the center of the strip. A displacement sensor, connected to the DAQ is then used to measure the vertical displacement of the center of the strip. The four point probe measurement explained earlier is used to monitor the change in resistance of the hybrid nanocomposites.

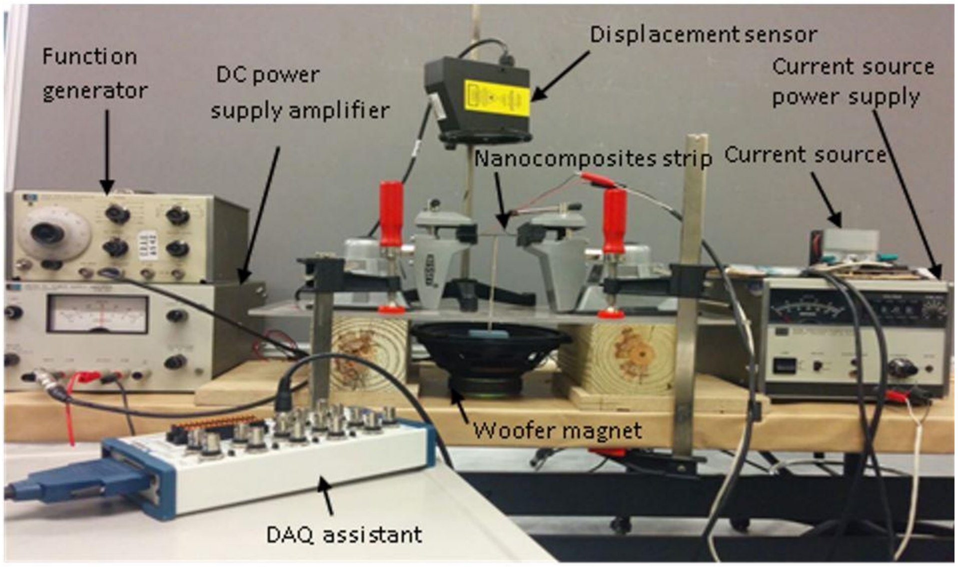

Figure 6.5 Experimental set-up for transverse cyclic loading.

Figure 6.6 shows the resistance variation along with the flexural strain with respect to time. An increase of electrical resistance is shown with the application of strain. The investigator was only able to apply small strains (compared to the uniaxial test) through this experimental set up. The resistance change correlates with the applied deformation, with a maximum resistance change ratio of 0.95 % at a flexural strain of 400 micro strain. That corresponds to a gauge factor of 23.75. Figure 6.6 shows that the piezoresistive sensing performance under transverse dynamic loads is consistent and repeatable. Moreover, the sensitivity of the nanocomposites is much higher at small strain when compared to the uniaxial tensile test. Overall, Figure 6.4 and Figure 6.6 show that the hybrid nanocomposite has good strain sensing performance in both uniaxial and transverse cyclic loadings. Also the gauge factor of the nanocomposites is much higher for small strains (23.75 for 0.04% of strain) compared to much larger strain (3.6 for 6.5% of strain).

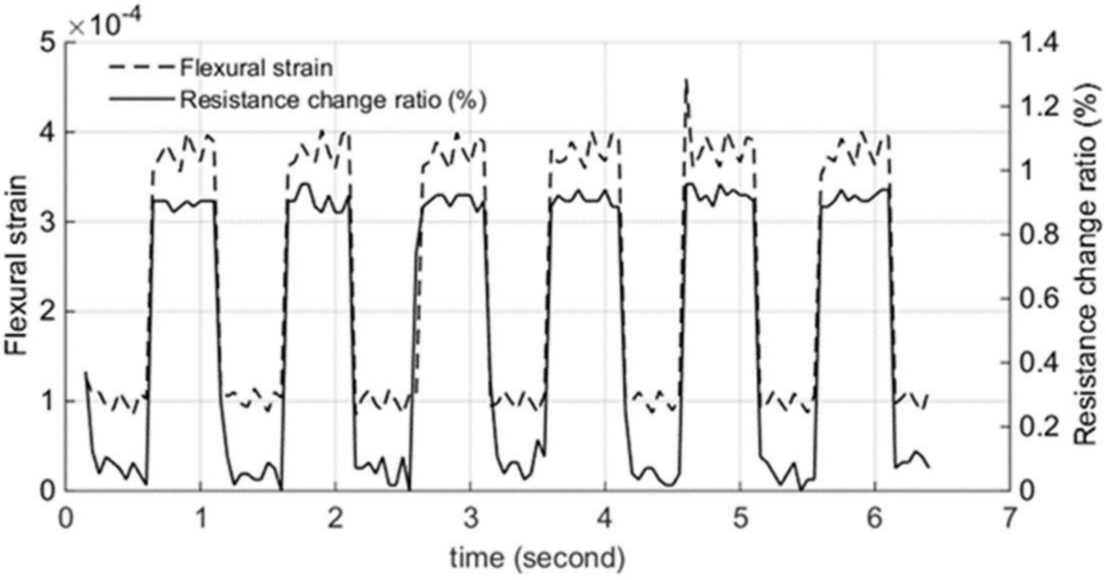

Figure 6.6 Variation of resistance change ratio and flexural strain of the hybrid nanocomposite with respect to time.

6.3. Thermomechanical Behavior of Hybrid Nanocomposites

After proving, the capability of the hybrid nanocomposites as strain sensor in different loading conditions, the effect of temperature and different loading frequencies on the nanocomposites was examined. A PerkinElmer Dynamic mechanical analyzer (DMA) 8000 was used for the thermomechanical tests, following ASTM standard (2015), to determine the storage modulus and the damping properties of the hybrid nanocomposites.

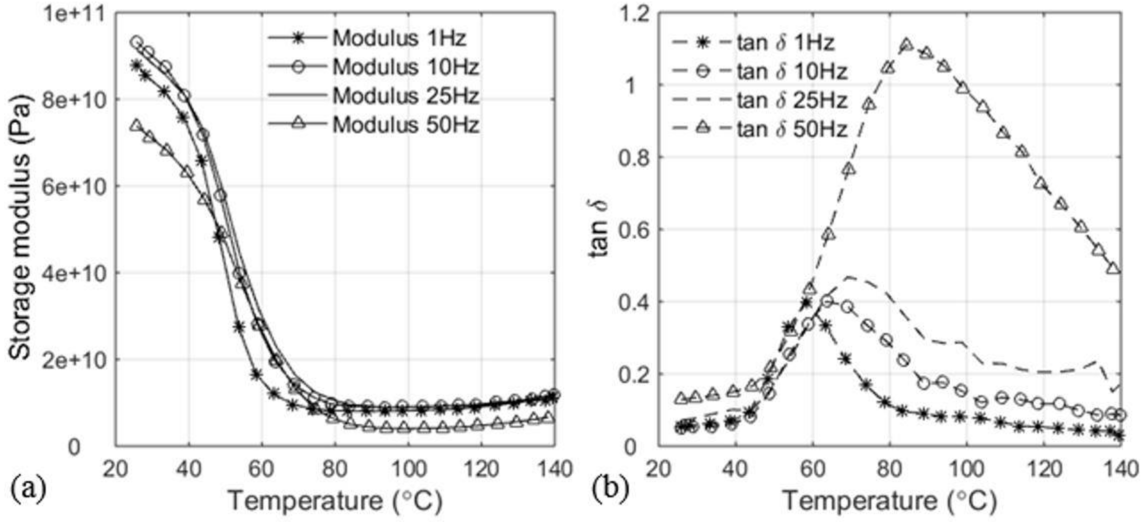

Figure 6.7 (a) Modulus and (b) tan δ for temperature sweep at four frequencies.

Specimens of length 40 mm, width 6 mm and thickness 0.1 mm, without copper electrodes attached were used for the DMA experiments, to examine the viscoelastic behavior of the hybrid nanocomposites. The sample was first mounted in the dual cantilever bending clamps and a multi-frequency temperature scan of the nanocomposites was performed. Temperature rate of 1.5 °C/min was observed from room temperature up to 140 °C. Figure 6.7(a) shows the thermal scan of the material for the frequency values of 1Hz, 10 Hz, 25 Hz and 50 Hz. A clear frequency dependence is observed in both the modulus and tan δ data indicating a relaxation event. As the material passes through the glass transition temperature, Tg a cure reaction also takes place. The material gets less stiff (decrease of modulus) as a result of the increasing temperature. Figure 6.7(a) shows that the storage modulus evolves in a nonlinear fashion with respect to the frequency. At room temperature, the modulus first increases from 1 Hz to 10 Hz, remains constant from 10 Hz to 25 Hz and then decreases at 50 Hz. Figure 4(b) shows that the frequency dependence of the material leads to higher glass transition temperatures with higher frequencies. Tg values of 59 °C, 63.6 °C, 70 °C and 85.3 °C respectively for frequencies of 1, 10, 25 and 50 Hz are observed on Figure 6.7(b), as the peak on tan δ curves.

An isothermal frequency scan at room temperature of the nanocomposite is then performed. Figure 6.8 shows the modulus and tan δ data for the nanocomposites as a function of frequency at a temperature of 24.2 °C. The values of modulus and tan δ are relatively similar in magnitude for low frequencies (less than 100 Hz). However, a jump in the values of tan δ followed by a sudden drop of the modulus is observed at 111 Hz. This merely reflects the sample undergoing resonance. Also, the modulus of the material after resonance goes to zero which indicates a total loss of stiffness of the material after resonance.

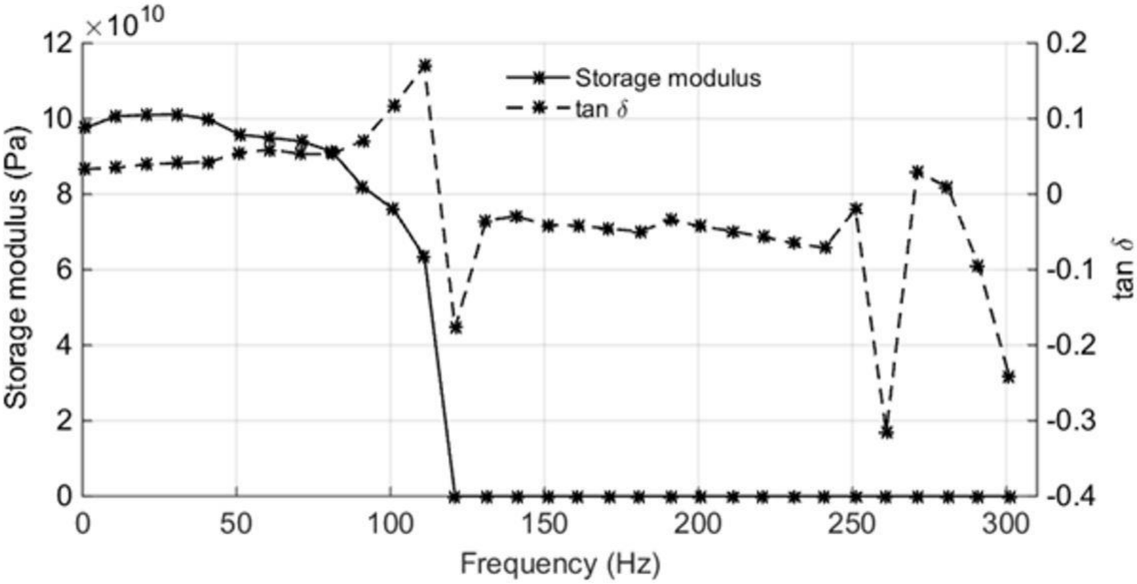

Figure 6.8 Modulus and tan δ for frequency sweep at room temperature.

6.4. Electrical Performance of Nanocomposites Under Static Damage Tests

In this second part of the chapter, the three type of sensors made of carbon nanotubes (CNT) in the form of buckypaper, with and without addition of graphene particles in form of fine nanoplatelets or coarse platelets fabricated in Section 6.1 are tested as impact sensors. First, their performance under static damage testing was observed in order to choose the sensor with the highest sensitivity of holes. For that preliminary study, smaller sensors of size $2.5\ in \times 0.5\ in$ are fabricated. $0.5\ in \times 0.125\ in$ copper electrodes are attached at the two ends of the sensors with the help of conductive silver epoxy and electrical wires are attached on the electrodes for electrical resistance measurements.

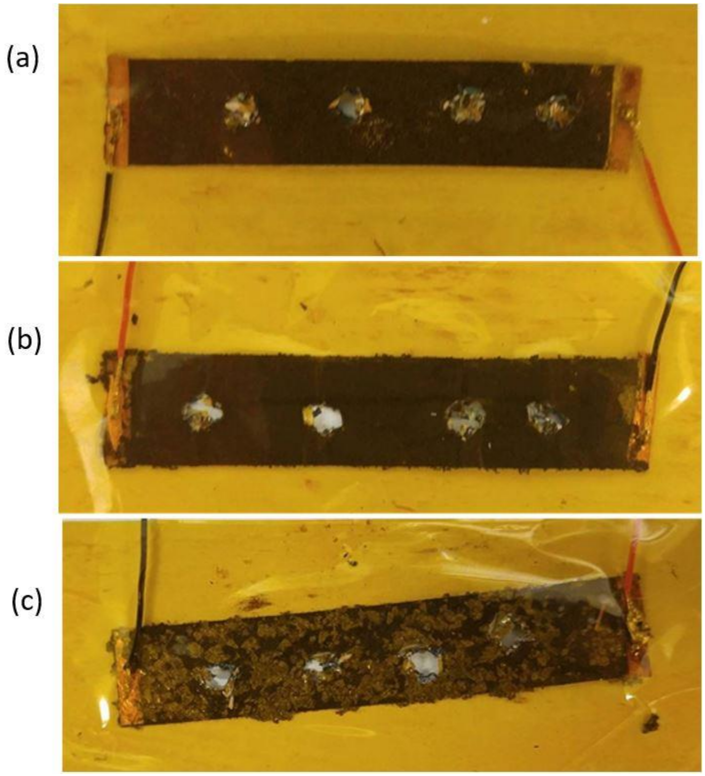

Figure 6.9 Sensors made of (a) neat buckypaper, (b) fine graphene nanoplatelets and (c) coarse graphene platelets of size 2.5 in×0.5 in with Kapton tape and after addition of four 3 mm holes.

The sensors are then covered with Kapton tape for protection. The resistivity of the nanocomposite sensors is measured using a four-point probe method by passing 0.05A current at 12V while subjecting them to static damage (indentation). NI USB 6001 DAQ and LabVIEW software are used to interface with the circuit and to collect and analyze the sensor signals.

Figure 6.9 shows the three type of sensors with their Kapton protective tape and their electrical wires, with four 3 mm holes, as induced static damage. The change of resistance of every specimen is continuously recorded throughout the experiment. A period of 1 min to 5 min is observed before the addition of any new hole, in order to capture the stability of the resistance measurements.

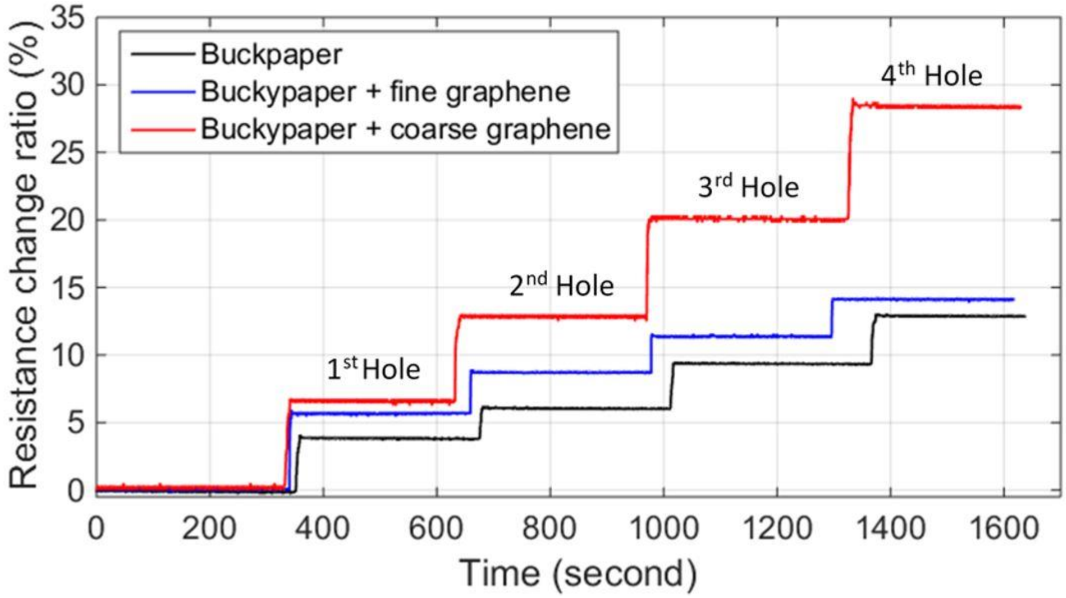

Figure 6.10 Variation of resistance change ratio with time and with addition of 3 mm holes to the three type of sensors.

Figure 6.10 shows a clear and noticeable increase of the sensor resistance, for each type of sensors after the addition of every hole. A resistance increase of 2%, 3% and 5%

was observed after addition of a hole respectively for the neat buckypaper sensor, the fine graphene sensor and the coarse graphene sensor. Also the resistance of the sensors remain constant before and after the addition of holes, which proves the effectiveness of the sensors in detecting damage.

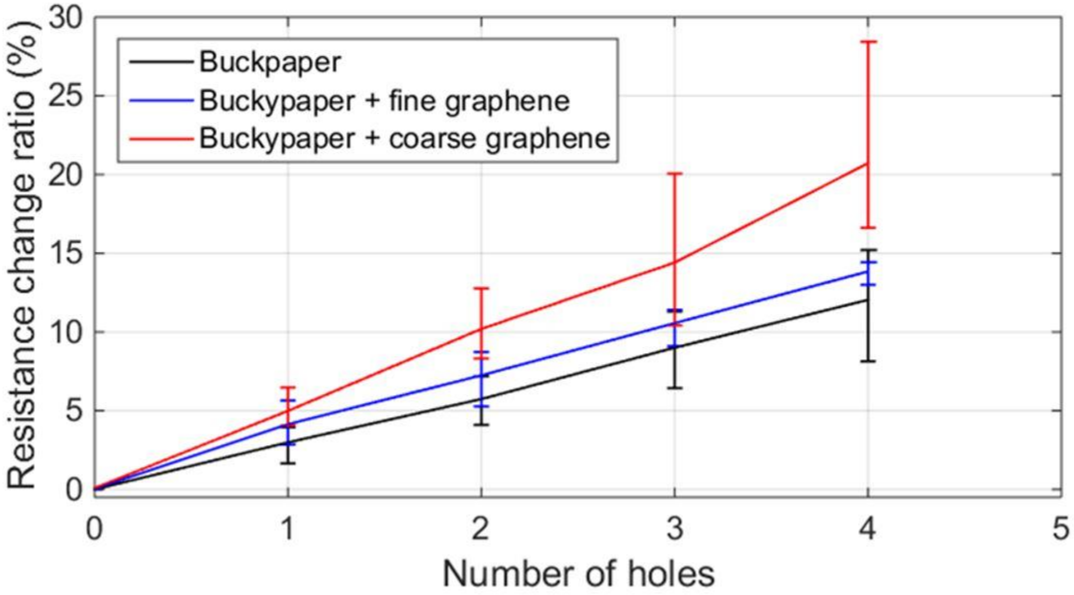

Figure 6.11 Variation of resistance change ratio with addition of 3 mm holes to the three type of sensors using the average of three samples per sensor type.

Figure 6.11 shows the overall performance of the sensors with the average of three specimen tested per sensor type. An average increase of 2.5%, 3.2% and 5% was observed after addition of a hole respectively for the neat buckypaper sensor, the fine graphene sensor and the coarse graphene sensor. As observed in (Jiukun Li & Namilae, 2016), when the sensors were used as strain sensors, the addition of any type of graphene to the neat buckypaper sensor, increases the sensitivity of the sensors, to damage (holes). Figure 6.10 and Figure 6.11 also show that the sensor with the coarse graphene platelets exhibit the highest sensitivity to damage and hence is more suitable for MMOD impact detection.

6.4.1. Static Damage Tests on Hybrid CNT-Coarse GP Nanocomposites

Following the observations from the preliminary study in the previous section, $2.5\ in \times 2.5\ in$ coarse graphene platelets (5 wt%) sensors with $2.5\ in \times 0.25\ in$ copper electrodes, are fabricated and tested under static damage, while a current of 0.5 A is used for resistance measurements. Figure 6.12 shows the MMOD sensor with its Kapton protective tape and the electrical wires, with six 3 mm holes, as induced static damage.

Figure 6.12 2.5 in×2.5 in coarse graphene sensor with Kapton tape, after addition of six 3 mm holes.

Figure 6.13 and Figure 6.14 show a clear and noticeable increase of the sensor resistance, with an average increase of 0.75%, after the addition of every hole. It is also noticed that the resistance change with the $2.5\ in \times 2.5\ in$ specimen is much lower than the one obtained with the $2.5\ in \times 0.5\ in$ specimen, due to the fact that the length-to-width ratio of the specimen has been decreased which decreases the resistance of the specimen itself.

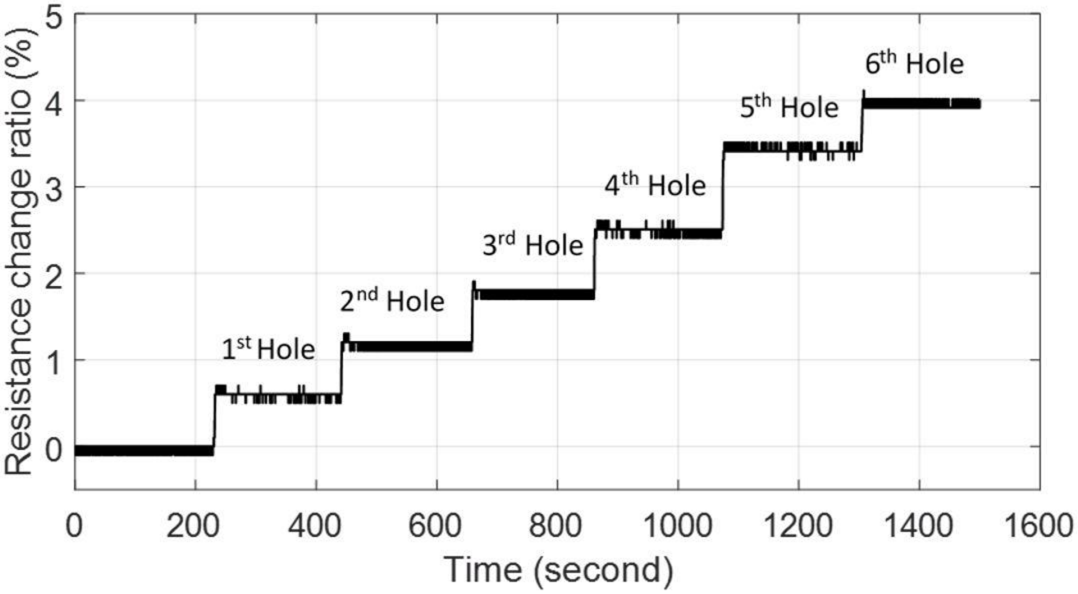

Figure 6.13 Variation of resistance change ratio with time and with addition of 3 mm holes to MMOD damage sensor.

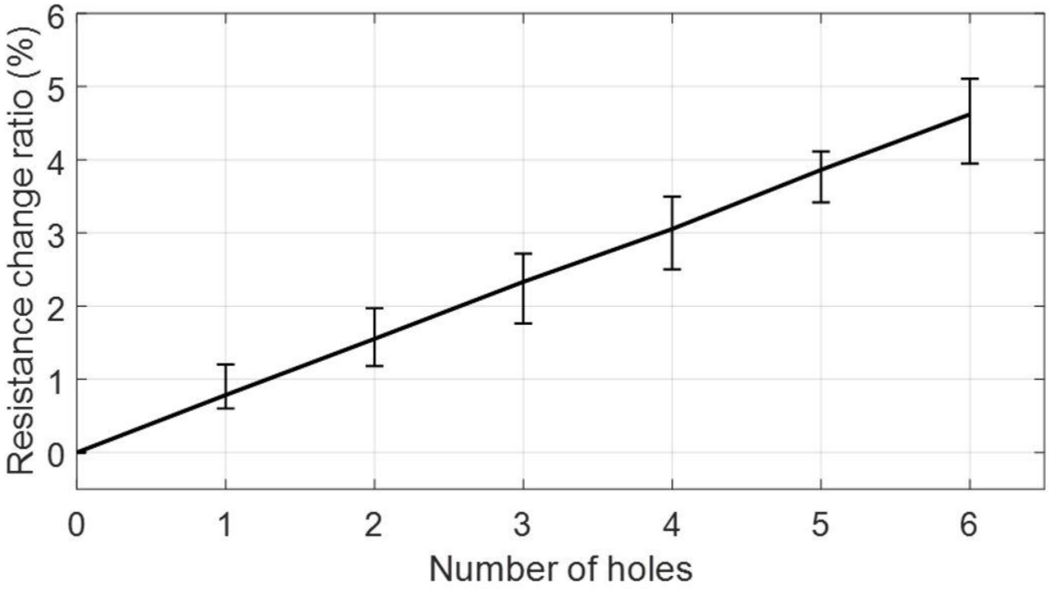

Figure 6.14 Variation of resistance change ratio with addition of 3 mm holes to MMOD sensor using the average of three samples.

Finally, the performance of the sensor with a very large number of holes was studied. Twenty, 3 mm holes were successively introduced to the specimen to see its sensitivity. Figure 6.15 shows that the sensor performance in detecting static damage is not altered with a very large number of damages.

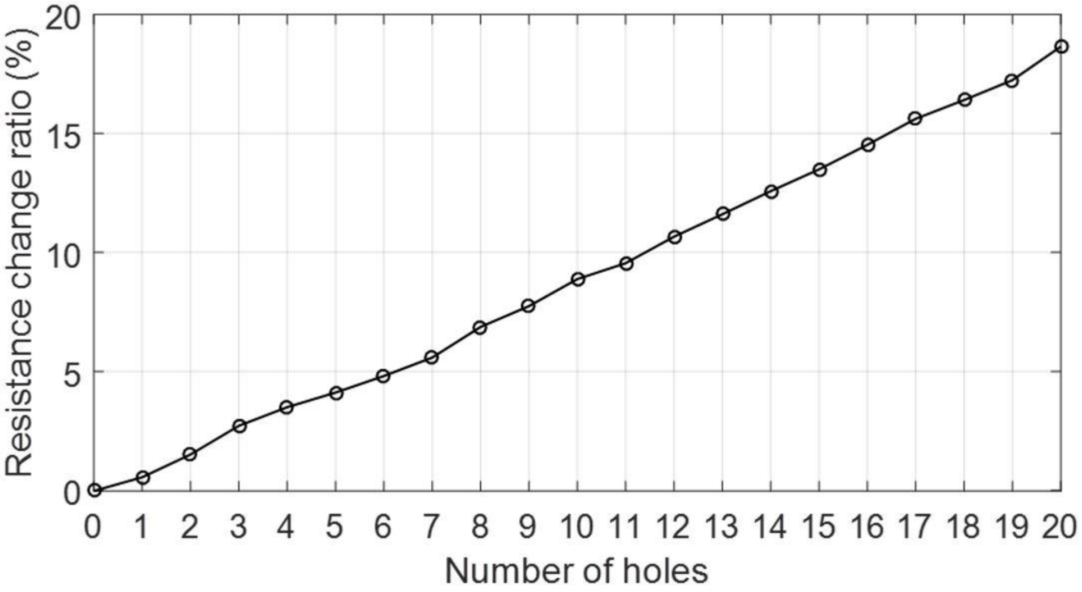

Figure 6.15 Variation of resistance change ratio with addition of very large number of 3 mm holes to MMOD sensor.

6.4.2. Low Velocity Impact Damage on Hybrid CNT-Coarse GP Nanocomposites

In the previous sections, the performance of the MMOD sensor was evaluated under static damage, where it is assumed that the damage is induced slowly enough such that the sensor remains in equilibrium. However, to guarantee the detection of damage in the event of impact, the Instron Dynatup 9250 drop tower is used to simulate a low velocity impact damage on the sensors. To simulate the sensor placement in between the soft goods layer of an inflatable habitat structures, during the MMOD impact, the sensor with its protective Kapton tape is bonded to a dry fiberglass cloth, which is attached to a metallic rectangular fixture. The clamp fixture creates a nearly fixed boundary condition at the edges of the layer. Two type of impact tests are performed, the first with a single layer and the second with a double layer of sensors.

6.4.2.1. Low Velocity Impact Damage on Single Layer of Nanocomposites

To induce the damage to the sensor layer, a 3 mm diameter indenter is used with an impact velocity of 1.38 m/s. The resistance measurements of the sensors are recorded continuously before and after the impact damage. The variation of the resistance of the sensor through a low velocity impact damage is shown in Figure 6.16. A spike in the resistance curve, which corresponds to the combined action of the sensor deformation (elastic) and a damage/hole in the sensor is ovserved. This is followed by a steady state of the resistance, of value higher than the resistance of the undeformed sensor but lower than the spike value. It corresponds to the permanent damage in the sensor, after the impact. Also, the resistance of the sensor, before and after impact remains stable.

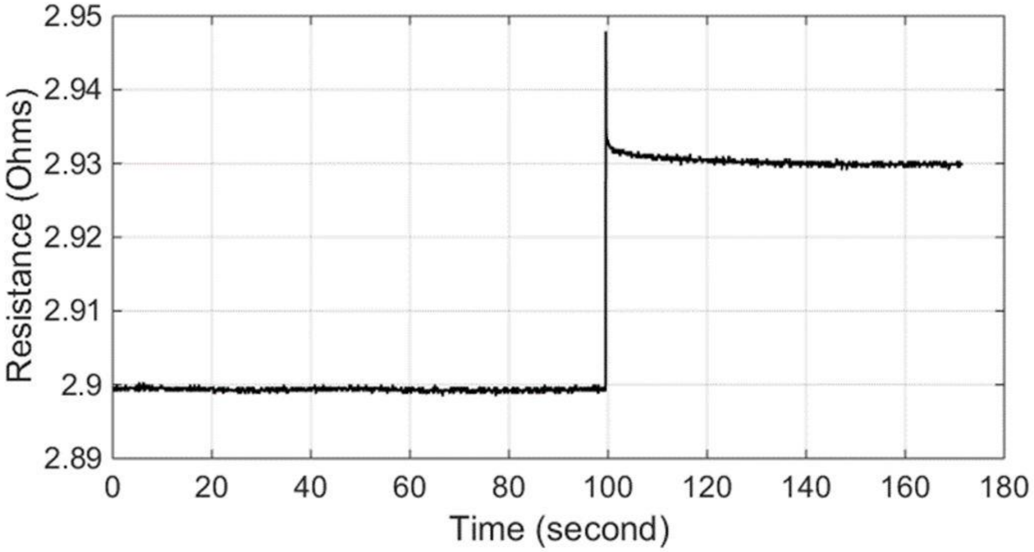

Figure 6.16 Variation of resistance after one low velocity impact damage, induced by 3 mm diameter indenter, to MMOD sensor layer.

Figure 6.17 show the overall performance of the sensors, after five successive impact, with the average of three specimen tested. An average change in resistance of 0.8% - 1% after every low velocity impact damage is observed, which clearly demonstrates the effectiveness of the sensor for MMOD impact damage detection.

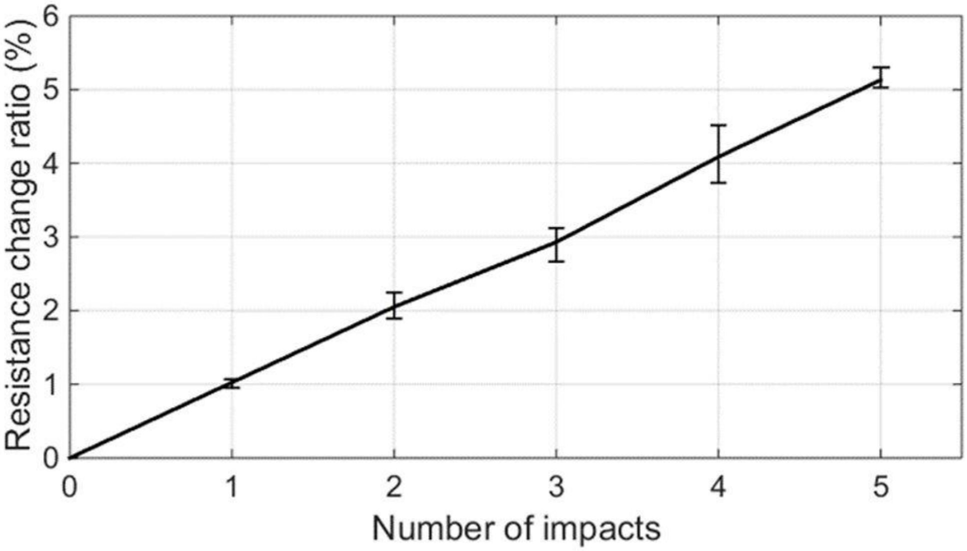

Figure 6.17 Variation of resistance change ratio with five consecutive low velocity impact damages to the MMOD sensors using the average of three samples.

Figure 6.18 shows the variation of the load and the energy absorbed during the impact of the sensing layer. The load is induced by the sensor layer to the indenter tip. It increases monotonically with contact of the indenter and the layer and then drops quickly after total penetration of the indenter through the sensor layer. The energy absorbed by the layer depicts the work perform by the indenter on the layer. It increases until a maximum value, which represents the work performed during impact.

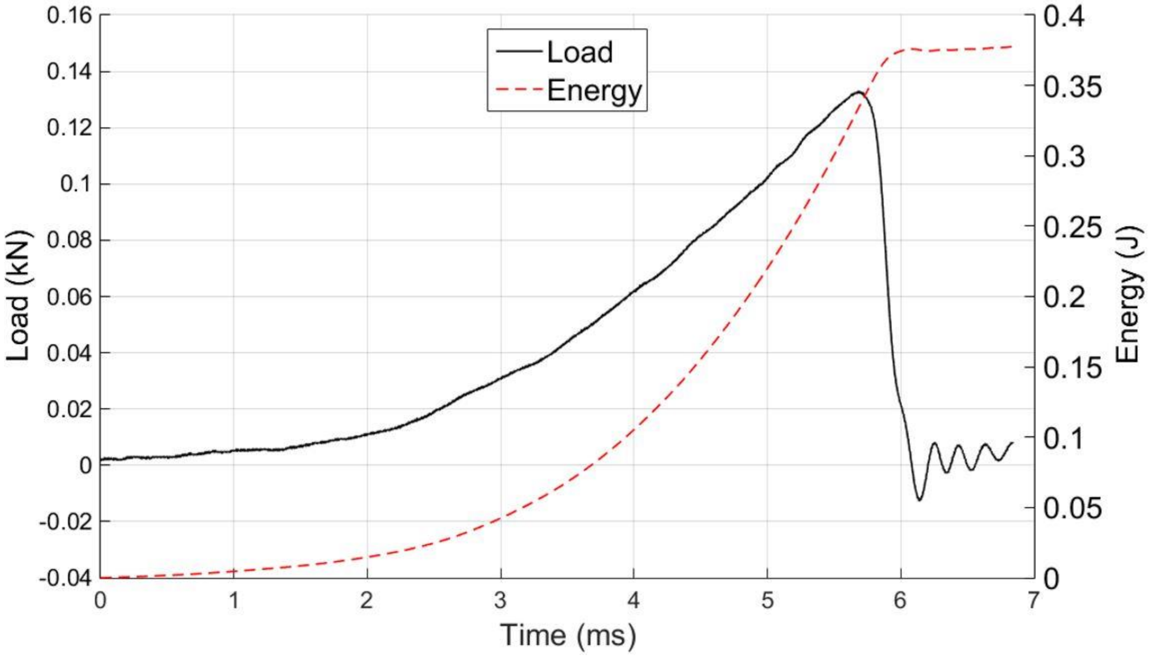

Figure 6.18 Variation of load and energy absorbed during impact.

6.4.2.2. Low Velocity Impact Damage on Double Layers of Nanocomposites

In the previous section, the performance of the sensor in a sensing layer was evaluated under low velocity impact damage to simulate MMOD impact detection. However, to determine how deep the MMOD penetrate the structure, multiple layers of sensors will be needed in between the soft goods layer of the inflatable structures. To simulate damage detection and depth perception, two layers of sensor, as described in the previous section are stacked on top of each other, with a separation distance of 4 inches between them, as shown in Figure 6.19(a). An indenter with thickness following a step function is used. It has a diameter of 3 mm at its lower part and a diameter of 6 mm on its upper part, as shown in Figure 6.19(b). This will induce a large damage on the top sensing layer and a smaller one on the bottom sensing layer, during the low velocity impact test. This replicates the decreasing size of damage created by MMOD through multiple layers, after impact. The test setup is shown in Figure 6.19(c).

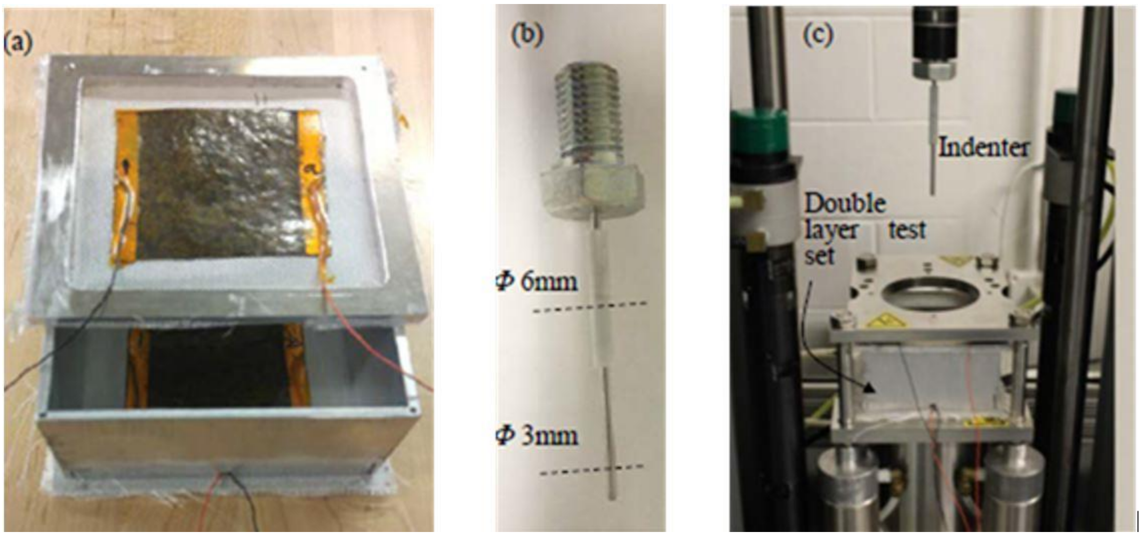

Figure 6.19 Double layer impact setup: (a) two sensors layers mounted on fixture, (b) indenter with two thicknesses along its length and (c) test setup with two sensor layers.

The variation of the resistance of each of the two sensors through a low velocity impact damage is shown in Figure 6.20. The resistance change of the top layer sensor is much higher than the bottom layer one. This is due to the fact that a damage of bigger size is induced in the top layer sensor. Also, the resistance of the top sensor increases suddenly, when the indenter tip hits the top sensor. A slight increase of the resistance is followed, when the top portion of the indenter (with bigger diameter) touches the top layer. A sudden drop of resistance is then observed when the top portion of the indenter penetrates the top layer. Next, the figure shows that the resistance of the bottom layer suddenly increases, followed by a drop of its value, due to the contact of the tip of the indenter with the bottom layer followed by its penetration, while the resistance of the top layer remains constant.

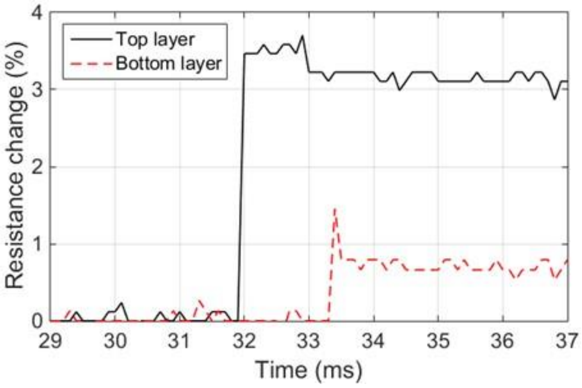

Figure 6.20 Variation of resistance change ratio with time, induced by one low velocity impact damage on a double sensing layer setup.

Figure 6.21(a) shows the induced damage (bigger size in top layer) in each of the two sensing layers, after impact. Figure 6.21(b) shows the variation of the load and the energy absorbed by both sensing layers, during the impact of the sensing layers. The three peaks observed in Figure 6.21(b) correspond respectively, to the penetration of the top layer by the indenter tip (3 mm diameter), then by the top portion of the indenter (6 mm diameter) and finally the penetration of the bottom layer by the top portion of the indenter.

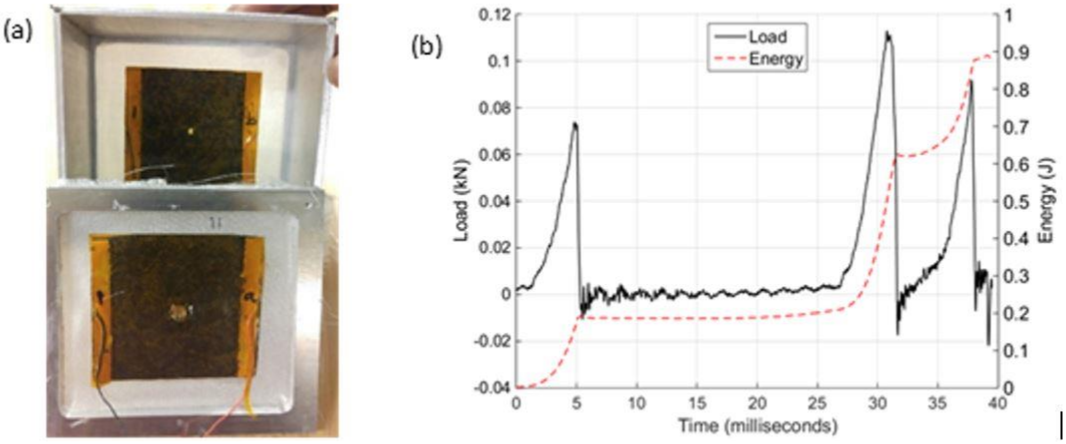

Figure 6.21 (a) Damaged double sensing layers and (b) Variation of load and energy absorbed by double layer during single impact.

Next, three low velocity impact damages were successively introduced into the two sensing layers to observe their performance. Figure 6.22(a) shows the damaged top sensing layer. Figure 6.22(b), the resistance of each of the two sensing layers increases with addition of new impact damage. Average resistance changes of 0.8% and 4% are observed respectively in the bottom layer and the top layer, with three specimen tested. This section clearly demonstrates the effectiveness of the two sensing layers setup in detecting MMOD impact as well as depth perception in the soft goods of the structure.

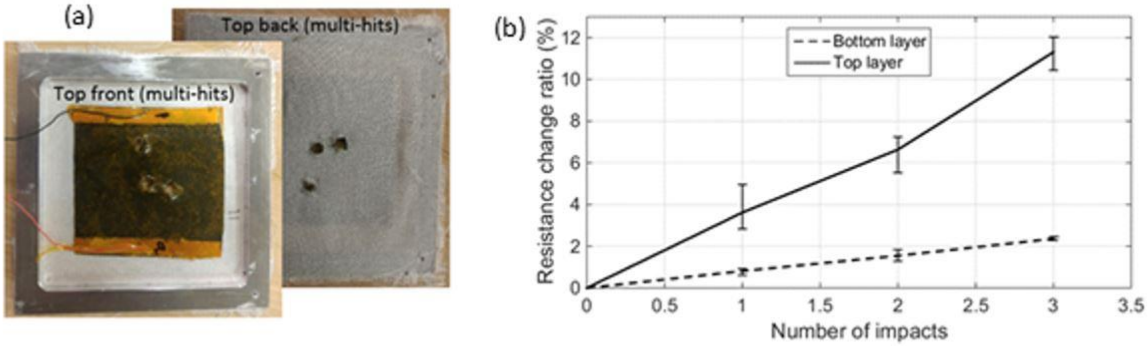

Figure 6.22 (a) Damaged top sensing layer and (b) Variation of resistance change ratio on each of the two sensing layers after three consecutive impact damages, on double sensing layer, using the average of three samples.

6.5. Summary

In this chapter, a simple fabrication process using resin infiltration was presented for hybrid nanocomposites, in order to evaluate their electromechanical and thermomechanical performance under different conditions. The piezoresistive nanocomposite sensors were used to prove their effectiveness in detecting impact damages has been developed, which potentially can be used in inflatable space habitat structures. An array of these sensors can form a soft blanket that can be incorporated into the composite laminates of the habitat structure as a sensing layer. The sensors can detect holes as small as 3 mm and the damage can be localized based on the location of the sensors. The sensor system with multiple impacts of different sizes and in multiple sensing layers has been demonstrated.

7. Multifunctional Inkjet Printed Sensors for MMOD Impact Detection of Inflatable Structures

The sensitivity of the electronic properties of carbon nanotube to gases, chemicals, temperature, and mechanical strain enables their use as fillers in nanocomposites for sensing applications. The strain sensing behavior of CNT nanocomposites is mainly due to the breaking and modification of conductive paths in the percolated network (Alamusi et al., 2011; Njuguna, 2012) due to induced strain. That mechanism in the nanocomposites could potentially be used in applications where the nanocomposites will experience stimuli that would change the percolated network of its microstructure, such as damage or material deterioration sensing (H. Liu, Liu, Chen, Heider, & Thostenson, 2016; Loh, Hou, Lynch, & Kotov, 2009; Loyola et al., 2013). Structural health monitoring of space inflatable structures is one challenging application where flexible printed nanocomposites could be used since conventional strain gages and fiber optics may not be suitable.

In this chapter, a framework based on inkjet printing technologies is developed to fabricate printed flexible sensors. This approach could result in a low-cost and high speed fabrication procedure for CNT nanocomposite sensors with tailored sensing performance. Further, the application of such sensor for micrometeoroid and orbital debris (MMOD) impact damage detection is demonstrated. To improve the printing quality of the sensors, a surface modification of the flexible substrates is performed before printing the conductive ink layers. The effectiveness of the printed devices as strain sensors and static damage sensors is then examined. The effect of the number of deposited ink layers, the type of substrate and the device's fabrication parameters on the strain and damage sensing behaviors of the sensors is investigated. Finally, the application of the inkjet-printed sensors is demonstrated for strain sensing and for MMOD damage detection, under hypervelocity impact. Part of this chapter previously appeared as (Gbaguidi, Madiyar, Kim, & Namilae, 2020).

7.1. Materials and Methods

7.1.1. Materials

The materials used for this work were carboxyl functionalized multi-walled carbon nanotubes, MWCNT-COOH (20-30 nm outer diameter, >95 wt% purity, 10-30 µm length, Cheap Tubes, Inc); sodium n-dodecyl sulfate (SDS, 99% dry wt., Alfa Aesar); potassium hydroxide (reagent grade, 90%, flakes from Sigma-Aldrich); isopropyl alcohol (91%, off the shelf); acetone (99.5%, off the shelf); silver conductive epoxy adhesive (8331-14G, MG Chemicals); deionized water (DI water, Milli-Q plus 185 model); and 500 FPC (0.005 in) Kapton film (American Durafilm CO., Inc). The polyimide film was treated on both sides. Regular copy paper was also used and referred as paper in the rest of this work.

7.1.2. Preparation of Carbon Nanotube Ink

Da Costa et al. (2015) developed a water-based conductive ink formulation with 1 wt% of CNT, 0.7 wt% of SDS and DI water, for printed electrochemical sensors on paper. The ingredients were sonicated for 30 minutes and centrifuged for 5 minutes at 12,000 rpm. The same ink’s ingredients, with the same content of CNT was used and the sonication time, the centrifugation speed and duration as well as the content of SDS and DI water were iteratively varied in order to obtain a more conductive material. To obtain the ink formulation used in this work, which has the highest conductivity, 0.2 g (1 wt%)

of carbon nanotubes was added to 0.16 g (0.8 wt%) of SDS and DI water to obtain 20 g of solution into a 22 mL glass vial. The solution was sonicated for 5 hours using an ultrasonic bath (SharperTek®, SH-150-6L), with magnetic stirring (5 minutes) every 30 minutes. The dispersed solution was centrifuged (Denville 260D) at 3000 rpm for 10 min. The centrifugation step can be repeated several times to remove the large agglomerates of CNT to avoid the clogging of the cartridge's nozzle during printing. The supernatant was recovered from the centrifuge tubes using a syringe to obtain the final ink.

7.1.3. Kapton Treatment

Kapton films made of polyimide polymer generally have chemically inert and highly hydrophobic surfaces. To facilitate the inkjet printing of the water-based ink on Kapton films, the Kapton surface is modified using a wet chemical treatment. X. D. Huang, Bhangale, Moran, Yakovlev, and Pan (2003) reported a surface modification procedure for 125 µm Kapton HN and 50 µm Kapton H using a solution of potassium hydroxide. The films were cleaned with acetone, then DI water and dried in air. They were immersed in a 1M solution of KOH for a maximum of 30 minutes, washed twice for 3 minutes with water and then with isopropanol, dried with air and stored in vacuum for 12 hours. Since a different Kapton film is used in the present work, a similar approach as reported earlier was performed while the different steps of the approach were iteratively varied to find the recipe that leads to the printed ink on Kapton FPC with the best conductivity. In this work, the Kapton films were first cleaned in acetone for 10 min and an additional 10 min in DI water using an ultrasonic bath and dried in air. The dried films were immersed in a 1M aqueous solution of KOH for 45 min and rinsed with water (for 3 min twice) and then isopropyl alcohol (for 3 min twice) to remove the excess of KOH. The films were dried in air and stored under vacuum for 14 hours before the printing.

7.1.4. Inkjet Printing

A standard commercial office HP Deskjet D4260 printer with a maximum resolution of 1200 x 1200 dots per inch (dpi) was used to print on the substrates. The ink was injected into a previously cleaned HP 74 ink cartridge with a syringe. The patterns were designed using Microsoft Word and printed on both paper and Kapton film substrates using the best printing quality settings. During printing, submicron-sized (from 4 to 15 picoliters) drops are ejected from the nozzle of HP 74 cartridges in a few microseconds. The printed specimens were dried in an ambient atmosphere after every printed layer for 3 min.

7.1.5. Device Fabrication

To be able to print on a large area of the substrate using a millimeter size printhead, the printer uses a bi-directional raster setting where the cartridge together with the printhead is belt-driven in the y-direction by a stepper motor while the nozzles fire ink droplets on the substrate to form an array of dots in the y-direction. To cover rectangular areas, the pickup rollers move the paper forward a little, in the x-direction, into the main rollers while the printhead deposits a new successive array of dots in the y-direction. Because of the bi-directional printing, two resistance measurements are performed, in the x-direction and the y-direction respectively called R_X and R_Y. Figure 7.1 shows a schematic of the different motions involved in the printing.

For the sheet resistance measurement and scanning electron microscopy (SEM) observations, several rectangular patterns of 1.3 mm x 13 mm (x by y dimensions) were printed on paper and Kapton substrates. The number of printed ink layers for each of the rectangular patterns was varied from 2 to 34 with an increment of 2. The printed ink was allowed to dry in air for at least 3 min after each print. At the end of the printing step, the substrates are then heated in an oven at 90°C for 15 min to dry the ink.

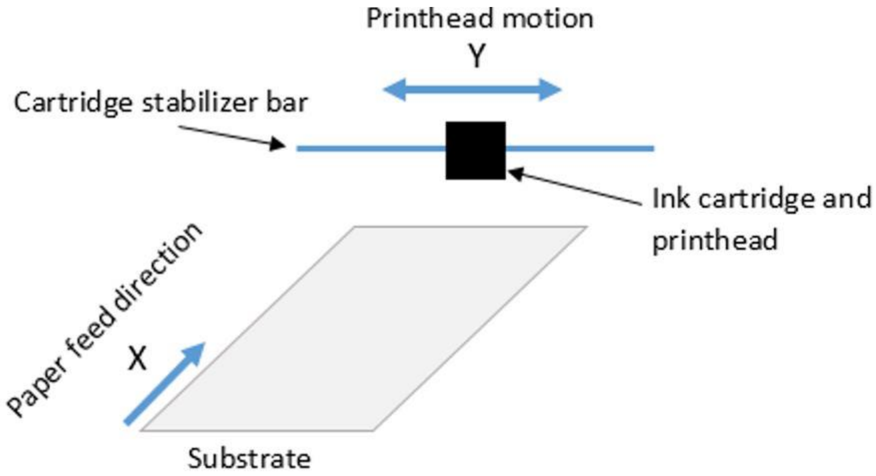

Figure 7.1 Schematic of inkjet printing with bi-directional raster printing with paper and ink cartridge motions.

For the damage sensors, rectangular patterns of 2 in x 2 in were printed on the paper and Kapton substrates. The ink drying process is the same as above. 3/16 inch wide copper foils were attached as electrodes to the four edges of the printed sensors using silver adhesive, with sufficient gaps between the electrodes. The sensors are then put inside a composite press with a pressure of 0.5 Torr and at 90°C for 45 min for the electrodes to adhere to the substrates.

For the strain sensors, rectangular patterns of 0.5 in x 3.5 in (x by y dimensions) were printed on Kapton substrates. The ink drying process and the fabrication of the electrodes are the same as above. In this case, electrodes were attached only on the two edges, across the y-direction, 2.5 in apart. Fiberglass grips were attached on top of the electrodes for tensile testing.

7.1.6. Device Characterization

7.1.6.1. Device Characterization Under Static Load Environments

In this section, the devices are characterized under no mechanical loads, for the sheet resistance measurements and under static/quasi-static loads in case of sensitivity to static damage or strains. The devices fabricated for sheet resistance measurements are microstructurally characterized using SEM. The sheet resistance, R_Y is measured using a 2-probe ohmmeter following (Mikkonen, 2017).

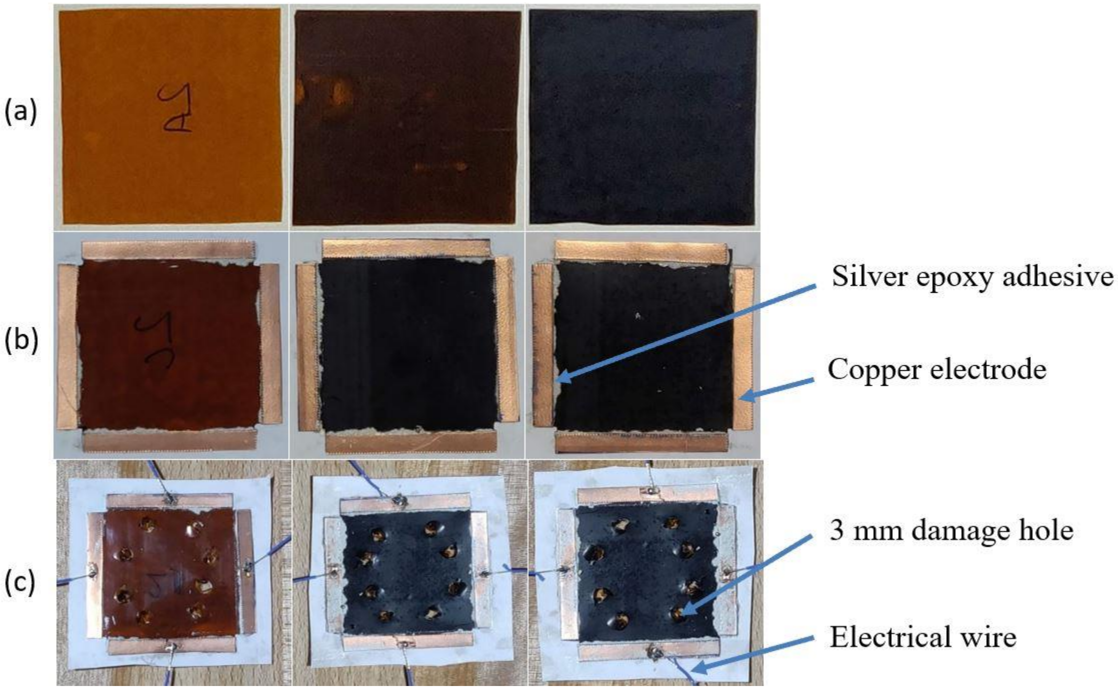

Figure 7.2 Fabrication process for inkjet-printed damage sensors with 2, 10 and 20 printed layers (Left to right) on Kapton. It includes (a) printing on Kapton, (b) addition of electrodes and (c) damaged sensors with 8 holes with electrical wires soldered.

For the damage sensors, to perform resistance measurements, electrical contact was achieved by soldering thin copper wires to each of the four copper electrodes. The electrical resistances R_X and R_Y of the damage sensors were measured, separately, in the x and y directions. Damage is introduced to the sensors as four 3 mm size holes respectively for R_X and R_Y measurements, using a power drill. The KIKUSUI DME 1600 was used with a computer to record the variation of the resistance of the sensors with time.

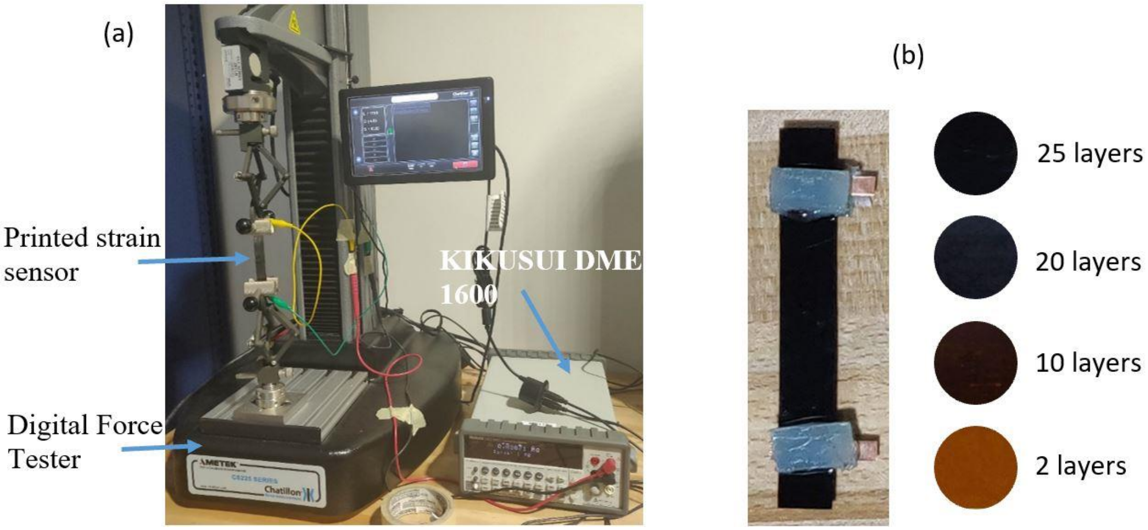

Figure 7.3 (a) Test setup for electromechanical characterization of strain sensors. (b) Surface color change due to inkjet-printing of strain sensors with 2, 10, 20 and 25 printed layers on Kapton.

For the strain sensors, longitudinal tensile deformation (along the length) is applied to the sensor between the fiberglass grips using the Chatillon CS225 Series Digital Force Tester (capacity up to 1 kN). The displacement-time data is obtained and converted to strain-time data. The electrical resistance, R_Y of the sensors was simultaneously measured using the KIKUSUI DME 1600 with a computer to record the resistance-time data.

7.1.6.2. Device Characterization Under Hypervelocity Impact Damage

A report from the National Aeronautics and Space Administration, NASA, describes that the impact velocity for space debris can reach up to 15 km/s and up to 70 km/s for meteoroids (E. Christiansen et al., 2009). Hence, to characterize the damage devices for MMOD impacts, hypervelocity impact tests were necessary. The damage sensors described earlier, but with only the two electrodes perpendicular to the y-direction were used. The test was performed on Range 4, a 50 mm/20mm two-stage, light-gas gun, in near-vacuum environment, in the Impact Physics Laboratory at the University of Dayton Research Institute.

Figure 7.4 Test Range 4 (Left) at UDRI hypervelocity impact laboratory.

Figure 7.4 shows the picture of the gas gun used, where Range 4 can be seen on the left. The test article supporting the damage sensor was mounted to the target support frame inside the gas chamber, shown in Figure 7.5(a). Since the characterization of damage sensors under static damage hole gives a clear indication of the sensing behavior of the sensors before and after the damage, the main goal of the instrumentation was to measure the dynamic behavior of the sensor during the high-velocity impact. A four-point probe measurement was performed to monitor the voltage signal (in the y-direction) of the printed device on an oscilloscope using a triggering system from the gas gun chamber. All the instrumentations for electrical measurements were connected to the sensor through BNC feedthroughs as shown in Figure 7.5(b).

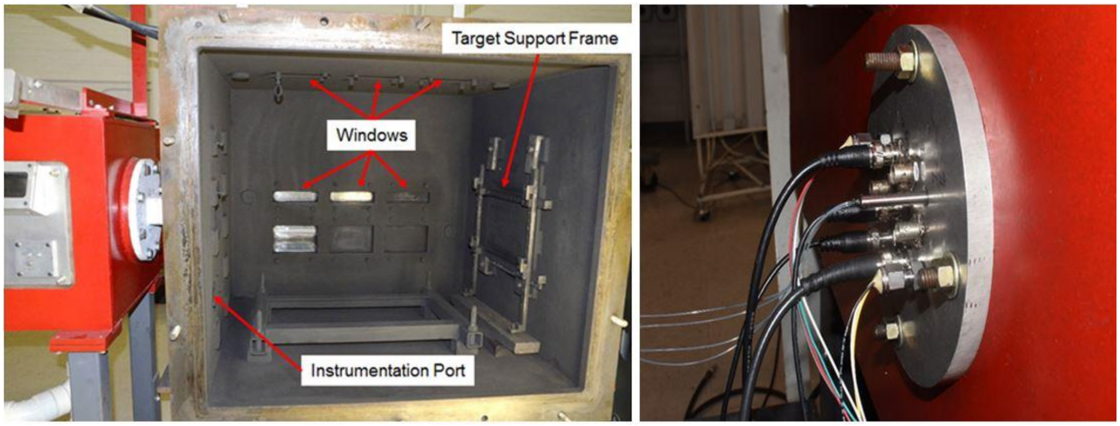

Figure 7.5 (Left) Gas gun chamber range 4 and (Right) BNC feedthroughs for instrumentation during impact test.

7.2. Results and Discussion

Functional inkjet-printed devices are composed of a substrate, usually an insulator and the deposited conductive fillers from the functional ink. The insulating substrate is transformed into a conductive material following the percolation process (Kirkpatrick, 1973). When conductive CNT ink is printed on the substrate, the solvent evaporates, leaving a random network of dry CNTs (R. P. Tortorich, 2014). Percolated paths made of high number of CNTs are needed on the substrate to obtain a conductive material for electronics and sensing applications as discussed in numerical models (Gbaguidi et al., 2018b, 2019b). The percolation threshold is the minimum amount of CNT needed to transition the substrate from and insulator to a conductor.

In the case of inkjet printing a few printed layers are needed to achieve percolation. It was observed that agglomeration leads to high percolation threshold values with reduced electrical conductivity and piezoresistivity (Blanchet et al., 2003; Gbaguidi et al., 2019b; Jing Li, Ma, et al., 2007; Ramasubramaniam et al., 2003; Y. S. Song & Youn, 2005). Hence it is necessary to reduce the extent of agglomeration in the fabricated CNT ink. In the present ink's fabrication procedure, a longer sonication time was used to reduce the size and number of the agglomerates. In addition, the lower centrifugation speed helps retain the small agglomerates in the final ink, leading to a solution of higher CNT concentration. This combination of processing steps was shown to produce nanocomposites with improved electrical properties (Jing Li, Ma, et al., 2007; Socher et al., 2012). The present ink formulation similarly results in a more conductive material with a lower percolation threshold as shown in Figure 7.7.

Even though paper is one of the most used substrates in the literature of inkjet-printed devices (da Costa et al., 2015; Kwon et al., 2013), aerospace grade Kapton is more attractive for space applications because of its good outgassing properties. Good outgassing properties are required to qualify materials for their suitability for space applications (Secretariat, 2008). Poly(pyromellitic dianhydride-oxydianiline), commercialized by DuPont under the name Kapton is made of polyimide polymer and, contains a slip additive based on calcium phosphate, dibasic in the case of Kapton FPC. Kapton is a flexible substrate and has a high elongation before failure, coupled with good mechanical properties at elevated temperatures which makes it a highly desirable material for sensing applications. However, Kapton features inert and highly hydrophobic surfaces, which prevent the deposition of water-based inks.

Water-based inks are desirable because they are non-corrosive, environmentally friendly, easy and safe to store, handle and discard. Several surface modification techniques have been used in literature to improve the wettability of Kapton films (Fang et al., 2016; Guo, Dai, Gong, Qu, & Helseth, 2015; X. D. Huang et al., 2003; Inagaki, Tasaka, & Hibi, 1992). For example, immersing a Kapton film into an aqueous solution of KOH, leads to the modification of a thin layer of the polyamide film into polyamate. The depth of the polyamate layer increases up to a maximum value with increasing immersion time. The polyamate thin layer on top of the unmodified polyimide leads to better wettability properties (X. D. Huang et al., 2003). However, the immersion time should be carefully chosen to avoid excessive etching of the film, since it leads to the degradation of the film properties. The present surface modification procedure was successfully able to improve the wettability of Kapton FPC with limited etching. This resulted in good electrical and sensing performance of the printed Kapton sensors as shown in the following section.

7.2.1. Morphology and Electrical Conductivity of the Printed Carbon Nanotube Network

From previous work on CNT inkjet-printed composites, the electrical resistance of an ink layer deposited onto a substrate in a single print is usually too high for electronic applications due to the inhomogeneous CNT network in the printed material (Kwon et al., 2013; Michelis et al., 2015). Thus the printed material is usually printed in the same position on the substrate as many times as needed, using the overwriting method (da

Costa et al., 2015; Kwon et al., 2013; Lesch et al., 2014). This leads to a conductive material with a homogeneous and densely packed CNT network. To investigate the morphology of the printed MWCNT, SEM images of the ink printed on paper and Kapton with different number of deposited layers are examined in Figure 7.6.

With a single deposited layer on paper, Figure 7.6(a) shows that a decent number of closely packed CNTs are printed; which indicates that a well-concentrated ink with well-dispersed fillers is obtained through the present ink formulation. However, the non-uniformity/homogeneity of the print, revealed by the presence of areas of the substrate not covered by CNTs shows the necessity of more deposited layers to have uniform and conductive printed materials. The homogeneity of the printed materials is seen to improve when the number of deposited layers is increased, leading to full coverage of the paper surface by the CNTs. Figure 7.6(b) shows that with only four printed layers, the paper substrate is fully covered with very uniform, homogenous and dense deposition of CNTs. In the case of Kapton’s surface, the same improvement of the homogeneity of the printed material is observed with the increase of the number of deposited layers. However, a better coverage of the entire surface is observed with a single printed layer, compared to paper substrate.

Figure 7.7 presents the sheet resistance of the printed CNT on paper as a function of the number of deposited layers. The sheet resistance is extremely high for 1 to 2 printed layers. A decrease in resistivity is observed with the deposition of each additional layer due to the improvement in the uniformity of conductive materials. It decreases rapidly until the 16 printed layers and then decreases slowly until it reaches a minimum of 500 Ω/sq with 34 layers.

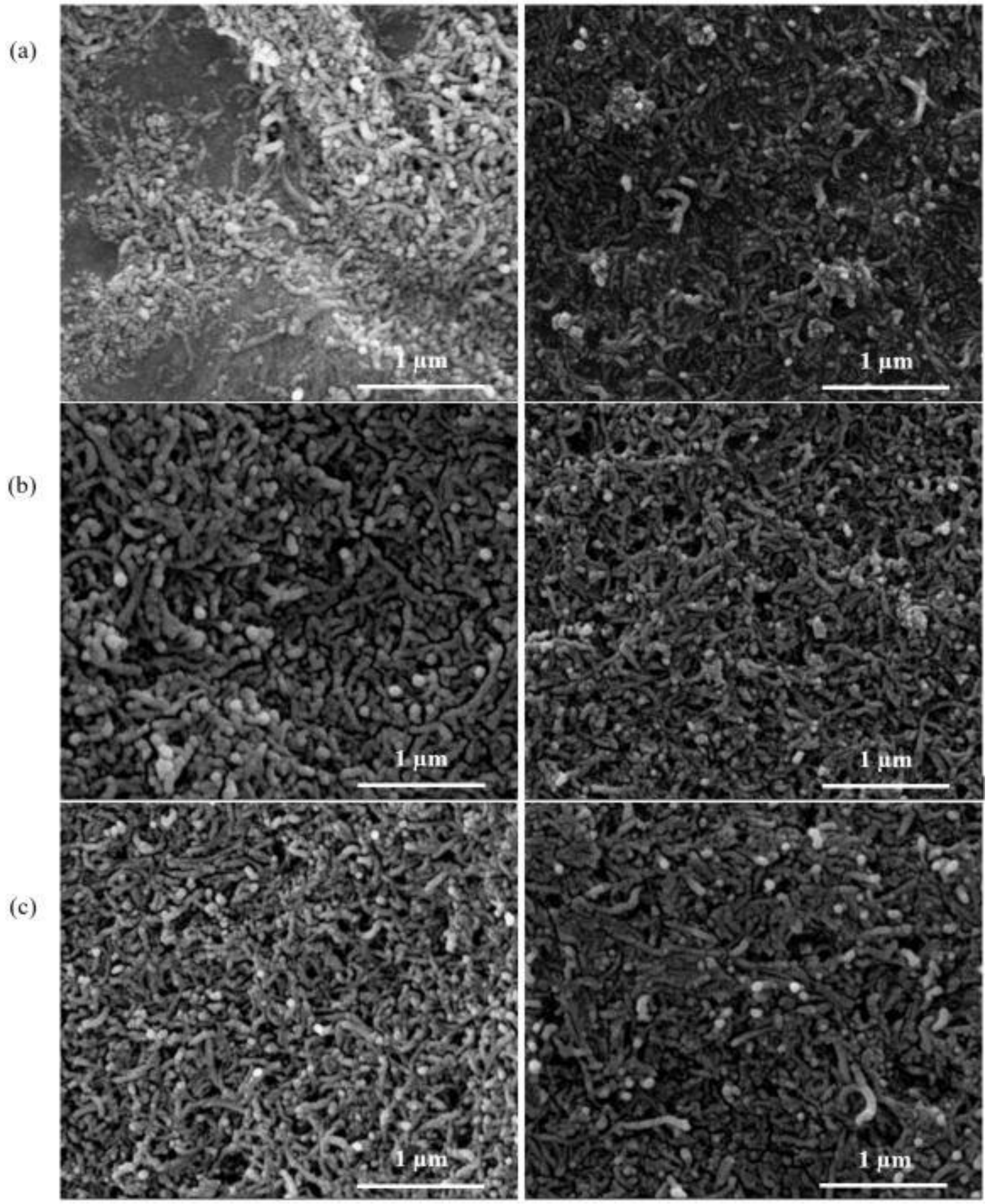

Figure 7.6 SEM images of CNT ink printed on paper (left) and Kapton (right) with (a) one, (b) four and (c) ten deposited layers.

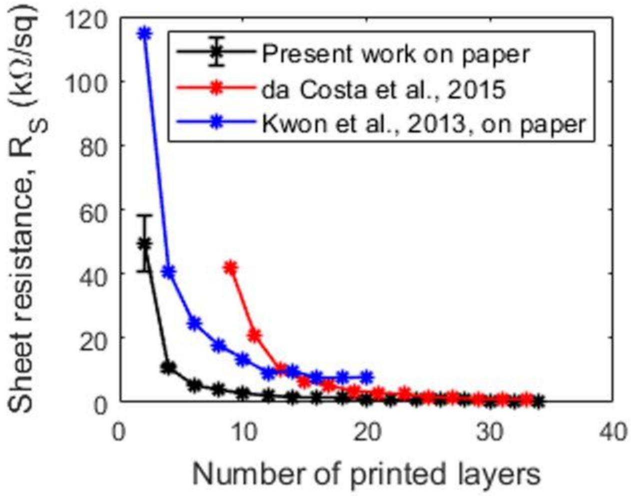

Figure 7.7 Sheet resistance (R_Y) of printed CNT ink on paper with respect to the number of deposited layers. Comparison with previous works in literature, for a paper substrate.

The ink formulation used in this work is obtained by modifying the work in (da Costa et al., 2015) in order to obtain a more conductive material. A comparison of the sheet resistance of both inks, which have the same initial content of CNT, printed on paper shows that the modification added to the formulation leads to a more conductive ink. The longer sonication time in this work, with the addition of stirring steps, leads to a more homogeneous ink with better dispersion and fewer agglomerates. Combined with a much lower centrifugation speed, a supernatant with higher CNT concentration is obtained as the final ink. Figure 7.7 shows that the printed ink in this work reached electrical percolation with 2 printed layers compared to 10 layers for the previous authors. In addition, the conductivity of the present ink is generally greater than the one in (da Costa et al., 2015). Current work is also compared to the work of Kwon (Kwon et al., 2013). A lower content of CNT (1g/200ml) was used and the ink was printed on both paper and glossy-finished photo paper. The sheet resistance values shown here are the ones on paper which were ten times higher than the ones on photo paper. The better surface finish of the photo paper due to the coated resin layer was linked to the improvement in conductance.

7.2.2. Strain sensors Performance

CNT nanocomposites are known to be sensitive to mechanical strain due to the tunneling mechanism in their microstructures. Sensing devices of 3.5 in by 0.5 in were printed on Kapton and their performance under longitudinal tensile strains was examined. Four devices with 2, 10, 20 and 25 printed layers were fabricated. The electrical resistance, R_Y was monitored while tensile strain up to 8% was induced. The strain was obtained using $\varepsilon = (L-L_0)/L_0$, where L_0 and L are respectively the un-deformed length and the length during deformation of the devices, between the grips. Figure 7.8(a) shows the average initial resistance of the sensing device, which decreases with the increasing number of printed layers. The variation in the resistance values of the devices with the same number of printed layers is higher when the number of printed layers is smaller.

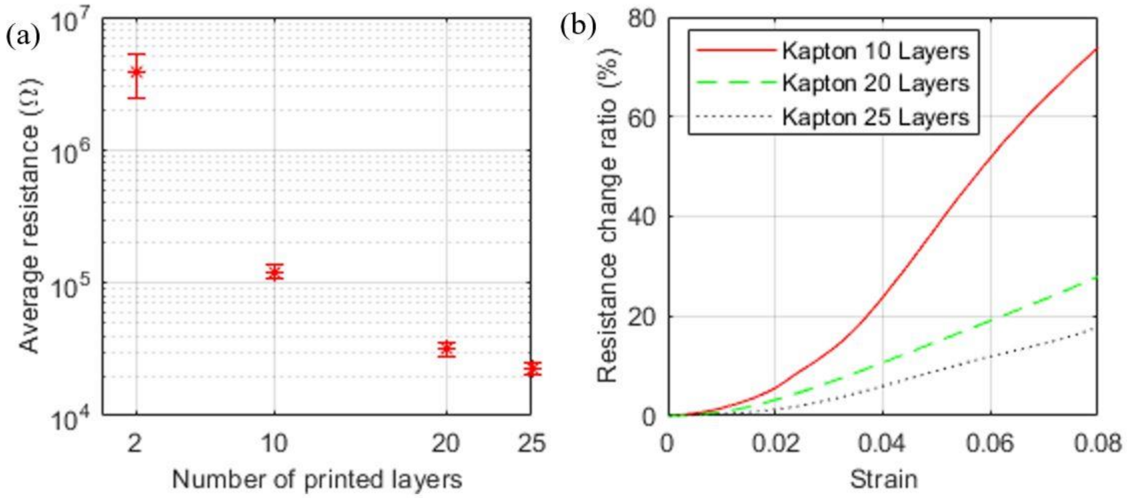

Figure 7.8 Effect of the number of printed layers on (a) average resistance of unstrained sensors and (b) sensitivity to tensile strain. Sensors printed on Kapton.

Due to the high resistance value of the devices with 2 printed layers, inducing strains leads to the increase of the resistance to values above the limit of the digital multimeter used in this work. Hence only devices with 10, 20 and 25 layers are tested for their strain sensing behavior as shown in Figure 7.8(b). The resistance of the three types of sensors increases nonlinearly due to the applied strain. Increasing the number of printed layers leads to a decrease of the strain sensing performance of the devices. In addition, Figure 7.9 shows that the gage factor of each of the devices, varies nonlinearly, unlike strain gages which have a constant gage factor.

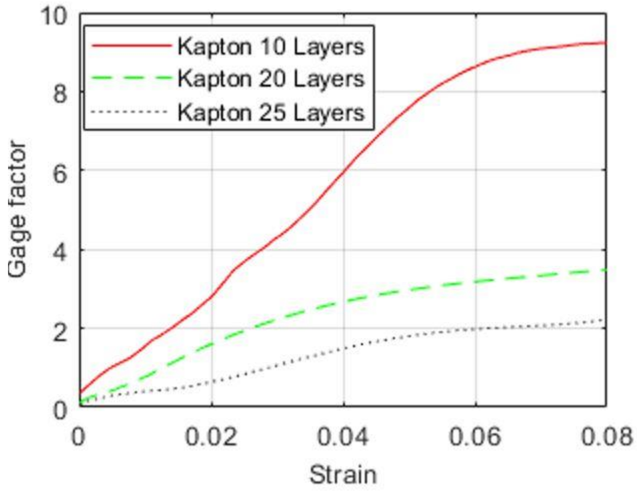

Figure 7.9 Gage factor of strain sensors with different printed layers on Kapton.

This nonlinearity is explained in numerical simulations by the nonlinear (exponential) relationship in Equation 4.5 between the tunneling resistance and the tunneling distance between adjacent CNTs (B. Hu et al., 2012). Hence several experimental works observed nonlinear gage factor in the nanocomposites (Gbaguidi, Anees, et al., 2017; N. Hu et al., 2010; N. Hu, Karube, et al., 2008; J. Hwang et al., 2011). It is however possible to calibrate the gage factor vs strain plot into an approximate linear form with a log-log plot (N. Hu, Karube, et al., 2008). In Figure 7.9 the gage factor increases rapidly as the strain increases to about 6% and asymptotically reached its maximum around 8% strain.

7.2.3. Damage Sensors Performance Under Static Damage Holes

From the literature on CNT nanocomposites, the conductivity or the resistance of the devices vary due to mechanical strain, temperature or some chemical solutions (J. Kong et al., 2000; Rochefort et al., 1998; Zettl, 2000). In this section, the resistance is shown to also vary due to damages and the use of the devices for damage sensing is demonstrated. Compared to lager particles, the probability of MMOD impact is higher for particles of size between 0.01 mm to 10 mm, due to their high flux (E. Christiansen et al., 2009). Hence, 3 mm holes were chosen to represent average damage size in the static testing. Eight 3 mm holes are consecutively added to each sensor, while the resistance is measured in x and y directions (four holes for each measurement's direction).

7.2.3.1. Effect of the Number of Deposited Layers and Damage Holes on the Electrical Resistance of Printed Sensors

Damage sensors of size 2 in by 2 in were printed on Kapton and a 3 mm hole was added every 2 minutes to the sensor area, except on the copper electrodes using a power drill. Since the devices are sensitive to strain, deformation in the device was prevented by applying Kapton tape all over it, to keep it flat during the application of holes. Three types of damage sensors, with 2, 10 and 20 layers were fabricated. The resistance signal of the sensors was measured in the x-direction, R_X and then in the y-direction, R_Y. Figure 7.10(a) shows the resistance signal (R_Y) of the three types of damage sensors as the damages are added.

The resistance of each of all three types of devices is sensitive to the damage with a clear increase of the resistance with each addition of hole. Also, the resistance change value induced by the damage varies for each hole for the same device. For example, a resistance change variation from 7 % to 22% is observed for damage holes of the same size on the device with 2 layers. Finally, the resistance signal of the three types of sensors is fairly stable before and after any damage, proving their effectiveness to be used as damage sensors. Figure 7.10(b) shows the average resistance (R_Y) change of each of the three types of devices with the corresponding standard error, over five specimens per device type. Increasing the number of printed layers leads to devices less sensitive to damage holes, but with smaller standard errors. Hence the devices with microstructure closer to electrical percolation (in this case 2 layers) have the highest resistance change due to damage.

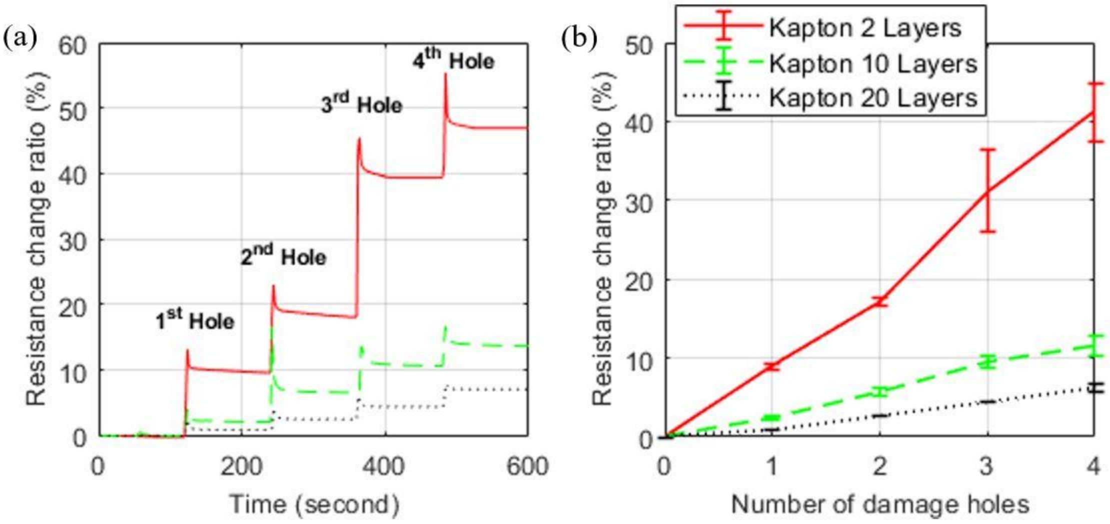

Figure 7.10 Sensitivity in the y-direction of damage sensors on Kapton to the number of printed CNT layers with the addition of four 3 mm holes. (a) Resistance (R_Y) change ratio to time. (b) Resistance (R_Y) change ratio to each damage hole, with standard error bars.

7.2.3.2. Effect of Resistance Measurement's Direction on the Electrical Performance of Printed Sensors

As explained in Section 7.1.5, the deposition of ink on substrates happens in two directions. First, the cartridge, controlled by the step motor, deposits the ink as a line of serially well-connected drops in the y-direction. Then a feeding of the paper in the x-direction, controlled by the rollers moves the paper a little forward and allows the cartridge to deposit another line of well-connected drops in the y-direction until the needed area is fully covered. In this section, to understand the effect of this bi-directional motion of the printer on the sensor performance, the difference of the resistance measurement, in the x (R_X) and y (R_Y) directions was examined. Figure 7.11(a) shows the average electrical resistance of the devices fabricated in function of the number of printed layers and the direction of resistance measurement. The resistances of the devices in both directions (R_X and R_Y) decrease when the number of printed layers increases. This makes sense since the conductivity of the material increases with more content of CNT. Also, the standard error of the resistance values within the same device type (same number of printed layers) is higher when the number of printed layers is smaller. Besides, for each type of device, irrespective of the number of printed layers, the resistance R_X is always higher than the resistance R_Y.

Figure 7.11(b) shows that in general, the resistance sensitivity (denoted sensitivity in the rest of the paper) of the devices due to damage increases with a decrease of the number of printed layers, for both resistances R_X and R_Y. However, the standard error of the resistance change values due to the randomness of the location of the damage holes and the variability between samples is higher with a smaller number of printed layers.

Note that four 3 mm holes are introduced for the resistance measurement in each direction, with a total of eight holes per sensor. Moreover, the resistance sensitivity of the devices is higher with R_Y than with R_X. Kwon studied the fixation of ink drops on paper substrates using an inkjet printer (Kwon et al., 2013). Using a transmission optical microscope, they show that the ink drops serially connected in the y-direction overlap each other perfectly to form a continuous path (line) of conductive material. However, micrometer gaps (less than 10 µm) in the x-direction exist between two consecutive lines of ink drops in the y-directions.

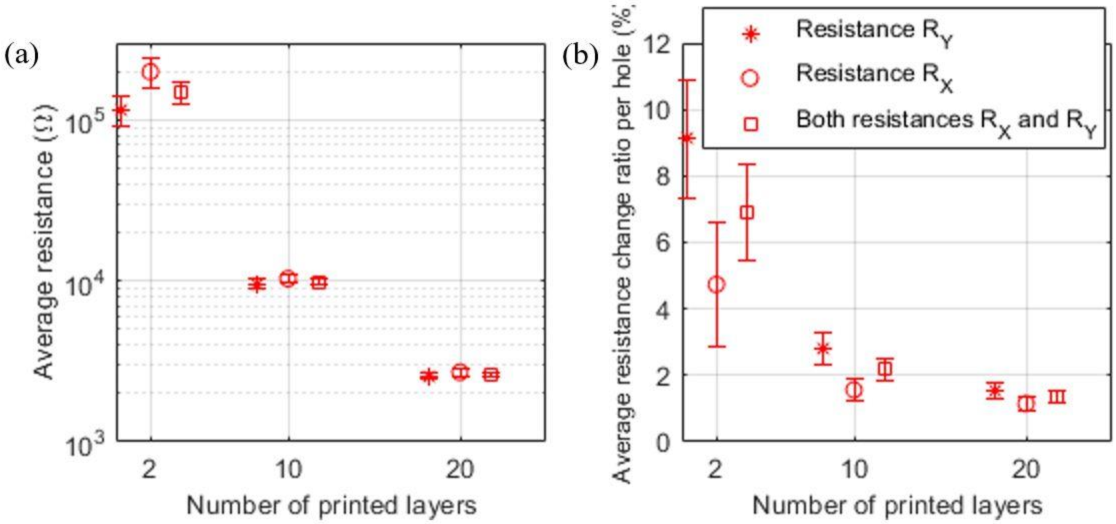

Figure 7.11 Effect of the number of printed layers and resistance measurement direction onto (a) the resistance of undamaged sensors and (b) the sensitivity of damage sensors to four 3 mm holes, with standard error bars. Sensors with 2, 10 and 20 layers on Kapton.

This is because the digital motion of the cartridge in the y-direction, controlled electronically by a step motor is much precise than the motion in the x-direction of the substrate, controlled by mechanical friction between the substrate and the rollers. Also due to the overwriting process, any tilt or wear of the substrate due to its feeding inside the rollers will lead to a much lower resolution of the printing in the x-direction. This difference in print resolution and continuity of ink drops in the x and y directions explains the lower values of R_Y resistance of the devices and better sensitivity of the R_Y resistance to damage holes compared to R_X resistance measurements. The ease of formation of a percolated path in the y-direction between the electrodes is directly linked to the fixation of ink drop on the substrates and dictates the improvement of the electrical and sensing performance of the devices in that direction.

Figure 7.11(a) and (b) also shows that the difference in the resistance and sensitivity measurements between R_X and R_Y directions decreases drastically from two printed layers to 10 printed layers and then decreases more slowly with 20 printed layers. This is explained by the overwriting process where the addition of more ink drops and the irregular motion of the substrate through the rollers reduce the gaps in the x-direction between the ink drop lines. After 10 printed layers a homogenous material of high print resolution with reinforced inter-connections between ink drops is formed (Kwon et al., 2013). Hence, inkjet-printed devices should be carefully designed so that the electrodes are placed in the optimum direction depending on the type of printer used. Advanced inkjet printers incorporate printheads that can move anywhere in the x-y plane, where the print quality can be optimized in terms of velocity of printing, the temperature of the substrate and the volume of an ejected ink drop. Thus devices with improved resolution, homogeneity and electrical performance in both x and y directions can be obtained.

7.2.3.3. Effect of Type of Substrate on the Electrical Performance of Printed Sensors

To examine the influence of the substrate on the inkjet-printed device performance, damage sensors were also printed on paper, since it is one of the most used substrates in the literature of inkjet-printed devices (da Costa et al., 2015; Kwon et al., 2013). The same procedure as for the Kapton device was followed for fabrication, characterization, and testing. Figure 7.12 shows how the resistance and the sensitivity to damage of the paper devices vary with respect to the resistance measurement direction and the number of printed layers. The effect of resistance measurement direction and number of layers is the same for both the paper and Kapton devices. However, the variation of the resistance values within the same device type is very small compared to Kapton devices. When the Kapton and paper devices with the same number of printed layers are compared, the resistance of the device on paper, with 2 layers is 10 times higher, while its resistance change to damage is lower. However, with 10 layers (and also 20 layers), both the resistance and the resistance change to hole values are very similar when the devices on the two substrates are compared. Kwon et al. (2013) reported a sheet resistance ten times lower on photo paper substrate compared to a paper substrate for their inkjet printed CNT materials. This was explained by the difference in surface roughness and finish between the two substrates.

While the ink should percolate into the empty spaces between the cellulose fibers in the paper substrates, it only has to penetrate the resin layer on the photo paper which leads to a better homogeneity of the printed material. The same can be said with the Kapton substrate where a more homogeneous finish is obtained after the surface treatment and allows for uniform deposition of the ink. Figure 7.7(a) shows that after one deposited ink layer, the paper substrate was not entirely covered. However, a more uniform spread of the ink on Kapton surface was observed for the same number of ink layers. Printed devices on substrates with a better finish is then necessary for high conductive materials and sensors with high electrical performance.

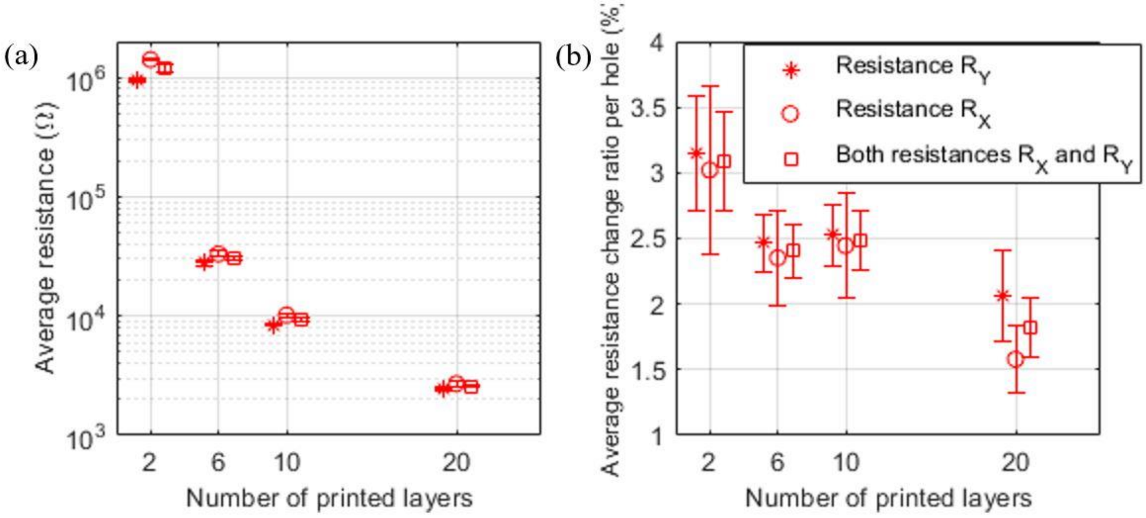

Figure 7.12 Effect of the number of printed layers and resistance measurement direction onto (a) the resistance of undamaged sensors and (b) the sensitivity of damage sensors to four 3 mm hole, with standard error bars. Sensors with 2, 6, 10 and 20 layers on paper.

7.2.4. High Impact Velocity Damage Sensing

During the characterization of the sensors under static damage holes in the previous section, the devices were very sensitive to 3 mm impact holes with a clear and consistent increase in their resistance for every damage. However, to be used for MMOD impact damage, which can happen at velocities up to 15 km/s or 70 km/s depending on the debris type, the sensors should be tested under high-velocity impact. The high flux of the debris usually leads to damage much bigger than the debris size. In this section, a four-layer test article consisting of three sensors layers and one structural layer was used. Each of the three sensor layers was composed of sensors attached to thin fiberglass fabric, which were held along their perimeters between two aluminum frames. The four layers were placed two inches apart but held together by four all-thread rods through the corners of the frames. Only the first layer of the frame consisting of one damage sensor with 2 printed CNT ink layers on Kapton is examined in this work.

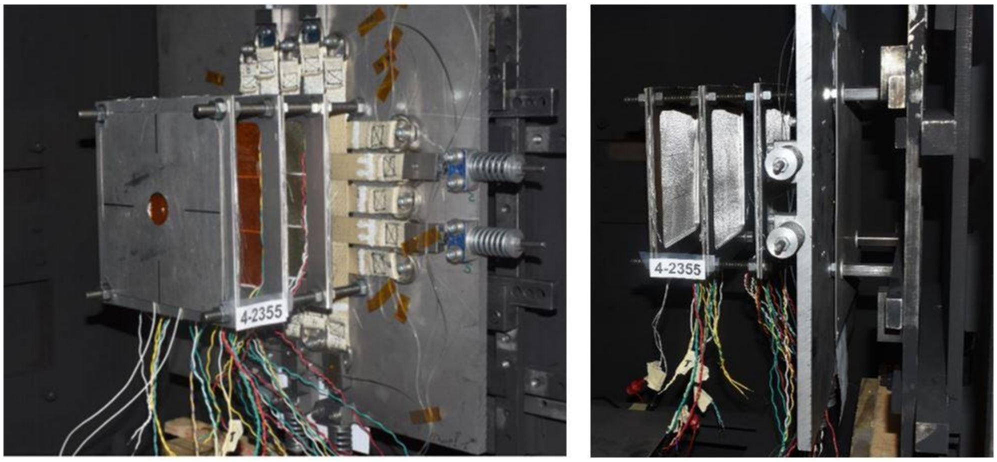

Figure 7.13 Four-layer test article mounted in the gas chamber. Damage sensor with 2 printed layer on Kapton attached on the first layer.

Figure 7.13 shows the top and side views of the four-layer test article. For the hypervelocity test, a 3/16 inch (4.760 mm) 2017-T4 aluminum spherical projectile of mass 0.1583 g was fired at 6.88 km/s to hit the test article. All three layers of the test article were penetrated. A damage of size 6.07 mm was observed on the damage sensor on the first layer. Figure 7.14 shows the damage induced to the printed sensor. Despite the high velocity of the impact, the integrity of the sensor and of the fabric layer was not compromised. During the impact, an oscilloscope triggered by the gas gun was used to record 500 milliseconds of the voltage signal of the damage sensor to see the sensor behavior right at the time of impact. Figure 7.15 shows the resistance signal R_Y of the sensor during the hypervelocity impact.

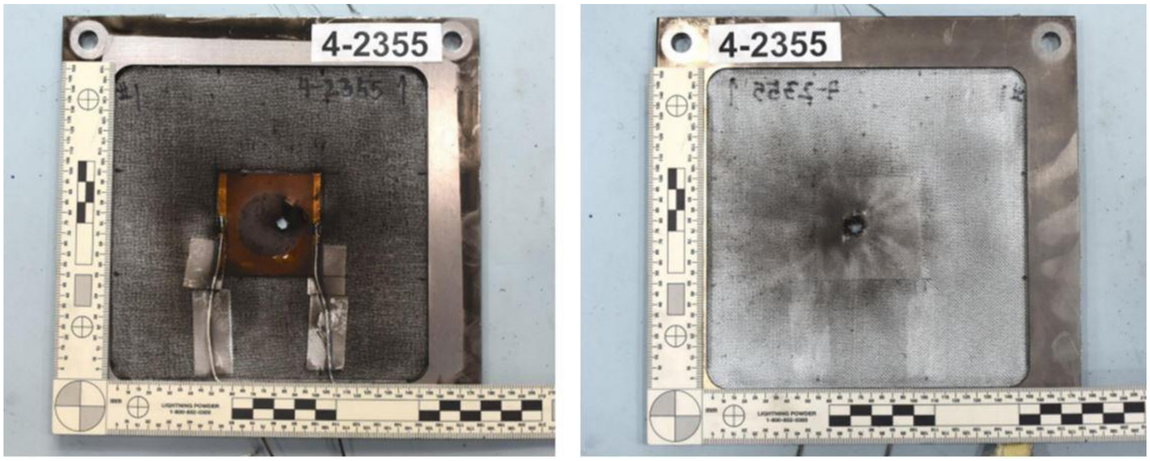

Figure 7.14 Hypervelocity impact damage on the damage sensor with 2 printed layers on Kapton. (a) Front side and (b) backside.

Unlike the static impact damage testing, where the sensor was held flat with tape to limit induced mechanical strain, in the hypervelocity test, the sensor layer (fiberglass + sensor) experience both elastic (mechanical strain) and permanent (hole) damage. That is shown in Figure 7.15 where a sudden increase in the resistance is seen, followed by fluctuations in the resistance reading due to the induced strain on the sensor substrate. As examined in Section 7.2.2, the printed sensors are also very sensitive to mechanical strain. For comparison, the maximum value of resistance change observed in the static damage testing, with the peak value included is about 26%, while in the hypervelocity case a resistance increase of up to 150% is observed. This is due not only to the bigger size of damage in the hypervelocity test (6 mm against 3 mm for static impact) but also to the strain induced to the sensor layer during impact.

The resistance is then seen to start decreasing 200 milliseconds after the impact once the layer is unstrained and would most likely reach a steady-state higher that the initial unstrained resistance value of the sensor but lower than the resistance value at the signal peak. That steady-state value as shown in Figure 7.10(a) represents the change in resistance due to the permanent damage hole. Both the strain sensitivity as well as hole sensitivity of the printed CNT nanocomposites as examined in Sections 7.2.2 and 7.2.3 are important to understand the performance of the sensor under MMOD impact damage.

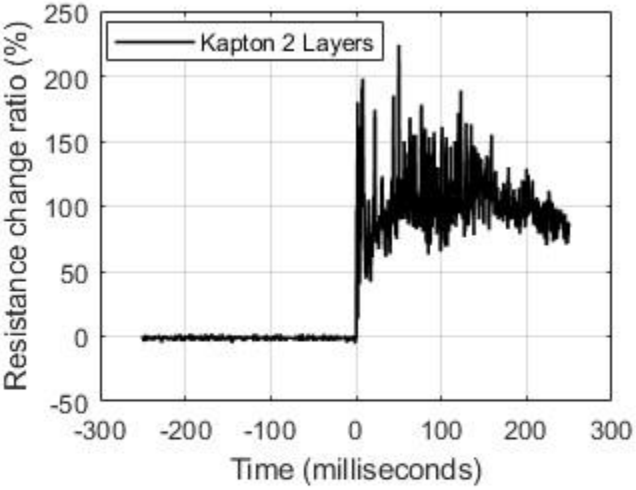

Figure 7.15 Resistance change ratio (R_Y) of the damage sensor during the hypervelocity impact test.

7.3. Summary

A well dispersed and conductive MWCNT water-based ink was formulated and used to print conductive materials on both paper and Kapton substrates. SEM images showed that a very homogeneous, uniform and conductive material was deposited on the substrates only after four printed layers. A minimum sheet resistance of respectively 3 kΩ/sq and 500 Ω/sq was obtained with 10 and 34 layers printed on paper. The author demonstrated the applicability of the printed device as strain and damage sensors. Devices with less printed layers and close to percolation lead to sensors with improved electrical performance. The author showed that due to the restrictions on the printer, mainly the difference in the printing precision and resolution in the two in-plane directions, the direction of the electrical resistance measurement affects the resistance and sensing performance of the sensors. Also, the author showed that the type of substrate used for the devices also affects the conductivity and sensitivity to strain and damage. A substrate with a better finish through optimum surface treatment or a coating layer leads to a device with improved electrical performance. The inkjet-printed sensors were finally used to detect MMOD impact damage under hypervelocity impact using their sensitivity to both elastic strain and permanent damage.

8. Conclusions and Future Work

8.1. Conclusions

In this dissertation, the author developed an experimental and numerical framework to study CNT and GNP monofiller nanocomposites and their hybrid nanocomposites. A review of the fabrication methods, behavior, performance, and applications of nanocomposites made of the two fillers is first performed. Several applications of the nanocomposites were considered to examine their effectiveness as multifunctional sensors. The outcome of the dissertation is discussed below.

A two-dimensional percolation based numerical model was developed to study nanocomposites made of both CNT and GNP fillers. The tunneling effect between the fillers was modeled as the main mechanism of electrical percolation and conductivity. This model considered for the first time, the effect of the addition of GNP on the piezoresistivity behavior of hybrid nanocomposites. The author found that the addition of GNP particles to CNT nanocomposites enhanced significantly the electrical conductivity and piezoresistive behavior of the nanocomposites. Furthermore, the author showed that higher GNP loading and the increase of the size and aspect ratio of the GNP particles led to an improvement of the percolation threshold, of the electrical conductivity and the piezoresistivity of the hybrid nanocomposites. The author showed that the alignment of the GNP particles had a big effect on both the piezoresistivity and the electrical conductivity of the hybrid nanocomposites. GNPs uniformly aligned in the direction of electrical conductivity measurements (or in a direction close to that) led to a significantly higher piezoresistive behavior, up to 6 times greater than that of nanocomposites based on only CNT. The present results were discussed and validated against experimental observations of thin film nanocomposites.

A new agglomeration model, using the two-dimensional model was developed to quantify the effect of CNT agglomeration on the electrical behavior of the hybrid nanocomposites. One of the new findings in the present results was that the agglomerate morphology (equiaxed vs rope-like) had an important effect on the electrical and piezoresistive properties of both CNT monofiller and CNT-GNP hybrid nanocomposites. The author found that in general, the percolation threshold and piezoresistivity are respectively higher and lower for rope-like agglomerates compared to equiaxed agglomerates. The present results match experimental observations, which showed that high agglomeration level was detrimental to the electrical percolation threshold and conductivity as well as the piezoresistivity of the nanocomposites, for all the different agglomerate morphologies. However, the author found that small levels of agglomeration enhanced the aforementioned properties, especially when the CNT density within the agglomerates was low. The author also showed that while the addition of more CNTs, after percolation reduced the piezoresistivity of CNT nanocomposites with or without agglomeration, the addition of GNPs instead, led to higher piezoresistivity. This implied that the negative effect of high agglomeration level on the conductivity and piezoresistivity of CNT nanocomposites could be counterbalanced by the addition of GNP. Finally, the author identified the microstructures that achieved the optimal agglomeration level for improved electrical and piezoresistive behaviors.

The author developed a three-dimensional Monte Carlo model to understand the mechanisms and microstructural features that control the electrical behavior of hybrid nanocomposites filled with CNT and GNP and potentially lead to a synergistic effect.

Unlike the two-dimensional model, this model allowed for the substitution of GNP fillers with CNT fillers and vice versa. The primary conclusions of the study were as follows: (a) Increasing either the planar or transversal aspect ratio of the GNP filler led to the improvement of both percolation threshold and electrical conductivity of all the hybrid composites. (b) When the percolation threshold of the GNP fillers in its monofiller composite was within 20% of the percolation threshold of the CNT fillers in its monofiller composite, the hybrid composites made of those two specific fillers achieved synergistic improvement in electrical properties. The present model suggested an improvement in electrical conductivity as high as 800% in hybrid nanocomposites due to the synergy achieved using the above combination of fillers. (c) A review of past experimental data matched the present numerical results and confirmed the correlation between the closeness of the percolation threshold values of the two monofiller nanocomposites and the synergy effect in the corresponding hybrid. (d) The author found that a key microstructural parameter that controlled the electrical performance of the hybrid composites was the number of tunneling junctions per filler, in the percolated network. Improvement or synergy of that parameter led to an improvement or synergy in percolation threshold and electrical conductivity in the hybrid nanocomposites.

The author used a resin infiltration technique to fabricate hybrid nanocomposites made of CNT buckypaper and GNP platelets. The electromechanical behavior of CNT sheet-Graphite platelet hybrid nanocomposites under static and dynamic loading conditions was examined. Also, dynamic mechanical analysis of the nanocomposites specimen was performed to characterize the thermal and dynamic behavior of the nanocomposites. The present results indicated that these hybrid nanocomposites exhibit a distinct piezoresistive response under a wide range of dynamic loading conditions. The changes in piezoresistive behavior at low frequencies were correlated to the changes in elastic behavior observed in the DMA testing. Next, the hybrid nanocomposites, in addition to monofiller nanocomposites made of CNT buckypaper were used as damage sensors to detect damage holes. Static and low-velocity impact damages were introduced to the sensors. Both sensors were able to detect the existence and location of the damage holes, through the sudden increase in the electrical resistance. The author showed that the hybrid nanocomposite sensors were more sensitive to damage holes than the CNT nanocomposite ones.

The author developed a fabrication framework based on inkjet printing technique, substrate surface modification and conductive ink fabrication to design low-cost and very performant CNT printed devices. A well dispersed and conductive MWCNT water-based ink was formulated and used to print conductive materials on both paper and Kapton substrates. A very homogeneous, uniform and conductive material was deposited on the substrates only after four printed layers, from SEM observations. Sheet resistance as low as 500 Ω/sq was obtained on paper. Surface treatment of the hydrophobic Kapton surface was performed for good resolution of the printed devices. The author demonstrated the applicability of the printed device as strain and damage sensors. Devices with less printed layers and close to percolation lead to sensors with improved electrical performance. The author showed that due to the restrictions on the printer, mainly the difference in the printing precision and resolution in the two in-plane directions, the direction of the electrical resistance measurement affects the resistance and sensing performance of the sensors.

Also, the author showed that the type of substrate used for the devices also affects the conductivity and sensitivity to strain and damage. A substrate with a better finish through optimum surface treatment or a coating layer leads to a device with improved electrical performance. The inkjet-printed sensors were finally used to detect MMOD impact damage under hypervelocity impact using their sensitivity to both elastic strain and permanent damage. A computational framework and an experimental fabrication methodology were developed and validated in this study to evaluate the electrical and piezoresistive properties of monofiller and hybrid polymer nanocomposites with CNT and GNP fillers. While many important features where included in the present numerical models, few additions could be added to make the model more realistic.

8.2. Future Work

A computational framework and an experimental fabrication methodology were developed and validated in this dissertation to evaluate the electrical and piezoresistive properties of monofiller and hybrid polymer nanocomposites with CNT and GNP fillers. While many important features were included in the present numerical model, few additions could be made to make it more realistic. Similarly, an improvement of the inkjet fabrication process with additional testing of printed devices will increase the effectiveness and readiness of the sensors for space applications. Some of those additions would be to:

Incorporate CNT curvature and entanglement. While many important features such as filler's alignment and agglomeration were included in the present numerical models, the control of the CNT curvature will allow a more realistic microstructure's model. An inspection of SEM images of CNT polymer nanocomposites usually features entangled and curved CNTs. This can be modeled by breaking each CNT tube in many consecutive tubes of different orientation. Even though the curvature of the CNTs has been previously shown to affect the electrical properties of the nanocomposites, the computational requirements are much higher than with straight CNTs.

Develop an accurate fillers' reorientation model during mechanical deformation. So far in the literature, to characterize the piezoresistivity of nanocomposites, the analytical fiber reorientation model has mostly been used to update the location and orientation of the fillers after deformation of the composite. This model works well for CNT fillers (1D geometry), despite several assumptions such as a uniform strain field, a perfect interface between polymer matrix and fillers, affine transformation, and incompressibility of the polymer matrix. However, it has several limitations for hardcore particles with 2D or 3D geometry such as GNP. The planar geometry of GNP fillers is not taken into account in the current fiber reorientation model and there is no way to enforce the impenetrability of CNT and GNP fillers during the fillers' reorientation after the polymer deformation. A multiscale framework using the current Monte Carlo model for fillers' generation and electrical properties calculation, coupled with a realistic FEM model for the reorientation of the fillers during the mechanical deformation of the nanocomposites can be developed. This will help for an accurate analysis of the piezoresistivity of monofiller GNP and hybrid CNT-GNP nanocomposites.

Understand the wetting process of inks on polymer substrates using atomistic models. While the filler's content and dispersion state of the ink are important parameters affecting the inkjet-printed sensor's properties, the author showed in this work that the type of substrate through the wetting process also dictates the electrical properties of the printed devices. A molecular dynamics model could help understand how different parameters related to the ink fabrication and the surface finish and surface modification of the substrate affect the contact angle of the droplets of ink on the substrate.

Develop a hybrid ink with CNT and GNP fillers for fully inkjet-printed devices. Hybrid polymer nanocomposites made of CNT and GNP have been fabricated using various processes. However, to the author's knowledge, it has never been done using inkjet printing technology, so far. Challenges such as, finding the right solvent with low contact angle for both fillers, for their exfoliation in an hybrid ink, or using monofiller inks for CNT and GNP into separate cartridges for effective printing of hybrid devices need to be solved. Also, an inkjet printing framework for the fabrication of fully printed devices is still challenging due to the need for copper foil as electrodes to allow soldering. Using the multi-cartridge option of most inkjet printers with a solder-able silver or copper inks, the devices' electrodes could also potentially be printed to obtain fully inkjet-printed nanocomposites.

Investigate the microstructure - electrical properties dependence of hybrid printed nanocomposites in comparison to the present numerical model results. The author has shown in this work that the different steps of inkjet printing technique and ink fabrication affect the nanocomposites' microstructure morphology such as agglomeration, filler aspect ratios, and filler content. It is then important to study how those fabrication steps control the electrical properties of hybrid inkjet-printed nanocomposites. With the help of SEM images and the present numerical simulations, an experimental framework for the fabrication of hybrid printed devices with optimum sensing performance can be obtained.

Perform more comprehensive hypervelocity testing on the inkjet-printed devices for space applications. Even though static and hypervelocity impact tests were performed in this dissertation, additional testing is necessary to fully qualify the printed devices for space application. Testing of arrays/grids of the sensors inserted as layers through the thickness of the structures will be useful. Also, degassing testing of the printed sensors will help make sure that they are space compliant.

REFERENCES

Abad, S. N. K., Ganjeh, E., Zolriasatein, A., Shabani-Nia, F., & Siadati, M. H. (2017). Predicting carbon nanotube diameter using artificial neural network along with characterization and field emission measurement. *Iranian Journal of Science and Technology, Transaction A: Science*, *41*(1), 151–163. https://doi.org/10.1007/s40995-017-0198-9

Abdelhalim, A., Abdellah, A., Scarpa, G., & Lugli, P. (2013). Fabrication of carbon nanotube thin films on flexible substrates by spray deposition and transfer printing. *Carbon*, *61*, 72–79. https://doi.org/10.1016/j.carbon.2013.04.069

Abera, A., & Choi, J. W. (2010). Quantitative lateral flow immunosensor using carbon nanotubes as label. *Analytical Methods*, *2*(11), 1819–1822. https://doi.org/10.1039/c0ay00412j

Abulikemu, M., Da'As, E. H., Haverinen, H., Cha, D., Malik, M. A., & Jabbour, G. E. (2014). Insitu synthesis of self-assembled gold nanoparticles on glass or silicon substrates through reactive inkjet printing. *Angewandte Chemie - International Edition*, *53*(2), 420–423. https://doi.org/10.1002/anie.201308429

Acquaviva, D., Arun, A., Esconjauregui, S., Bouvet, D., Robertson, J., Smajda, R., … Ionescu, A. M. (2010). Capacitive nanoelectromechanical switch based on suspended carbon nanotube array. *Applied Physics Letters*, *97*(23), 233508. https://doi.org/10.1063/1.3525165

Aguilar, J. O., Bautista-Quijano, J. R., & Avilés, F. (2010). Influence of carbon nanotube clustering on the electrical conductivity of polymer composite films. *Express Polymer Letters*, *4*(5), 292–299. https://doi.org/10.3144/expresspolymlett.2010.37

Ajayan, P. M., Schadler, L. S., & Braun, P. V. (2003). Nanocomposite science and technology. *Materials Today*, *6*(11), 52. https://doi.org/10.1016/s1369-7021(03)01139-8

Akima, N., Iwasa, Y., Brown, S., Barbour, A. M., Cao, J., Musfeldt, J. L., … Zhou, O. (2006). Strong anisotropy in the far-infrared absorption spectra of stretch-aligned single-walled carbon nanotubes. *Advanced Materials*, *18*(9), 1166–1169. https://doi.org/10.1002/adma.200502505

Akita, S., Nakayama, Y., Mizooka, S., Takano, Y., Okawa, T., Miyatake, Y., … Nosaka, T. (2001). Nanotweezers consisting of carbon nanotubes operating in an atomic force microscope. *Applied Physics Letters*, *79*(11), 1691–1693. https://doi.org/10.1063/1.1403275

Al-Saleh, M. H. (2015). Electrical and mechanical properties of graphene/carbon nanotube hybrid nanocomposites. *Synthetic Metals, 209*, 41–46.

https://doi.org/10.1016/j.synthmet.2015.06.023

Alamusi, Hu, N., Fukunaga, H., Atobe, S., Liu, Y., & Li, J. (2011). Piezoresistive strain sensors made from carbon nanotubes based polymer nanocomposites. *Sensors*, *11*(11), 10691–10723. https://doi.org/10.3390/s111110691

Anand, S. V., & Roy Mahapatra, D. (2009). Quasi-static and dynamic strain sensing using carbon nanotube/epoxy nanocomposite thin films. *Smart Materials and Structures*, *18*(4), 045013. https://doi.org/10.1088/0964-1726/18/4/045013

Andrew Ng, M. H., Hartadi, L. T., Tan, H., & Patrick Poa, C. H. (2008). Efficient coating of transparent and conductive carbon nanotube thin films on plastic substrates. *Nanotechnology*, *19*(20), 205703. https://doi.org/10.1088/0957-4484/19/20/205703

Andrews, R., Jacques, D., Minot, M., & Rantell, T. (2002). Fabrication of carbon multiwall nanotube/polymer composites by shear mixing. *Macromolecular Materials and Engineering*, *287*(6), 395–403. https://doi.org/10.1002/1439-2054(20020601)287:6<395::AID-MAME395>3.0.CO;2-S

Anees, M., Gbaguidi, A., Kim, D., & Namilae, S. (2017, April). Structural health monitoring of inflatable structures for MMOD impacts. In *Nondestructive Characterization and Monitoring of Advanced Materials, Aerospace, and Civil Infrastructure 2017* (Vol. 10169, p. 101690D), Portland, Oregon, United States. https://doi.org/10.1117/12.2260195

Anees, M., Gbaguidi, A., Kim, D., & Namilae, S. (2018, March). Numerical and experimental investigation of matrix effect on sensing behavior of piezoresistive hybrid nanocomposites. In *Sensors and Smart Structures Technologies for Civil, Mechanical, and Aerospace Systems 2018* (Vol. 10598, p. 1059809), Denver, Colorado, United States. https://doi.org/10.1117/12.2296715

ASTM International. (2007). *D257-14 Standard test methods for DC resistance or conductance of insulating materials*. *i*(C), 1–18. https://doi.org/10.1520/D0257-07

ASTM International. (2011). *D4496-24781 Standard test method for D-C resistance or conductance of moderately conductive materials*. *87*(Reapproved 1998), 2–6. https://doi.org/10.1520/D4496-13.2

ASTM International. (2015). *D5418-15 Standard test method for plastics: dynamic mechanical properties: in flexure (dual cantilever beam).* https://doi.org/10.1520/D5418-15

Azoubel, S., Shemesh, S., & Magdassi, S. (2012). Flexible electroluminescent device with inkjet-printed carbon nanotube electrodes. *Nanotechnology*, *23*(34), 344003. https://doi.org/10.1088/0957-4484/23/34/344003

Bae, S. H., Lee, Y., Sharma, B. K., Lee, H. J., Kim, J. H., & Ahn, J. H. (2013). Graphene-based transparent strain sensor. *Carbon, 51*(1), 236–242. https://doi.org/10.1016/j.carbon.2012.08.048

Bahr, J. L., Yang, J., Kosynkin, D. V., Bronikowski, M. J., Smalley, R. E., & Tour, J. M. (2001). Functionalization of carbon nanotubes by electrochemical reduction of aryl diazonium salts: A bucky paper electrode. *Journal of the American Chemical Society*, *123*(27), 6536–6542. https://doi.org/10.1021/ja010462s

Bai, J. B., & Allaoui, A. (2003). Effect of the length and the aggregate size of MWNTs on the improvement efficiency of the mechanical and electrical properties of nanocomposites - Experimental investigation. *Composites Part A: Applied Science and Manufacturing, 34*(8), 689–694. https://doi.org/10.1016/S1359-835X(03)00140-4

Baljon, A. R. C., Lee, J. Y., & Loring, R. F. (1999). Molecular view of polymer flow into a strongly attractive slit. *Journal of Chemical Physics*, *111*(19), 9068–9072. https://doi.org/10.1063/1.480248

Bandaru, P. R. (2007). Electrical properties and applications of carbon nanotube structures. *Journal of Nanoscience and Nanotechnology*, *7*(4–5), 1239–1267. https://doi.org/10.1166/jnn.2007.307

Bao, Q., Tang, D., Zhang, H., & Loh, K. P. (2012). Graphene-polymer composites for pulse lasers. In *Graphite, Graphene, and Their Polymer Nanocomposites* (pp. 283–314), Boca Raton, FL: CRC Press. https://doi.org/10.1201/b13051

Bao, W. S., Meguid, S. A., Zhu, Z. H., Pan, Y., & Weng, G. J. (2012). A novel approach to predict the electrical conductivity of multifunctional nanocomposites. *Mechanics of Materials, 46,* 129–138. https://doi.org/10.1016/j.mechmat.2011.12.006

Bao, W. S., Meguid, S. A., Zhu, Z. H., & Weng, G. J. (2012). Tunneling resistance and its effect on the electrical conductivity of carbon nanotube nanocomposites. *Journal of Applied Physics*, *111*(9), 093726. https://doi.org/10.1063/1.4716010

Barber, A. H., Zhao, Q., Wagner, H. D., & Baillie, C. A. (2004). Characterization of E-glass-polypropylene interfaces using carbon nanotubes as strain sensors. *Composites Science and Technology*, *64*(13–14), 1915–1919. https://doi.org/10.1016/j.compscitech.2004.02.004

Baughman, R. H., Zakhidov, A. A., & De Heer, W. A. (2002). Carbon nanotubes - The route toward applications. *Science, 297*(5582), 787–792. https://doi.org/10.1126/science.1060928

Bauhofer, W., & Kovacs, J. Z. (2009). A review and analysis of electrical percolation in carbon nanotube polymer composites. *Composites Science and Technology*, *69*(10), 1486–1498. https://doi.org/10.1016/j.compscitech.2008.06.018

Bautista-Quijanoa, J. R., Avilésa, F., Aguilara, J. O., & Tapia, A. (2010). Strain sensing capabilities of a piezoresistive MWCNT-polysulfone film. *Sensors and Actuators, A: Physical*, *159*(2), 135–140. https://doi.org/10.1016/j.sna.2010.03.005

Beecher, P., Servati, P., Rozhin, A., Colli, A., Scardaci, V., Pisana, S., … Milne, W. I. (2007). Ink-jet printing of carbon nanotube thin film transistors. *Journal of Applied Physics*, *102*(4), 043710. https://doi.org/10.1063/1.2770835

Behnam, A., Guo, J., & Ural, A. (2007). Effects of nanotube alignment and measurement direction on percolation resistivity in single-walled carbon nanotube films. *Journal of Applied Physics*, *102*(4), 044313. https://doi.org/10.1063/1.2769953

Behnam, A., & Ural, A. (2007). Computational study of geometry-dependent resistivity scaling in single-walled carbon nanotube films. *Physical Review B - Condensed Matter and Materials Physics*, *75*(12), 125432. https://doi.org/10.1103/PhysRevB.75.125432

Benchirouf, A., Sowade, E., Al-Hamry, A., Blaudeck, T., Kanoun, O., & Baumann, R. (2012, March). Investigation of RFID passive strain sensors based on carbon nanotubes using inkjet printing technology. In *International Multi-Conference on Systems, Signals & Devices* (pp. 1–6), Chemnitz, Germany. https://doi.org/10.1109/SSD.2012.6198081

Berger, C., Poncharal, P., Yi, Y., & De Heer, W. (2003). Ballistic conduction in multiwalled carbon nanotubes. *Journal of Nanoscience and Nanotechnology*, *3*(1–2), 171–177. https://doi.org/10.1166/jnn.2003.180

Berhan, L., & Sastry, A. M. (2007). Modeling percolation in high-aspect-ratio fiber systems. I. Soft-core versus hard-core models. *Physical Review E - Statistical, Nonlinear, and Soft Matter Physics*, *75*(4), 041120. https://doi.org/10.1103/PhysRevE.75.041120

Berson, S., De Bettignies, R., Bailly, S., Guillerez, S., & Jousselme, B. (2007). Elaboration of P3HT/CNT/PCBM composites for organic photovoltaic cells. *Advanced Functional Materials*, *17*(16), 3363–3370. https://doi.org/10.1002/adfm.200700438

Bethune, D. S., Klang, C. H., De Vries, M. S., Gorman, G., Savoy, R., Vazquez, J., & Beyers, R. (1993). Cobalt-catalysed growth of carbon nanotubes with single-atomic-layer walls. *Nature*, *363*(6430), 605–607. https://doi.org/10.1038/363605a0

Biswas, S., Fukushima, H., & Drzal, L. T. (2011). Mechanical and electrical property enhancement in exfoliated graphene nanoplatelet/liquid crystalline polymer nanocomposites. *Composites Part A: Applied Science and Manufacturing*, *42*(4), 371–375. https://doi.org/10.1016/j.compositesa.2010.12.006

Blanchet, G. B., Fincher, C. R., & Gao, F. (2003). Polyaniline nanotube composites: A high-resolution printable conductor. *Applied Physics Letters*, *82*(8), 1290–1292. https://doi.org/10.1063/1.1553991

Bolotin, K. I., Sikes, K. J., Jiang, Z., Klima, M., Fudenberg, G., Hone, J., … Stormer, H. L. (2008). Ultrahigh electron mobility in suspended graphene. *Solid State Communications*, *146*(9–10), 351–355. https://doi.org/10.1016/j.ssc.2008.02.024

Bonavolontà, C., Camerlingo, C., Carotenuto, G., De Nicola, S., Longo, A., Meola, C., … Valentino, M. (2016). Characterization of piezoresistive properties of graphene-supported polymer coating for strain sensor applications. *Sensors and Actuators, A: Physical*, *252*, 26–34. https://doi.org/10.1016/j.sna.2016.11.002

Bora, C., Bharali, P., Baglari, S., Dolui, S. K., & Konwar, B. K. (2013). Strong and conductive reduced graphene oxide/polyester resin composite films with improved mechanical strength, thermal stability and its antibacterial activity. *Composites Science and Technology*, *87*, 1–7. https://doi.org/10.1016/j.compscitech.2013.07.025

Brandon, E. J., Vozoff, M., Kolawa, E. A., Studor, G. F., Lyons, F., Keller, M. W., … Champaigne, K. (2011). Structural health management technologies for inflatable/deployable structures: Integrating sensing and self-healing. *Acta Astronautica*, *68*(7–8), 883–903. https://doi.org/10.1016/j.actaastro.2010.08.016

Breuer, O., & Sundararaj, U. (2004). Big returns from small fibers: A review of polymer/carbon nanotube composites. *Polymer Composites*, *25*(6), 630–645. https://doi.org/10.1002/pc.20058

Briggs, B. D., Nagabhirava, B., Rao, G., Geer, R., Gao, H., Xu, Y., & Yu, B. (2010). Electromechanical robustness of monolayer graphene with extreme bending. *Applied Physics Letters*, *97*(22), 223102. https://doi.org/10.1063/1.3519982

Byrne, M. T., & Guin’Ko, Y. K. (2010). Recent advances in research on carbon nanotube - polymer composites. *Advanced Materials*, *22*(15), 1672–1688. https://doi.org/10.1002/adma.200901545

Cadogan, D., Scheir, C., Dixit, A., Ware, J., Ferl, J., Cooper, E., & Kopf, P. (2006, May). Intelligent flexible materials for deployable space structures (InFlex). In *In 47th AIAA/ASME/ASCE/AHS/ASC Structures, Structural Dynamics, and Materials Conference 14th AIAA/ASME/AHS Adaptive Structures Conference 7th* (p. 1897), Newport, Rhode Island, United States. https://doi.org/10.4271/2006-01-2065

Cao, C., Andrews, J. B., & Franklin, A. D. (2017). Completely printed, flexible, stable, and hysteresis-free carbon nanotube thin-film transistors via aerosol jet printing. *Advanced Electronic Materials*, *3*(5), 1700057.

https://doi.org/10.1002/aelm.201700057

Cao, J., Wang, Q., & Dai, H. (2003). Electromechanical properties of metallic, quasimetallic, and semiconducting carbon nanotubes under stretching. *Physical Review Letters*, *90*(15), 157601. https://doi.org/10.1103/PhysRevLett.90.157601

Castrejón-Pita, J. R., Baxter, W. R. S., Morgan, J., Temple, S., Martin, G. D., & Hutchings, I. M. (2013). Future, opportunities and challenges of inkjet technologies. *Atomization and Sprays*, *23*(6), 571–595. https://doi.org/10.1615/AtomizSpr.2013007653

Castro Neto, A. H., Guinea, F., Peres, N. M. R., Novoselov, K. S., & Geim, A. K. (2009). The electronic properties of graphene. *Reviews of Modern Physics*, *81*(1), 109–162. https://doi.org/10.1103/RevModPhys.81.109

Cataldi, P., Athanassiou, A., & Bayer, I. S. (2018). Graphene nanoplatelets-based advanced materials and recent progress in sustainable applications. *Applied Sciences (Switzerland)*, *8*(9), 1438. https://doi.org/10.3390/app8091438

Cha, S. N., Jang, J. E., Choi, Y., Amaratunga, G. A. J., Kang, D. J., Hasko, D. G., … Kim, J. M. (2005). Fabrication of a nanoelectromechanical switch using a suspended carbon nanotube. *Applied Physics Letters*, *86*(8), 1–3. https://doi.org/10.1063/1.1868064

Chandra, N., Namilae, S., & Shet, C. (2004). Local elastic properties of carbon nanotubes in the presence of Stone-Wales defects. *Physical Review B - Condensed Matter and Materials Physics*, *69*(9), 1–12. https://doi.org/10.1103/PhysRevB.69.094101

Chandrasekaran, S., Seidel, C., & Schulte, K. (2013). Preparation and characterization of graphite nano-platelet (GNP)/epoxy nano-composite: Mechanical, electrical and thermal properties. *European Polymer Journal*, *49*(12), 3878–3888. https://doi.org/10.1016/j.eurpolymj.2013.10.008

Chang, F. Y., Wang, R. H., Yang, H., Lin, Y. H., Chen, T. M., & Huang, S. J. (2010). Flexible strain sensors fabricated with carbon nano-tube and carbon nano-fiber composite thin films. *Thin Solid Films*, *518*(24), 7343–7347. https://doi.org/10.1016/j.tsf.2010.04.108

Charlier, J. C., Eklund, P. C., Zhu, J., & Ferrari, A. C. (2008). Electron and phonon properties of graphene: Their relationship with carbon nanotubes. *Topics in Applied Physics*, *111*, 673–709. https://doi.org/10.1007/978-3-540-72865-8_21

Charlier, Jean Christophe, Blase, X., & Roche, S. (2007). Electronic and transport properties of nanotubes. *Reviews of Modern Physics*, *79*(2), 677–732. https://doi.org/10.1103/RevModPhys.79.677

Chauraya, A., Whittow, W. G., Vardaxoglou, Y. C., Li, Y., Torah, R., Yang, K., … Tudor, J. (2013). Inkjet printed dipole antennas on textiles for wearable communications. *IET Microwaves, Antennas and Propagation*, *7*(9), 760–767. https://doi.org/10.1049/iet-map.2013.0076

Chen, G., Wu, D., Weng, W., & Wu, C. (2003). Exfoliation of graphite flake and its nanocomposites. *Carbon*, *41*(3), 619–621. https://doi.org/10.1016/S0008-6223(02)00409-8

Chen, G. Z., Shaffer, M. S. P., Coleby, D., Dixon, G., Zhou, W., Fray, D. J., & Windle, A. H. (2000). Carbon nanotube and polypyrrole composites: Coating and doping. *Advanced Materials*, *12*(7), 522–526. https://doi.org/10.1002/(SICI)1521-4095(200004)12:7<522::AID-ADMA522>3.0.CO;2-S

Chen, P., Chen, H., Qiu, J., & Zhou, C. (2010). Inkjet printing of single-walled carbon nanotube/RuO2 nanowire supercapacitors on cloth fabrics and flexible substrates. *Nano Research*, *3*(8), 594–603. https://doi.org/10.1007/s12274-010-0020-x

Chen, Yong, Li, C., Tu, J. C., & An, L. N. (2012). Synthesis of short multi-walled carbon nanotubes by molecular self-assembly. *Xinxing Tan Cailiao/New Carbon Materials*, *27*(6), 416–420. https://doi.org/10.1016/S1872-5805(12)60025-0

Chen, Yuli, Pan, F., Wang, S., Liu, B., & Zhang, J. (2015). Theoretical estimation on the percolation threshold for polymer matrix composites with hybrid fillers. *Composite Structures*, *124*, 292–299. https://doi.org/10.1016/j.compstruct.2015.01.013

Cheng, S. H., Zou, K., Okino, F., Gutierrez, H. R., Gupta, A., Shen, N., … Zhu, J. (2010). Reversible fluorination of graphene: Evidence of a two-dimensional wide bandgap semiconductor. *Physical Review B - Condensed Matter and Materials Physics*, *81*(20), 205435. https://doi.org/10.1103/PhysRevB.81.205435

Chiacchiarelli, L. M., Rallini, M., Monti, M., Puglia, D., Kenny, J. M., & Torre, L. (2013). The role of irreversible and reversible phenomena in the piezoresistive behavior of graphene epoxy nanocomposites applied to structural health monitoring. *Composites Science and Technology*, *80*, 73–79. https://doi.org/10.1016/j.compscitech.2013.03.009

Chou, T. W., Gao, L., Thostenson, E. T., Zhang, Z., & Byun, J. H. (2010). An assessment of the science and technology of carbon nanotube-based fibers and composites. *Composites Science and Technology*, *70*(1), 1–19. https://doi.org/10.1016/j.compscitech.2009.10.004

Christiansen, E., Arnold, J., Davis, A., Hyde, J., Lear, D., Liou, J.-C., … Studor, G. (2009). Handbook for designing MMOD protection. *NASA Johnson Space Center, NASA/TM-2009-214785*. Retrieved from https://ston.jsc.nasa.gov/collections/trs/_techrep/TM-2009-214785.pdf

Christiansen, E. L., & Rollins, M. (2012). MMOD risk/external inspection needs for re-entry TPS. *NASA Johnson Space Center, NASA/2009-0010053*. Retrieved from https://www.nasa.gov/pdf/626427main_1-5_Rollins_Christiansen.pdf

Chun, S., Choi, Y., & Park, W. (2017). All-graphene strain sensor on soft substrate. *Carbon, 116*, 753–759. https://doi.org/10.1016/j.carbon.2017.02.058

Coleman, J. N., Blau, W. J., Dalton, A. B., Muñoz, E., Collins, S., Kim, B. G., … Baughman, R. H. (2003). Improving the mechanical properties of single-walled carbon nanotube sheets by intercalation of polymeric adhesives. *Applied Physics Letters, 82*(11), 1682–1684. https://doi.org/10.1063/1.1559421

Coleman, J. N., Khan, U., Blau, W. J., & Gun'ko, Y. K. (2006). Small but strong: A review of the mechanical properties of carbon nanotube-polymer composites. *Carbon*, *44*(9), 1624–1652. https://doi.org/10.1016/j.carbon.2006.02.038

Coleman, J. N., Khan, U., & Gun'ko, Y. K. (2006). Mechanical reinforcement of polymers using carbon nanotubes. *Advanced Materials*, *18*(6), 689–706. https://doi.org/10.1002/adma.200501851

Crawford, J. D. (1991). Introduction to bifurcation theory. *Reviews of Modern Physics*, *63*(4), 991–1037. https://doi.org/10.1103/RevModPhys.63.991

Crespi, V. H., Cohen, M. L., & Rubio, A. (1997). In situ b and gap engineering of carbon nanotubes. *Physical Review Letters*, *79*(11), 2093–2096. https://doi.org/10.1103/PhysRevLett.79.2093

D'Aloia, A. G., Tamburrano, A., De Bellis, G., & Sarto, M. S. (2011, August). Electromechanical modeling of GNP nanocomposites for stress sensors applications. In *2011 11th IEEE International Conference on Nanotechnology* (pp. 1648–1651), Portland, Oregon, United States. https://doi.org/10.1109/NANO.2011.6144649

da Costa, T. H., Song, E., Tortorich, R. P., & Choi, J.-W. (2015). A paper-based electrochemical sensor using inkjet-printed carbon nanotube electrodes. *ECS Journal of Solid State Science and Technology*, *4*(10), S3044–S3047. https://doi.org/10.1149/2.0121510jss

Das, T. K., & Prusty, S. (2013). Graphene-based polymer composites and their applications. *Polymer - Plastics Technology and Engineering, 52*(4), 319–331. https://doi.org/10.1080/03602559.2012.751410

de la Fuente, H., Raboin, J. L., Spexarth, G. R., & Valle, G. D. (2000, April). Transhab: NASA's large-scale inflatable spacecraft. In *41st Structures, Structural Dynamics, and Materials Conference and Exhibit* (p. 1822), Atlanta, Georgia, United States. https://doi.org/AIAA 2000-1822

De Volder, M. F. L., Tawfick, S. H., Baughman, R. H., & Hart, A. J. (2013). Carbon nanotubes: Present and future commercial applications. *Science*, *339*(6119), 535–539. https://doi.org/10.1126/science.1222453

Deegan, R. D., Bakajin, O., Dupont, T. F., Huber, G., Nagel, S. R., & Witten, T. A. (1997). Capillary flow as the cause of ring stains from dried liquid drops. *Nature*, *389*(6653), 827–829. https://doi.org/10.1038/39827

Denneulin, A., Bras, J., Carcone, F., Neuman, C., & Blayo, A. (2011). Impact of ink formulation on carbon nanotube network organization within inkjet printed conductive films. *Carbon*, *49*(8), 2603–2614. https://doi.org/10.1016/j.carbon.2011.02.012

Dey, A., Bajpai, O. P., Sikder, A. K., Chattopadhyay, S., & Shafeeuulla Khan, M. A. (2016). Recent advances in CNT/graphene based thermoelectric polymer nanocomposite: A proficient move towards waste energy harvesting. *Renewable and Sustainable Energy Reviews*, *53*, 653–671. https://doi.org/10.1016/j.rser.2015.09.004

Dharap, P., Li, Z., Nagarajaiah, S., & Barrera, E. V. (2004). Nanotube film based on single-wall carbon nanotubes for strain sensing. *Nanotechnology*, *15*(3), 379–382. https://doi.org/10.1088/0957-4484/15/3/026

Dinh, N. T., Sowade, E., Blaudeck, T., Hermann, S., Rodriguez, R. D., Zahn, D. R. T., … Kanoun, O. (2016). High-resolution inkjet printing of conductive carbon nanotube twin lines utilizing evaporation-driven self-assembly. *Carbon*, *96*, 382–393. https://doi.org/10.1016/j.carbon.2015.09.072

Dodoo-Arhin, D., Howe, R. C. T., Hu, G., Zhang, Y., Hiralal, P., Bello, A., … Hasan, T. (2016). Inkjet-printed graphene electrodes for dye-sensitized solar cells. *Carbon*, *105*, 33–41. https://doi.org/10.1016/j.carbon.2016.04.012

Doh, J., Park, S. I., Yang, Q., & Raghavan, N. (2019). The effect of carbon nanotube chirality on the electrical conductivity of polymer nanocomposites considering tunneling resistance. *Nanotechnology*, *30*(46), 465701. https://doi.org/10.1088/1361-6528/ab3b79

Du, F., Fischer, J. E., & Winey, K. I. (2003). Coagulation method for preparing single-walled carbon nanotube/poly(methyl methacrylate) composites and their modulus, electrical conductivity, and thermal stability. *Journal of Polymer Science, Part B: Polymer Physics*, *41*(24), 3333–3338. https://doi.org/10.1002/polb.10701

Du, F., Fischer, J. E., & Winey, K. I. (2005). Effect of nanotube alignment on percolation conductivity in carbon nanotube/polymer composites. *Physical Review B - Condensed Matter and Materials Physics*, *72*(12), 121404. https://doi.org/10.1103/PhysRevB.72.121404

Du, J., Zhao, L., Zeng, Y., Zhang, L., Li, F., Liu, P., & Liu, C. (2011). Comparison of electrical properties between multi-walled carbon nanotube and graphene nanosheet/high density polyethylene composites with a segregated network structure. *Carbon*, *49*(4), 1094–1100. https://doi.org/10.1016/j.carbon.2010.11.013

Eda, G., & Chhowalla, M. (2009). Graphene-based composite thin films for electronics. *Nano Letters*, *9*(2), 814–818. https://doi.org/10.1021/n18035367

Eda, G., Fanchini, G., & Chhowalla, M. (2008). Large-area ultrathin films of reduced graphene oxide as a transparent and flexible electronic material. *Nature Nanotechnology*, *3*(5), 270–274. https://doi.org/10.1038/nnano.2008.83

Erukhimovich, I., & de la Cruz, M. O. (2004). Phase equilibria and charge fractionation in polydisperse polyelectrolyte solutions. *MRS Bulletin*, *32*, 314–358. https://doi.org/10.1002/polb

Eswaraiah, V., Balasubramaniam, K., & Ramaprabhu, S. (2011). Functionalized graphene reinforced thermoplastic nanocomposites as strain sensors in structural health monitoring. *Journal of Materials Chemistry*, *21*(34), 12626–12628. https://doi.org/10.1039/c1jm12302e

Eswaraiah, V., Balasubramaniam, K., & Ramaprabhu, S. (2012). One-pot synthesis of conducting graphene-polymer composites and their strain sensing application. *Nanoscale*, *4*(4), 1258–1262. https://doi.org/10.1039/c2nr11555g

Faiella, G., Piscitelli, F., Lavorgna, M., Antonucci, V., & Giordano, M. (2009). Effect of fabrication process on the electrical and morphological properties of MWNT-epoxy composites. *ICCM International Conferences on Composite Materials*. Retrieved from http://www.scopus.com/inward/record.url?eid=2-s2.0-80052071454&partnerID=40&md5=a3e718d06019e8f590a40d42172533ea

Fang, Y., Hester, J. G. D., Su, W., Chow, J. H., Sitaraman, S. K., & Tentzeris, M. M. (2016). A bio-enabled maximally mild layer-by-layer Kapton surface modification approach for the fabrication of all-inkjet-printed flexible electronic devices. *Scientific Reports*, *6*, 39909. https://doi.org/10.1038/srep39909

Fang, Y., & Tentzeris, M. M. (2018). Surface modification of polyimide films for inkjet-printing of flexible electronic devices. In S. Rackauskas (Ed.), *Flexible Electronics* (Open Acess). https://doi.org/10.5772/intechopen.76450

Filippidou, M. K., Tegou, E., Tsouti, V., & Chatzandroulis, S. (2015). A flexible strain sensor made of graphene nanoplatelets/polydimethylsiloxane nanocomposite. *Microelectronic Engineering*, *142*, 7–11. https://doi.org/10.1016/j.mee.2015.06.007

Filippone, G., Salzano De Luna, M., Acierno, D., & Russo, P. (2012). Elasticity and structure of weak graphite nanoplatelet (GNP) networks in polymer matrices through viscoelastic analyses. *Polymer*, *53*(13), 2699–2704. https://doi.org/10.1016/j.polymer.2012.04.037

Fraysse, J., Minett, A. I., Gu, G., Roth, S., Rinzler, A. G., & Baughman, R. H. (2001). Towards the demonstration of actuator properties of a single carbon nanotube. *Current Applied Physics, 1*(4–5), 407–411. https://doi.org/10.1016/S1567-1739(01)00048-7

Fung, C. K. M., Zhang, M. Q. H., Chan, R. H. M., & Li, W. J. (2005, February). A PMMA-based micro pressure sensor chip using carbon nanotubes as sensing elements. In *Proceedings of the 18th IEEE International Conference on Micro Electro Mechanical Systems (MEMS)* (pp. 251–254), Miami Beach, Florida, United States. https://doi.org/10.1109/memsys.2005.1453914

Fung, C. K. M., Zhang, M. Q. H., Dong, Z., & Li, W. J. (2005, July). Fabrication of CNT-based MEMS piezoresistive pressure sensors using DEP nanoassembly. In *2005 5th IEEE Conference on Nanotechnology* (Vol. 1, pp. 369–372), Nagoya, Japan. https://doi.org/10.1109/NANO.2005.1500728

Gao, Y., Picot, O. T., Bilotti, E., & Peijs, T. (2017). Influence of filler size on the properties of poly(lactic acid) (PLA)/graphene nanoplatelet (GNP) nanocomposites. *European Polymer Journal*, *86*, 117–131. https://doi.org/10.1016/j.eurpolymj.2016.10.045

Garboczi, E. J., Snyder, K. A., Douglas, J. F., & Thorpe, M. F. (1995). Geometrical percolation threshold of overlapping ellipsoids. *Physical Review E*, *52*(1), 819–828. https://doi.org/10.1103/PhysRevE.52.819

Gbaguidi, A., Anees, M., Namilae, S., & Kim, D. (2017, April). Dynamic piezoresistive response of hybrid nanocomposites. In *Sensors and Smart Structures Technologies for Civil, Mechanical, and Aerospace Systems 2017* (Vol. 10168, p. 1016817), Portland, Oregon, United States. https://doi.org/10.1117/12.2260208

Gbaguidi, A., & Kim, D. (2014). Fatigue damage prognosis using affine arithmetic. In *AIP Conference Proceedings* (Vol. 1581, pp. 719–726). https://doi.org/10.1063/1.4864891

Gbaguidi, A., Konduru, V. K., & Kim, D. (2016). Analytical approach on the performance of helical dielectric elastomer actuator. In *Electroactive Polymer Actuators and Devices (EAPAD) 2016* (Vol. 9798, p. 979814). https://doi.org/10.1117/12.2219911

Gbaguidi, A., Madiyar, F., Kim, D., & Namilae, S. (2020). Multifunctional Inkjet Printed Sensors for MMOD Impact Detection. *Smart Materials and Structures*, *29*(8), 085052. https://doi.org/10.1088/1361-665X/ab98eb

Gbaguidi, A., Namilae, S., & Kim, D. (2017). Numerical and experimental investigation of the piezoresistive behavior of hybrid carbon nanotube sheet – Graphene nanocomposites. In *58th AIAA/ASCE/AHS/ASC Structures, Structural Dynamics, and Materials Conference* (p. 0795). https://doi.org/10.2514/6.2017-0795

Gbaguidi, A., Namilae, S., & Kim, D. (2018a). Comparison of 3D and 2D monte carlo models for piezoresistive behavior of hybrid nanocomposites. In *2018 AIAA/ASCE/AHS/ASC Structures, Structural Dynamics, and Materials Conference* (p. 0908). https://doi.org/10.2514/6.2018-0908

Gbaguidi, A., Namilae, S., & Kim, D. (2018b). Monte Carlo model for piezoresistivity of hybrid nanocomposites. *Journal of Engineering Materials and Technology, Transactions of the ASME*, *140*(1), 11007. https://doi.org/10.1115/1.4037024

Gbaguidi, A., Namilae, S., & Kim, D. (2019a). Numerical and experimental investigation of the sensitivity of carbon nanotube and graphene nanocomposites to MMOD impact damage for inflatable structures. In *AIAA Scitech 2019 Forum* (p. 1461). https://doi.org/10.2514/6.2019-1461

Gbaguidi, A., Namilae, S., & Kim, D. (2019b). Stochastic percolation model for the effect of nanotube agglomeration on the conductivity and piezoresistivity of hybrid nanocomposites. *Computational Materials Science*, *166*, 9–19. https://doi.org/10.1016/j.commatsci.2019.04.045

Gbaguidi, A., Namilae, S., & Kim, D. (2020). Synergy effect in hybrid nanocomposites based on carbon nanotubes and graphene nanoplatelets. *Nanotechnology, 31*(25), 255704. https://doi.org/10.1088/1361-6528/ab7fcc

Geim, A. K., & Novoselov, K. S. (2007). The rise of graphene. *Nature Materials*, *6*(3), 183–191. https://doi.org/10.1038/nmat1849

Geim, A., & Novoselov, K. (2010). The nobel prize in physics 2010. *Nature Physics*, *6*, 836. Retrieved from http://www.ecum.uminho.pt/uploads/eventos/EV_3221/20101006443838636250.pdf

Ghaleb, Z. A. A., Jaafar, M., & Rashid, A. A. (2019). Fabrication methods of carbon-based rubber nanocomposites and their applications. In S. Yaragalla, R. K. Mishra, S. Thomas, N. Kalarikkal, & H. J. B. T.-C.-B. N. and T. R. N. Maria (Eds.), *Carbon-Based Nanofiller and Their Rubber Nanocomposites* (pp. 49–63). https://doi.org/https://doi.org/10.1016/B978-0-12-817342-8.00003-2

Gibson, T. L., Williams, M. K., Lewis, M. E., Roberson, L. B., Snyder, S. J., & Medelius, P. J. (2016). *Patent No. 9,233,765*. USA: U.S. Patent and Trademark Office.

Gojny, F. H., Wichmann, M. H. G., Köpke, U., Fiedler, B., & Schulte, K. (2004). Carbon nanotube-reinforced epoxy-composites: Enhanced stiffness and fracture toughness at low nanotube content. *Composites Science and Technology*, *64*(15), 2363–2371. https://doi.org/10.1016/j.compscitech.2004.04.002

Gómez, H., Ram, M. K., Alvi, F., Villalba, P., Stefanakos, E., & Kumar, A. (2011). Graphene-conducting polymer nanocomposite as novel electrode for supercapacitors. *Journal of Power Sources*, *196*(8), 4102–4108. https://doi.org/10.1016/j.jpowsour.2010.11.002

Gong, S., & Zhu, Z. H. (2015). Giant piezoresistivity in aligned carbon nanotube nanocomposite: Account for nanotube structural distortion at crossed tunnel junctions. *Nanoscale*, *7*(4), 1339–1348. https://doi.org/10.1039/c4nr05656f

Gong, S., Zhu, Z. H., & Meguid, S. A. (2014). Carbon nanotube agglomeration effect on piezoresistivity of polymer nanocomposites. *Polymer*, *55*(21), 5488–5499. https://doi.org/10.1016/j.polymer.2014.08.054

Gong, S., Zhu, Z. H., & Meguid, S. A. (2015). Anisotropic electrical conductivity of polymer composites with aligned carbon nanotubes. *Polymer*, *56*, 498–506. https://doi.org/10.1016/j.polymer.2014.11.038

Gong, Shen, & Zhu, Z. H. (2014). On the mechanism of piezoresistivity of carbon nanotube polymer composites. *Polymer*, *55*(16), 4136–4149. https://doi.org/10.1016/j.polymer.2014.06.024

Gordon, R. B., & Petroski, H. (1992). The pencil: A history of design and circumstance. In *Technology and Culture* (Vol. 33, p. 142). https://doi.org/10.2307/3105814

Grand View Research. (2019a). Graphene market size, share & trends analysis report by application (electronics, composites, energy), by product (graphene nanoplatelets, graphene oxide), by region, and segment forecasts, 2019 - 2025. Retrieved from https://www.researchandmarkets.com/reports/4751759/graphene-market-size-share-and-trends-analysis

Grand View Research. (2019b). Graphene market size worth $552.3 million by 2025 | CAGR: 38.0%. Retrieved from https://www.grandviewresearch.com/press-release/global-graphene-market

Grande, L., Chundi, V. T., Wei, D., Bower, C., Andrew, P., & Ryhänen, T. (2012). Graphene for energy harvesting/storage devices and printed electronics. *Particuology*, *10*(1), 1–8. https://doi.org/10.1016/j.partic.2011.12.001

Graphene supermarket. (n.d.). Graphene sheet: Material data sheet. Retrieved from http://graphene-supermarket.com/

Grow, R. J., Wang, Q., Cao, J., Wang, D., & Dai, H. (2005). Piezoresistance of carbon nanotubes on deformable thin-film membranes. *Applied Physics Letters*, *86*(9), 1–3.

https://doi.org/10.1063/1.1872221

Grujicic, M., Cao, G., & Roy, W. N. (2004). A computational analysis of the percolation threshold and the electrical conductivity of carbon nanotubes filled polymeric materials. *Journal of Materials Science*, *39*(14), 4441–4449. https://doi.org/10.1023/b:jmsc.0000034136.11779.96

Guo, X. D., Dai, Y., Gong, M., Qu, Y. G., & Helseth, L. E. (2015). Changes in wetting and contact charge transfer by femtosecond laser-ablation of polyimide. *Applied Surface Science*, *349*, 952–956. https://doi.org/10.1016/j.apsusc.2015.05.089

Halperin, B. I., Feng, S., & Sen, P. N. (1985). Differences between lattice and continuum percolation transport exponents. *Physical Review Letters*, *54*(22), 2391–2394. https://doi.org/10.1103/PhysRevLett.54.2391

Han, M. Y., Brant, J. C., & Kim, P. (2010). Electron transport in disordered graphene nanoribbons. *Physical Review Letters*, *104*(5), 056801. https://doi.org/10.1103/PhysRevLett.104.056801

Han, M. Y., Özyilmaz, B., Zhang, Y., & Kim, P. (2007). Energy band-gap engineering of graphene nanoribbons. *Physical Review Letters*, *98*(20), 206805. https://doi.org/10.1103/PhysRevLett.98.206805

Haslam, M. D., & Raeymaekers, B. (2013). A composite index to quantify dispersion of carbon nanotubes in polymer-based composite materials. *Composites Part B: Engineering*, *55*(1), 16–21. https://doi.org/10.1016/j.compositesb.2013.05.038

Hassoun, J., Bonaccorso, F., Agostini, M., Angelucci, M., Betti, M. G., Cingolani, R., … Scrosati, B. (2014). An advanced lithium-ion battery based on a graphene anode and a lithium iron phosphate cathode. *Nano Letters*, *14*(8), 4901–4906. https://doi.org/10.1021/nl502429m

He, L., & Tjong, S. C. (2013). Low percolation threshold of graphene/polymer composites prepared by solvothermal reduction of graphene oxide in the polymer solution. *Nanoscale Research Letters*, *8*(1), 132. https://doi.org/10.1186/1556-276X-8-132

Hempel, M., Nezich, D., Kong, J., & Hofmann, M. (2012). A novel class of strain gauges based on layered percolative films of 2D materials. *Nano Letters, 12*(11), 5714–5718. https://doi.org/10.1021/nl302959a

Hernandez, Y., Nicolosi, V., Lotya, M., Blighe, F. M., Sun, Z., De, S., … Coleman, J. N. (2008). High-yield production of graphene by liquid-phase exfoliation of graphite. *Nature Nanotechnology*, *3*(9), 563–568. https://doi.org/10.1038/nnano.2008.215

Hicks, J., Behnam, A., & Ural, A. (2009). A computational study of tunneling-percolation electrical transport in graphene-based nanocomposites. *Applied Physics Letters*, *95*(21), 213103. https://doi.org/10.1063/1.3267079

Hierold, C., Jungen, A., Stampfer, C., & Helbling, T. (2007). Nano electromechanical sensors based on carbon nanotubes. *Sensors and Actuators, A: Physical*, *136*(1), 51–61. https://doi.org/10.1016/j.sna.2007.02.007

Homenick, C. M., James, R., Lopinski, G. P., Dunford, J., Sun, J., Park, H., … Malenfant, P. R. L. (2016). Fully printed and encapsulated SWCNT-based thin film transistors via a combination of R2R gravure and inkjet printing. *ACS Applied Materials and Interfaces*, *8*(41), 27900–27910. https://doi.org/10.1021/acsami.6b06838

Hong, S., & Myung, S. (2007). Nanotube electronics: A flexible approach to mobility. *Nature Nanotechnology*, *2*(4), 207–208. https://doi.org/10.1038/nnano.2007.89

Hosseinzadegan, H., Todd, C., Lal, A., Pandey, M., Levendorf, M., & Park, J. (2012). Graphene has ultra high piezoresistive gauge factor. In *2012 IEEE 25th international conference on micro electro mechanical systems (MEMS)* (pp. 611–614). https://doi.org/10.1109/MEMSYS.2012.6170262

Hsueh, H. Bin, & Chen, C. Y. (2003). Preparation and properties of LDHs/epoxy nanocomposites. *Polymer*, *44*(18), 5275–5283. https://doi.org/10.1016/S0032-3861(03)00579-2

Hu, B., Hu, N., Li, Y., Akagi, K., Yuan, W., Watanabe, T., & Cai, Y. (2012). Multi-scale numerical simulations on piezoresistivity of CNT/polymer nanocomposites. *Nanoscale Research Letters*, *7*(1), 402. https://doi.org/10.1186/1556-276X-7-402

Hu, G., Zhao, C., Zhang, S., Yang, M., & Wang, Z. (2006). Low percolation thresholds of electrical conductivity and rheology in poly(ethylene terephthalate) through the networks of multi-walled carbon nanotubes. *Polymer*, *47*(1), 480–488. https://doi.org/10.1016/j.polymer.2005.11.028

Hu, L., Hecht, D. S., & Gruner, G. (2004). Percolation in transparent and conducting carbon nanotube networks. *Nano Letters*, *4*(12), 2513–2517. https://doi.org/10.1021/nl048435y

Hu, N., Karube, Y., Arai, M., Watanabe, T., Yan, C., Li, Y., … Fukunaga, H. (2010). Investigation on sensitivity of a polymer/carbon nanotube composite strain sensor. *Carbon*, *48*(3), 680–687. https://doi.org/10.1016/j.carbon.2009.10.012

Hu, N., Karube, Y., Yan, C., Masuda, Z., & Fukunaga, H. (2008). Tunneling effect in a polymer/carbon nanotube nanocomposite strain sensor. *Acta Materialia*, *56*(13), 2929–2936. https://doi.org/10.1016/j.actamat.2008.02.030

Hu, N., Masuda, Z., Yamamoto, G., Fukunaga, H., Hashida, T., & Qiu, J. (2008). Effect of fabrication process on electrical properties of polymer/multi-wall carbon nanotube nanocomposites. *Composites Part A: Applied Science and Manufacturing*, *39*(5), 893–903. https://doi.org/10.1016/j.compositesa.2008.01.002

Hu, N., Masuda, Z., Yan, C., Yamamoto, G., Fukunaga, H., & Hashida, T. (2008). The electrical properties of polymer nanocomposites with carbon nanotube fillers. *Nanotechnology*, *19*(21), 215701. https://doi.org/10.1088/0957-4484/19/21/215701

Huang, W., Wang, Y., Luo, G., & Wei, F. (2003). 99.9% purity multi-walled carbon nanotubes by vacuum high-temperature annealing. *Carbon*, *41*(13), 2585–2590. https://doi.org/10.1016/S0008-6223(03)00330-0

Huang, X. D., Bhangale, S. M., Moran, P. M., Yakovlev, N. L., & Pan, J. (2003). Surface modification studies of Kapton® HN polyimide films. *Polymer International*, *52*(7), 1064–1069. https://doi.org/10.1002/pi.1143

Huang, X., Yin, Z., Wu, S., Qi, X., He, Q., Zhang, Q., … Zhang, H. (2011). Graphene-based materials: Synthesis, characterization, properties, and applications. *Small*, *7*(14), 1876–1902. https://doi.org/10.1002/smll.201002009

Huang, Y. Y., & Terentjev, E. M. (2012). Dispersion of carbon nanotubes: Mixing, sonication, stabilization, and composite properties. *Polymers*, *4*(1), 275–295. https://doi.org/10.3390/polym4010275

Hussain, F., Hojjati, M., Okamoto, M., & Gorga, R. E. (2006). Polymer-matrix nanocomposites, processing, manufacturing, and application: An overview. *Journal of Composite Materials*, *40*(17), 1511–1575. https://doi.org/10.1177/0021998306067321

Hwang, J., Jang, J., Hong, K., Kim, K. N., Han, J. H., Shin, K., & Park, C. E. (2011). Poly(3-hexylthiophene) wrapped carbon nanotube/poly(dimethylsiloxane) composites for use in finger-sensing piezoresistive pressure sensors. *Carbon*, *49*(1), 106–110. https://doi.org/10.1016/j.carbon.2010.08.048

Hwang, S. H., Park, H. W., & Park, Y. Bin. (2013). Piezoresistive behavior and multi-directional strain sensing ability of carbon nanotube-graphene nanoplatelet hybrid sheets. *Smart Materials and Structures*, *22*(1), 015013. https://doi.org/10.1088/0964-1726/22/1/015013

Hwang, S. H., Park, H. W., Park, Y. Bin, Um, M. K., Byun, J. H., & Kwon, S. (2013). Electromechanical strain sensing using polycarbonate-impregnated carbon nanotube-graphene nanoplatelet hybrid composite sheets. *Composites Science and Technology*, *89*, 1–9. https://doi.org/10.1016/j.compscitech.2013.09.005

Hyun, W. J., Secor, E. B., Hersam, M. C., Frisbie, C. D., & Francis, L. F. (2015). High-resolution patterning of graphene by screen printing with a silicon stencil for highly flexible printed electronics. *Advanced Materials*, *27*(1), 109–115. https://doi.org/10.1002/adma.201404133

IEEE. (2009). 62624-2009-Test methods for measurement of electrical properties of carbon nanotubes. *IEC 62624 Edition 1.0 2009-08 IEEE Std 1650*, 1–0. https://doi.org/10.1109/IEEESTD.2009.5782922

Iijima, S. (1991). Helical microtubules of graphitic carbon. *Nature*, *354*(6348), 56–58. https://doi.org/10.1038/354056a0

Iijima, S., & Ichihashi, T. (1993). Single-shell carbon nanotubes of 1-nm diameter. *Nature*, *363*(6430), 603–605. https://doi.org/10.1038/363603a0

Inagaki, N., Tasaka, S., & Hibi, K. (1992). Surface modification of Kapton film by plasma treatments. *Journal of Polymer Science Part A: Polymer Chemistry*, *30*(7), 1425–1431. https://doi.org/10.1002/pola.1992.080300722

Ishida, M., & Nihey, F. (2008). Estimating the yield and characteristics of random network carbon nanotube transistors. *Applied Physics Letters*, *92*(16), 163507. https://doi.org/10.1063/1.2901165

Ismail, N. M., Aziz, A., & Jaafar, M. (2012). Thermal stability and electrical conductivity of multi-walled carbon nanotube (MWCNT)/polymethyl methacrylite (PMMA) nanocomposite prepared via the coagulation method. In *AIP Conference Proceedings 2nd* (Vol. 1455, pp. 212–215). https://doi.org/10.1063/1.4732494

Jabari, E., & Toyserkani, E. (2015). Micro-scale aerosol-jet printing of graphene interconnects. *Carbon*, *91*, 321–329. https://doi.org/10.1016/j.carbon.2015.04.094

Jang, B. Z., & Zhamu, A. (2008). Processing of nanographene platelets (NGPs) and NGP nanocomposites: A review. *Journal of Materials Science*, *43*(15), 5092–5101. https://doi.org/10.1007/s10853-008-2755-2

Jarali, C. S., Basavaraddi, S. R., Kiefer, B., Pilli, S. C., & Lu, Y. C. (2014). Modeling of the effective elastic properties of multifunctional carbon nanocomposites due to agglomeration of straight circular carbon nanotubes in a polymer matrix. *Journal of Applied Mechanics, Transactions ASME*, *81*(2), 021010. https://doi.org/10.1115/1.4024414

Javey, A., Guo, J., Wang, Q., Lundstrom, M., & Dai, H. (2003). Ballistic carbon nanotube field-effect transistors. *Nature*, *424*(6949), 654–657. https://doi.org/10.1038/nature01797

Javidjam, A., Hekmatshoar, M. H., Hedayatifar, L., & Abad, S. N. K. (2019). Effect of surface roughness on electrical conductivity and hardness of silver plated copper.

Materials Research Express, *6*(3), 036407. https://doi.org/10.1088/2053-1591/aaf4c5

Jeong, Y. R., Park, H., Jin, S. W., Hong, S. Y., Lee, S. S., & Ha, J. S. (2015). Highly stretchable and sensitive strain sensors using fragmentized graphene foam. *Advanced Functional Materials*, *25*(27), 4228–4236. https://doi.org/10.1002/adfm.201501000

Jiang, M. J., Dang, Z. M., Xu, H. P., Yao, S. H., & Bai, J. (2007). Effect of aspect ratio of multiwall carbon nanotubes on resistance-pressure sensitivity of rubber nanocomposites. *Applied Physics Letters*, *91*(7), 072907. https://doi.org/10.1063/1.2772671

Jiang, X., & Drzal, L. T. (2012). Reduction in percolation threshold of injection molded high-density polyethylene/exfoliated graphene nanoplatelets composites by solid state ball milling and solid state shear pulverization. *Journal of Applied Polymer Science*, *124*(1), 525–535. https://doi.org/10.1002/app.34891

Jordan, J., Jacob, K. I., Tannenbaum, R., Sharaf, M. A., & Jasiuk, I. (2005). Experimental trends in polymer nanocomposites - A review. *Materials Science and Engineering A*, *393*(1–2), 1–11. https://doi.org/10.1016/j.msea.2004.09.044

Joselevich, E., & Lieber, C. M. (2002). Vectorial growth of metallic and semiconducting single-wall carbon nanotubes. *Nano Letters*, *2*(10), 1137–1141. https://doi.org/10.1021/nl025642u

Jung, D., Han, M., & Lee, G. S. (2014). Gas sensor using a multi-walled carbon nanotube sheet to detect hydrogen molecules. *Sensors and Actuators, A: Physical*, *211*, 51–54. https://doi.org/10.1016/j.sna.2014.03.005

Kalaitzidou, K., Fukushima, H., & Drzal, L. T. (2007). A new compounding method for exfoliated graphite-polypropylene nanocomposites with enhanced flexural properties and lower percolation threshold. *Composites Science and Technology*, *67*(10), 2045–2051. https://doi.org/10.1016/j.compscitech.2006.11.014

Kalaitzidou, K., Fukushima, H., & Drzal, L. T. (2010). A route for polymer nanocomposites with engineered electrical conductivity and percolation threshold. *Materials*, *3*(2), 1089–1103. https://doi.org/10.3390/ma3021089

Kang, I., Heung, Y. Y., Kim, J. H., Lee, J. W., Gollapudi, R., Subramaniam, S., … Ruggles-Wren, M. (2006). Introduction to carbon nanotube and nanofiber smart materials. *Composites Part B: Engineering*, *37*(6), 382–394. https://doi.org/10.1016/j.compositesb.2006.02.011

Kang, I., Schulz, M. J., Kim, J. H., Shanov, V., & Shi, D. (2006). A carbon nanotube strain sensor for structural health monitoring. *Smart Materials and Structures*, *15*(3), 737–748. https://doi.org/10.1088/0964-1726/15/3/009

Kang, S. J., Kocabas, C., Ozel, T., Shim, M., Pimparkar, N., Alam, M. A., … Rogers, J. A. (2007). High-performance electronics using dense, perfectly aligned arrays of single-walled carbon nanotubes. *Nature Nanotechnology*, *2*(4), 230–236. https://doi.org/10.1038/nnano.2007.77

Karim, N., Afroj, S., Malandraki, A., Butterworth, S., Beach, C., Rigout, M., … Yeates, S. G. (2017). All inkjet-printed graphene-based conductive patterns for wearable e-textile applications. *Journal of Materials Chemistry C*, *5*(44), 11640–11648. https://doi.org/10.1039/c7tc03669h

Karuwan, C., Wisitsoraat, A., Chaisuwan, P., Nacapricha, D., & Tuantranont, A. (2017). Screen-printed graphene-based electrochemical sensors for a microfluidic device. *Analytical Methods*, *9*(24), 3689–3695. https://doi.org/10.1039/c7ay00379j

Kasaliwal, G. R., Pegel, S., Göldel, A., Pötschke, P., & Heinrich, G. (2010). Analysis of agglomerate dispersion mechanisms of multiwalled carbon nanotubes during melt mixing in polycarbonate. *Polymer*, *51*(12), 2708–2720. https://doi.org/10.1016/j.polymer.2010.02.048

Khan, F., Kausar, A., & Siddiq, M. (2015). A review on properties and fabrication techniques of polymer/carbon nanotube composites and polymer intercalated buckypapers. *Polymer - Plastics Technology and Engineering*, *54*(14), 1524–1539. https://doi.org/10.1080/03602559.2015.1021486

Kholghi Eshkalak, S., Chinnappan, A., Jayathilaka, W. A. D. M., Khatibzadeh, M., Kowsari, E., & Ramakrishna, S. (2017). A review on inkjet printing of CNT composites for smart applications. *Applied Materials Today*, *9*, 372–386. https://doi.org/10.1016/j.apmt.2017.09.003

Kilbride, B. E., Coleman, J. N., Fraysse, J., Fournet, P., Cadek, M., Drury, A., … Blau, W. J. (2002). Experimental observation of scaling laws for alternating current and direct current conductivity in polymer-carbon nanotube composite thin films. *Journal of Applied Physics*, *92*(7), 4024–4030. https://doi.org/10.1063/1.1506397

Kim, D. H., Lu, N., Ma, R., Kim, Y. S., Kim, R. H., Wang, S., … Rogers, J. A. (2011). Epidermal electronics. *Science*, *333*(6044), 838–843. https://doi.org/10.1126/science.1206157

Kim, H., Abdala, A. A., & MacOsko, C. W. (2010). Graphene/polymer nanocomposites. *Macromolecules*, *43*(16), 6515–6530. https://doi.org/10.1021/ma100572e

Kim, H., Kobayashi, S., Abdurrahim, M. A., Zhang, M. J., Khusainova, A., Hillmyer, M. A., … MacOsko, C. W. (2011). Graphene/polyethylene nanocomposites: Effect of polyethylene functionalization and blending methods. *Polymer*, *52*(8), 1837–1846.

https://doi.org/10.1016/j.polymer.2011.02.017

Kim, H., & Macosko, C. W. (2008). Morphology and properties of polyester/exfoliated graphite nanocomposites. *Macromolecules*, *41*(9), 3317–3327. https://doi.org/10.1021/ma702385h

Kim, H., & Macosko, C. W. (2009). Processing-property relationships of polycarbonate/graphene composites. *Polymer*, *50*(15), 3797–3809. https://doi.org/10.1016/j.polymer.2009.05.038

Kim, I. H., & Jeong, Y. G. (2010). Polylactide/exfoliated graphite nanocomposites with enhanced thermal stability, mechanical modulus, and electrical conductivity. *Journal of Polymer Science, Part B: Polymer Physics*, *48*(8), 850–858. https://doi.org/10.1002/polb.21956

Kim, K. S., Zhao, Y., Jang, H., Lee, S. Y., Kim, J. M., Kim, K. S., … Hong, B. H. (2009). Large-scale pattern growth of graphene films for stretchable transparent electrodes. *Nature*, *457*(7230), 706–710. https://doi.org/10.1038/nature07719

Kim, P., & Lieber, C. M. (1999). Nanotube nanotweezers. *Science*, *286*(5447), 2148–2150. https://doi.org/10.1126/science.286.5447.2148

Kim, S., Yim, J., Wang, X., Bradley, D. D. C., Lee, S., & DeMello, J. C. (2010). Spin- and spray-deposited single-walled carbon-nanotube electrodes for organic solar cells. *Advanced Functional Materials*, *20*(14), 2310–2316. https://doi.org/10.1002/adfm.200902369

Kim, Y. J., Cha, J. Y., Ham, H., Huh, H., So, D. S., & Kang, I. (2011). Preparation of piezoresistive nano smart hybrid material based on graphene. *Current Applied Physics*, *11*(1), S350–S352. https://doi.org/10.1016/j.cap.2010.11.022

Kinaret, J. M., Nord, T., & Viefers, S. (2003). A carbon-nanotube-based nanorelay. *Applied Physics Letters*, *82*(8), 1287–1289. https://doi.org/10.1063/1.1557324

Kirkpatrick, S. (1973). Percolation and conduction. *Reviews of Modern Physics*, *45*(4), 574–588. https://doi.org/10.1103/RevModPhys.45.574

Kong, J., Franklin, N. R., Zhou, C., Chapline, M. G., Peng, S., Cho, K., & Dai, H. (2000). Nanotube molecular wires as chemical sensors. *Science*, *287*(5453), 622–625. https://doi.org/10.1126/science.287.5453.622

Kong, L., & Chen, W. (2014). Carbon nanotube and graphene-based bioinspired electrochemical actuators. *Advanced Materials*, *26*(7), 1025–1043. https://doi.org/10.1002/adma.201303432

Kornmann, X. (2001). *Synthesis and characterisation of thermoset-layered silicate* *nanocomposites*. (Doctoral dissertation, Luleå tekniska universitet).

Koshti, A. M. (2015). Considerations for ultrasonic testing application for on-orbit NDE. In *Structural Health Monitoring and Inspection of Advanced Materials, Aerospace, and Civil Infrastructure 2015* (Vol. 9437, p. 94372H). https://doi.org/10.1117/12.2083245

Kotov, N. A. (2006). Carbon sheet solutions. *Nature*, *442*(7100), 254–255. https://doi.org/10.1038/442254a

Kovacs, J. Z., Velagala, B. S., Schulte, K., & Bauhofer, W. (2007). Two percolation thresholds in carbon nanotube epoxy composites. *Composites Science and Technology*, *67*(5), 922–928. https://doi.org/10.1016/j.compscitech.2006.02.037

Krishnan, A., Dujardin, E., & Ebbesen, T. (1998). Young's modulus of single-walled nanotubes. *Physical Review B - Condensed Matter and Materials Physics*, *58*(20), 14013–14019. https://doi.org/10.1103/PhysRevB.58.14013

Kuilla, T., Bhadra, S., Yao, D., Kim, N. H., Bose, S., & Lee, J. H. (2010). Recent advances in graphene based polymer composites. *Progress in Polymer Science (Oxford)*, *35*(11), 1350–1375. https://doi.org/10.1016/j.progpolymsci.2010.07.005

Kulkarni, M. V., Apte, S. K., Naik, S. D., Ambekar, J. D., & Kale, B. B. (2013). Ink-jet printed conducting polyaniline based flexible humidity sensor. *Sensors and Actuators, B: Chemical*, *178*, 140–143. https://doi.org/10.1016/j.snb.2012.12.046

Kumar, S., Pimparkar, N., Murthy, J. Y., & Alam, M. A. (2006). Theory of transfer characteristics of nanotube network transistors. *Applied Physics Letters*, *88*(12), 123505. https://doi.org/10.1063/1.2187401

Kumar, S., Sun, L. L., Caceres, S., Li, B., Wood, W., Perugini, A., … Zhong, W. H. (2010). Dynamic synergy of graphitic nanoplatelets and multi-walled carbon nanotubes in polyetherimide nanocomposites. *Nanotechnology*, *21*(10), 105702. https://doi.org/10.1088/0957-4484/21/10/105702

Kurzepa, L., Lekawa-Raus, A., Patmore, J., & Koziol, K. (2014). Replacing copper wires with carbon nanotube wires in electrical transformers. *Advanced Functional Materials*, *24*(5), 619–624. https://doi.org/10.1002/adfm.201302497

Kwon, O. S., Kim, H., Ko, H., Lee, J., Lee, B., Jung, C. H., … Shin, K. (2013). Fabrication and characterization of inkjet-printed carbon nanotube electrode patterns on paper. *Carbon*, *58*, 116–127. https://doi.org/10.1016/j.carbon.2013.02.039

Kymakis, E., Alexandou, I., & Amaratunga, G. A. J. (2002). Single-walled carbon nanotube-polymer composites: Electrical, optical and structural investigation. *Synthetic Metals*, *127*(1–3), 59–62. https://doi.org/10.1016/S0379-6779(01)00592-6

Lee, B. M., & Loh, K. J. (2015). A 2D percolation-based model for characterizing the piezoresistivity of carbon nanotube-based films. *Journal of Materials Science*, *50*(7), 2973–2983. https://doi.org/10.1007/s10853-015-8862-y

Lee, B. M., Loh, K. J., Burton, A. R., & Loyola, B. R. (2014). Modeling the electromechanical and strain response of carbon nanotube-based nanocomposites. In *Sensors and Smart Structures Technologies for Civil, Mechanical, and Aerospace Systems 2014* (Vol. 9061, p. 906117). https://doi.org/10.1117/12.2044566

Lee, Changgu, Wei, X., Kysar, J. W., & Hone, J. (2008). Measurement of the elastic properties and intrinsic strength of monolayer graphene. *Science*, *321*(5887), 385–388. https://doi.org/10.1126/science.1157996

Lee, Curtis, Jug, L., & Meng, E. (2013). High strain biocompatible polydimethylsiloxane-based conductive graphene and multiwalled carbon nanotube nanocomposite strain sensors. *Applied Physics Letters*, *102*(18), 183511. https://doi.org/10.1063/1.4804580

Lee, J. H., Loya, P. E., Lou, J., & Thomas, E. L. (2014). Dynamic mechanical behavior of multilayer graphene via supersonic projectile penetration. *Science*, *346*(6213), 1092–1096. https://doi.org/10.1126/science.1258544

Lee, J., & Kim, S. (2005). Manufacture of a nanotweezer using a length controlled CNT arm. *Sensors and Actuators, A: Physical*, *120*(1), 193–198. https://doi.org/10.1016/j.sna.2004.11.012

Lehman, J. H., Terrones, M., Mansfield, E., Hurst, K. E., & Meunier, V. (2011). Evaluating the characteristics of multiwall carbon nanotubes. *Carbon*, *49*(8), 2581–2602. https://doi.org/10.1016/j.carbon.2011.03.028

Lekawa-Raus, A., Patmore, J., Kurzepa, L., Bulmer, J., & Koziol, K. (2014). Electrical properties of carbon nanotube based fibers and their future use in electrical wiring. *Advanced Functional Materials*, *24*(24), 3661–3682. https://doi.org/10.1002/adfm.201303716

Lesch, A., Cortés-Salazar, F., Prudent, M., Delobel, J., Rastgar, S., Lion, N., … Girault, H. H. (2014). Large scale inkjet-printing of carbon nanotubes electrodes for antioxidant assays in blood bags. *Journal of Electroanalytical Chemistry*, *717*, 61–68. https://doi.org/10.1016/j.jelechem.2013.12.027

Li, C., & Chou, T. W. (2009). Electrical conductivities of composites with aligned carbon nanotubes. *Journal of Nanoscience and Nanotechnology*, *9*(4), 2518–2524. https://doi.org/10.1166/jnn.2009.456

Li, C., Thostenson, E. T., & Chou, T. W. (2008). Sensors and actuators based on carbon nanotubes and their composites: A review. *Composites Science and Technology*, *68*(6), 1227–1249. https://doi.org/10.1016/j.compscitech.2008.01.006

Li, Jing, & Kim, J. K. (2007). Percolation threshold of conducting polymer composites containing 3D randomly distributed graphite nanoplatelets. *Composites Science and Technology*, *67*(10), 2114–2120. https://doi.org/10.1016/j.compscitech.2006.11.010

Li, Jing, Ma, P. C., Chow, W. S., To, C. K., Tang, B. Z., & Kim, J. K. (2007). Correlations between percolation threshold, dispersion state, and aspect ratio of carbon nanotubes. *Advanced Functional Materials*, *17*(16), 3207–3215. https://doi.org/10.1002/adfm.200700065

Li, Jing, Vaisman, L., Marom, G., & Kim, J. K. (2007). Br treated graphite nanoplatelets for improved electrical conductivity of polymer composites. *Carbon*, *45*(4), 744–750. https://doi.org/10.1016/j.carbon.2006.11.031

Li, Jing, Wong, P. S., & Kim, J. K. (2008). Hybrid nanocomposites containing carbon nanotubes and graphite nanoplatelets. *Materials Science and Engineering A*, *483*, 660–663. https://doi.org/10.1016/j.msea.2006.08.145

Li, Jiukun. (2016). *Mechanical and electrical characterization of hybrid carbon nanotube sheet-graphene nanocomposites for sensing applications*. (Master's thesis, Embry–Riddle Aeronautical University).

Li, Jiukun, & Namilae, S. (2016). Nanotube sheet - graphite hybrid nanocomposite for damage detection. In *TMS 2016 145th Annual Meeting & Exhibition* (pp. 69–76). https://doi.org/10.1007/978-3-319-48254-5_9

Li, W., Dichiara, A., & Bai, J. (2013). Carbon nanotube-graphene nanoplatelet hybrids as high-performance multifunctional reinforcements in epoxy composites. *Composites Science and Technology*, *74*, 221–227. https://doi.org/10.1016/j.compscitech.2012.11.015

Li, X., Zhang, R., Yu, W., Wang, K., Wei, J., Wu, D., … Zhu, H. (2012). Stretchable and highly sensitive graphene-on-polymer strain sensors. *Scientific Reports*, *2*, 870. https://doi.org/10.1038/srep00870

Li, Y. C., Tjong, S. C., & Li, R. K. Y. (2010). Electrical conductivity and dielectric response of poly(vinylidene fluoride)-graphite nanoplatelet composites. *Synthetic Metals*, *160*(17–18), 1912–1919. https://doi.org/10.1016/j.synthmet.2010.07.009

Li, Y., Zhu, J., Wei, S., Ryu, J., Sun, L., & Guo, Z. (2011). Poly(propylene)/graphene nanoplatelet nanocomposites: Melt rheological behavior and thermal, electrical, and electronic properties. *Macromolecular Chemistry and Physics*, *212*(18), 1951–1959. https://doi.org/10.1002/macp.201100263

Liang, G. D., Bao, S. P., & Tjong, S. C. (2007). Microstructure and properties of polypropylene composites filled with silver and carbon nanotube nanoparticles prepared by melt-compounding. *Materials Science and Engineering B: Solid-State Materials for Advanced Technology*, *142*(2–3), 55–61. https://doi.org/10.1016/j.mseb.2007.06.028

Liang, J., Wang, Y., Huang, Y., Ma, Y., Liu, Z., Cai, J., … Chen, Y. (2009). Electromagnetic interference shielding of graphene/epoxy composites. *Carbon*, *47*(3), 922–925. https://doi.org/10.1016/j.carbon.2008.12.038

Liang, J., Xu, Y., Huang, Y., Zhang, L., Wang, Y., Ma, Y., … Chen, Y. (2009). Infrared-triggered actuators from graphene-based nanocomposites. *Journal of Physical Chemistry C*, *113*(22), 9921–9927. https://doi.org/10.1021/jp901284d

Liang, W., Bockrath, M., Bozovic, D., Hafner, J. H., Tinkham, M., & Park, H. (2001). Fabry-Perot interference in a nanotube electron waveguide. *Nature*, *411*(6838), 665–669. https://doi.org/10.1038/35079517

Liu, H., Liu, K., Chen, G., Heider, D., & Thostenson, E. (2016). Design of carbon nanotube sheet embedded fiber composites with in situ structural health monitoring capability. In *Proceedings of the American Society for Composites - 31st Technical Conference, ASC 2016* (p. 2404).

Liu, J., Hua, L., Li, S., & Yu, M. (2015). Graphene dip coatings: An effective anticorrosion barrier on aluminum. *Applied Surface Science*, *327*, 241–245. https://doi.org/10.1016/j.apsusc.2014.11.187

Liu, N., Luo, F., Wu, H., Liu, Y., Zhang, C., & Chen, J. (2008). One-step ionic-liquid-assisted electrochemical synthesis of ionic-liquid-functionalized graphene sheets directly from graphite. *Advanced Functional Materials*, *18*(10), 1518–1525. https://doi.org/10.1002/adfm.200700797

Liu, Y., Zhang, D., Wang, K., Liu, Y., & Shang, Y. (2016). A novel strain sensor based on graphene composite films with layered structure. *Composites Part A: Applied Science and Manufacturing*, *80*, 95–103. https://doi.org/10.1016/j.compositesa.2015.10.010

Loh, K. J., Hou, T. C., Lynch, J. P., & Kotov, N. A. (2009). Carbon nanotube sensing skins for spatial strain and impact damage identification. *Journal of Nondestructive Evaluation*, *28*(1), 9–25. https://doi.org/10.1007/s10921-009-0043-y

Loh, K. J., Lynch, J. P., Shim, B. S., & Kotov, N. A. (2008). Tailoring piezoresistive sensitivity of multilayer carbon nanotube composite strain sensors. *Journal of Intelligent Material Systems and Structures*, *19*(7), 747–764. https://doi.org/10.1177/1045389X07079872

Loyola, B. R., Briggs, T. M., Arronche, L., Loh, K. J., La Saponara, V., O’Bryan, G., &

Skinner, J. L. (2013). Detection of spatially distributed damage in fiber-reinforced polymer composites. *Structural Health Monitoring*, *12*(3), 225–239. https://doi.org/10.1177/1475921713479642

Lu, J., Miao, J., Xu, T., Yan, B., Yu, T., & Shen, Z. (2011). Erratum: Growth of horizontally aligned dense carbon nanotubes from trench sidewalls. *Nanotechnology*, *22*(26), 265614. https://doi.org/10.1088/0957-4484/22/47/479502

Luo, S., & Liu, T. (2013). SWCNT/graphite nanoplatelet hybrid thin films for self-temperature- compensated, highly sensitive, and extensible piezoresistive sensors. *Advanced Materials*, *25*(39), 5650–5657. https://doi.org/10.1002/adma.201301796

Lynch, M. D., & Patrick, D. L. (2002). Organizing carbon nanotubes with liquid crystals. *Nano Letters*, *2*(11), 1197–1201. https://doi.org/10.1021/nl025694j

Ma, P. C., Siddiqui, N. A., Marom, G., & Kim, J. K. (2010). Dispersion and functionalization of carbon nanotubes for polymer-based nanocomposites: A review. *Composites Part A: Applied Science and Manufacturing*, *41*(10), 1345–1367. https://doi.org/10.1016/j.compositesa.2010.07.003

Madaras, E. I., Anastasi, R. F., Seebo, J. P., Studor, G., McMakin, D. L., Nellums, R., & Winfree, W. P. (2008). The potential for imaging in situ damage in inflatable space structures. In *34th Annual Review of Progress in Quantitative Nondestructive Evaluation (QNDE 2007) AIP Conference Proceedings* (Vol. 975, pp. 437–444). https://doi.org/10.1063/1.2902693

Mahmoud, W. E. (2011). Morphology and physical properties of poly(ethylene oxide) loaded graphene nanocomposites prepared by two different techniques. *European Polymer Journal*, *47*(8), 1534–1540. https://doi.org/10.1016/j.eurpolymj.2011.05.011

Maiti, S., & Khatua, B. B. (2016). Graphene nanoplate and multiwall carbon nanotube–embedded polycarbonate hybrid composites: High electromagnetic interference shielding with low percolation threshold. *Polymer Composites*, *37*(7), 2058–2069. https://doi.org/10.1002/pc.23384

Marquardt, C. W., Grunder, S., Błaszczyk, A., Dehm, S., Hennrich, F., Löhneysen, H. V., … Krupke, R. (2010). Electroluminescence from a single nanotube-molecule-nanotube junction. *Nature Nanotechnology*, *5*(12), 863–867. https://doi.org/10.1038/nnano.2010.230

Martin, C. A., Sandler, J. K. W., Shaffer, M. S. P., Schwarz, M. K., Bauhofer, W., Schulte, K., & Windle, A. H. (2004). Formation of percolating networks in multi-wall carbon-nanotube-epoxy composites. *Composites Science and Technology*, *64*(15), 2309–2316. https://doi.org/10.1016/j.compscitech.2004.01.025

Martone, A., Formicola, C., Giordano, M., & Zarrelli, M. (2010). Reinforcement efficiency of multi-walled carbon nanotube/epoxy nano composites. *Composites Science and Technology*, *70*(7), 1154–1160. https://doi.org/10.1016/j.compscitech.2010.03.001

Maser, W. K., Benito, A. M., Callejas, M. A., Seeger, T., Martínez, M. T., Schreiber, J., … Biró, L. P. (2003). Synthesis and characterization of new polyaniline/nanotube composites. *Materials Science and Engineering C*, *23*(1–2), 87–91. https://doi.org/10.1016/S0928-4931(02)00235-7

Mattana, G., & Briand, D. (2016). Recent advances in printed sensors on foil. *Materials Today*, *19*(2), 88–99. https://doi.org/10.1016/j.mattod.2015.08.001

Maxian, O., Pedrazzoli, D., & Manas-Zloczower, I. (2015). Modeling the electrical percolation behavior of hybrid nanocomposites based on carbon nanotubes and graphene nanoplatelets. *Materials Research Express*, *2*(9), 95013–95013. https://doi.org/10.1088/2053-1591/2/9/095013

Maxwell, K. S. (2013). *Computational analysis of carbon nanotube networks in multifunctional polymer nanocomposites*. (Doctoral dissertation, Texas A&M University).

McNally, T., Pötschke, P., Halley, P., Murphy, M., Martin, D., Bell, S. E. J., … Quinn, J. P. (2005). Polyethylene multiwalled carbon nanotube composites. *Polymer*, *46*(19), 8222–8232. https://doi.org/10.1016/j.polymer.2005.06.094

Meincke, O., Kaempfer, D., Weickmann, H., Friedrich, C., Vathauer, M., & Warth, H. (2004). Mechanical properties and electrical conductivity of carbon-nanotube filled polyamide-6 and its blends with acrylonitrile/butadiene/styrene. *Polymer*, *45*(3), 739–748. https://doi.org/10.1016/j.polymer.2003.12.013

Mejias-Morillo, C. R., Gbaguidi, A., Kim, D. W., Namilae, S., & Rojas-Nastrucci, E. A. (2019). UHF RFID-based additively manufactured passive wireless sensor for detecting micrometeoroid and orbital debris impacts. In *2019 IEEE International Conference on Wireless for Space and Extreme Environments, (WiSEE)* (pp. 41–47). https://doi.org/10.1109/WiSEE.2019.8920352

Meyyappan, M. (2005). *Carbon nanotubes: Science and applications* (1st ed.; M. Meyyappan, Ed.). New York: CRC Press.

Michelis, F., Bodelot, L., Bonnassieux, Y., & Lebental, B. (2015). Highly reproducible, hysteresis-free, flexible strain sensors by inkjet printing of carbon nanotubes. *Carbon*, *95*, 1020–1026. https://doi.org/10.1016/j.carbon.2015.08.103

Mikkonen, R. (2017). *Evaluation of commercially available silver inks* (Master's thesis, Tampere University of Technology). Retrieved from https://trepo.tuni.fi/bitstream/handle/123456789/24723/Mikkonen.pdf?sequence=4&isAllowed=y

Min, H., Sahu, B., Banerjee, S. K., & MacDonald, A. H. (2007). Ab initio theory of gate induced gaps in graphene bilayers. *Physical Review B - Condensed Matter and Materials Physics*, *75*(15), 155115. https://doi.org/10.1103/PhysRevB.75.155115

Minot, E. D., Yaish, Y., Sazonova, V., Park, J. Y., Brink, M., & McEuen, P. L. (2003). Tuning carbon nanotube band gaps with strain. *Physical Review Letters*, *90*(15), 4. https://doi.org/10.1103/PhysRevLett.90.156401

Mittal, G., Dhand, V., Rhee, K. Y., Park, S. J., & Lee, W. R. (2015). A review on carbon nanotubes and graphene as fillers in reinforced polymer nanocomposites. *Journal of Industrial and Engineering Chemistry*, *21*, 11–25. https://doi.org/10.1016/j.jiec.2014.03.022

Mittal, V. (2009). Polymer layered silicate nanocomposites: A review. *Materials*, *2*(3), 992–1057. https://doi.org/10.3390/ma2030992

Mittal, V. (2014). Functional polymer nanocomposites with graphene: A review. *Macromolecular Materials and Engineering*, *299*(8), 906–931. https://doi.org/10.1002/mame.201300394

Miyashita, H., Ono, T., & Esashi, M. (2003). Nanomechanical structures with an integrated carbon nanotube. In *TRANSDUCERS 2003 - 12th International Conference on Solid-State Sensors, Actuators and Microsystems, Digest of Technical Papers (Cat. No. 03TH8664)* (Vol. 1, pp. 182–185). https://doi.org/10.1109/SENSOR.2003.1215283

Moniruzzaman, M., & Winey, K. I. (2006). Polymer nanocomposites containing carbon nanotubes. *Macromolecules*, *39*(16), 5194–5205. https://doi.org/10.1021/ma060733p

Montazeri, A., Javadpour, J., Khavandi, A., Tcharkhtchi, A., & Mohajeri, A. (2010). Mechanical properties of multi-walled carbon nanotube/epoxy composites. *Materials and Design*, *31*(9), 4202–4208. https://doi.org/10.1016/j.matdes.2010.04.018

Monti, M., Rallini, M., Puglia, D., Peponi, L., Torre, L., & Kenny, J. M. (2013). Morphology and electrical properties of graphene-epoxy nanocomposites obtained by different solvent assisted processing methods. *Composites Part A: Applied Science and Manufacturing*, *46*(1), 166–172. https://doi.org/10.1016/j.compositesa.2012.11.005

Moriche, R., Jiménez-Suárez, A., Sánchez, M., Prolongo, S. G., & Ureña, A. (2017). Graphene nanoplatelets coated glass fibre fabrics as strain sensors. *Composites*

Science and Technology, *146*, 59–64. https://doi.org/10.1016/j.compscitech.2017.04.019

Moriche, R., Sánchez, M., Jiménez-Suárez, A., Prolongo, S. G., & Ureña, A. (2016). Strain monitoring mechanisms of sensors based on the addition of graphene nanoplatelets into an epoxy matrix. *Composites Science and Technology*, *123*, 65–70. https://doi.org/10.1016/j.compscitech.2015.12.002

Moujahid, E. M., Besse, J. P., & Leroux, F. (2003). Poly(styrene sulfonate) layered double hydroxide nanocomposites. Stability and subsequent structural transformation with changes in temperature. *Journal of Materials Chemistry*, *13*(2), 258–264. https://doi.org/10.1039/b208551h

Mutlay, I., & Tudoran, L. B. (2014). Percolation behavior of electrically conductive graphene nanoplatelets/polymer nanocomposites: Theory and experiment. *Fullerenes Nanotubes and Carbon Nanostructures*, *22*(5), 413–433. https://doi.org/10.1080/1536383X.2012.684186

Nagarajaiah, S., Li, Z., Dharap, P., & Barrera, E. V. (2008). Carbon nanotube film sensor. *Proceedings of the World Forum on Smart Materials and Smart Structures Technology, SMSST'07*, *16*(7), 345. https://doi.org/10.1002/adma.200306310

Namilae, S., Chandra, N., & Shet, C. (2004). Mechanical behavior of functionalized nanotubes. *Chemical Physics Letters*, *387*(4–6), 247–252. https://doi.org/10.1016/j.cplett.2004.01.104

Namilae, S., & Choudhary, S. (2018). Piezoresistive nanocomposites for sensing the effectiveness of composite patch repair. *Composites Communications*, *10*, 41–44. https://doi.org/10.1016/j.coco.2018.06.001

Nardelli, M. B., Yakobson, B. I., & Bernholc, J. (1998). Brittle and ductile behavior in carbon nanotubes. *Physical Review Letters*, *81*(21), 4656–4659. https://doi.org/10.1103/PhysRevLett.81.4656

Ni, X., Hui, C., Su, N., Cutler, R., & Liu, F. (2019). A 3D percolation model for multicomponent nanocarbon composites: The critical role of nematic transition. *Nanotechnology*, *30*(18), 185302. https://doi.org/10.1088/1361-6528/ab012f

Ni, X., Hui, C., Su, N., Jiang, W., & Liu, F. (2018). Monte Carlo simulations of electrical percolation in multicomponent thin films with nanofillers. *Nanotechnology*, *29*(7), 075401. https://doi.org/10.1088/1361-6528/aaa0be

Ni, Z. H., Yu, T., Lu, Y. H., Wang, Y. Y., Feng, Y. P., & Shen, Z. X. (2008). Uniaxial strain on graphene: Raman spectroscopy study and band-gap opening. *ACS Nano*, *2*(11), 2301–2305. https://doi.org/10.1021/nn800459e

Nishio, M., Sawaya, S., Akita, S., & Nakayama, Y. (2005). Carbon nanotube oscillators toward zeptogram detection. *Applied Physics Letters*, *86*(13), 1–3. https://doi.org/10.1063/1.1896426

Njuguna, M. (2012). *Characterisation of multi wall carbon nanotube–polymer composites for strain sensing applications* (Doctoral dissertation, Queensland University of Technology). Retrieved from http://eprints.qut.edu.au/54671

Nogales, A., Broza, G., Roslaniec, Z., Schulte, K., Šics, I., Hsiao, B. S., … Ezquerra, T. A. (2004). Low percolation threshold in nanocomposites based on oxidized single wall carbon nanotubes and poly(butylene terephthalate). *Macromolecules*, *37*(20), 7669–7672. https://doi.org/10.1021/ma049440r

Novoselov, K. S., Geim, A. K., Morozov, S. V., Jiang, D., Zhang, Y., Dubonos, S. V., … Firsov, A. A. (2004). Electric field in atomically thin carbon films. *Science*, *306*(5696), 666–669. https://doi.org/10.1126/science.1102896

O’Neill, A., Bakirtzis, D., & Dixon, D. (2014). Polyamide 6/graphene composites: The effect of in situ polymerisation on the structure and properties of graphene oxide and reduced graphene oxide. *European Polymer Journal*, *59*, 353–362. https://doi.org/10.1016/j.eurpolymj.2014.07.038

Oliva-Avilés, A. I., Avilés, F., & Sosa, V. (2011). Electrical and piezoresistive properties of multi-walled carbon nanotube/polymer composite films aligned by an electric field. *Carbon*, *49*(9), 2989–2997. https://doi.org/10.1016/j.carbon.2011.03.017

Oliva-Avilés, A. I., Sosa, V., & Avilés, F. (2013). Predicting the piezoresistance contribution of carbon nanotubes in a polymer matrix through finite element modeling. *Revista Mexicana de Fisica*, *59*(6), 511–516.

Oskouyi, A. B., & Mertiny, P. (2011). Monte Carlo model for the study of percolation thresholds in composites filled with circular conductive nano-disks. *Procedia Engineering*, *10*, 403–408. https://doi.org/10.1016/j.proeng.2011.04.068

Oskouyi, A. B., Sundararaj, U., & Mertiny, P. (2014a). Current-voltage characteristics of nanoplatelet-based conductive nanocomposites. *Nanoscale Research Letters*, *9*(1), 1–8. https://doi.org/10.1186/1556-276X-9-369

Oskouyi, A. B., Sundararaj, U., & Mertiny, P. (2014b). Tunneling conductivity and piezoresistivity of composites containing randomly dispersed conductive nano-platelets. *Materials*, *7*(4), 2501–2521. https://doi.org/10.3390/ma7042501

Ounaies, Z., Park, C., Wise, K. E., Siochi, E. J., & Harrison, J. S. (2003). Electrical properties of single wall carbon nanotube reinforced polyimide composites. *Composites Science and Technology*, *63*(11), 1637–1646. https://doi.org/10.1016/S0266-3538(03)00067-8

Paek, J., Kim, J., Wan An, B., Park, J., Ji, S., Kim, S. Y., … Park, J. U. (2017). Stretchable electronic devices using graphene and its hybrid nanostructures. *FlatChem*, *3*, 71–91. https://doi.org/10.1016/j.flatc.2017.06.002

Paleo, A. J., Van Hattum, F. W. J., Pereira, J., Rocha, J. G., Silva, J., Sencadas, V., & Lanceros-Méndez, S. (2010). The piezoresistive effect in polypropylene-carbon nanofibre composites obtained by shear extrusion. *Smart Materials and Structures*, *19*(6), 065013. https://doi.org/10.1088/0964-1726/19/6/065013

Palza, H., Garzón, C., & Arias, O. (2012). Modifying the electrical behaviour of polypropylene/carbon nanotube composites by adding a second nanoparticle and by annealing processes. *Express Polymer Letters*, *6*(8), 639–646. https://doi.org/10.3144/expresspolymlett.2012.68

Pang, H., Chen, T., Zhang, G., Zeng, B., & Li, Z. M. (2010). An electrically conducting polymer/graphene composite with a very low percolation threshold. *Materials Letters*, *64*(20), 2226–2229. https://doi.org/10.1016/j.matlet.2010.07.001

Papadakis, S. J., Hall, A. R., Williams, P. A., Vicci, L., Falvo, M. R., Superfine, R., & Washburn, S. (2004). Resonant oscillators with carbon-nanotube torsion springs. *Physical Review Letters*, *93*(14), 146101. https://doi.org/10.1103/PhysRevLett.93.146101

Papageorgiou, D. G., Kinloch, I. A., & Young, R. J. (2015). Graphene/elastomer nanocomposites. *Carbon*, *95*, 460–484. https://doi.org/10.1016/j.carbon.2015.08.055

Park, C., Wilkinson, J., Banda, S., Ounaies, Z., Wise, K. E., Sauti, G., … Harrison, J. S. (2006). Aligned single-wall carbon nanotube polymer composites using an electric field. *Journal of Polymer Science, Part B: Polymer Physics*, *44*(12), 1751–1762. https://doi.org/10.1002/polb.20823

Park, E. J., Kim, K. J., Park, D. W., & Shim, S. E. (2011). Colloidal heterocoagulation for preparation of multi-walled carbon nanotube/PMMA nanocomposite started with bulk resin. *Journal of Dispersion Science and Technology*, *32*(11), 1574–1581. https://doi.org/10.1080/01932691.2010.516415

Park, M., Kim, H., & Youngblood, J. P. (2008). Strain-dependent electrical resistance of multi-walled carbon nanotube/polymer composite films. *Nanotechnology*, *19*(5), 55705. https://doi.org/10.1088/0957-4484/19/05/055705

Pavlidou, S., & Papaspyrides, C. D. (2008). A review on polymer-layered silicate nanocomposites. *Progress in Polymer Science (Oxford)*, *33*(12), 1119–1198. https://doi.org/10.1016/j.progpolymsci.2008.07.008

Peigney, A., Laurent, C., Flahaut, E., Bacsa, R. R., & Rousset, A. (2001). Specific surface area of carbon nanotubes and bundles of carbon nanotubes. *Carbon*, *39*(4), 507–514. https://doi.org/10.1016/S0008-6223(00)00155-X

Peng, B., Locascio, M., Zapol, P., Li, S., Mielke, S. L., Schatz, G. C., & Espinosa, H. D. (2008). Measurements of near-ultimate strength for multiwalled carbon nanotubes and irradiation-induced crosslinking improvements. *Nature Nanotechnology*, *3*(10), 626–631. https://doi.org/10.1038/nnano.2008.211

Pham, G. T. (2008). *Characterization and modeling of piezo-resistive properties of carbon nanotube-based conductive polymer composites*. (Doctoral dissertation, Florida State University).

Pham, G. T., Park, Y. Bin, Liang, Z., Zhang, C., & Wang, B. (2008). Processing and modeling of conductive thermoplastic/carbon nanotube films for strain sensing. *Composites Part B: Engineering*, *39*(1), 209–216. https://doi.org/10.1016/j.compositesb.2007.02.024

Pham, V. H., Cuong, T. V., Hur, S. H., Shin, E. W., Kim, J. S., Chung, J. S., & Kim, E. J. (2010). Fast and simple fabrication of a large transparent chemically-converted graphene film by spray-coating. *Carbon*, *48*(7), 1945–1951. https://doi.org/10.1016/j.carbon.2010.01.062

Plyushch, A., Lamberti, P., Spinelli, G., Macutkevič, J., & Kuzhir, P. (2018). Numerical simulation of the percolation threshold in non-overlapping ellipsoid composites: Toward bottom-up approach for carbon based electromagnetic components realization. *Applied Sciences (Switzerland)*, *8*(6), 882. https://doi.org/10.3390/app8060882

Popov, A. M., Bichoutskaia, E., Lozovik, Y. E., & Kulish, A. S. (2007). Nanoelectromechanical systems based on multi-walled nanotubes: Nanothermometer, nanorelay, and nanoactuator. *Physica Status Solidi (A) Applications and Materials Science*, *204*(6), 1911–1917. https://doi.org/10.1002/pssa.200675322

Pothen, A., & Fan, C. J. (1990). Computing the block triangular form of a sparse matrix. *ACM Transactions on Mathematical Software (TOMS)*, *16*(4), 303–324. https://doi.org/10.1145/98267.98287

Pötschke, P., Abdel-Goad, M., Alig, I., Dudkin, S., & Lellinger, D. (2004). Rheological and dielectrical characterization of melt mixed polycarbonate-multiwalled carbon nanotube composites. *Polymer*, *45*(26), 8863–8870. https://doi.org/10.1016/j.polymer.2004.10.040

Pötschke, P., Bhattacharyya, A. R., & Janke, A. (2004). Carbon nanotube-filled polycarbonate composites produced by melt mixing and their use in blends with polyethylene. *Carbon*, *42*(5–6), 965–969. https://doi.org/10.1016/j.carbon.2003.12.001

Potts, J. R., Dreyer, D. R., Bielawski, C. W., & Ruoff, R. S. (2011). Graphene-based polymer nanocomposites. *Polymer*, *52*(1), 5–25. https://doi.org/10.1016/j.polymer.2010.11.042

Prakash, N., & Seidel, G. D. (2016). Electromechanical peridynamics modeling of piezoresistive response of carbon nanotube nanocomposites. *Computational Materials Science*, *113*, 154–170. https://doi.org/10.1016/j.commatsci.2015.11.008

Rahman, R., & Servati, P. (2012). Effects of inter-tube distance and alignment on tunnelling resistance and strain sensitivity of nanotube/polymer composite films. *Nanotechnology*, *23*(5), 55703. https://doi.org/10.1088/0957-4484/23/5/055703

Ramasubramaniam, R., Chen, J., & Liu, H. (2003). Homogeneous carbon nanotube/polymer composites for electrical applications. *Applied Physics Letters*, *83*(14), 2928–2930. https://doi.org/10.1063/1.1616976

Ravindran, A. R., Feng, C., Huang, S., Wang, Y., Zhao, Z., & Yang, J. (2018). Effects of graphene nanoplatelet size and surface area on the AC electrical conductivity and dielectric constant of epoxy nanocomposites. *Polymers*, *10*(5), 477. https://doi.org/10.3390/polym10050477

Rein, M. D., Breuer, O., & Wagner, H. D. (2011). Sensors and sensitivity: Carbon nanotube buckypaper films as strain sensing devices. *Composites Science and Technology*, *71*(3), 373–381. https://doi.org/10.1016/j.compscitech.2010.12.008

Ren, P. G., Di, Y. Y., Zhang, Q., Li, L., Pang, H., & Li, Z. M. (2012). Composites of ultrahigh-molecular-weight polyethylene with graphene sheets and/or MWCNTs with segregated network structure: Preparation and properties. *Macromolecular Materials and Engineering*, *297*(5), 437–443. https://doi.org/10.1002/mame.201100229

Robertson, D. H., Brenner, D. W., & Mintmire, J. W. (1992). Energetics of nanoscale graphitic tubules. *Physical Review B*, *45*(21), 12592–12595. https://doi.org/10.1103/PhysRevB.45.12592

Rochefort, A., Salahub, D. R., & Avouris, P. (1998). The effect of structural distortions on the electronic structure of carbon nanotubes. *Chemical Physics Letters*, *297*(1–2), 45–50. https://doi.org/10.1016/S0009-2614(98)01105-1

Rommes, J., & Schilders, W. H. A. (2010). Efficient methods for large resistor networks. *IEEE Transactions on Computer-Aided Design of Integrated Circuits and Systems*, *29*(1), 28–39. https://doi.org/10.1109/TCAD.2009.2034402

Rosca, I. D., & Hoa, S. V. (2009). Highly conductive multiwall carbon nanotube and epoxy composites produced by three-roll milling. *Carbon*, *47*(8), 1958–1968. https://doi.org/10.1016/j.carbon.2009.03.039

Roth, S., & Baughman, R. H. (2002). Actuators of individual carbon nanotubes. *Current Applied Physics*, *2*(4), 311–314. https://doi.org/10.1016/S1567-1739(02)00116-5

Rueckes, T., Kim, K., Joselevich, E., Tseng, G. Y., Cheung, C. L., & Lieber, C. M. (2000). Carbon nanotube-based nonvolatile random access memory for molecular computing. *Science*, *289*(5476), 94–97. https://doi.org/10.1126/science.289.5476.94

Safdari, M., & Al-Haik, M. (2012). Electrical conductivity of synergistically hybridized nanocomposites based on graphite nanoplatelets and carbon nanotubes. *Nanotechnology*, *23*(40), 405202. https://doi.org/10.1088/0957-4484/23/40/405202

Safdari, Masoud. (2012). *A computational and experimental study on the electrical and thermal properties of hybrid nanocomposites based on carbon nanotubes and graphite nanoplatelets* (Doctoral dissertation, Virginia Tech). Retrieved from https://vtechworks.lib.vt.edu/bitstream/handle/10919/49570/Safdari_M_D_2012.pdf?sequence=1&isAllowed=y

Safdari, Masoud, & Al-Haik, M. S. (2013). Synergistic electrical and thermal transport properties of hybrid polymeric nanocomposites based on carbon nanotubes and graphite nanoplatelets. *Carbon*, *64*, 111–121. https://doi.org/10.1016/j.carbon.2013.07.042

Sagalianov, I., Vovchenko, L., Matzui, L., & Lazarenko, O. (2017). Synergistic enhancement of the percolation threshold in hybrid polymeric nanocomposites based on carbon nanotubes and graphite nanoplatelets. *Nanoscale Research Letters*, *12*(1), 140. https://doi.org/10.1186/s11671-017-1909-z

Saini, P. (2013). Electrical properties and electromagnetic interference shielding response of electrically conducting thermosetting nanocomposites. In V. Mittal (Ed.), *Thermoset Nanocomposites* (pp. 211–237). https://doi.org/10.1002/9783527659647.ch10

Saini, P. (2015). Conjugated polymer blends, copolymers and composites: Synthesis, properties, and applications. In P. Saini (Ed.), *Fundamentals of Conjugated Polymer Blends, Copolymers and Composites: Synthesis, Properties, and Applications*. https://doi.org/10.1002/9781119137160

Salvetat, J. P., Bonard, J. M., Thomson, N. B., Kulik, A. J., Forró, L., Benoit, W., & Zuppiroli, L. (1999). Mechanical properties of carbon nanotubes. *Applied Physics A: Materials Science and Processing*, *69*(3), 255–260. https://doi.org/10.1007/s003390050999

Sanchez, M., Moriche, R., Prolongo, S. G., Rams, J., & Ureña, A. (2014). Graphene nanocomposites as strain-damage sensor. *16th European Conference on Composite Materials, ECCM 2014*, (June), 22–26. Retrieved from http://www.escm.eu.org/eccm16/assets/1075.pdf

Sandler, J. K. W., Kirk, J. E., Kinloch, I. A., Shaffer, M. S. P., & Windle, A. H. (2003). Ultra-low electrical percolation threshold in carbon-nanotube-epoxy composites. *Polymer*, *44*(19), 5893–5899. https://doi.org/10.1016/S0032-3861(03)00539-1

Sang, W. L., Dong, S. L., Morjan, R. E., Sung, H. J., Sveningsson, M., Nerushev, O. A., … Campbell, E. E. B. (2004). A three-terminal carbon nanorelay. *Nano Letters, 4*(10), 2027–2030. https://doi.org/10.1021/nl049053v

Schönenberger, C., Bachtold, A., Strunk, C., Salvetat, J. P., & Forró, L. (1999). Interference and interaction in multi-wall carbon nanotubes. *Applied Physics A: Materials Science and Processing*, *69*(3), 283–295. https://doi.org/10.1007/s003390051003

Seager, C. H., & Pike, G. E. (1974). Percolation and conductivity: A computer study. II. *Physical Review B, 10*(4), 1435–1446. https://doi.org/10.1103/PhysRevB.10.1435

Secor, E. B., Prabhumirashi, P. L., Puntambekar, K., Geier, M. L., & Hersam, M. C. (2013). Inkjet printing of high conductivity, flexible graphene patterns. *Journal of Physical Chemistry Letters, 4*(8), 1347–1351. https://doi.org/10.1021/jz400644c

Secretariat, E. (2008). *Space product assurance, thermal vacuum outgassing test for the screening of space materials*. Technical Report ECSS-Q-ST-70-02C, ESA-ESTEC Requirements & Standards.

Seidel, G. D., Boehringer, K. L., & Lagoudas, D. C. (2008). Analysis of clustering and interphase region effects on the electrical conductivity of carbon nanotube-polymer nanocomposites via computational micromechanics. In *Proceedings of the ASME Conference on Smart Materials, Adaptive Structures and Intelligent Systems, SMASIS2008* (pp. 159–165). https://doi.org/10.1115/SMASIS2008-670

Seifert, T., Sowade, E., Roscher, F., Wiemer, M., Gessner, T., & Baumann, R. R. (2015). Additive manufacturing technologies compared: Morphology of deposits of silver ink using inkjet and aerosol jet printing. *Industrial and Engineering Chemistry Research*, *54*(2), 769–779. https://doi.org/10.1021/ie503636c

Sennett, M., Welsh, E., Wright, J. B., Li, W. Z., Wen, J. G., & Ren, Z. F. (2003). Dispersion and alignment of carbon nanotubes in polycarbonate. *Applied Physics A: Materials Science and Processing, 76*(1), 111–113. https://doi.org/10.1007/s00339-002-1449-x

Seo, M. K., & Park, S. J. (2004). Electrical resistivity and rheological behaviors of carbon nanotubes-filled polypropylene composites. *Chemical Physics Letters*, *395*(1–3), 44–48. https://doi.org/10.1016/j.cplett.2004.07.047

Serra, N., Maeder, T., & Ryser, P. (2012). Piezoresistive effect in epoxy-graphite composites. *Sensors and Actuators, A: Physical*, *186*, 198–202.

https://doi.org/10.1016/j.sna.2012.04.025

Shang, S., Zeng, W., & Tao, X. M. (2011). High stretchable MWNTs/polyurethane conductive nanocomposites. *Journal of Materials Chemistry*, *21*(20), 7274–7280. https://doi.org/10.1039/c1jm10255a

Shen, J., Huang, W., Zuo, S., & Hou, J. (2005). Polyethylene/grafted polyethylene/graphite nanocomposites: Preparation, structure, and electrical properties. *Journal of Applied Polymer Science*, *97*(1), 51–59.

Simien, D., Fagan, J. A., Luo, W., Douglas, J. F., Migler, K., & Obrzut, J. (2008). Influence of nanotube length on the optical and conductivity properties of thin single-wall carbon nanotube networks. *ACS Nano*, *2*(9), 1879–1884. https://doi.org/10.1021/nn800376x

Simmons, J. G. (1963a). Electric tunnel effect between dissimilar electrodes separated by a thin insulating film. *Journal of Applied Physics*, *34*(9), 2581–2590. https://doi.org/10.1063/1.1729774

Simmons, J. G. (1963b). Generalized formula for the electric tunnel effect between similar electrodes separated by a thin insulating film. *Journal of Applied Physics*, *34*(6), 1793–1803. https://doi.org/10.1063/1.1702682

Singh, V., Joung, D., Zhai, L., Das, S., Khondaker, S. I., & Seal, S. (2011). Graphene based materials: Past, present and future. *Progress in Materials Science*, *56*(8), 1178–1271. https://doi.org/10.1016/j.pmatsci.2011.03.003

Smith, A. D., Niklaus, F., Paussa, A., Vaziri, S., Fischer, A. C., Sterner, M., … Lemme, M. C. (2013). Electromechanical piezoresistive sensing in suspended graphene membranes. *Nano Letters*, *13*(7), 3237–3242. https://doi.org/10.1021/nl401352k

Snow, E. S., Novak, J. P., Campbell, P. M., & Park, D. (2003). Random networks of carbon nanotubes as an electronic material. *Applied Physics Letters*, *82*(13), 2145–2147. https://doi.org/10.1063/1.1564291

Socher, R., Krause, B., Müller, M. T., Boldt, R., & Pötschke, P. (2012). The influence of matrix viscosity on MWCNT dispersion and electrical properties in different thermoplastic nanocomposites. *Polymer*, *53*(2), 495–504. https://doi.org/10.1016/j.polymer.2011.12.019

Son, Y. W., Cohen, M. L., & Louie, S. G. (2006). Energy gaps in graphene nanoribbons. *Physical Review Letters*, *97*(21), 216803. https://doi.org/10.1103/PhysRevLett.97.216803

Song, D., Mahajan, A., Secor, E. B., Hersam, M. C., Francis, L. F., & Frisbie, C. D. (2017). High-resolution transfer printing of graphene lines for fully printed, flexible electronics. *ACS Nano*, *11*(7), 7431–7439. https://doi.org/10.1021/acsnano.7b03795

Song, J. W., Kim, J., Yoon, Y. H., Choi, B. S., Kim, J. H., & Han, C. S. (2008). Inkjet printing of single-walled carbon nanotubes and electrical characterization of the line pattern. *Nanotechnology*, *19*(9), 095702. https://doi.org/10.1088/0957-4484/19/9/095702

Song, P., Cao, Z., Cai, Y., Zhao, L., Fang, Z., & Fu, S. (2011). Fabrication of exfoliated graphene-based polypropylene nanocomposites with enhanced mechanical and thermal properties. *Polymer*, *52*(18), 4001–4010. https://doi.org/10.1016/j.polymer.2011.06.045

Song, Y. S., & Youn, J. R. (2005). Influence of dispersion states of carbon nanotubes on physical properties of epoxy nanocomposites. *Carbon*, *43*(7), 1378–1385. https://doi.org/10.1016/j.carbon.2005.01.007

Soum, V., Park, S., Brilian, A. I., Kim, Y., Ryu, M. Y., Brazell, T., … Shin, K. (2019). Inkjet-printed carbon nanotubes for fabricating a spoof fingerprint on paper. *ACS Omega*, *4*(5), 8626–8631. https://doi.org/10.1021/acsomega.9b00936

Spinks, G. M., Wallace, G. G., Fifield, L. S., Dalton, L. R., Mazzoldi, A., De Rossi, D., … Baughman, R. H. (2002). Pneumatic carbon nanotube actuators. *Advanced Materials*, *14*(23), 1728–1732. https://doi.org/10.1002/1521-4095(20021203)14:23<1728::AID-ADMA1728>3.0.CO;2-8

Stampfer, C., Jungen, A., Linderman, R., Obergfell, D., Roth, S., & Hierold, C. (2006). Nano-electromechanical displacement sensing based on single-walled carbon nanotubes. *Nano Letters*, *6*(7), 1449–1453. https://doi.org/10.1021/nl0606527

Stampfer, R. C., Helbling, T., Obergfell, D., Schöberle, B., Tripp, M. K., Jungen, A., … Hierold, C. (2006). Fabrication of single-walled carbon-nanotube-based pressure sensors. *Nano Letters*, *6*(2), 233–237. https://doi.org/10.1021/nl052171d

Stankovich, S., Dikin, D. A., Dommett, G. H. B., Kohlhaas, K. M., Zimney, E. J., Stach, E. A., … Ruoff, R. S. (2006). Graphene-based composite materials. *Nature*, *442*(7100), 282–286. https://doi.org/10.1038/nature04969

Starr, F. W., Schrøder, T. B., & Glotzer, S. C. (2002). Molecular dynamics simulation of a polymer melt with a nanoscopic particle. *Macromolecules*, *35*(11), 4481–4492. https://doi.org/10.1021/ma010626p

Stauffer, D. (2009). Classical percolation. *Lecture Notes in Physics*, *762*, 1–19. https://doi.org/10.1007/978-3-540-85428-9_1

Studor, & George. (2007). Lessons learned JSC micro-wireless instrumentation systems on space shuttle and international space station CANEUS 2006. *NASA Johnson*

Space Center, Structural Engineering Division. Retrieved from https://ntrs.nasa.gov/archive/nasa/casi.ntrs.nasa.gov/20070022439.pdf

Sullivan, E. M., Flowers, R., Oh, Y. J., Gerhardt, R. A., Wang, B., & Kalaitzidou, K. (2015). The effect of processing on the electrical properties of exfoliated graphite nanoplatelet/polylactic acid nanocomposite films. In *Proceedings of the American Society for Composites - 30th Technical Conference, ACS 2015* (p. 1677). Retrieved from http://www.dpi-proceedings.com/index.php/ASC30/article/view/1426

Svedberg, T., & Pedersen, K. O. (1940). The ultracentrifuge. In *The Ultracentrifuge.* Oxford: Clarendon Press.

Takeda, T., Shindo, Y., Kuronuma, Y., & Narita, F. (2011). Modeling and characterization of the electrical conductivity of carbon nanotube-based polymer composites. *Polymer*, *52*(17), 3852–3856. https://doi.org/10.1016/j.polymer.2011.06.046

Tanaka, G., & Goettler, L. A. (2002). Predicting the binding energy for nylon 6,6/clay nanocomposites by molecular modeling. *Polymer*, *43*(2), 541–553. https://doi.org/10.1016/s1089-3156(01)00014-9

Taya, M., Kim, W. J., & Ono, K. (1998). Piezoresistivity of a short fiber/elastomer matrix composite. *Mechanics of Materials*, *28*(1–4), 53–59. https://doi.org/10.1016/S0167-6636(97)00064-1

Theodosiou, T. C., & Saravanos, D. A. (2010). Numerical investigation of mechanisms affecting the piezoresistive properties of CNT-doped polymers using multi-scale models. *Composites Science and Technology*, *70*(9), 1312–1320. https://doi.org/10.1016/j.compscitech.2010.04.003

Tian, H., Shu, Y., Cui, Y. L., Mi, W. T., Yang, Y., Xie, D., & Ren, T. L. (2014). Scalable fabrication of high-performance and flexible graphene strain sensors. *Nanoscale*, *6*(2), 699–705. https://doi.org/10.1039/c3nr04521h

Tombler, T. W., Zhou, C., Alexseyev, L., Kong, J., Dai, H., Liu, L., … Wu, S. Y. (2000). Reversible electromechanical characteristics of carbon nanotubes under local-probe manipulation. *Nature*, *405*(6788), 769–772. https://doi.org/10.1038/35015519

Tomori, H., Kanda, A., Goto, H., Ootuka, Y., Tsukagoshi, K., Moriyama, S., … Tsuya, D. (2011). Introducing nonuniform strain to graphene using dielectric nanopillars. *Applied Physics Express*, *4*(7), 075102. https://doi.org/10.1143/APEX.4.075102

Topinka, M. A., Rowell, M. W., Goldhaber-Gordon, D., McGehee, M. D., Hecht, D. S., & Gruner, G. (2009). Charge transport in interpenetrating networks of semiconducting and metallic carbon nanotubes. *Nano Letters*, *9*(5), 1866–1871. https://doi.org/10.1021/nl803849e

Torrisi, F., Hasan, T., Wu, W., Sun, Z., Lombardo, A., Kulmala, T. S., … Ferrari, A. C. (2012). Inkjet-printed graphene electronics. *ACS Nano*, *6*(4), 2992–3006. https://doi.org/10.1021/nn2044609

Tortorich, R., & Choi, J.-W. (2013). Inkjet printing of carbon nanotubes. *Nanomaterials*, *3*(3), 453–468. https://doi.org/10.3390/nano3030453

Tortorich, R. P. (2014). *Carbon nanotube inkjet printing for flexible electronics and chemical sensor applications* (Master's thesis, Louisiana State University). Retrieved from https://digitalcommons.lsu.edu/cgi/viewcontent.cgi?article=2809&context=gradschool_theses

Treacy, M. M. J., Ebbesen, T. W., & Gibson, J. M. (1996). Exceptionally high Young's modulus observed for individual carbon nanotubes. *Nature*, *381*(6584), 678–680. https://doi.org/10.1038/381678a0

Trichur, R. K. (2014). Next-generation printable conductive nanotube materials and sensors . *Coating International*, *47*(5), 18–19. Retrieved from https://www.scopus.com/inward/record.uri?eid=2-s2.0-84903481415&partnerID=40&md5=45db971b726345d2ac19f3f96b041c85

Ugarte, L., Gómez-Fernández, S., Tercjak, A., Martínez-Amesti, A., Corcuera, M. A., & Eceiza, A. (2017). Strain sensitive conductive polyurethane foam/graphene nanocomposites prepared by impregnation method. *European Polymer Journal*, *90*, 323–333. https://doi.org/10.1016/j.eurpolymj.2017.03.035

Ural, A., Li, Y., & Dai, H. (2002). Electric-field-aligned growth of single-walled carbon nanotubes on surfaces. *Applied Physics Letters*, *81*(18), 3464–3466. https://doi.org/10.1063/1.1518773

Vaisman, L., Wagner, H. D., & Marom, G. (2006). The role of surfactants in dispersion of carbon nanotubes. *Advances in Colloid and Interface Science*, *128*, 37–46. https://doi.org/10.1016/j.cis.2006.11.007

Varghese, S. S., Lonkar, S., Singh, K. K., Swaminathan, S., & Abdala, A. (2015). Recent advances in graphene based gas sensors. *Sensors and Actuators, B: Chemical*, *218*, 160–183. https://doi.org/10.1016/j.snb.2015.04.062

Vink, R. L. C., & Schilling, T. (2005). Interfacial tension of the isotropic-nematic interface in suspensions of soft spherocylinders. *Physical Review E - Statistical, Nonlinear, and Soft Matter Physics*, *71*(5), 051716. https://doi.org/10.1103/PhysRevE.71.051716

Walter, F., Bertoidl, F., Carilli, C., Cox, P., Lo, K. Y., Neri, R., … Menten, K. M. (2003). Molecular gas in the host galaxy of a quasar at redshift z = 6.42. *Nature*, *424*(6947), 406–408. https://doi.org/10.1038/nature01821

Walters, D. A., Ericson, L. M., Casavant, M. J., Liu, J., Colbert, D. T., Smith, K. A., & Smalley, R. E. (1999). Elastic strain of freely suspended single-wall carbon nanotube ropes. *Applied Physics Letters*, *74*(25), 3803–3805. https://doi.org/10.1063/1.124185

Wang, B., Lee, B. K., Kwak, M. J., & Lee, D. W. (2013). Graphene/polydimethylsiloxane nanocomposite strain sensor. *Review of Scientific Instruments*, *84*(10), 105005. https://doi.org/10.1063/1.4826496

Wang, Jialiang, Shi, Z., Ge, Y., Wang, Y., Fan, J., & Yin, J. (2012). Solvent exfoliated graphene for reinforcement of PMMA composites prepared by in situ polymerization. *Materials Chemistry and Physics*, *136*(1), 43–50. https://doi.org/10.1016/j.matchemphys.2012.06.017

Wang, Jingchao, Wang, X., Xu, C., Zhang, M., & Shang, X. (2011). Preparation of graphene/poly(vinyl alcohol) nanocomposites with enhanced mechanical properties and water resistance. *Polymer International*, *60*(5), 816–822. https://doi.org/10.1002/pi.3025

Wang, Q., & Liew, K. M. (2009). Mechanical properties of carbon nanotubes. *Carbon Nanotubes: New Research*, *327*(2001), 157–174. https://doi.org/10.24144/2415-8038.2004.16.104-108

Wang, Qing, Dai, J., Li, W., Wei, Z., & Jiang, J. (2008). The effects of CNT alignment on electrical conductivity and mechanical properties of SWNT/epoxy nanocomposites. *Composites Science and Technology*, *68*(7–8), 1644–1648. https://doi.org/10.1016/j.compscitech.2008.02.024

Wang, Shiren, Liang, Z., Wang, B., & Zhang, C. (2006). Statistical characterization of single-wall carbon nanotube length distribution. *Nanotechnology*, *17*(3), 634–639. https://doi.org/10.1088/0957-4484/17/3/003

Wang, Siliang, Liu, N., Tao, J., Yang, C., Liu, W., Shi, Y., … Gao, Y. (2015). Inkjet printing of conductive patterns and supercapacitors using a multi-walled carbon nanotube/Ag nanoparticle based ink. *Journal of Materials Chemistry A*, *3*(5), 2407–2413. https://doi.org/10.1039/c4ta05625f

Wang, W. P., & Pan, C. Y. (2004). Preparation and characterization of polystyrene/graphite composite prepared by cationic grafting polymerization. *Polymer*, *45*(12), 3987–3995. https://doi.org/10.1016/j.polymer.2004.04.023

Wang, Yan, Wang, L., Yang, T., Li, X., Zang, X., Zhu, M., … Zhu, H. (2014). Wearable and highly sensitive graphene strain sensors for human motion monitoring. *Advanced Functional Materials*, *24*(29), 4666–4670.

https://doi.org/10.1002/adfm.201400379

Wang, Yu, Di, C. A., Liu, Y., Kajiura, H., Ye, S., Cao, L., … Noda, K. (2008). Optimizing single-walled carbon nanotube films for applications in electroluminescent devices. *Advanced Materials*, *20*(23), 4442–4449. https://doi.org/10.1002/adma.200801088

Wang, Z., & Ye, X. (2013). A numerical investigation on piezoresistive behaviour of carbon nanotube/polymer composites: Mechanism and optimizing principle. *Nanotechnology*, *24*(26), 265704. https://doi.org/10.1088/0957-4484/24/26/265704

Watson, J. (2019). Carbon nanotubes market to reach USD 15.02 billion by 2026. Retrieved from https://www.globenewswire.com/news-release/2019/07/17/1884106/0/en/Carbon-Nanotubes-Market-To-Reach-USD-15-02-Billion-By-2026-Reports-And-Data.html

Wegrzyn, M., Ortega, A., Benedito, A., & Gimenez, E. (2015). Thermal and electrical conductivity of melt mixed polycarbonate hybrid composites co-filled with multi-walled carbon nanotubes and graphene nanoplatelets. *Journal of Applied Polymer Science*, *132*(37), 1–8. https://doi.org/10.1002/app.42536

White, S. I., DiDonna, B. A., Mu, M., Lubensky, T. C., & Winey, K. I. (2009). Simulations and electrical conductivity of percolated networks of finite rods with various degrees of axial alignment. *Physical Review B - Condensed Matter and Materials Physics*, *79*(2), 024301. https://doi.org/10.1103/PhysRevB.79.024301

Wichmann, M. H. G., Buschhorn, S. T., Böger, L., Adelung, R., & Schulte, K. (2008). Direction sensitive bending sensors based on multi-wall carbon nanotube/epoxy nanocomposites. *Nanotechnology*, *19*(47), 475503. https://doi.org/10.1088/0957-4484/19/47/475503

Wichmann, M. H. G., Buschhorn, S. T., Gehrmann, J., & Schulte, K. (2009). Piezoresistive response of epoxy composites with carbon nanoparticles under tensile load. *Physical Review B - Condensed Matter and Materials Physics*, *80*(24), 245437. https://doi.org/10.1103/PhysRevB.80.245437

Williams, P. A., Papadakis, S. J., Patel, A. M., Falvo, M. R., Washburn, S., & Superfine, R. (2003). Fabrication of nanometer-scale mechanical devices incorporating individual multiwalled carbon nanotubes as torsional springs. *Applied Physics Letters*, *82*(5), 805–807. https://doi.org/10.1063/1.1538346

Wong, E. W., Sheehan, P. E., & Lieber, C. M. (1997). Nanobeam mechanics: Elasticity, strength, and toughness of nanorods and nanotubes. *Science*, *277*(5334), 1971–1975. https://doi.org/10.1126/science.277.5334.1971

Woodard, S. E., Taylor, B. D., Jones, T. W., Shams, Q. A., Lyons, F., & Henderson, D. J.

(2011). Method to have multilayer thermal insulation provide damage detection. *Journal of Spacecraft and Rockets*, *48*(6), 920–930. https://doi.org/10.2514/1.44400

Wu, H., & Drzal, L. T. (2013). High thermally conductive graphite nanoplatelet/polyetherimide composite by precoating: Effect of percolation and particle size. *Polymer Composites*, *34*(12), 2148–2153. https://doi.org/10.1002/pc.22624

Wu, J., Huang, G., Li, H., Wu, S., Liu, Y., & Zheng, J. (2013). Enhanced mechanical and gas barrier properties of rubber nanocomposites with surface functionalized graphene oxide at low content. *Polymer*, *54*(7), 1930–1937. https://doi.org/10.1016/j.polymer.2013.01.049

Wu, Z. S., Ren, W., Gao, L., Liu, B., Jiang, C., & Cheng, H. M. (2009). Synthesis of high-quality graphene with a pre-determined number of layers. *Carbon*, *47*(2), 493–499. https://doi.org/10.1016/j.carbon.2008.10.031

Xu, W., Chen, H., & Lv, Z. (2010). A 2D elliptical model of random packing for aggregates in concrete. *Journal of Wuhan University of Technology-Mater. Sci. Ed.*, *25*(4), 717–720. https://doi.org/10.1007/s11595-010-0078-z

Xu, Y., Hennig, I., Freyberg, D., James Strudwick, A., Georg Schwab, M., Weitz, T., & Chih-Pei Cha, K. (2014). Inkjet-printed energy storage device using graphene/polyaniline inks. *Journal of Power Sources*, *248*, 483–488. https://doi.org/10.1016/j.jpowsour.2013.09.096

Yakobson, B. I., Brabec, C. J., & Bernholc, J. (1996). Nanomechanics of carbon tubes: Instabilities beyond linear response. *Physical Review Letters*, *76*(14), 2511–2514. https://doi.org/10.1103/PhysRevLett.76.2511

Yang, L., Staiculescu, D., R. Zhang, Wong, C. P., & Tentzeris, M. M. (2009). A novel “green” fully-integrated ultrasensitive RFID-enabled gas sensor utilizing inkjet-printed antennas and carbon nanotubes. In *IEEE Antennas and Propagation Society, AP-S International Symposium (Digest)* (pp. 1–4). https://doi.org/10.1109/APS.2009.5171787

Yang, Li, Zhang, R., Staiculescu, D., Wong, C. P., & Tentzeris, M. M. (2009). A novel conformal RFID-enabled module utilizing inkjet-printed antennas and carbon nanotubes for gas-detection applications. *IEEE Antennas and Wireless Propagation Letters*, *8*, 653–656. https://doi.org/10.1109/LAWP.2009.2024104

Yasuoka, T., Shimamura, Y., & Todoroki, A. (2007). Electrical resistance change under strain of CNF/flexible-epoxy composite. *Journal of the Japan Society for Composite Materials*, *33*(3), 95–103. https://doi.org/10.6089/jscm.33.95

Ye, L., Meng, X. Y., Ji, X., Li, Z. M., & Tang, J. H. (2009). Synthesis and characterization of expandable graphite-poly(methyl methacrylate) composite particles and their application to flame retardation of rigid polyurethane foams. *Polymer Degradation and Stability*, *94*(6), 971–979. https://doi.org/10.1016/j.polymdegradstab.2009.03.016

Yeo, W. H., Kim, Y. S., Lee, J., Ameen, A., Shi, L., Li, M., … Rogers, J. A. (2013). Multifunctional epidermal electronics printed directly onto the skin. *Advanced Materials*, *25*(20), 2773–2778. https://doi.org/10.1002/adma.201204426

Yi, Y. B., & Tawerghi, E. (2009). Geometric percolation thresholds of interpenetrating plates in three-dimensional space. *Physical Review E - Statistical, Nonlinear, and Soft Matter Physics*, *79*(4), 041134. https://doi.org/10.1103/PhysRevE.79.041134

Yin, G., Hu, N., Karube, Y., Liu, Y., Li, Y., & Fukunaga, H. (2011). A carbon nanotube/polymer strain sensor with linear and anti-symmetric piezoresistivity. *Journal of Composite Materials*, *45*(12), 1315–1323. https://doi.org/10.1177/0021998310393296

Yu, A., Ramesh, P., Sun, X., Bekyarova, E., Itkis, M. E., & Haddon, R. C. (2008). Enhanced thermal conductivity in a hybrid graphite nanoplatelet - Carbon nanotube filler for epoxy composites. *Advanced Materials*, *20*(24), 4740–4744. https://doi.org/10.1002/adma.200800401

Yu, C., Masarapu, C., Rong, J., Wei, B. Q. M., & Jiang, H. (2009). Stretchable supercapacitors based on buckled single-walled carbon nanotube macrofilms. *Advanced Materials*, *21*(47), 4793–4797. https://doi.org/10.1002/adma.200901775

Yu, J., Lu, K., Sourty, E., Grossiord, N., Koning, C. E., & Loos, J. (2007). Characterization of conductive multiwall carbon nanotube/polystyrene composites prepared by latex technology. *Carbon*, *45*(15), 2897–2903. https://doi.org/10.1016/j.carbon.2007.10.005

Yu, M. F., Files, B. S., Arepalli, S., & Ruoff, R. S. (2000). Tensile loading of ropes of single wall carbon nanotubes and their mechanical properties. *Physical Review Letters*, *84*(24), 5552–5555. https://doi.org/10.1103/PhysRevLett.84.5552

Yu, M. F., Lourie, O., Dyer, M. J., Moloni, K., Kelly, T. F., & Ruoff, R. S. (2000). Strength and breaking mechanism of multiwalled carbon nanotubes under tensile load. *Science*, *287*(5453), 637–640. https://doi.org/10.1126/science.287.5453.637

Yue, L., Pircheraghi, G., Monemian, S. A., & Manas-Zloczower, I. (2014). Epoxy composites with carbon nanotubes and graphene nanoplatelets - Dispersion and synergy effects. *Carbon*, *78*, 268–278. https://doi.org/10.1016/j.carbon.2014.07.003

Zeng, Q. H., Yu, A. B., & Lu, G. Q. (2008). Multiscale modeling and simulation of polymer nanocomposites. *Progress in Polymer Science (Oxford)*, *33*(2), 191–269.

https://doi.org/10.1016/j.progpolymsci.2007.09.002

Zettl, A. (2000). Extreme oxygen sensitivity of electronic properties of carbon nanotubes. *Science*, *287*(5459), 1801–1804. https://doi.org/10.1126/science.287.5459.1801

Zha, J. W., Zhang, B., Li, R. K. Y., & Dang, Z. M. (2016). High-performance strain sensors based on functionalized graphene nanoplates for damage monitoring. *Composites Science and Technology*, *123*, 32–38. https://doi.org/10.1016/j.compscitech.2015.11.028

Zhang, H. Bin, Zheng, W. G., Yan, Q., Yang, Y., Wang, J. W., Lu, Z. H., … Yu, Z. Z. (2010). Electrically conductive polyethylene terephthalate/graphene nanocomposites prepared by melt compounding. *Polymer*, *51*(5), 1191–1196. https://doi.org/10.1016/j.polymer.2010.01.027

Zhang, G., Chen, J., Deng, S. Z., She, J. C., & Xu, N. S. (2009). Damages of screen-printed carbon nanotube cold cathode during the field emission process. *Ultramicroscopy*, *109*(5), 385–389. https://doi.org/10.1016/j.ultramic.2008.11.002

Zhang, L., Tu, S., Wang, H., & Du, Q. (2018). Preparation of polymer/graphene oxide nanocomposites by a two-step strategy composed of in situ polymerization and melt processing. *Composites Science and Technology*, *154*, 1–7. https://doi.org/10.1016/j.compscitech.2017.10.030

Zhang, P., Ma, L., Fan, F., Zeng, Z., Peng, C., Loya, P. E., … Lou, J. (2014). Fracture toughness of graphene. *Nature Communications*, *5*, 3782. https://doi.org/10.1038/ncomms4782

Zhang, R., Zhang, Y., Zhang, Q., Xie, H., Qian, W., & Wei, F. (2013). Growth of half-meter long carbon nanotubes based on Schulz-Flory distribution. *ACS Nano*, *7*(7), 6156–6161. https://doi.org/10.1021/nn401995z

Zhang, T., Mubeen, S., Myung, N. V., & Deshusses, M. A. (2008). Recent progress in carbon nanotube-based gas sensors. *Nanotechnology*, *19*(33), 332001. https://doi.org/10.1088/0957-4484/19/33/332001

Zhang, W., Suhr, J., & Koratkar, N. (2006). Carbon nanotube/polycarbonate composites as multifunctional strain sensors. *Journal of Nanoscience and Nanotechnology*, *6*(4), 960–964. https://doi.org/10.1166/jnn.2006.171

Zhang, X., Li, Q., Holesinger, T. G., Arendt, P. N., Huang, J., Kirven, P. D., … Zhu, Y. (2007). Ultrastrong, stiff, and lightweight carbon-nanotube fibers. *Advanced Materials*, *19*(23), 4198–4201. https://doi.org/10.1002/adma.200700776

Zhao, D., Liu, T., Zhang, M., Chen, J. M., & Wang, B. (2012). Nanotube-enhanced aerosol-jet printed electronics for embedded sensing of composite structural health.

Materials Research Society Symposium Proceedings, *1407*, 177–182. https://doi.org/10.1557/opl.2012.708

Zhao, J., He, C., Yang, R., Shi, Z., Cheng, M., Yang, W., … Zhang, G. (2012). Ultra-sensitive strain sensors based on piezoresistive nanographene films. *Applied Physics Letters*, *101*(6), 063112. https://doi.org/10.1063/1.4742331

Zhao, J., Wang, G., Yang, R., Lu, X., Cheng, M., He, C., … Zhang, G. (2015). Tunable piezoresistivity of nanographene films for strain sensing. *ACS Nano*, *9*(2), 1622–1629. https://doi.org/10.1021/nn506341u

Zhao, J., Zhang, G. Y., & Shi, D. X. (2013). Review of graphene-based strain sensors. *Chinese Physics B*, *22*(5), 057701. https://doi.org/10.1088/1674-1056/22/5/057701

Zhao, Q., Nardelli, M. B., & Bernholc, J. (2002). Ultimate strength of carbon nanotubes: A theoretical study. *Physical Review B - Condensed Matter and Materials Physics*, *65*(14), 1–6. https://doi.org/10.1103/PhysRevB.65.144105

Zheng, W., Lu, X., & Wong, S. C. (2004). Electrical and mechanical properties of expanded graphite-reinforced high-density polyethylene. *Journal of Applied Polymer Science*, *91*(5), 2781–2788. https://doi.org/10.1002/app.13460

Zhou, H., Han, G., Xiao, Y., Chang, Y., & Zhai, H. J. (2015). A comparative study on long and short carbon nanotubes-incorporated polypyrrole/poly(sodium 4-styrenesulfonate) nanocomposites as high-performance supercapacitor electrodes. *Synthetic Metals*, *209*, 405–411. https://doi.org/10.1016/j.synthmet.2015.08.014

Zhu, Y., Murali, S., Stoller, M. D., Ganesh, K. J., Cai, W., Ferreira, P. J., … Ruoff, R. S. (2011). Carbon-based supercapacitors produced by activation of graphene. *Science*, *332*(6037), 1537–1541. https://doi.org/10.1126/science.1200770

APPENDIX A – LIST OF PUBLICATIONS

Journal Publications

Gbaguidi, A., Madiyar, F., Kim, D., & Namilae, S. (2020). Multifunctional Inkjet Printed Sensors for MMOD Impact Detection. *Smart Materials and Structures, 29*(8), 085052. https://doi.org/10.1088/1361-665X/ab98eb

Gbaguidi, A., Namilae, S., & Kim, D. (2020). Synergy Effect in Hybrid Nanocomposites Based on Carbon Nanotubes and Graphene Nanoplatelets. *Nanotechnology, 31*(25), 255704. https://doi.org/10.1088/1361-6528/ab7fcc

Gbaguidi, A., Namilae, S., & Kim, D. (2019). Stochastic percolation model for the effect of nanotube agglomeration on the conductivity and piezoresistivity of hybrid nanocomposites. *Computational Materials Science*, *166*, 9–19. https://doi.org/10.1016/j.commatsci.2019.04.045

Zhu, F., Lei, J., Du, X., Currier, P., Gbaguidi, A., & Sypeck, D. (2018). Crushing Behavior of Vehicle Battery Pouch Cell and Module: A Combined Experimental and Theoretical Study. *SAE International Journal of Materials and Manufacturing*, *11*(4), 341–348. https://doi.org/10.4271/2018-01-1446

Gbaguidi, A., Namilae, S., & Kim, D. (2018). Monte Carlo model for piezoresistivity of hybrid nanocomposites. *Journal of Engineering Materials and Technology, Transactions of the ASME*, *140*(1), 11007. https://doi.org/10.1115/1.4037024

Conference Presentations and Publications

Gbaguidi, A., Namilae, S., & Kim, D. (2020). Stochastic Percolation Network Model for Hybrid Nanocomposites. In *IEEE Aerospace Conference*, March 2020

Mejias-Morillo, C. R., Gbaguidi, A., Kim, D. W., Namilae, S., & Rojas-Nastrucci, E. A. (2019). UHF RFID-based additively manufactured passive wireless sensor for detecting micrometeoroid and orbital debris impacts. In *2019 IEEE International Conference on Wireless for Space and Extreme Environments, (WiSEE)* (pp. 41–47). https://doi.org/10.1109/WiSEE.2019.8920352

Gbaguidi, A., Namilae, S., & Kim, D. (2019). Numerical and experimental investigation of the sensitivity of carbon nanotube and graphene nanocomposites to mmod impact damage for inflatable structures. In *AIAA Scitech 2019 Forum* (p. 1461). https://doi.org/10.2514/6.2019-1461

Anees, M., Gbaguidi, A., Kim, D., & Namilae, S. (2018). Numerical and experimental investigation of matrix effect on sensing behavior of piezoresistive hybrid nanocomposites. In *Sensors and Smart Structures Technologies for Civil, Mechanical, and Aerospace Systems 2018* (Vol. 10598, p. 1059809).

https://doi.org/10.1117/12.2296715

Gbaguidi, A., Namilae, S., & Kim, D. (2018). Comparison of 3D and 2D monte carlo models for piezoresistive behavior of hybrid nanocomposites. In *2018 AIAA/ASCE/AHS/ASC Structures, Structural Dynamics, and Materials Conference* (p. 0908). https://doi.org/10.2514/6.2018-0908

Anees, M., Gbaguidi, A., Kim, D., & Namilae, S. (2017). Structural health monitoring of inflatable structures for MMOD impacts. In *Nondestructive Characterization and Monitoring of Advanced Materials, Aerospace, and Civil Infrastructure 2017* (Vol. 10169, p. 101690D). https://doi.org/10.1117/12.2260195

Gbaguidi, A., Anees, M., Namilae, S., & Kim, D. (2017). Dynamic piezoresistive response of hybrid nanocomposites. In *Sensors and Smart Structures Technologies for Civil, Mechanical, and Aerospace Systems 2017* (Vol. 10168, p. 1016817). https://doi.org/10.1117/12.2260208

Gbaguidi, A., Namilae, S., & Kim, D. (2017). Numerical and experimental investigation of the piezoresistive behavior of hybrid carbon nanotube sheet – Graphene nanocomposites. In *58th AIAA/ASCE/AHS/ASC Structures, Structural Dynamics, and Materials Conference* (p. 0795). https://doi.org/10.2514/6.2017-0795